ANL/CTR-76-3
Controlled Thermonuclear
Processes and Plasma
Physics (UC-20)

CTR Program
ARGONNE NATIONAL LABORATORY
9700 South Cass Avenue
Argonne, Illinois 60439

TOKAMAK EXPERIMENTAL POWER REACTOR CONCEPTUAL DESIGN

VOLUME II

Weston M. Stacey, Jr.—Project Manager
Mohamed A. Abdou
Peter J. Bertoncini
Christian C. Bolta
Jeffrey N. Brooks
Kenneth Evans, Jr.
John A. Fasolo
Jung C. Jung
Robert L. Kustom
Victor A. Maroni
Richard F. Mattas
Frederick E. Mills
Balabhadra Misra
John S. Moenich
Alfred Moretti
James H. Norem
John S. Patten
Walter F. Praeg
Peter Smelser
Dale L. Smith
Herbert C. Stevens
Larry Turner
Sou-Tien Wang
Carl K. Youngdahl

August, 1976

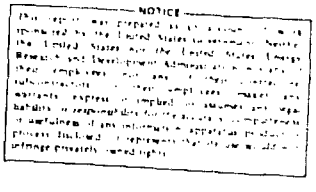

ABSTRACT

A conceptual design has been developed for a tokamak Experimental Power Reactor to operate at net electrical power conditions with a plant capacity factor of 50% for 10 years. The EPR operates in a pulsed mode at a frequency of 1/min., with a 75% duty cycle, is capable of producing ~ 72 MWe and requires 42 MWe. The annual tritium consumption is 16 kg.

The EPR vacuum chamber is 6.25 m in major radius and 2.4 m in minor radius, is constructed of 2-cm thick stainless steel, and has 2-cm thick detachable, beryllium-coated coolant panels mounted on the interior. An 0.25 m stainless steel blanket and a shield ranging from 0.6 to 1.0 m surround the vacuum vessel. The coolant is H_2O.

Sixteen niobium-titanium superconducting toroidal-field coils provide a field of 10 T at the coil and 4.47 T at the plasma. Superconducting ohmic-heating and equilibrium-field coils provide 135 V-s to drive the plasma current. Plasma heating is accomplished by 12 neutral beam injectors, which provide 60 MW. The energy transfer and storage system consists of a central superconducting storage ring, a homopolar energy storage unit, and a variety of inductor-converters.

TABLE OF CONTENTS

VOLUME I

LIST OF FIGURES

LIST OF TABLES

APPENDIX A

SUMMARY OF EPR DESIGN PARAMETERS

For conveneince of reference, the principle parameters that characterize the EPR design are summarized in this appendix. The design is discussed in Volume I.

Table A-1. Geometrical Parameters

Radius (m)	
Major, R_0	6.25
Plasma, a	2.1
First wall, r_w	2.4
Aspect ratio, A = R/a	2.98
Plasma volume (m^3)	544
Toroidal vacuum chamber volume (m^3)	711
First wall area (m^2)	592
Blanket thickness (m)	0.28
Shield thickness (m)	
Inside	0.58
Outside	0.97
Toroidal-field coils	
Number	16
Horizontal bore, R_{bore} (m)	7.78
Vertical bore, Z_{eff} (m)	12.6

Table A-2. Steady-State Plasma Parameters — Reference Design

Poloidal beta, β_p	1.7	
Total beta, β_t	0.048	
Safety factor		
Magnetic axis, q(0)	1.0	
Plasma surface, q(a)	3.05	
Plasma radius, a (m)	2.1	
Aspect ratio, A	2.98	
Average temperature $\overline{T}$ (keV)	10	
Effective ion charge, Z_{eff}	1.3	
Confinement for ignition, $n\tau_E$ (s/m^3)	2.4×10^{20}	
Peak field at TF coils, B_{max}^{TFC} (T)	10.0	8.0
Field at centerline, B_{t0} (T)	4.47	3.58
Plasma current, I_p (MA)	7.58	6.06
Average D-T ion density, $\overline{n}_{DT}$ (m^{-3})	9.4×10^{19}	6.0×10^{19}
Power output, P_T (MW)	638	261
Neutron wall load, P_w (MW/m^2)	0.86	0.35
Ratio of $n\tau_E$ required for ignition to TIM value of $n\tau_E$, α_{TIM}	1.0	4.0

Table A-3. Power Performance Parameters

Burn cycle	
Burn pulse (s)	55
Duty cycle (%)	75
Gross electrical power (MW)	72
Net electrical power (MW)	30
Plant availability (%)	67
Design lifetime	
Integrated neutron wall load (MW-yr/m^2)	2.5
Years	10

Table A-4. Toroidal-Field Coil System

Superconductor/Stabilizer/ Insulator/Support	Nb-Ti/Cu/ fiberglass epoxy/SS
Number of coils	16
Coil shape	Pure tension R_{10} = 2.45 m R_{20} = 11.1 m
Field ripple (%)	1.3
Maximum access (m)	∿ 3
Peak field (T)	10 at 3°K 8 at 4.2°K
Bore (m)	
Vertical	12.6
Horizontal	7.78
Field in plasma, B_f (T)	
10 T peak field	4.32
8 T peak field	3.46
Stability	Cryostatic
Temperature allowance (°K)	0.5
Conductor design	Monolithic
Cooling	Pool boiling
Operational current (kA/turn)	60

(Continued)

Table A-4. Toroidal-Field Coil System (Continued)

Stored energy (GJ)	
Total	30
Coil	1.875
Inductance (H)	
Total	16.7
Coil	1.04
Ampere-turns (MAT)	
Total	134
Coil	9.37
Turns/coil	70 × 2
Mean turn length (m)	36
Total conductor length/coil (A-m)	151.2×10^6
Coil weight/coil (Ton)	∿ 208
Coil and bobbin cross section (m^2)	0.619
Bobbin	
Material	316 SS
Thickness (cm)	1.25
Winding cross section (m^2)	0.572
Average current density (A/cm^2)	
Over bobbin and coil	1352
Over coil winding	1463
Over copper	3660
Smallest radius of curvature at ∿ 10 T field region (m)	1.98
Average hoop force/turn (lb)	133×10^3
Average turn cross section (cm^2)	40.6
Cross section ratio, SS/Cu	∿ 1.5
Overall average stress (psi)	
Stainless steel	26,000
Copper	14,500
Length of straight segment (m)	8.56
Compressive pressure (psi)	7,660
Circumferential stress (psi)	< 74,000
Refrigeration power (MW)	14.3

Table A-5. OH/EF Coil Magnet System

	OH Coil	EF Coil
Superconductor/stabilizer	Nb-Ti/Cu	
Coil design	Single layer	
Conductor design	Fully transposed cable	
Stability	Cryostatic	
Cooling	Pool boiling	
Operating temperature (°K)	4.2	
Average current density (A/cm^2)	2640	2946
Magnetic field (T)		
At flux core	∿ 5	
At plasma center		∿ 0.46
Ampere-turns (MAT)	67	± 18.6
Total conductor length (MA meters)	847	996
Maximum dB/dt in conductor (T/s)	6.7	∿ 1
Stored energy in OH/EF/plasma field (MJ)	2262	
Maximum operational current (kA)	80	80
Number of turns	837	464
Self-inductance (H)	0.48	0.52
Mutual coupling	$K_{OHEF} = 0.0158$	
Power supply voltage (kV)	48	21
Volt-seconds to plasma (V-s)	85	50
Coupling coefficient to plasma ring	$K_{OHP} = -0.2422$	$K_{EFP} = -0.2566$

Table A-6. Neutral Beam Injection System

	(Reference) Design 1	Design 2	Design 3a	Design 3b
Atomic ion	D^+	D^+	D^-	D^-
Target for $D^{\pm} \rightarrow D^o$	D_2 gas	D_2 gas	D_2 gas	Li plasma
Beam composition (D^+, D_2^+, D_3^+/D^-)	(0.75,0.18,0.07/-)	(0.95,0.03,0.2/-)	(-/0.95)	(-/0.95)
Neutral beam power (MW)	60	60	60	60
Neutral beam energy (keV)	180	180	180	180
Neutral beam current (Equiv. A)	333	333	333	333
Number of injectors	12	12	6	6
Number of ion sources/injector	2	2	2	2
Type of grid	multiaperture	multiaperture	multiaperture	multiaperture
Ion beam current density (A/cm^2)	0.135	0.175	0.135	0.135
Ion beam power (MW)	441	338	113	81
Gas load/injector (Torr-ℓ)	110	57	41	11
Direct conversion efficiency	0.85	0.85	0.85	0.85
Thermal conversion efficiency	0.30	0.30	0.30	0.30
Electrical power efficiency	0.29	0.41	0.66	0.77
Overall power efficiency	0.34	0.45	0.66	0.77
Net power input (MW)	207	145	91	78

Table A-7. RF Heating System

	ICRH	LHRH
Pump frequency (MHz)		
8 T	54.0	1120
10 T	68.6	1190
Output power (MW)		
4 ports	25	25
10 ports	60	60
Transmission efficiency from source to port (%)	64	48
Pulse duration, heating (s)		
25 MW	12.9	12.9
60 MW	5.4	5.4
Duty cycle (%)		
25 MW	17.2	17.2
60 MW	7.2	7.2
Launcher	1/4 turn loops	"Grill" waveguide 8 across by 2 high
Transmission scheme	Coaxial cables	Waveguides
High power source	Tetrode amplifier	Klystron

Table A-8. Energy Transfer and Storage Systems — Maximum Ratings

Ohmic Heating Systems	
Drum homopolar generators	
Number of generators in series	16
Number of drums/generator	6
Total energy transfer (MJ)	1200
Peak power (MW)	1900
Peak voltage (kV)	51
Peak current (kA)	68
Equivalent capacitance (F)	0.897
Rectifier system	
Type	Inductor-converter bridge
Energy transfer (MJ)	600
Peak power (MW)	66
Peak current (kA)	80
Peak voltage (kV)	0.8
Equilibrium Field System	
Type	Inductor-converter bridge
Energy transfer (MJ)	1500
Peak power (MW)	416
Peak current (kA)	80
Peak voltage (kV)	21
Peak switching frequency (Hz)	1330
Neutral Beam System[a,b]	
Type	SCR, dc/ac/dc at 10 kHz
Energy transfer (GJ)	1
Voltage (kV)	180
Power (MW)	207
RF System (60 MW)[b]	
Type	5-phase inductor-converter bridge
Voltage (kV)	
ICR	18.0
LHR	64.5
Power (MW)	
ICR	94
LHR	125
Central Energy Storage Inductor	
Type	Superconductive ring dipole inductor
Energy stored (GJ)	3.2
Energy transfer (GJ)	2.4
Peak current (kA)	80
Peak power (MW)	620
Average power from 60 Hz line (MW)	21

[a] Assumes electrical energy recovery in power supply.

[b] Neutral beam and rf are alternative options.

Table A-9. Vacuum Systems

	Toroidal	Neutral Beam
Volume	754 m^3	250 m^3/injector
Surface area	771 m^2	254 m^2/injector
Gas load	2588 Torr-ℓ	110 Torr-ℓ/s per injector
Cryosorption pumping	32 - 25,000 ℓ/s pumps	100 m^2 panel/injector
Effective pumping speed	4.25×10^5 ℓ/s	5×10^6 ℓ/s per injector
Secondary pumps		
Al/Zr getter pumps	32 - 10,000 ℓ/s	12 - 25,000 ℓ/s
Number of 1300 CFM blower stations	16	Use same pumps
Number of 1400 ℓ/s turbomolecular pumps	16	Use same pumps

Table A-10. First-Wall System

Design Description

- Free-standing, stainless steel vacuum wall with rib and spar reinforcing.
- Detachable, water-cooled stainless steel panels to shield vacuum wall from plasma.
- Low-Z coating on plasma-exposed face of coolant panel for high-Z impurity control.

Design Parameters

Vacuum chamber	
Material	316 SS
Design stress (ksi)	10
Major radius (m)	6.25
Minor radius (m)	2.4
Volume (m^3)	711
Wall area (m^2)	592
Wall thickness (cm)	2
Ring and spar (cm)	
Width	5
Depth	11
Ports	
Vacuum (0.95 m diameter)	32
Heating (0.75 m diameter)	16
Experimental (1.5 m diameter)	4
Total port area (m^2)	31
Current breaker	
Material	Cr_2O_3
Form	Coating
Preparation	Chemical bond
Coolant panel	
Material	316 SS
Number	352
Area per panel (m^2)	1-2
Length (m)	1-2
Width (m)	$\sim$ 1
Total panel thickness (cm)	$\sim$ 1
Front wall thickness (cm)	0.5
Low-Z coating	
Material	Beryllium
Thickness (μm)	100-200
Preparation	Plasma spray
Coolant	H_2O

Table A-11. First-Wall Operating Parameters and Design Limits*

Nominal Operating Conditions	
Capacity factor (%)	50
Operating cycle (s)	
Startup	5
Burn	35
Shutdown	5
Exhaust and replenishment	15
Average power loading during burn (MW/m^2)	
Neutron	0.5
Radiation, conduction, convection	0.13
Operating Parameters	
Stainless steel vacuum wall	
Maximum temperature (°C)	< 500
Minimum yield stress at 500°C (ksi)	17
Maximum annual fluence (n/m^2)	6×10^{25}
Neutron damage (dpa/yr)	2.8
Helium generation (appm/yr)	54
Hydrogen generation (appm/yr)	133
Stainless steel coolant panel	
Maximum temperature (°C)	380
Minimum yield stress at 500°C (ksi)	17
Maximum annual fluence (n/m^2)	6×10^{25}
Neutron damage (dpa/yr)	2.8
Helium generation (appm/yr)	54
Hydrogen generation (appm/yr)	133
Maximum heat deposition (W/cm^3)	5.8
Maximum ΔT across panel surface (°C)	20
Maximum ΔT through panel face (°C)	
With argon shutdown	100
Without argon shutdown	75
Maximum ΔT during burn cycle (°C)	100
Maximum thermal strain range (%)	
Operating cycle	0.14
Burn cycle	0.09

Continued

* Based on a neutron wall load of 0.5 MW/m^2 and a plant capacity factor of 50%.

Table A-11. First-Wall Operating Parameters and Design Limits* (Continued)

Operating Parameters (Continued)	
Beryllium coating	
Maximum surface temperature (°C)	407
Helium generation (appm/yr)	780
Hydrogen generation (appm/yr)	13
Maximum erosion rate (μm/yr)	30
Water coolant	
Maximum pressure (psi)	2000
Velocity (m/s)	1.6
Inlet temperature — first panel (°C)	40
Exit temperature — eighth panel (°C)	310
Pumping power (MW)	<1
Vacuum wall	
Design life (yr)	10
Integrated neutron wall loading (MW-yr/m^2)	2.5
Yield strength — 10 yr (ksi)	75
Uniform elongation — 10 yr (%)	~1
Radiation swelling — 10 yr (%)	~4
Limiting criterion	Ductility
Coolant panel	
Design life (yr)	5
Total burn cycles — 5 yr	10^6
Fatigue lifetime (yr)	5
Radiation lifetime (yr)	8
Limiting criterion	Thermal fatigue
Low-Z coating	
Design life (yr)	3-5
Limiting criterion	D-T sputtering

*Based on a neutron wall load of 0.5 MW/m^2 and a plant capacity factor of 50%.

Table A-12. Blanket System

Design basis operating life (yr)	10
Nominal power during burn (MW)	400
Design basis neutron wall loading (MW/m^2)	0.5
Plant capacity factor (%)	50
Blanket structure	
Thickness (m)	0.28
Type metal/volume fraction	316-SS/0.9
Type coolant/volume fraction	H_2O/$\leq$ 0.05
Penetration volume fraction	
Inner blanket	$\sim$ 0.02
Outer blanket	$\sim$ 0.05
Maximum temperatures (°C)	
In support structures	500
In bulk materials	550
Nuclear parameters	
Maximum heat deposition (W/cm^3)	3.5
Maximum fluence at 2.5 MW-yr/m^2 (n/m^2)	5×10^{26}
Maximum dpa at 2.5 MW-yr/m^2 (dpa)	17
Maximum helium production at 2.5 MW-yr/m^2 (appm)	230
Maximum hydrogen production at 2.5 MW-yr/m^2 (appm)	600
Mechanical parameters	
Design stress in support structure (ksi)	$\leq$ 10
Minimum material yield stress (ksi)	20
Ductility at 2.5 MW-yr/m^2 (% uniform elongation)	$\geq$ 3
Swelling at 2.5 MW-yr/m^2 (% of initial volume)	$\leq$ 2
Maximum torque from pulsed fields (ft-lb)	125,000
Coolant parameters	
Type	H_2O
Maximum pressure (psig)	2000
Pressure drop (psig)	< 15
Maximum velocity (m/s)	2.4
Pumping power (MW)	< 1
Coolant inlet temperature (°C)	40
Maximum coolant exit temperature (°C)	309
Residual activity from the first wall/blanket/shield after two years of operation in Ci/MWt	
Immediately after shutdown	3.5×10^6
1 year after removal	8.0×10^5
10 years after removal	7.0×10^4
100 years after removal	60

Table A-13. Shield System

Design basis operating life (yr)	10
Shield structure	
Thickness (m)	
Inner bulk shield	0.58
Outer bulk shield	0.97
Beam duct shield	0.75
Evacuation duct shield (movable plug)	0.90
Biological shield	1.5
Materials	
Inner shield	304-SS/B_4C
Outer shield	304-SS/Pb mortar/C/Al
Beam duct shield	304-SS/B_4C/Pb/Al
Evacuation duct shield (movable plug)	306-SS/B_4C
Biological shield	Concrete
Temperature (°C)	$\leq$ 90°C
Coolant	H_2O
Maximum torque from pulsed fields (ft-lb)	253,000
Maximum nuclear heating in bulk shield (W/cm^3)	0.3
Fraction of fusion power deposited in shield	$\sim$ 0.07
Maximum energy current at outer surface of bulk shield (W/cm^2)	
Neutrons	$\sim 2 \times 10^{-4}$
Gammas	$\sim 5 \times 10^{-5}$

Table A-14. Tritium-Handling System

	B_{max}^{TFC}	
	8 T	10 T
General		
Power during burn (MW)	200	500
Burn cycle duty cycle (%)	75	75
Plant availability factor (%)	67	67
Tritium burnup (g/day)	26	64
Throughput/burnup ratio	50	50
Tritium delivery rate (g/hr)	60	150
Fuel cycle turnaround time (hr)	4	4
Plant inventory (kg)	0.6	0.6
Annual tritium consumption at 50% capacity factor (kg)	6.4	16
Tritium Inventory Disposition		
Cryosorption pumps (g)	240[a]	600[a]
Getter beds (g)	240[a]	600[a]
Distillation columns (g)	10[a]	25[a]
Fuel cycle hardware (g)	10[a]	25[a]
Storage (g)	∿ 500[a]	∿ 1300[a]
Anticipated mean inventory (g)	600	1500
Fuel Cycle		
Nature of fuel processing and recycle systems	Nonmetallic element removal Debris removal Isotopic enrichment Fuel storage Fuel delivery	
Type of mainstream enrichment	Cryogenic distillation	
Number of columns	6	
Number of equilibrators	1	

[a] Maximum value at any single time.

Table A-15. Plant Capital Investment Direct Cost Estimate

	$M*
Structures and Site Facilities	67.3
Reactor	248.6
Reactor Plant Facilities	245.0
Auxiliaries	18.0
Total	578.9
Engineering (25%)	144.7
Contingency	144.7
Grand Total	868.3

* FY 1976 dollars.

APPENDIX B

IMPURITY CONTROL

The problem of plasma contamination by wall-sputtered impurities in the EPR is examined in this appendix. A critical review of the relevant surface data is incorporated in a plasma-wall interaction model that is employed, together with a plasma power and particle balance model. In the analysis, impurity control by charged-particle diversion and by modification of the first-wall surface are simulated, and the adequacy of these methods for the EPR is assessed.

A major purpose of this work is to determine if modification of the first-wall surface can provide adequate impurity control for near-term tokamak reactors, in general, and the EPR, in particular. A qualitative assessment of the technological feasibility and limitations of a low-Z coating, a low-Z separated liner, a carbon curtain, and a low-sputter coating is presented.

It is concluded from these studies that adequate control of sputtered impurities to sustain burn pulses on the order of a minute and to achieve net power conditions can be obtained in the EPR by suitable modification of the first wall surface. Of the wall modifications considered, a low-Z material (e.g. beryllium) coated on a structural substrate appears the most feasible technologically.

1. Computational Model

The basic computational model consists of a set of time-dependent, space-independent particle and power balance equations for the plasma, and a plasma-wall interaction model. Coupled balance equations for D-T ions, alpha particles, wall-sputtered impurities, electron temperature and ion temperature are solved. Neutral beam and fusion-alpha heating and power loss by radiation and transport are treated. Transport processes within the plasma are modeled with particle and energy confinement parameters which are computed from a multi-regime (pseudo-classical, neoclassical, trapped-particle-mode) model depending upon the value of the collision frequency. Details of the plasma balance equations are given in Appendix C.

The plasma-wall interaction model is depicted schematically in Figure B-1. Charged (D^+, T^+, He^{++}, impurity) and neutral (D^0, T^0, n) particle fluxes emerg

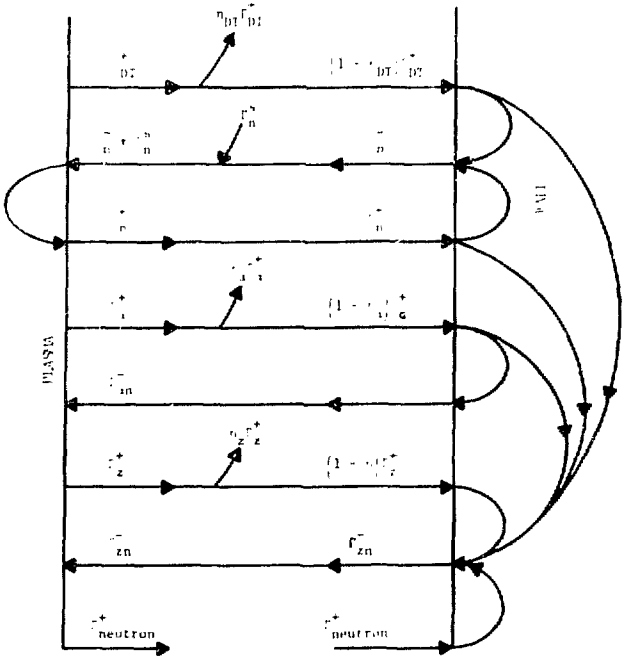

Balance Equations:

$$\Gamma_n^+ = \Gamma_{n(x}^- A_{cx} + \Gamma_{n(x}^{s} A_{cx}^{b}$$

$$\Gamma_n^- = \Gamma_n^+ \cdot R_n + (1 - \eta_{DT})\Gamma_{DT}^+ + \Gamma_{DT}$$

$$\Gamma_{\alpha n}^- = (1 - \eta_\alpha)\Gamma_\alpha^+ + S_\alpha$$

$$\Gamma_{zn}^- = (1 - \eta_{DT})\Gamma_{DT}^+ + S_{DT} \cdot \Gamma_n^+ + S_n$$

$$+ (1 - \eta_\alpha)\Gamma_\alpha^+ + S_\alpha + (1 - \eta_z)\Gamma_z^+ + (S_z + R_z)$$

$$\Gamma_{neutron}^+ = S_{neutron}$$

Subscripts:

n	neutral D-T atom
DT	D-T ions
α	alpha
αn	neutral helium atom
z	impurity ions
zn	neutral impurity atom

Definitions:

$\Gamma^{+/-}$ = outward/inward particle flux.

Γ^{s} = *external neutral D-T source.*

A_{cx} = charge-exchange re-emission probability.

R = wall reflection coefficient

S = wall sputtering coefficient.

η = charged particle removal efficiency.

Figure B-1. Plasma-Wall Interaction Model

from the plasma and strike the wall, with the charged particle fluxes being reduced by a factor η due to particle removal (e.g. by a divertor). A fraction of these particles are reflected, predominantly as neutrals, from the wall with reflection coefficient R.* The impinging particles produce wall erosion by sputtering with coefficient S. The returning particles are either ionized in the plasma or may initiate a series of charge-exchange interactions leading to the re-emergence of a D^0 or T^0 from the plasma with a probability A_{cx} which depends upon the relative charge-exchange and ionization cross sections and upon neutral transport.

Energy-dependent physical sputtering coefficients for the incident particles, viz., D^+, T^+, He^{++}, and impurity ions, on candidate first-wall materials are used for the calculation. Since insufficient experimental sputtering data are available for the range of parameters of interest (1-5 are general references that give a good indication of the state of technology), the sputtering coefficients used for the calculation have been developed from both theoretical and empirical considerations. The shapes of the energy-dependent sputtering curves are developed primarily from Sigmund's theory[6] and the magnitude of the coefficients have been adjusted in some cases to better conform with available experimental data.

Since the Sigmund theory does not adequately predict light ion sputtering at low energies, energy-dependent sputtering yield curves for light ions (deutrium, tritium, and helium) have been obtained by combining the theoretical curve at higher energies with an empirical relation for the lower ion energies.[7] The empirical curve assumes a direct energy dependence of the sputtering yield, which is in general agreement with reported helium sputtering data for a number of target materials.[8] The transition between the two segments forms a peak in the sputter curve at the ionization cut-off energy calculated from the Kinchin-Pease theory.[9] The threshold energies for sputtering have been determined by the method of Hotston.[10] Since the curves developed in this manner[7] give yields that are substantially higher than experimentally observed yields, these curves have been adjusted in magnitude to better conform to the available experimental data. Curves for the deuterium and tritium sputtering yields have been reduced by one order of magnitude and those for helium have been reduced by a factor of five. Figures B-2 to B-4 are the resultant mono-energetic sputtering curves for

*R includes backscattering and re-emission.

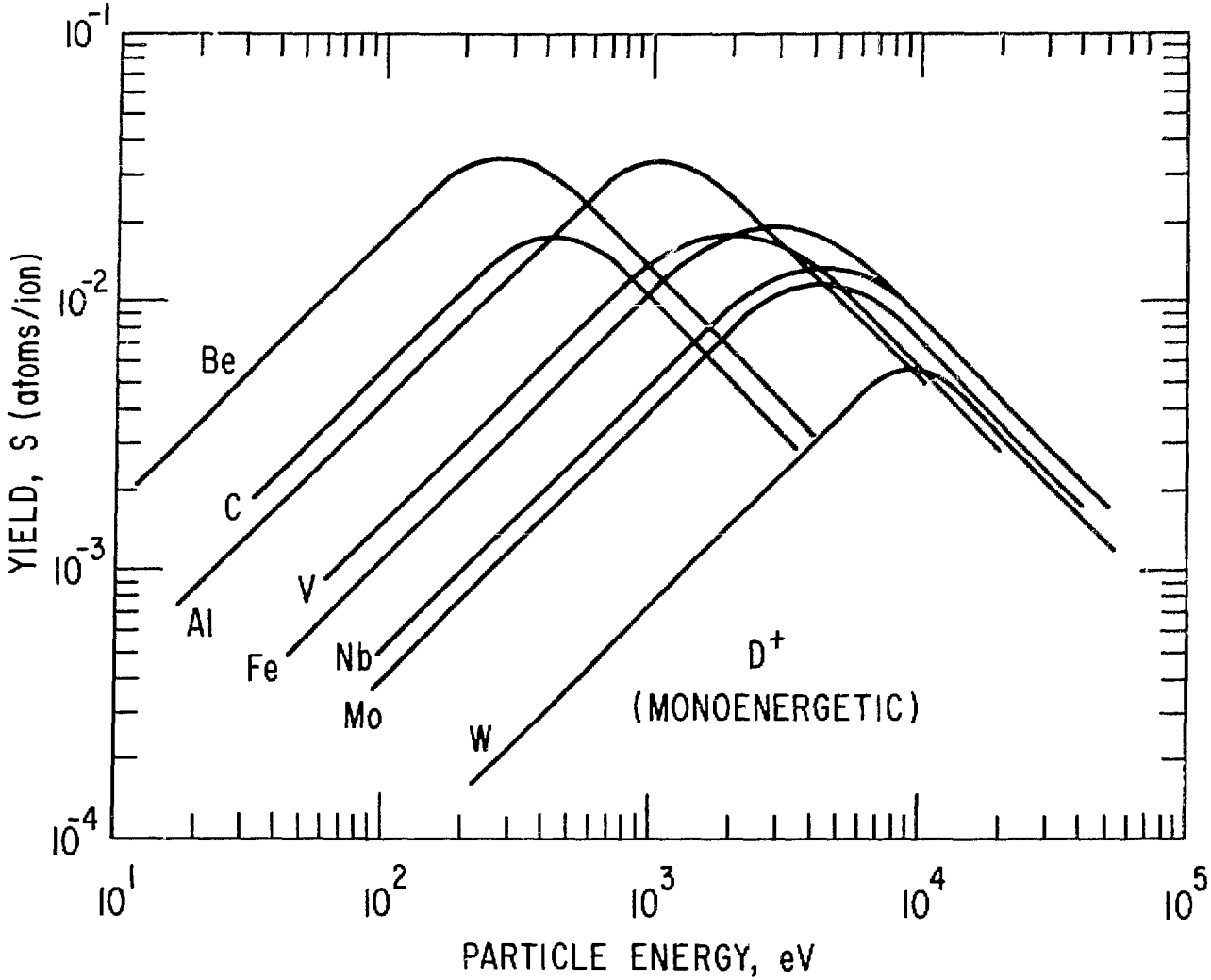

Figure B-2. Energy-dependent physical sputtering yields of potential first-wall materials irradiated with monoenergetic D^+ ions.

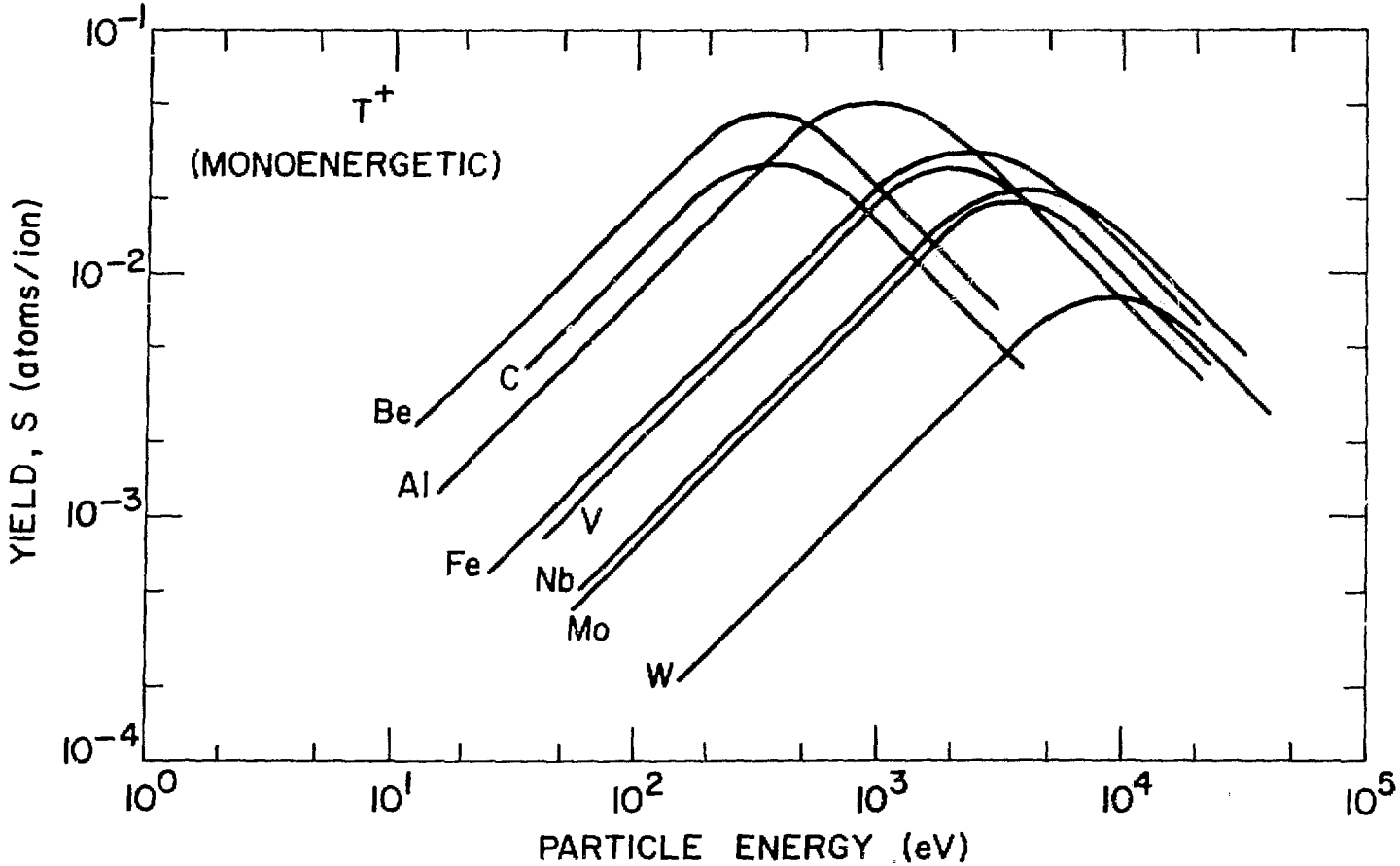

Figure B-3. Energy-dependent physical sputtering yields of potential first-wall materials irradiated with monoenergetic T^+ ions

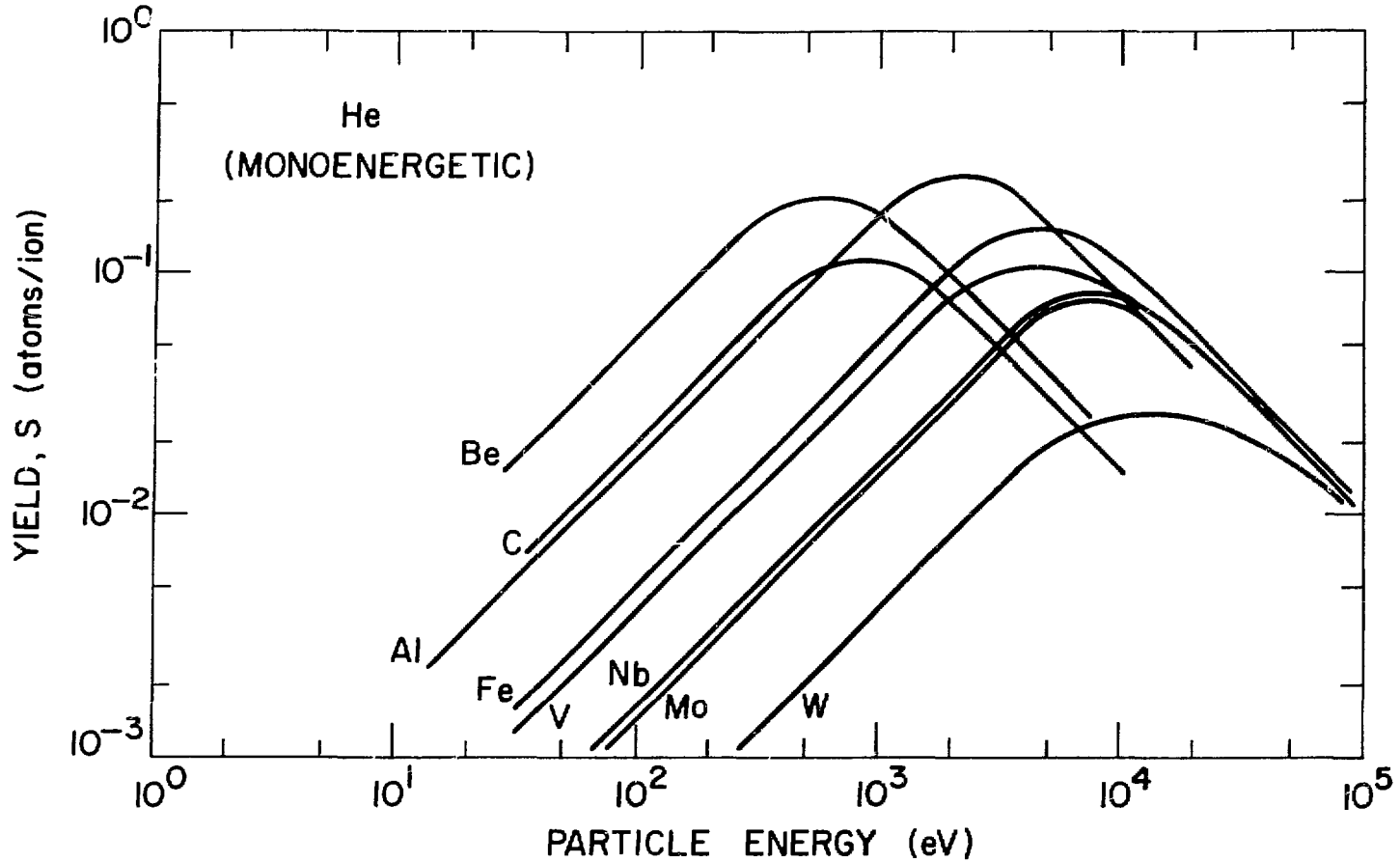

Figure B-4. Energy-dependent physical sputtering yields of potential first-wall materials irradiated with monoenergetic He^{++} ions.

deutrium, tritium, and helium on several wall materials of interest. Figures B-5 to B-7 compare the selected energy-dependent light-ion sputtering curves with available experimental data. As indicated in Fig. B-7, the sputtering curves developed here for niobium are in fairly good agreement with similar curves proposed by Behrisch[11] for the same target material. In general, the present development gives sputter coefficients that are slightly higher than the corresponding experimental data for low-Z wall materials, and coefficients that are slightly lower than the corresponding experimental data for the higher-Z wall materials. Sputtering by the neutral D^0 and T^0 particles are assumed to be identical to that by D^+ and T^+ ions, respectively.

In the present study three of the first-wall materials of interest are compounds, viz., BeO, B_4C, and SiC. Since sputtering data for these compounds are very limited, yields equivalent to those for beryllium, boron, and silicon, respectively, have been assumed for these compounds. This assumption appears plausible in view of the data of Kelly and Lam,[12] which indicate that sputter yields produced by 10-keV Krypton on a number of stable oxides are within a factor of 2-3 of the corresponding metals. The yields for these compounds are assumed to correspond to their stoichiometry, e.g., four boron atoms to one carbon atom for B_4C.

The Sigmund theory is a better representation of the yields observed for heavy (impurity) ion sputtering. Therefore, the self-sputter coefficients used for the calculations are derived from the Sigmund theory with slight modifications at low energies to compensate for electronic losses.[7] At the lower energies the curves are adjusted to approach a slope of unity on the log S versus log E plot. Figure B-8 shows the energy-dependent self-ion sputter coefficients for beryllium, niobium, and tungsten.

Large variations in the 14-MeV neutron sputter yields have been reported in the literature for various transition metals.[1-5,13-18] These differences are due primarily to chunk-type deposits that have been observed by some investigators.[13-14] Recent analyses indicate that yields for the chunk-type sputtering, which are dependent on both surface roughness and degree of cold-work, are typically less than 10^{-4} atoms/neutron.[13] Single atom sputtering yields in the range 10^{-5} to 5×10^{-4} have been reported.[13-18] A total yield of 10^{-4} atoms/neutron is considered reasonable for the present analysis. Since the contribution of neutron sputtering to the total sputtering yield turns out

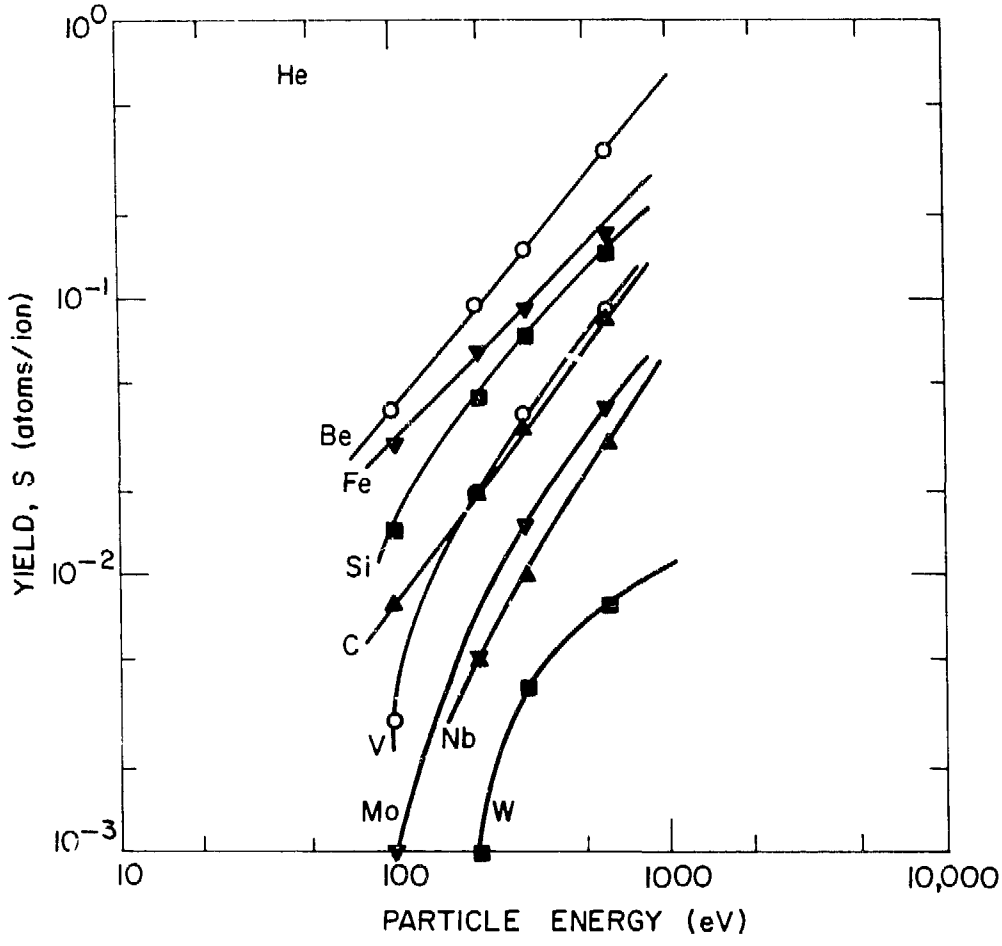

Figure B-5. Plot of selected energy-dependent He^{++} sputtering Curves showing comparison with available experimental data.[8]

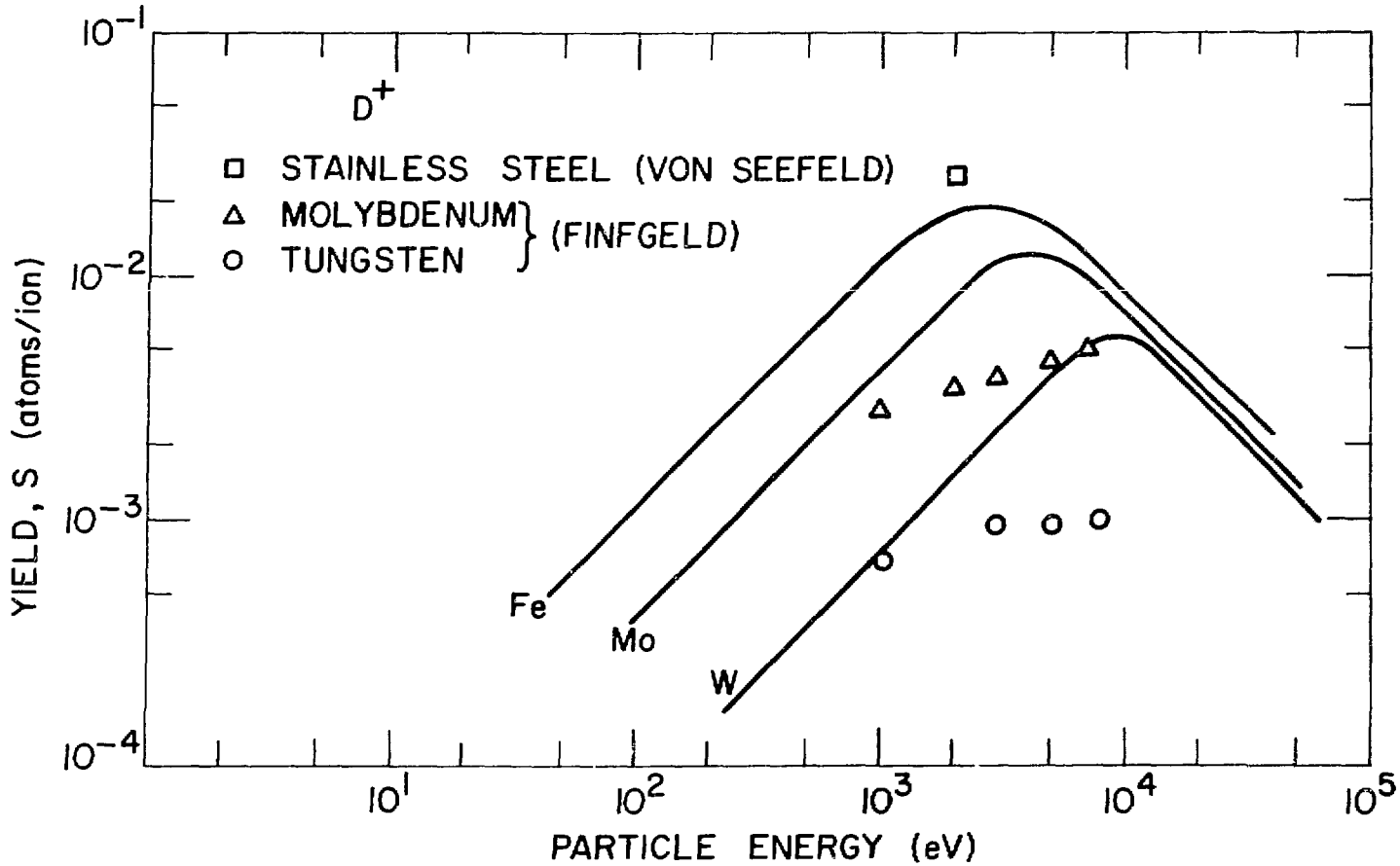

Figure B-6. Plot of selected energy-dependent D^+ sputtering curves showing comparison with available experimental data.

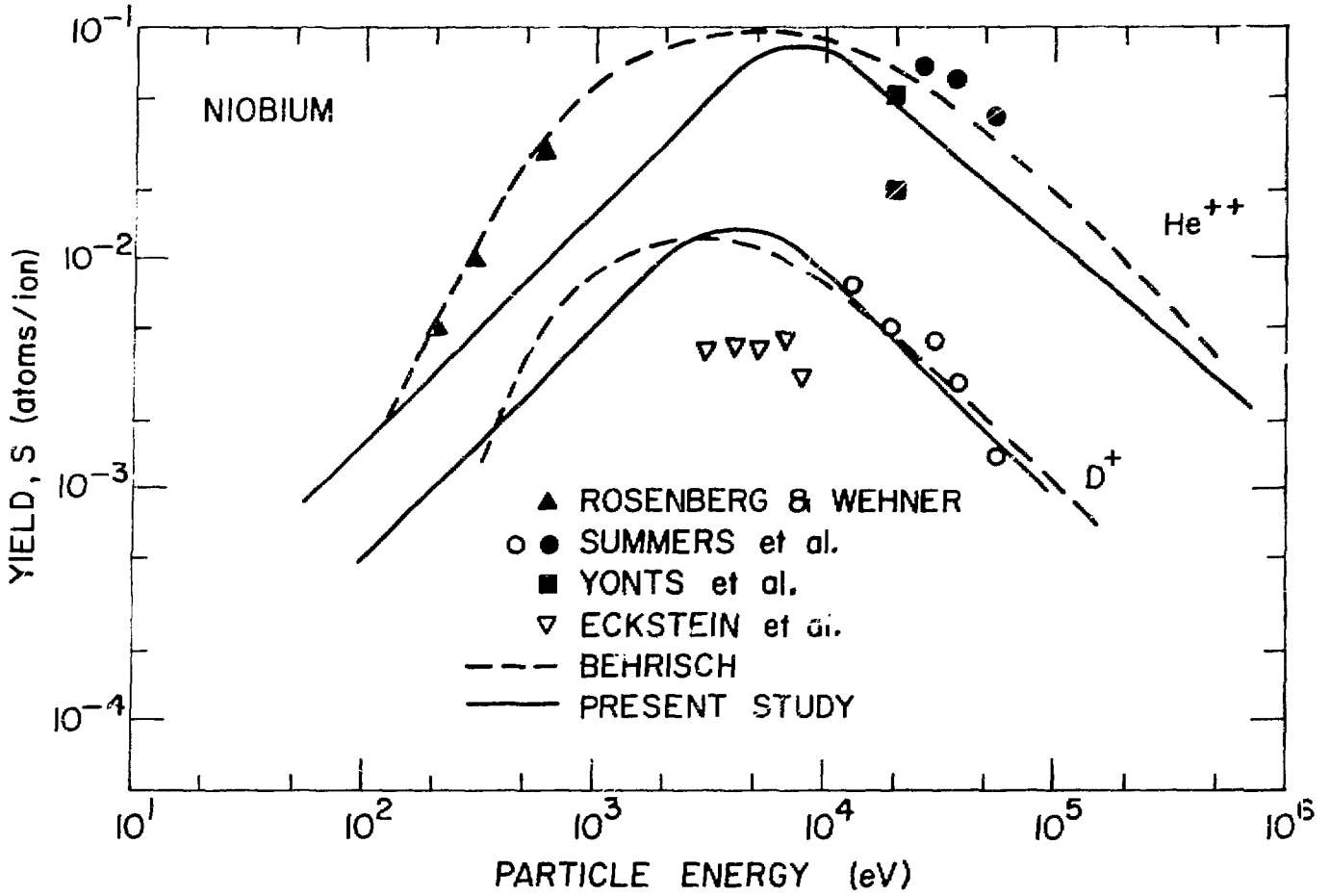

Figure B-7. Plot of light ion sputtering curves for niobium showing comparison with available experimental data.

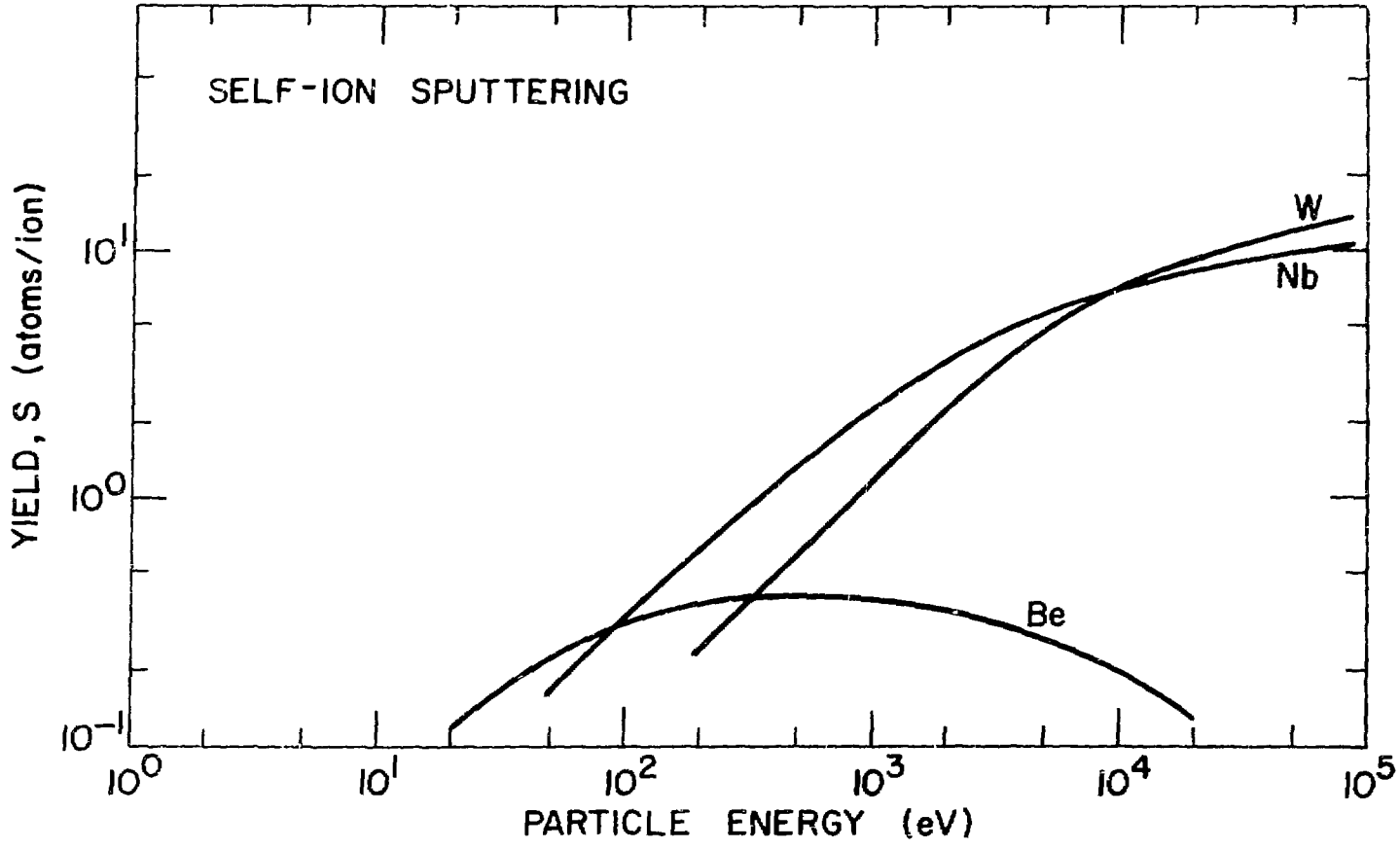

Figure B-8. Energy-dependent self-ion sputter coefficients for beryllium, niobium, and tungsten.

to be very small for the EPR parameters, the results are not very sensitive to variations or uncertainties in the neutron sputtering coefficient.

Chemical interaction between the incident particle and the target material can influence sputtering rates because of the effect of compound formation on lattice displacement energies, on sputtering mechanisms, and on the nature of the sputtered products.[19] Although this so-called chemical sputtering occurs in a number of systems, it is most commonly associated with the formation of hydrocarbons upon bombardment of carbon or graphite by the hydrogen isotopes.[19-27] In line with the chemical interaction energies, the chemical sputtering coefficients, in contrast to the physical sputtering coefficients, are sensitive to the target or wall temperature. For example, greatly enhanced (approximately 10X) chemical sputtering leading to CH_4 formation has been observed for H^+ ion bombardment of graphite at temperatures of 400 to 705°C.[20-25] Sputtering yields of nearly 0.1 atoms/ion are reported by these investigators. Figure B-9 shows the temperature dependence of sputtering yields observed for H^+ bombardment of carbon. For the present investigation, chemical sputtering coefficients for deuterium and tritium incident on carbon were assumed to be a factor of 10 higher than the physical sputtering yield at temperatures of 600 to 750°C, and negligible at higher and lower temperatures. Similar enhancement of sputtering yields for silicon-carbide has not been observed,[20,21,28] and hydrides of the structural metals are not stable under anticipated EPR conditions. Therefore, chemical sputtering has been considered in the present analysis only for the case of carbon or graphite.

The "reflection" coefficient, R, used in the plasma-wall interaction model includes both backscattering and re-emission. The backscattered particles are the incident particles that return from the wall via elastic and inelastic collisions (<<1 s) whereas the re-emitted particles are those which have penetrated the wall at an earlier time and are subsequently released by diffusion to the surface or by erosion of the wall material. Several models have been developed and experiments conducted to interpret the backscattering and re-emission of light ions (H^+ and He^{++}) from several materials.[29-38] The backscattering coefficients for the light ions typically increase with a decrease in incident ion energy below 1 keV, and the values may exceed 50% at energies below 100 eV.[29,36-38] Backscattering coefficients calculated from the theory of Weissmann and Sigmund[29] are shown in Fig. B-10 for D^+ and He^{++} on beryllium and iron as a function of incident ion energy. The use of such

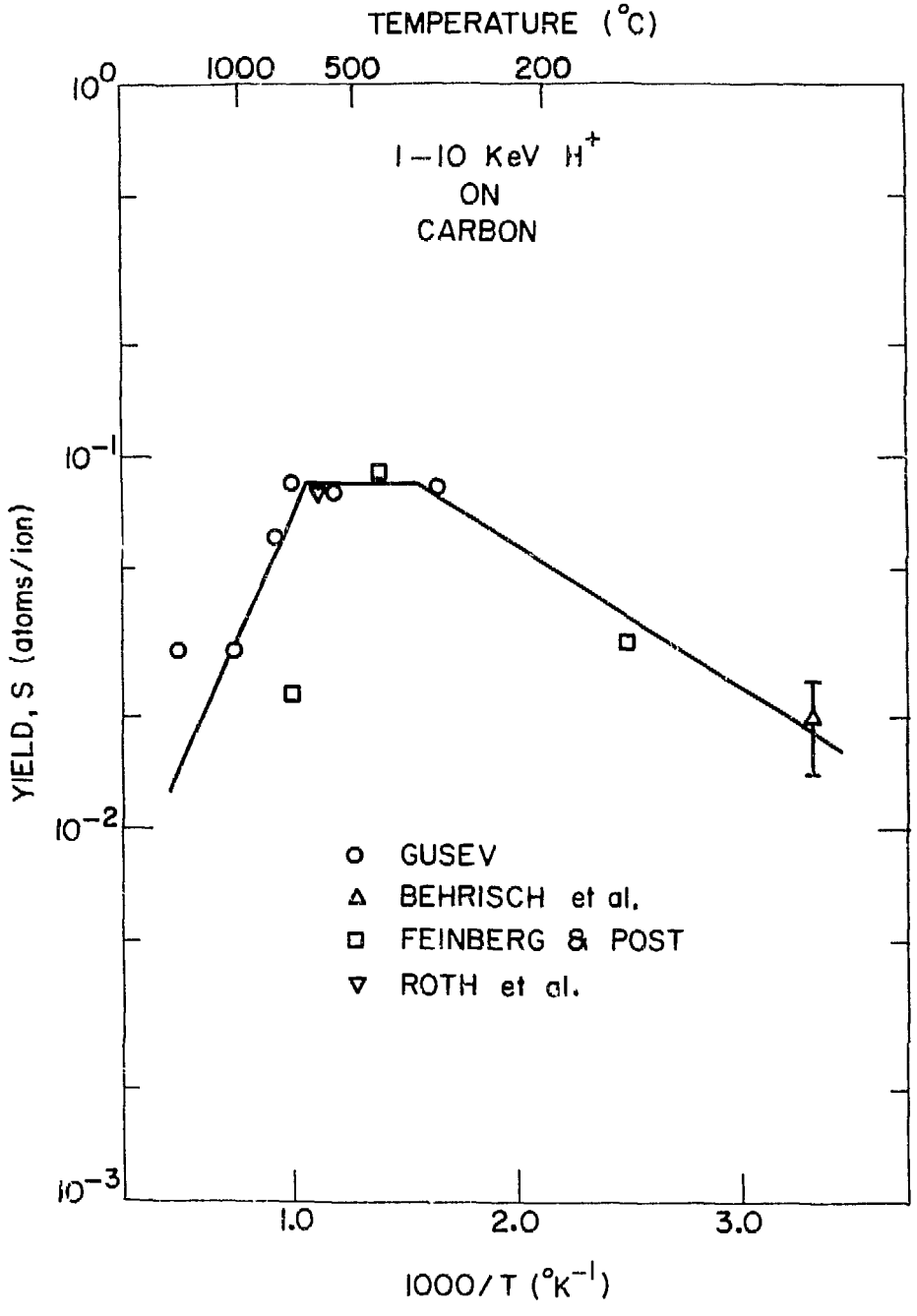

Figure B-9. Temperature dependence of sputter yields for hydrogen ions on carbon.

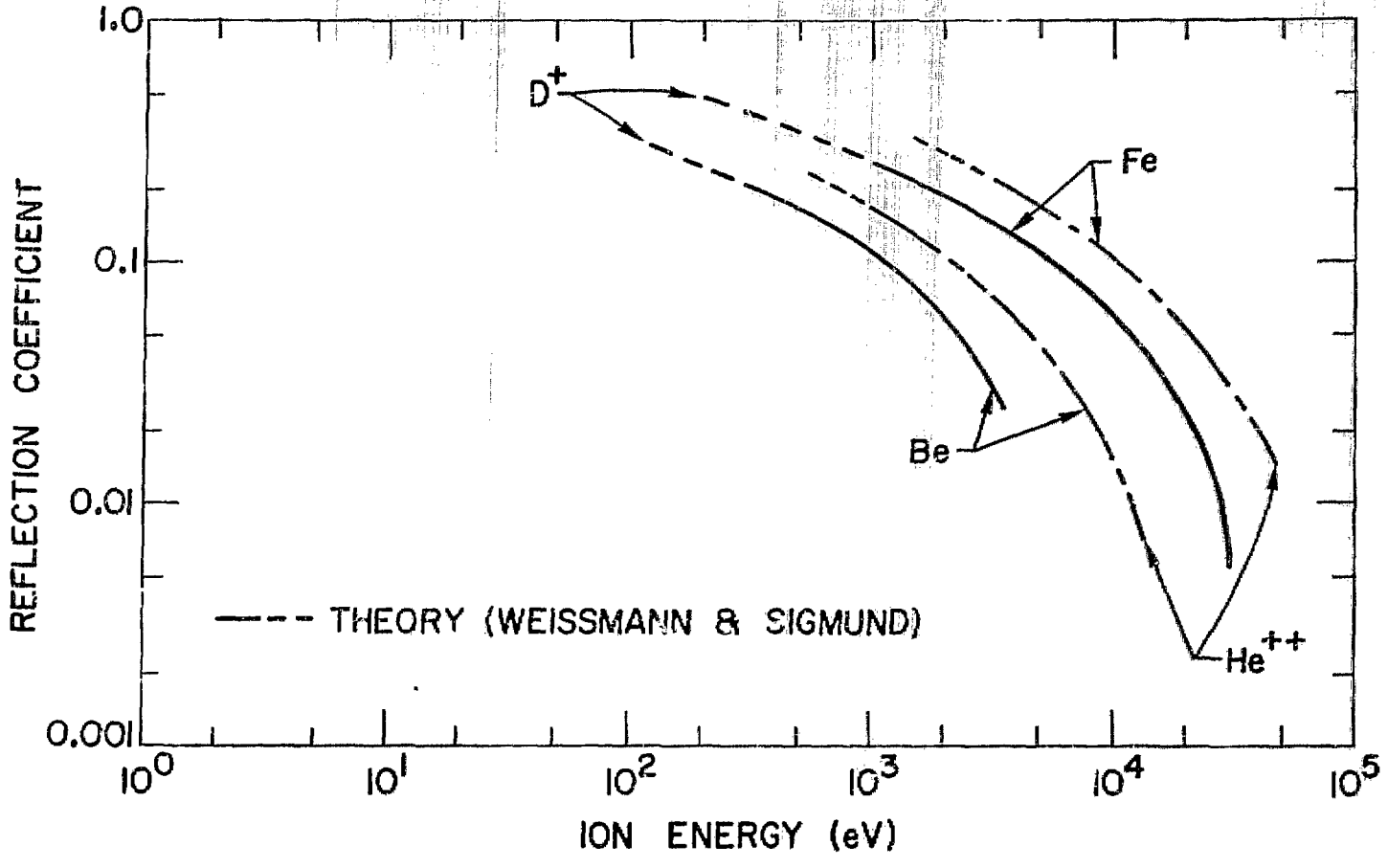

Figure B-10. Calculated reflection coefficients for deuterium and helium incident on beryllium and iron.

coefficients is appropriate only for the initial startup, since the concentrations of light atoms (helium, deuterium, and tritium) in the surface regions build up in a matter of hours during operation. Therefore, re-emission of the hydrogen isotopes and helium from the surface of the first wall will occur during normal operation. Data of several investigators indicate that high percentages of light ions injected into a variety of target materials are re-emitted after fluences of the order of 10^{17} ion/cm^2.[30-38] This re-emission is further enhanced by the elevated wall temperatures. For purposes of the present calculation it is assumed that a steady state is reached and that the combination of backscattering and re-emission results in the return of almost all of the incident light particles.

For the case of self-ions incident on the first wall, a high sticking probability is expected for a clean metal surface. In addition, the measured sputtering coefficients probably include any backscattered component. Therefore, a near-zero reflection coefficient can be assumed for self ions.

These surface data were incorporated into the calculational model as follows. The mono-energetic sputtering coefficients shown in Figures B-2 to B-4, and B-8 were averaged over Maxwellian distributions of incident particle energies, with the Maxwellian being characterized by the plasma-edge temperature. These results are given in Table B-1. A neutron sputtering coefficient $S_n = 0.0005$ was used for all materials, and a chemical sputtering coefficient $S_{DT} = 0.07$ was used for carbon. Particle reflection coefficients $R_{DT} = R_\alpha = 0.98$ were used in the calculations to represent unity reflection probability and an allowance for a small loss during operation through ports in the vacuum wall, and $R_z = 0.05$ was used to represent the high retention probability for an ion of the surface material.

The charge exchange re-emission probability was computed from

$$\bar{A}_{cx} = \frac{\overline{\sigma v}_{cx}}{\overline{\sigma v}_{cx} + \overline{\sigma v}_{ion}}, \qquad A_{cx} \equiv \bar{A}_{cx}\gamma$$

where $\overline{\sigma v}_{cx}$ and $\overline{\sigma v}_{ion}$ are averages of the charge exchange ($D^+,T^+ \leftrightarrow D^0,T^0$) and ionization cross sections of References 39-43 over Maxwellian distributions corresponding to the plasma edge ion temperature. The results are $\bar{A}_{cx} = 0.50$ at $T_{DT}^{edge} = 100$ eV, $\bar{A}_{cx} = 0.56$ at $T_{DT}^{edge} = 200$ eV, and $\bar{A}_{cx} = 0.73$ at $T_{DT}^{edge} = 1$ keV. The factor γ represents the probability that a primary charge-exchange

Table B-1. Maxwellian-Averaged Physical Sputtering Coefficients

Material	Plasma Edge Temperature (eV)	Sputtering Coefficient (atoms/part)		
		S_{DT}[a]	S_{α}	S_z[b]
Be	60	0.016	0.017	0.26
	200	0.028	0.070	0.35
	1000	0.018	0.115	0.36
BeO	60	0.016	0.017	0.26
	200	0.028	0.070	0.35
	1000	0.018	0.115	0.36
C	60	0.007	0.018	0.26
	200	0.015	0.050	0.35
	1000	0.012	0.079	0.36
B_4C	60	0.011	0.017	0.26
	200	0.022	0.060	0.35
	1000	0.016	0.098	0.36
SiC	60	0.0055	0.015	0.26
	200	0.016	0.048	0.47
	1000	0.033	0.160	0.64
Fe	60	0.0015	0.0046	0.27
	200	0.005	0.015	0.59
	1000	0.016	0.067	1.49
Nb	60	0.006	0.0016	0.29
	200	0.002	0.005	0.83
	1000	0.009	0.023	2.62
W	60	0.0001	0.0004	0.11
	200	0.0003	0.0012	0.35
	1000	0.0016	0.0061	1.61

[a] $S_{DT} = \frac{1}{2} S_D + \frac{1}{2} S_T$.

[b] Self-sputtering.

event for an incident neutral will result in the re-emergence of a neutral (either directly or as the result of subsequent secondary charge-exchange events) from the plasma. $\gamma = 0.75$ is used in this work.

The wall-sputtered impurities entering the plasma affect the energy balance both through the transport loss, which goes as Z_{eff} for pseudoclassical and neoclassical scaling and as Z_{eff}^{-1} for trapped-ion-mode scaling, and through the radiative power loss. The radiation model is a modification of a model proposed by Hopkins,[45] which is based on the results of calculations using coronal equilibrium models.[46-49] The results of the coronal equilibrium calculations have been shown to be good approximations under reactor conditions by comparison with the results of a more general radiative-collisional model.[50,51]

The model may be summarized as follows: When $T_e \geq T_z$,

$$P_{rad}^z = n_e n_z \left\{ K_1 Z^2 T_e^{\frac{1}{2}} + K_2 Z^4 T_e^{-\frac{1}{2}} + K_3 Z^6 T_e^{-3/2} \right\} ,$$

where P_{rad} is the radiated power per cubic meter in W/m^3, n_e is the electron density and n_z is the ion density of the z-*th* ionic species, T_e is the electron temperature in keV, and T_z is the ionization potential, in keV, for the beryllium-like ion sequence. $K_1 = 4.8 \times 10^{-37}$, $K_2 = 1.82 \times 10^{-38}$, and $K_3 = 4.13 \times 10^{-40}$, when T is in keV and n in m^{-3}. When $T_e \leq T_z$, we insure $P_{rad} \to 0$ as $T_e \to 0$ by using,

$$P_{rad}^z = n_e n_z \left\{ K_1 Z^2 T_e^{\frac{1}{2}} + K_2 Z^4 T_z^{-\frac{1}{2}} + K_3 Z^6 T_z^{-3/2} \right\} \left(T_e / T_z \right)^2 , \qquad \text{(B-1)}$$

T_z is given by[8]

$$T_z(\text{keV}) = \left[1.033 \times 10^{-7} \, (Z - 3)^3 + 3.4266 \times 10^{-3} \, (Z - 3)^2 + 5.5574 \times 10^{-3} \, (Z - 3) + 0.529 \times 10^{-3} \right] . \qquad \text{(B-2)}$$

The total radiated power is thus given by

$$P_{rad} = \sum_z P_{rad}^z , \qquad \text{(B-3)}$$

where the sum includes all ionic species.

The above model was developed from radiation loss studies for nuclei with nuclear charge in the range $5 \leq Z \leq 18$. For impurities with $Z \geq 30$, the model

was modified to account for radiation from high-Z materials which are not completely stripped at the 10-keV operating temperatures. In the formula for radiation loss, the nuclear charge, Z, was replaced by the actual ionic charge attained by the impurity at the plasma temperatures. Ionization potentials for various ions up to Z = 103 have been tabulated.[52] The radiation loss as calculated by Eq. (B-1) is reduced by a substantial factor for high-Z ions (e.g. 20 for tungsten), relative to a calculation using the atomic number. This reduced radiation power is consistent with results reported in Reference 51.

2. Analysis

The analysis was carried out for a specific tokamak reactor model with parameters that are characteristic of the ANL EPR design: R = 6.25 m, A = 2.98, I = 6.4 MA, q(a) = 2.5, B_t = 4.4 T. The confinement times were scaled up from the theoretical prediction by a factor $\alpha_{TIM} = 1.79$ so that ignition would obtain at $\bar{T}$ = 10 keV, in the absence of wall-sputtered impurities and without helium recycling, in the trapped-ion-mode (TIM) transport regime. The thermonuclear power output of a reactor operating under these conditions at $\beta_p = 2.25$ is P_T = 410 MWt.

The analysis consisted of a dynamic simulation of the entire burn pulse. Ions escaping from the plasma were assumed to be recycled back as described in Figure B-1, so that essentially total (98%) recycling of deuterium, tritium, and helium occurred unless the particle removal (e.g. divertor) efficiency $\eta > 0$. Deuterium and tritium ion densities were maintained at their maximum allowable value by refueling, subject to the constraint that $\beta_p(t) \leq \beta_p^{max} = 2.25$. Wall-sputtered impurity ions were assumed to be able to penetrate immediately to the central region of the plasma, where they resided with a confinement time equal to that of the D-T ions. These impurity ions increase the radiative power loss as described in the previous section, modify the particle and energy confinement times ($\tau \propto Z_{eff}$ for TIM scaling) and reduce the allowable D-T ion density for a fixed β^{max}. Supplemental neutral beam heating, up to a maximum power of 80 MW, was used in some cases to offset excessive radiative power losses. The burn pulse simulation was carried out to the point at which the accumulation of helium and wall-sputtered impurities quenched the plasma.

A figure-of-merit for the burn cycle performance is the net electrical power averaged over the burn pulse,

$$P_{net} \equiv \left[U_T \eta_T - \frac{U_B}{\eta_B} - U_{REF} - U_{PUMP} - U_\Omega - U_{PS}\left(1 - \eta_{PS}\right) \right] \Big/ \Delta t_{burn} ,$$

where

$U_T \equiv$ plasma thermal energy to wall during burn pulse

$U_B \equiv$ beam heating energy during burn pulse

$U_{REF} \equiv$ refrigeration energy during burn pulse

$U_{PUMP} \equiv$ coolant and vacuum pumping energy during burn pulse

$U_\Omega \equiv$ plasma ohmic heating energy dissipated during burn pulse

$U_{PS} \equiv$ energy transferred by plasma driving system during burn pulse

$$\equiv \int_0^{\Delta t} |P| \, dt$$

$\eta_T \equiv$ thermal-to-electrical conversion efficiency = 30%

$\eta_B \equiv$ neutral beam power efficiency = 35%

$\eta_{PS} \equiv$ energy transfer efficiency = 95%

$\Delta t_{burn} \equiv$ length of the burn pulse.

The compressive refrigeration power for the superconducting toroidal field coils was U_{REF} = 660 MJ,* the coolant and vacuum pumping energy was $U_{PUMP} = 0.02\ U_T$, and the energy transferred by the plasma driving system was $U_{PS} \approx$ 2400 MJ.

The quantity P_{net} is plotted in Figure B-11 as a function of the length of the burn pulse for several first-wall surface materials. The assumed edge temperature is 200 eV for all cases. The burn cycle performance that would result in the absence of sputtering is also shown to provide a point of reference. In the absence of sputtering, the minimum burn pulse for which $P_{net} > 0$ is 20 s, including ~4 s for startup. In this case, the burn pulse is ultimately (~157 s) quenched by the accumulation of helium, and the maximum value of P_{net} is 66.5 MW.

---

*This refrigeration load arose principally from ac field heating of the toroidal field coils, and is smaller than the value used in Chapter III to define refrigeration requirements.

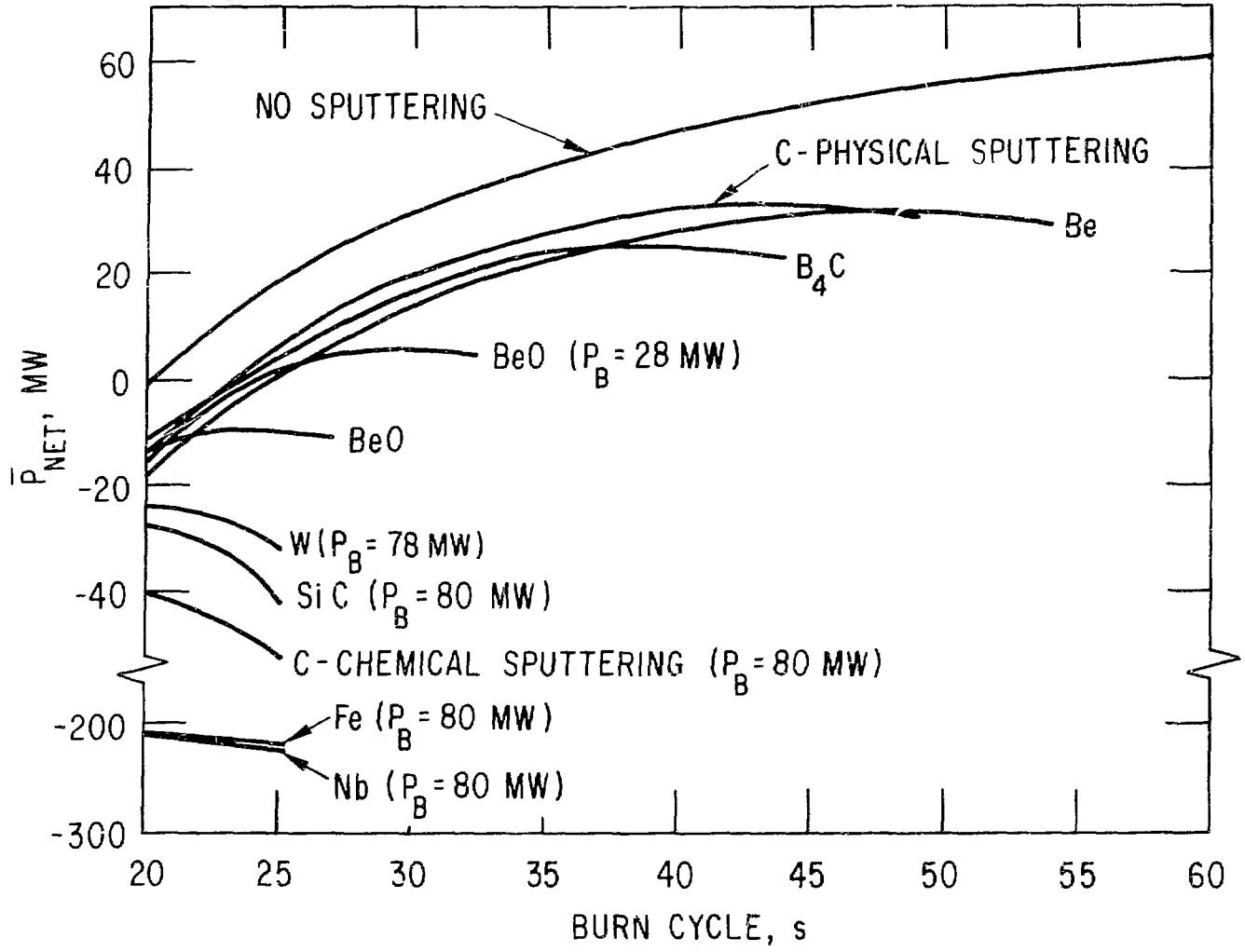

Figure B-11. Effect of First-Wall Surface Material on Power Performance-

Wall-sputtered impurities from a stainless steel (represented by iron) or refractory metal (niobium) first-wall surface have a devastating effect. A substantial supplemental beam heating is required to maintain the plasma at thermonuclear temperatures, resulting in a negative P_{net}, on the order of -200 MWe. The maximum length of the burn pulse could be extended beyond ~20 s by increasing the beam heating power P_B > 80 MW, but this would result in an even more negative P_{net}. Initially, the D-T sputtering is the main contributor to plasma contamination, but as the impurity concentration builds up to on the order of 1%, self-ion sputtering becomes a major contributor, as may be inferred from Table B-1. The situation is somewhat improved if the plasma edge temperature is less than the 200 eV used in these calculations; however, even for T_{edge} = 60 eV, P_{net} ~ -100 MWe and the maximum burn pulse is ~20 s. Thus, it appears extremely unlikely that a reactor of this type will be able to operate with a stainless steel or refractory metal wall without some form of impurity control.

One form of impurity control is suggested by Figure B-11, namely to interpose between the plasma and the structural first wall a low-Z material, either as a coating or as a stand-off liner. Burn pulses of ~45-55 s can be achieved with very low-Z surfaces, viz. beryllium, carbon (without chemical sputtering), B_4C, which result in P_{net} about one-half of the value that obtains without wall sputtering. With a small supplemental beam heating (P_B = 10 MW) to offset radiative losses, burn pulses in excess of 60 s with maximum P_{net} of ~35 MWe can be achieved with a beryllium surface. If a carbon surface operates in the temperature range ~400-700°C, then chemical sputtering precludes $P_{net} > 0$, which implies that carbon would be suitable as a standoff liner operating at temperatures in excess of 1000°C but would be unsuitable as a coating operating at 400-600°C. Surfaces with silicon or oxygen compounds are less satisfactory for impurity control in reactors of this type. In the case of beryllium oxide, $P_B \leq 28$ MW was adequate to offset radiative losses, but the accumulation of oxygen in the β_p-limited plasma forced a reduction in the D-T density which eventually quenched the plasma. For the beryllium surface, the self-sputtering rate is about half the D-T sputtering rate, the alpha-sputtering rate is about 5% of the D-T sputtering rate, and the neutron sputtering rate is negligible.

Another possibility for reducing plasma contamination is to use a low-sputtering first-wall material such as tungsten. Although the plasma performance is better with tungsten than with stainless steel or niobium as the first-wall surface material, the performance with tungsten is considerably inferior to that with a low-Z material such as beryllium. Moreover, the plasma performance is much more sensitive to variations in the sputtering coefficients for a high-Z material than for a low-Z material. In the case of tungsten, the self-sputtering rate is ~30% of the D-T sputtering rate and the neutron sputtering rate is ~10% of the D-T sputtering rate.

The performance summarized in Figure B-11 is based upon a plasma edge temperature of 200 eV, which corresponds to the maximum in the beryllium sputtering yield curves of Figures B-2 to B-4. Reduced sputtering, hence improved performance, occurs if the plasma edge temperature is higher or lower for beryllium, as shown in Figure B-12. At an edge temperature of 60 eV, a burn pulse of 102 s with a maximum P_{net} = 57 MWe is obtained with a beryllium surface, which is close to the performance in the absence of wall sputtering. The effect of the plasma edge temperature is even more dramatic for silicon-carbide, with $P_{net} > 0$ becoming possible for an edge temperature of 60 eV.

Another method of impurity control which has been proposed is to remove ions that escape from the plasma before they strike the wall — e.g. by means of a magnetic divertor. This process can be represented by the efficiency of charged particle removal, η. Results of a series of calculations for a stainless steel first-wall surface and various values of the charged particle removal efficiency are shown in Figure B-13. For a very low plasma edge temperature (60 eV) and a very efficient charged particle removal mechanism (η = 0.9), tolerable equilibrium iron (0.03%) and helium (1.5%) concentrations are maintained and the burn pulse is virtually unlimited. For a more realistic value of η = 0.5, the performance is marginal and $P_{net} > 0$ requires a low plasma edge temperature (60 eV) in addition to substantial supplemental beam heating (P_B = 44 MW). If the plasma edge temperature is 200 eV, a very high charged particle removal efficiency (η = 0.9) and some supplemental beam heating (P_B = 15 MW) are required to achieve $P_{net} > 0$. Thus, it appears that the success of a divertor or other impurity control mechanisms based upon charged particle removal depends critically upon the achievement of high particle removal efficiency and upon the operation of the plasma with a low edge temperature.

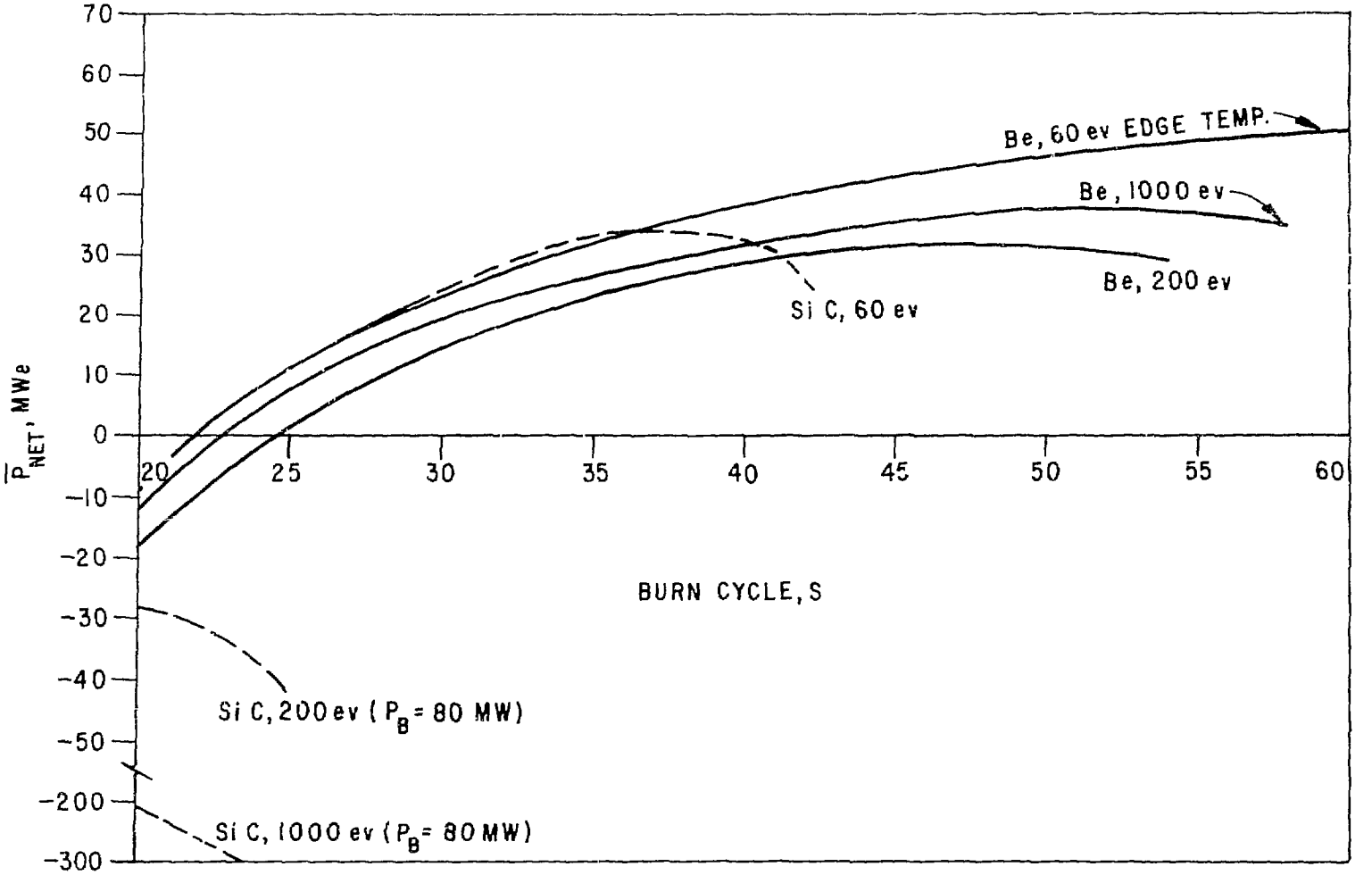

Figure B-12. Effect of Plasma Edge Temperature on Power Performance.

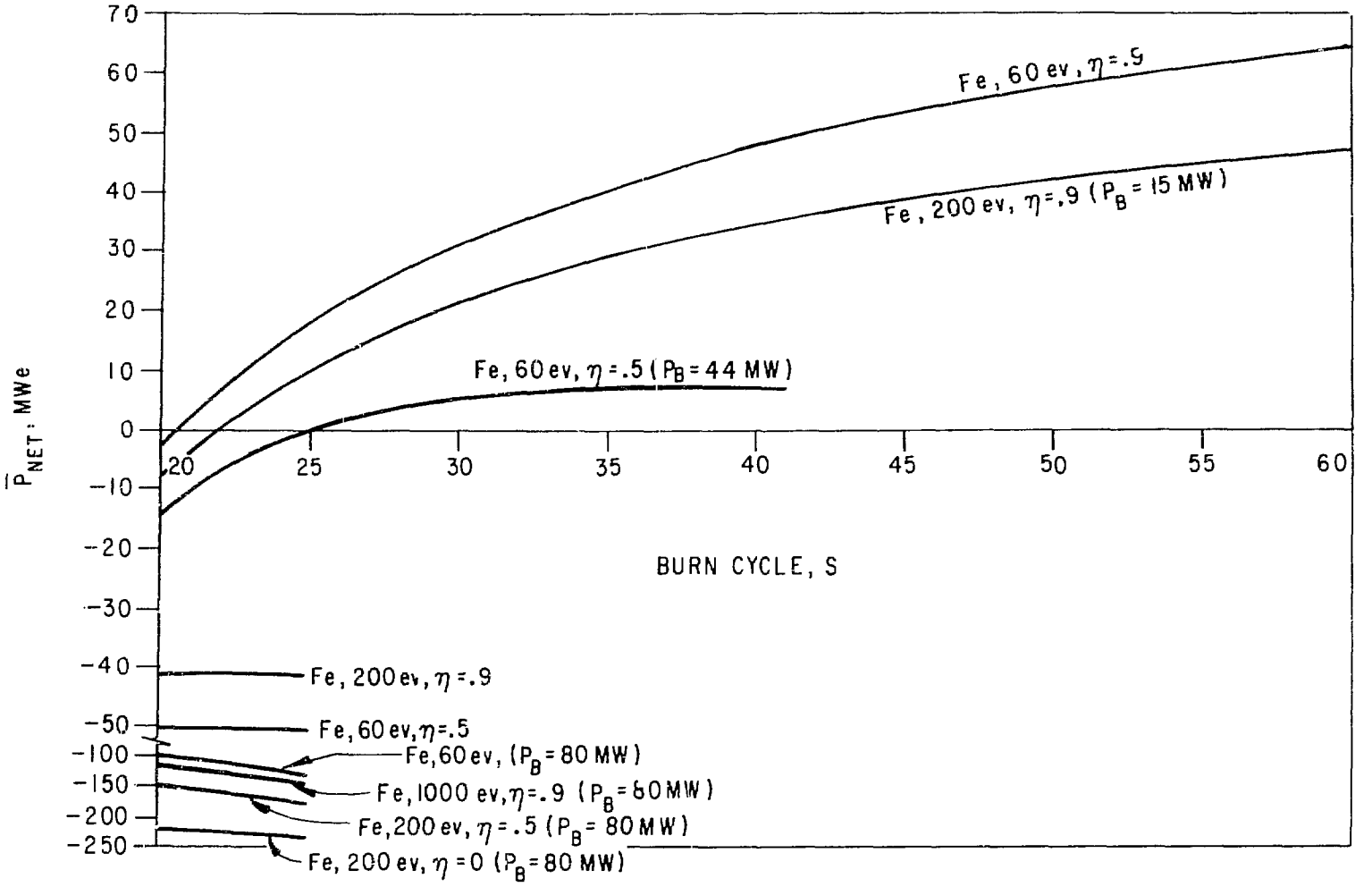

Figure B-13. Effect of Divertors on Power Performance — Bare Stainless Steel Wall.

Combining a low-Z surface with a charged particle removal mechanism reduces the critical dependence upon high particle removal efficiency. Performance obtainable with beryllium and silicon-carbide surfaces are shown in Figure B-14, for a range of charged particle removal efficiencies. With a beryllium surface, $\eta \geq 0.5$ suffices to achieve very long burns.

The particle and energy confinement times were generally in the range 5-10 s during the peak portion of the burn pulse, and the particle confinement times were the same for all ion species. As mentioned previously, the theoretical confinement time was scaled up by a factor $\alpha = 1.79$, which achieves an unlimited burn in the absence of wall-sputtered impurities and helium recycling, on the basis of the rationale that the reactor would be designed to achieve this "ignition-type" confinement once the actual scaling laws are known. If the confinement was substantially better, e.g., scaled up by $\alpha = 5$, the beryllium surface would enable a virtually unlimited burn to be achieved, the silicon-carbide and beryllium-oxide surfaces would enable $P_{net} > 0$ to be achieved, but the bare stainless steel surface would still be limited to burn pulses on the order of 25 s and negative P_{net} on the order of -200 MWe. On the other hand, if the confinement was as poor as predicted by the trapped particle theory ($\alpha = 1$), it would be difficult to achieve $P_{net} > 0$ even with a beryllium surface, as shown in Fig. B-15.

The quantitative results discussed above depend upon the particular reactor model and values for the sputtering coefficients used in the calculations, as well as upon the various assumptions in the calculational model, and are subject to change as understanding of the various processes improves. However, the general qualitative features should be relatively independent of the reactor model and the data.

3. Technological Feasibility of First-Wall Surface Modifications

On the basis of fabricability, vacuum properties, and economic impact, fusion reactor first walls constructed of transition metal alloys such as stainless steel are favored.[53] However, as indicated by the previous calculations, satisfactory plasma performance can only be attained with very low incident particle energies and an efficient divertor and/or supplemental heating. The unacceptable plasma performances were caused primarily by the high radiative losses produced by the high-Z transition metal impurities. An additional factor that will further degrade plasma performance will be the substantial

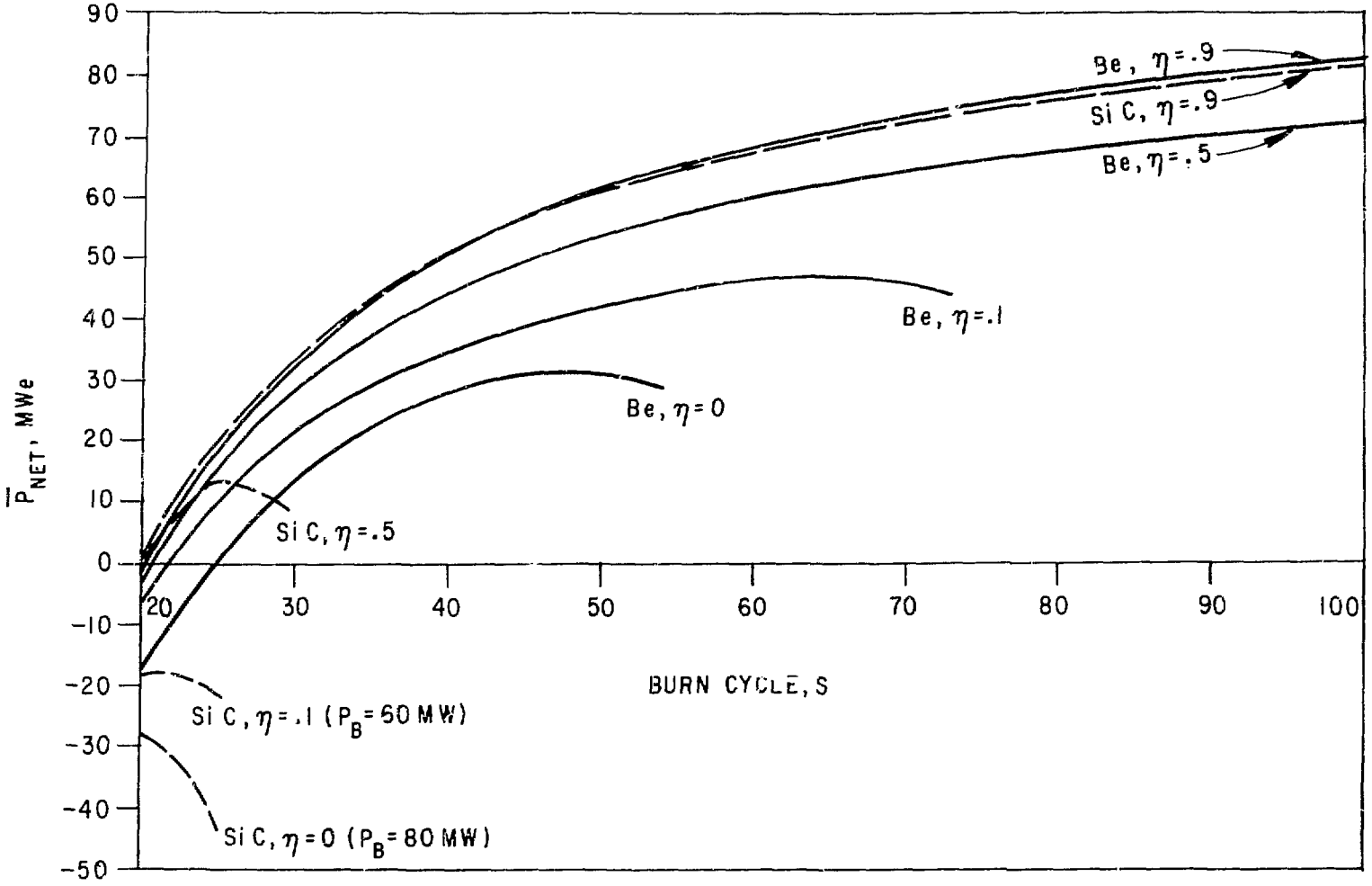

Figure B-14. Effect of Divertors on Power Performance — Low-Z Coated Walls.

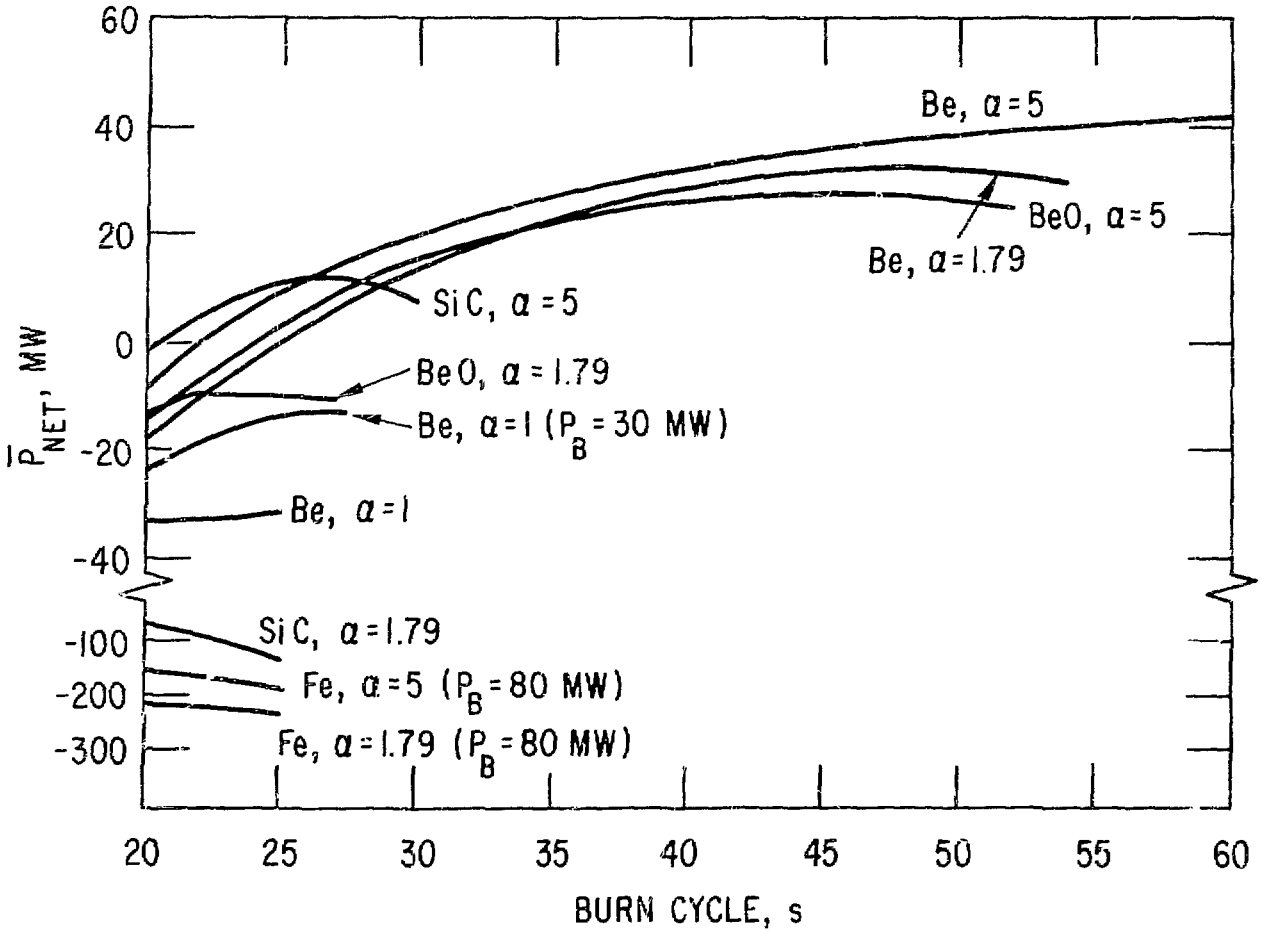

Figure B-15. Effect of Energy Confinement on Power Performance.

erosion of the wall by the blistering phenomenon.[1-5,54-58] For EPR conditions, erosion rates of structural materials such as niobium or stainless steel by blistering are greater than those by physical sputtering.[54-58] These erosion rates are temperature-dependent and peak at the temperature ranges of interest, viz., 400-500°C for stainless steel.[57-58] Although complete agreement on the contribution of the blistering phenomenon has not been reached because of uncertainties in incident particle energies and particle energy distribution, the data obtained by monoenergetic bombardments may be a reasonable representation of the 3.5-MeV contribution of the alpha-particle wall current. Effects produced by this component are probably independent of the other low-energy effects. An erosion rate greater than 10^{-1} atom/ion may be expected for stainless steel after a few days operation.[56,57] This contribution substantially exceeds that produced by He^{++} sputtering at the low energies (<100 eV) (see Figure B-4) and approaches the sputtering yields of D^{+} and T^{+} at low energies. Possible synergistic effects such as sputtering and vaporization of blister skins have not been investigated and, although likely to be detrimental, cannot be assessed at this time. Therefore, the conclusions presented in the previous section for the plasma performance with a stainless steel wall are probably quite optimistic.

Several concepts for modifying the first-wall surface are qualitatively assessed in this section: (1) a low-Z material coating on a structural substrate; (2) a separated monolithic low-Z material liner; (3) a carbon cloth liner; and (4) a low-sputter material coating on a structural substrate.

a. Low-Z Coating

The low-Z coating on a structural metal substrate has been proposed as a viable solution to the impurity control problem in EPR.[53] This concept utilizes the transition metal (stainless steel) substrate for structural support and the low-Z coating to protect the plasma from the high-Z transition metal atoms. Major considerations in this concept are the flexibility in first-wall design provided by the variety of low-Z coating materials that are considered feasible and the variety of coating procedures available. The coating selection and preparation can be optimized on the basis of its surface characteristics, and the substrate, which provides the structural support, can be selected primarily on the basis of desirable bulk properties.

Fabrication should not be much more difficult than for the simple metal wall discussed above. A substantial technology base exists for applying a variety of coatings to a number of substrate materials.[59] Much of this technology has been obtained recently under space and fission reactor programs. Although plasma spraying, chemical vapor deposition, chemical bonding, and sputtering can all be used to coat most of the materials considered,[59] the plasma spray process appears to be the most appropriate for the present application. Deposition rates necessary to obtain the desired coating thicknesses (~100 μm) can be achieved. The porosity and grain size can easily be varied in the plasma spray process to obtain optimum microstructures.[59-61] Graded coatings, which can also be prepared by the plasma spray process, may be desirable for better coating adherence. However, additional development work and modification of existing coating technology may be required to optimize selected properties for the present application. Since the coating material is not required to serve as a structural member, a wider variety of materials may be feasible. Materials requirements are minimized, since only thin coatings are being considered. As a result, materials cost and availability of more exotic materials are less restrictive for coatings than for low-Z monolithic structures.

The possibility of in situ coating may provide additional benefits for fabrication and repair of first-wall systems. Remote coating preparation by plasma spray, chemical vapor deposition, chemical bonding, and sputtering are all considered feasible, since the required environments can be attained in the vacuum chambers. However, further development work is required to develop an in situ coating technology.

The plasma performance calculations indicated that, on the basis of predicted physical sputtering and reflection coefficients, net power could be achieved in the EPR with several low-Z liner materials. However, other potential sources of wall impurities such as blistering and thermal evaporation were not considered in these calculations. Significant erosion rates from a blistering phenomenon can occur under certain conditions. In some cases the blistering yields exceed those from physical sputtering.[54-58] However, the blistering phenomenon is strongly affected by the microstructure of the target material.[62,63] Erosion rates produced by helium bombardment are much less for sintered material, both beryllium and aluminum, than for cast or sheet material. Microstructures similar to those of sintered products can be obtained by selected coating procedures, e.g., plasma spray techniques, in which grain

size and porosity can be adjusted over significant ranges. It appears that erosion by the blistering phenomenon can be maintained at acceptable levels by appropriate choice of coating parameters.

Depending on the proposed operating temperature and coating material, thermal vaporization may also contribute to impurity effects. Thin coatings on a convectively cooled substrate tend to minimize this contribution by maintaining the low-Z material at lower temperatures than are attained with separated liner concepts. Also, more refractory-type low-Z materials such as B_4C and beryllium oxide can be used if necessary to alleviate this problem.

Two types of impurity effects may be important with regard to the selection of the liner material. One relates to the presence of high-Z impurities in the coating that can reach the plasma by normal erosion phenomena and the second relates to absorbed gases on the wall that may be removed by photodesorption. Since a minimal amount of low-Z material is required for the coating concept, high quality base material can be effectively used to minimize high-Z concentrations. Predominant impurities typically picked up during coating preparation are oxygen and nitrogen. Since these elements are fairly low-Z, moderate amounts are not prohibitive. A major source of plasma impurities in present day physics machines is the desorption of gaseous impurities from the low temperature (room or cryogenic temperature) first walls. This problem will be considerably different for power reactors in which the first-wall is operated at elevated temperatures. For example, beryllium reacts chemically with oxygen at elevated temperatures to form a very stable compound. At elevated temperatures selected coating materials will chemically react with the impurities, e.g., beryllium with oxygen, to form stable compounds which will reduce the tendency for plasma contamination by gaseous impurity desorption. This effect, which is a major source of impurities in low-wall temperature devices, may not be of significant importance for power reactors.

Vacuum properties of coated walls should not differ substantially from those of a metal wall; in fact, sputter coating of walls in present day physics machines is used to produce clean walls.[64] High helium generation rates are typical of low-Z materials. Since steady-state release rates are reached in rather short times, this produces another impurity source. This effect is not significant for thin coatings, however, as discussed below, it may be significant for thick low-Z liners.

The mechanical integrity of the low-Z coating is an important consideration as it relates to the reliability, lifetime limitation, and failure mechanisms of the coating. An advantage of the coating concept is that the substrate provides the structural support. As a result, micro-cracking of the coating caused by swelling, gas production, or differential thermal expansion may not seriously degrade the effectiveness of the coating as long as it adhered to the substrate. By judicious selection of coating material and coating preparation, optimum properties can be obtained to accommodate these effects. For proposed coating thicknesses of a few hundred micrometers, lifetimes of three to five years are predicted on the basis of sputtering erosion rates in the EPR. However, evidence exists that a significant fraction of sputtered first-wall material is redeposited on the wall. This phenomenon may significantly enhance lifetime predictions for thin coatings.

The failure mechanism of most concern for the coatings is flaking or loss of adherency over significant areas. Excessive flaking or spalling of the coating is not tolerable, since exposure of more than a few percent of a high-Z substrate surface, e.g., stainless steel, would probably be unacceptable. This woul expose the plasma to excessive high-Z impurity from the substrate. Enhancement of the plasma impurity source would result from vaporization of the loose coating due to loss of heat transfer capability. Any loose particulate material collected at the bottom of the vacuum vessel would likely revaporize during each cycle because of the lack of heat removal capability. This problem may be alleviated if the flakes are vaporized and subsequently vapor-deposited on the wall at the end of a burn cycle. In either case, a capability for recoating appears essential, and an in situ coating capability may have important consequences.

b. Low-Z Separated Monolithic Liner

With respect to effects on plasma performance, a low-Z separated liner has much in common with the low-Z coating discussed above. The major differences relate to the technological aspects of fabricability and mechanical integrity. Therefore only the significant advantages and disadvantages of the separated liner in comparison with the coating will be discussed.

Although fabrication, installation, and repair of separated liners appears to be more difficult than that for coatings, several possibilities have been proposed that appear technologically feasible.[65-67] A major difference from

the coating relates to the much larger quantity of material required, which has a significant impact on cost and materials availability if the more exotic low-Z materials are used. Since a separated liner must provide a degree of its own structural support, the materials selection is probably more limited, and since most concepts operate with radiatively cooled separated liners, problems inherent to high temperature operation will be encountered.

In most cases the impurity control capability of a separated liner should be similar to that for a coating of the same material, since the physical sputtering and reflection coefficients should be the same in both cases. If chemical sputtering is important, as in the case of carbon or graphite, the wall temperature becomes critical. A separated liner will probably operate at temperatures above the chemical sputtering range for carbon, while the operating temperature of a coating is probably near the peak of the chemical sputtering range (Figure B-9). It is assumed that monolithic separated structures of the sintered product type can be used to maintain "blistering" erosion rates at acceptable levels. However, this requirement may further limit the selection of materials.

Impurity contributions from thermal vaporization will be more critical for the stand-off liner than for the coating because of the inherently higher operating temperature of the radiatively cooled liner. Decreases in thermal conductivity of the liner material as a result of thermally induced or radiation-induced micro-cracking will lead to higher surface temperatures that may subsequently lead to excessive thermal vaporization. Lower thermal conductivities characteristic of materials with substantial porosity, which is required to facilitate gas release and to minimize blistering, will also affect the operating temperature limitations.

Additional impurity effects produced by binders, which are commonly used in many sintered ceramic liner materials, must be considered. Helium generation in thick low-Z liners may also produce significant effects if complete helium release occurs at high temperatures, as expected. For example, the helium generation rate in an ISSEC[68] could exceed the helium generation rate from the fusion reaction. However, this is not expected to be excessive for liners less than 1 cm thick.

The fusion reactor vacuum requirements will be greater for a separated, monolithic liner of either the bumper or shingle type, since the total surface

area in the vacuum vessel will be substantially increased, i.e., probably a factor of three or four. The pumping problem may be further complicated by the geometric consideration, viz., the thin annulus behind the liner which are connected to the toroidal chamber.

Several problems relating to the reliability and mechanical integrity appear to be more severe for the separated liner than for the coating concept. Since the liner must provide its own structural support, micro-cracking and dimensional instabilities caused by thermal and neutronic effects may lead to premature failure. Accelerated deterioration of the liner caused by higher temperatures and more severe thermal cycling may also occur as a result of reduced thermal conductivity of the liner material during operation. Erosion of the liner by sputtering, blistering, etc., should not seriously affect the useful lifetime of the liner.

The failure mechanisms associated with the monolithic separated liners appear to be more critical than those of the coating concept with respect to the effect on reactor operation and subsequent repair and maintenance. Fracture of a liner section not only could expose the plasma to substantial areas of high-Z vacuum wall, but the fractured remnants could be a source of excessive plasma contamination caused by overheating and vaporization. Repair and maintenance of the separated liner plates would probably be more difficult than in situ recoating.

c. Carbon Curtain Liner

Since the carbon curtain liner has much in common with the separated monolithic liners, only those factors that are unique to the curtain will be discussed. The fabrication considerations with respect to technological feasibility, materials cost, and materials availability are all favorable for this concept. However, methods of attachment of the curtain have not been analyzed in detail.

Since carbon is particularly susceptible to chemical sputtering, high temperature operation, with its attendant problems, is mandatory. Gross differences in the behavior of carbon cloth after bombardment by helium and hydrogen have been observed.[20-25,69] The reasons for these differences must be resolved, since the gross damage reported by some investigators would probably be unacceptable.

Thermal vaporization of graphite may be critical for this concept because of thermal conductivity effects related to the geometric considerations. Low thermal conductivity through the cloth related to strand-to-strand heat transfer coefficients for the large number of fibers (of the order of a thousand per thread bundle) may create excessive temperatures at the plasma surface, leading to vaporization. Additional data and analysis are required to resolve this question.

Vacuum properties of the graphite cloth will require additional pumping capability relative to a metal or low-Z coated wall. Initial outgassing will be much more difficult than for some of the other concepts, because of the additional surface area and structure of the cloth.

Mechanical integrity limitations and unattractive failure modes may limit the usefulness of this concept. Although substantial variation in the degradation of graphite cloth from neutron and ion bombardment has been reported in the literature, severe degradation of the cloth has been reported for several conditions.[21,25,69] It is well known that neutron radiation effects in graphite are strongly dependent on the type of structure. The structure of the graphite filaments is similar to structures in which radiation-induced swelling and damage is large. Light ion irradiation can also lead to severe degradation of the cloth fibers. A major concern with the graphite cloth concept is the mode of failure. Degradation and fraying or breaking of the filiments as a result of neutron and ion bombardment may cause accelerated deterioration of the cloth and enhanced contamination of the plasma. Frayed or broken filaments protruding toward the plasma region will have a reduced heat transfer capability and will probably overheat and vaporize, further increasing plasma contamination. This potential for enhanced degradation of the cloth liner resulting from accelerated damage of frayed or fragmented pieces hanging in the plasma region is a major concern relating to the viability of this concept.

d. Low-Sputter Coating

As indicated by the light ion sputtering curves in Figures B-2 through B-4, some materials, particularly tungsten, have much lower sputtering coefficients at low incident particle energies than do the other materials. Tungsten also has a relatively high threshold energy, e.g., 217 eV for D^+,[10] for light ion sputtering. As a result, the feasibility of a low-sputtering first-wall surface has been assessed. Although the light-ion sputtering coefficients

are very low at ion energies below 1 keV, the allowable plasma impurity levels of these high-Z ions are extremely low. Therefore, impurity contributions from other sources such as blistering and neutron sputtering, which were negligible for the low-Z surfaces, become more important for this concept.

Tungsten is considered to be the prime candidate for the low-sputtering surface. Because of fabrication difficulties with tungsten, viz., welding and machining, the most appropriate near-term approach for this concept is a thin tungsten coating on a stainless steel substrate. This approach minimizes the quantity of material required and alleviates many of the fabrication and joining difficulties. Several coating procedures such as plasma spray, chemical vapor deposition (CVD), and sputtering have been used for applying tungsten coatings.[59] As in the case of the low-Z coatings, the plasma spray or detonation gun processes[59,60] are preferred in order to obtain appropriate microstructures to minimize blistering.[62,63] Most of the other technical considerations and the failure mechanisms will be similar to those discussed above for the low-Z coatings. Since tungsten has favorable high-temperature properties, thermal vaporization should be minimal. The maximum temperature limitations will probably be established by the substrate. A low-sputtering tungsten coating appears as technologically feasible as a low-Z coating; however, the low-Z coating seems preferable from a plasma contamination point of view, as shown in Figure B-11. A major consideration is the substantial increase in sputtering yield with an increase in incident ion energy (see Figures B-2 through B-4). The plasma performance becomes extremely unfavorable for the tungsten liner if incident ion energies exceed a few hundred eV.

---

1. H. Wiedersich, M. S. Kaminsky and K. M. Zwilsky, *Proc. Conf. on Surface Effects in Controlled Fusion* (1974), *J. Nucl. Mater.*, 53 (1974).

2. *Proc. First Topical Meeting on the Technology of Controlled Nuclear Fusion*, April 16-18, 1974, San Diego, California, USAEC Report CONF-740402 (1974).

3. *Proc. Symp. on Technology of Controlled Thermonuclear Experiments and Engineering Aspects of Fusion Reactors*, Nov. 20-22, 1976, Austin, Texas, USAEC Report CONF-72111 (1972).

4. *Proc. Sixth European Conf. on Controlled Fusion and Plasma Physics*, July 30-Aug. 4, 1973, Moscow (1973).

5. *Proc. Intern. Conf. on Surface Effects in Controlled Fusion Devices*, San Francisco (1976), *J. Nucl. Mater.* (to be published).

6. P. Sigmund, "Theory of Sputtering. I. Sputtering Yield of Amorphous and Polycrystalline Targets," *Phys. Rev.*, 184, 383 (1969).

7. S. Danyluk and P. Bratt, "Studies of CTR First-Wall Erosion by Physical Sputtering," Argonne National Laboratory Report ANL/CTR/TM-60 (1976).

8. D. Rosenberg and G. K. Wehner, "Sputtering Yields for Low Energy He^+, Kr^+, and Xe^+ — Ion Bombardment," *J. Appl. Phys.*, 33, 1842 (1962).

9. G. S. Kinchin and R. S. Pease, "The Mechanism of the Irradiation Disordering of Alloys," *Rep. Prog. Phys.*, 18, 1 (1955).

10. E. Hotston, "Threshold Energies for Sputtering," *Nucl. Fusion*, 15, 544 (1975).

11. R. Behrisch, "First-Wall Erosion in Fusion Reactors," *Nucl. Fusion*, 12, 695 (1972).

12. R. Kelly and N. Q. Lam, "The Sputtering of Oxides, Part I: A Survey of Experimental Results," *Radiat. Eff.*, 19, 39 (1973).

13. M. Kaminsky and S. K. Das, "14.1 MeV Neutron Sputtering of Polycrystalline and Monocrystalline Niobium with Different Surface Microstructures," *J. Nucl. Mater.*, 60, 111 (1976).

14. M. Kaminsky and S. K. Das, "Particle Emission from Solids Under 14 MeV Neutron Impact," *J. Nucl. Mater.*, 53, 162 (1974).

15. O. K. Harling, M. T. Thomas, R. L. Broksinski and L. A. Rancitelli, "Recent Neutron Sputtering Results and Status of Neutron Sputtering," *Proc. Intern. Conf. on Surface Effects in Controlled Fusion Devices*, San Francisco (1976), *J. Nucl. Mater.* (to be published).

16. R. G. Meisenheimer, "Some 14 MeV Neutron Sputtering Characteristic of a Polycrystalline Nb Sample," *Ibid.*

17. L. H. Jenkins, G. J. Smith, J. F. Wendelkin and M. J. Saltmarsh, "Neutron Sputtering Yields from Ni, Nb, and Au," *Ibid.*

18. J. P. Biersack, E. Santner, R. Neubert and J. Ney, "Simulation Experiments for the Sputtering of Nb by 14 MeV Neutrons," *Ibid.*

19. D. M. Gruen, "Chemical Effects of Plasma Interactions with Thermonuclear Reactor Surfaces," in *The Chemistry of Fusion Technology*, D. M. Gruen, Ed. (Plenum Press, N. Y., 1972), p. 215.

20. J. Roth, J. Bohdansky, W. Poschenrieder and M. K. Sinha, "Physical and Chemical Sputtering of Graphite and SiC by Hydrogen and Helium in the Energy Range of 300 to 6000 eV," *Proc. Intern. Conf. on Surface Effects in Controlled Fusion Devices*, San Francisco (1976), *J. Nucl. Mater.* (to be published).

21. S. Veprek, M. R. Haque and H. R. Oswald, "On the Chemical Erosion of Some Low-Z Materials by Hydrogen Plasma and on the Possibility of Regeneration of the First Wall by Low Pressure Plasma CVD," *Ibid.*

22. R. Behrisch and B. B. Kadomtsev, "Plasma Physics and Controlled Nuclear Fusion Research," *Proc. Fifth Intern. Conf. on Plasma Physics and Controlled Nuclear Fusion Research*, Tokyo (1974).

23. I. P. Busharov, E. A. Gorbatov, V. M. Gusev and Y. V. Martynenko, "Chemical Atomization of Graphite by H^+ Ions," ERDA-TR-50 (Trans.) (1975).

24. M. Balooch and D. R. Olander, "Reactions of Modulated Moleclear Beams with Pyrolytic Graphite-III Hydrogen," *J. Chem. Phys.*, 63, 4772 (1975).

25. B. Feinberg and R. S. Post, "Graphite Surface Erosion and Blistering," *J. Vac. Sci. Technol.*, 13, 443 (1976).

26. A. R. Krauss and D. M. Gruen, "Determination of Ion Fraction and Energy Deuterium Bombarded Surfaces," *Proc. Intern. Conf. on Surface Effects in Controlled Fusion Devices*, San Francisco (1976), *J. Nucl. Mater.* (to be published).

27. D. M. Gruen, P. A. Finn and D. L. Page, "Vaporization Thermodynamics and Molecular Sputtering of Binary Targets," *Nucl. Technol.*, 29, 309 (1976).

28. J. N. Smith, C. H. Meyer and J. K. Layton, "Sputtering Measurements on Controlled Thermonuclear Reactor Materials Using Auger Electron Spectroscopy," *Nucl. Technol.*, 29, 318 (1976).

29. R. Weissmann and P. Sigmund, "Sputtering and Backscattering of keV Light Ions Bombarding Random Targets," in *Ion Surface Interaction, Sputtering, and Related Phenomena*, R. Behrisch, Ed. (Gordon and Breach, N. Y., 1973), p. 47.

30. W. Bauer and G. J. Thomas, "Helium and Hydrogen Re-emission During Implantation of Molybdenum, Vanadium, and Stainless Steel," *J. Nucl. Mater.*, 53, 127 (1974).

31. K. L. Wilson, G. J. Thomas, and W. Bauer, "Low-Energy Proton Implantation of Stainless Steel," *Nucl. Technol.*, 29, 322 (1976).

32. G. Carter, "Ion Reflection, Penetration, and Entrapment in Solids," *J. Vac. Sci. Technol.*, 7, 31 (1970).

33. K. Erents and G. M. McCraken, "Trapping and Re-emission of Fast Deuterium Ions from Nickel," *Br. J. Appl. Phys.*, 2, 1397 (1969).

34. D. J. Reed, F. T. Harris, D. G. Armour and G. Carter, "Thermal Evolution Spectrometry of Low Energy Helium Ions Injected into Stainless Steel and Nickel Targets," *Vacuum*, 24, 179 (1974).

35. L. Johnson, M. J. Dresser and E. E. Donaldson, "Adsorption and Absorption of Hydrogen by Niobium," *J. Vac. Sci. Technol.*, 9, 857 (1972).

36. W. Eckstein, H. Verbeek and P. Matschke, "Backscattering of Hydrogen," *Proc. Intern. Conf. on Surface Effects in Controlled Fusion Devices*, San Francisco (1976), *J. Nucl. Mater.* (to be published).

37. E. W. Thomas, et al., "Scattering of H^+ and He^+ Ions from Surfaces: Charge State and Excited State Composition," *Ibid.*

38. O. S. Oen and M. T. Robinson, "Computer Studies of the Scattering of Low-Energy Hydrogen Ions from Polycrystalline Solids," *Ibid.*

39. K. Takayanagi and H. Suzuki, "Collection of Cross-Section Data for Atomic Processes," Plasma Physics Institute, Nagoya Univ. Report IPPJ-DT-48 (1975).

40. R. A. C. Riviere, "Penetration of Fast Hydrogen Atoms into a Fusion Reactor Plasma," *Nucl. Fusion*, 11, 363 (1971).

41. W. Lotz, "Electron-Impact Ionization Cross Sections and Ionization Rate Coefficients for Atoms and Ions," *Astrophys. J. Suppl.*, 14, 207 (1966-67).

42. R. L. Freeman and E. M. Jones,"Analytic Expressions for Selected Cross Sections and Maxwellian Rate Coefficients," Culham Report CLM-R-137 (1974).

43. C. E. Moore, "Atomic Energy Levels," National Bureau of Standards Circular 467 (1949).

44. R. L. Kelly and D. E. Harrison, Jr., "Ionization Potentials, Experimental and Theoretical, of the Elements Hydrogen to Krypton," *Atomic Data*, 3, 177 (1971).

45. G. R. Hopkins, "Estimation of Impurity Radiation Losses from Fusion-Reactor Plasma," *Proc. Symp. on Technology of Controlled Thermonuclear Fusion Experiments and the Engineering Aspects of Fusion Reactors*, Nov. 20-22, 1976, Austin, Texas, USAEC Report CONF-721111 (1974), p. 795.

46. R. F. Post, "Impurity Radiation Losses from a High Temperature Plasma," *J. Nucl. Energy*, C3, 273 (1961).

47. A. P. Vasilev, G. G. Dologov-Savelyev and V. I. Kogan, "Radiation by Impurities in a Rarefiel Hot Hydrogen Plasma," *Nucl. Fusion Suppl., Part 2*, 655 (1962).

48. E. Hinnov, "Multiple Ionization in High-Temperature Plasmas," Princeton Plasma Physics Laboratory Report MATT-777 (1970).

49. Yu. I. Galuskin and V. I. Kogan, "Radiation Losses in a Dense High-Temperature Hydrogen Plasma Containing Impurities," *Nucl. Fusion*, 11, 597 (1971).

50. I. Galuskin, V. I. Gervids and V. I. Kogan, "Radiation Losses in Certain Thermonuclear Systems," *Nucl. Fusion Suppl.*, 193 (1972).

51. V. M. Gusev, et al., "Conditions of Vacuum Physics for Selection of the Material of First Wall and Diaphram of the Demonstration Thermonuclear Reactor-Tokamak (T-20)," IAEA-2545 (1975).

52. T. A. Carlson, et al., "Calculated Ionization Potentials for Multiple Charged Ions," *Atomic Data*, 2, 63 (1970).

53. W. M. Stacey, Jr., et al., "Tokamak Experimental Power Reactor Studies," Argonne National Laboratory Report ANL/CTR-75-2 (1975).

54. S. K. Das and M. Kaminsky, "Effect of He^+ and D^+ Ion Beam Flux on Blister Formation in Niobium and Vanadium," in *Applications of Ion Beams to Metals*, S. T. Picraux, et al., Eds. (Plenum Press, N. Y., 1974), p. 543.

55. J. Roth, R. Behrisch and B. M. Scherezer, "Blistering of Niobium Due to Low Energy Helium Ion Bombardment Investigated by Rutherford Backscattering," *Ibid.*, p. 573.

56. H. Verbeek and W. Eckstein, "Radiation Blistering After H^+, D^+, and He^+ Ion Implantation into Surfaces of Stainless Steel, Mo, and Be," *Ibid.*, p. 597.

57. S. K. Das and M. Kaminsky, "Radiation Blistering of Structural Materials for Fusion Devices and Reactors," *J. Nucl. Mater.*, 53, 115 (1974).

58. G. J. Thomas and W. Bauer, "Surface Deformation in He and H Implanted Metals," *J. Nucl. Mater.*, 53, 134 (1974).

59. A. A. Bauer and J. L. Bates, "An Evaluation of Electrical Insulators for Fusion Reactors," Battelle Columbus Laboratory Report BMI-1930 (1974).

60. J. F. Pesek and R. Tucker, Union Carbide Corp., Indianapolis, Personal Communication.

61. W. Dodson, Oak Ridge National Laboratory, Personal Communication.

62. S. K. Das, M. Kaminsky and T. D. Rossing, "Reduction of Surface Erosion Caused by Helium Blistering: Microstructural Effects," *Appl. Phys. Lett.*, 27, 197 (1975).

63. S. K. Das and M. Kaminsky, "Reduction of Surface Erosion Caused by Helium Blistering in Sintered Beryllium and Sintered Aluminum Powder," *Proc. Intern. Conf. Surface Effects in Controlled Fusion Devices*, San Francisco (1975), *J. Nucl. Mater.* (to be published).

64. S. A. Cohen, "Plasma-Wall Interaction in the ATC Tokamak," *Ibid.*

65. C. C. Baker, et al., "Experimental Power Reactor Conceptual Design Study," General Atomic Company Report GA-A13534 (1975).

66. M. Roberts, et al., "Oak Ridge Tokamak Experimental Power Reactor Study — Reference Design," Oak Ridge National Laboratory Report ORNL/TM-5042 (1975).

67. L. H. Rovner and G. R. Hopkins, "Ceramic Materials for Fusion," *Nucl. Technol.*, 29, 274 (1976).

68. R. W. Conn, et al., "New Concepts for Controlled Fusion Reactor Blanket Design," University of Wisconsin Report UWFDM-115 (1974).

69. R. Ekern, S. K. Das and M. Kaminsky, "The Temperature Dependence of Surface Damage in Graphite Cloth Irradiated with Deuterons and Helium Ions," *Proc. Intern. Conf. on Surface Effects in Controlled Fusion Devices*, San Francisco (1976), *J. Nucl. Mater.* (to be published).

APPENDIX C

PLASMA CALCULATIONAL MODELS

1. Global Model

a. Balance Equations

Particle and power balance equations which have been averaged over given spatial profiles are used to represent the plasma during the heatup and burn phases.

D-T Ions

$$\frac{d\bar{n}_{DT}}{dt} = \overline{I_B(1-2f)} - \overline{2p(1-p)\,n_{DT}^2\langle\sigma v\rangle_f} + \bar{I}_c - \frac{\bar{n}_{DT}\left(1-f_{DT}\right)}{\tau_{DT}^P} \qquad \text{(C-1)}$$

$$\frac{3}{2}\frac{d}{dt}\overline{n_{DT}T_{DT}} = \overline{p(1-p)\,\langle\sigma v\rangle_f n_{DT}^2\left[\bar{U}_\alpha f_{\alpha DT} - 3T_{DT}\right]} - \bar{K}_{ie}$$

$$+ \overline{I_B\left[G_B U_B \hat{f}_{BDT} + \frac{3}{2}T_{DT}(1-2f)\right]} - \frac{3}{2}\frac{\overline{n_{DT}T_{DT}}}{\tau_{DT}^E}, \qquad \text{(C-2)}$$

where

$$K_{ie} = 1.2\times10^{-18}\,\frac{n_e n_{DT} T_{DT}}{T_e^{3/2}}\left(1-\frac{T_e}{T_{DT}}\right)A_{DT}\sum_j \frac{Z_j r_j}{A_j}. \qquad \text{(C-3)}$$

In these equations I_B is the injected source of energetic deuterons, p is the tritium fraction, f is the suprathermal fusion probability, U_B is the beam energy, G_B is the suprathermal fusion enhancement of the injected beam energy, $\hat{f}_{BDT}$ is the fraction of the beam energy acquired by the D-T ions, $\langle\sigma v\rangle_f$ is the Maxwellian-averaged fusion cross section, I_c is the source of D-T ions, τ_{DT}^P and τ_{DT}^E are the particle and energy confinement times, n_j and T_j are the particle density and temperature of plasma species j, U_α = 3.52 MeV is the fusion alpha energy, $f_{\alpha DT}$ is the fraction of the fusion alpha energy acquired by the D-T ions, A_j is the atomic mass, Z_j is the atomic number, and r_j is the fractional concentration of plasma species j. A bar over a quantity denotes a spatial average. The sum is over all ions. All quantities are in mks units except that temperatures and energies are in keV.

The quantity f_{DT} is the effective recycle fraction, including the effect of charge exchange,

$$f_{DT} \equiv \left(1 - \eta_{DT}\right) R_{DT} \frac{\left(1 - A_{cx}\right)}{\left(1 - R_{DT} A_{cx}\right)} , \tag{C-4}$$

where η_{DT} is the D-T ion removal efficiency, R_{DT} is the wall reflection coefficient (including backscattering and re-emission), and A_{cx} is the charge-exchange albedo for neutral D-T atoms incident upon the plasma. (See Appendix B for a discussion of the plasma-wall interaction model.)

If the charge-exchange albedo for neutral D-T atoms used to refuel the plasma (by whatever mechanism) is A_{cx}^{ext}, the actual refueling rate per unit volume which is required to supply the refueling source $\bar{I}_c$ is

$$F_{DT}^{ext} = \bar{I}_c \Bigg/ \left[\left(1 - A_{cx}^{ext}\right) + R_{DT} A_{cx}^{ext} \frac{\left(1 - A_{cx}\right)}{\left(1 - R_{DT} A_{cx}\right)} \right] . \tag{C-5}$$

The wall flux of D-T particles (ions + neutrals) is

$$F_{wall}^{DT} = \frac{F_{DT}^{ext} A_{cx}^{ext}}{1 - R_{DT} A_{cx}} + \frac{\eta_{DT}}{\tau_{DT}^{P}} \left(1 - \eta_{DT}\right) \left(\frac{1}{1 - R_{DT} A_{cx}}\right) . \tag{C-6}$$

Alpha Particles

$$\frac{d\bar{n}_\alpha}{dt} = p(1 - p) \langle \sigma v \rangle_f \bar{n}_{DT}^2 + \bar{f}\bar{I}_\beta - \frac{\bar{n}_\alpha \left(1 - \bar{f}_\alpha\right)}{\tau_\alpha^{\rho}} , \tag{C-7}$$

where

$$f_\alpha \equiv \left(1 - \eta_\alpha\right) R_\alpha . \tag{C-8}$$

The wall flux of alpha particles is

$$F_{wall}^{\alpha} = \frac{\bar{n}_\alpha}{\tau_\alpha^{P}} \left(1 - \eta_\alpha\right) . \tag{C-9}$$

Impurities

$$\frac{d\bar{n}_I}{dt} = \left[\overline{p(1-p)\langle\sigma v\rangle_f n_{DT}^2} + \overline{fI_B}\right] S_n + F_{wall}^{DT} S_{DT} + F_{wall}^{\alpha} S_{\alpha}$$

$$+ F_{wall}^{I} S_I - \frac{\bar{n}_I\left(1 - f_I\right)}{\tau_I^P} , \qquad \text{(C-10)}$$

where the S's are the sputtering coefficients, f_I is defined as in Eq. (C-8) with $\alpha \to I$, and F_{wall}^{I} is defined as in Eq. (C-9) with $\alpha \to I$.

Electrons

$$\bar{n}_e = \bar{n}_{DT} + 2\bar{n}_{\alpha} + \sum_I \overline{Z_I n_I} , \qquad \text{(C-11)}$$

$$\frac{3}{2}\frac{d}{dt}\overline{n_e T_e} = \overline{p(1-p)\langle\sigma v\rangle_f n_{DT}^2 U_{\alpha} f_{\alpha e}} + \overline{G_B I_B U_B \hat{f}_{Be}} + \eta\bar{J}^2$$

$$+ \bar{K}_{ie} - \bar{W}_R - \frac{3}{2}\frac{\overline{n_e T_e}}{\tau_e^E} , \qquad \text{(C-12)}$$

where

$$\eta = \frac{2.8 \times 10^{-8}\ \gamma\ \bar{Z}_{eff}}{\bar{T}_e^{3/2}} \qquad \text{(C-13)}$$

is the resistivity, with γ being the "anomaly factor", $\bar{J}$ is the average plasma current density, W_R is the radiative power (see Appendix B), and τ_e^E is the electron energy confinement. The sum in Eq. (C-11) is over impurities, I.

$$W_R = P_{rad} + P_c ,$$

where P_{rad} accounts for bremsstrahlung, line, and recombination radiation and was defined in Appendix B, and P_c accounts for cyclotron radiation

$$P_c = \frac{3.7 \times 10^3\ n_e B_{t0}^{5/2}\left(T_e^{11/4} + 0.0049\ T_e^{15/4}\right)}{\sqrt{n_{DT}}} .$$

Spatial distribution profiles for n_{DT}, n_α, n_I, T_{DT}, T_e, I_B, and Z_I are given a priori in the form:

$$x(r,t) = \bar{x}(t)P(r) , \tag{C-14}$$

where

$$P(r) = (\alpha + 1)\left[1 - \frac{r^2}{a^2}\right]^\alpha , \tag{C-15}$$

and the spatial average of any quantity is defined as:

$$\bar{x}(t) = \frac{2}{a}\int_0^a x(r,t)\, r\, dr . \tag{C-16}$$

(For the case of noncircular cross sections, a is taken to be $\tilde{a}$, the average radius of the cross section.)

In this report the density profiles for all plasma species are taken to be the same with $\alpha = \alpha_n$; all temperature profiles are taken to be the same with $\alpha = \alpha_T$; and the beam deposition profile and impurity charge (depending on ionization level) profile are taken to be flat ($\alpha = 0$). In the balance equations and in expressions for the various powers, wall loadings, etc., the various reaction rates are calculated as a function of r, then averaged. An exception is that the transport loss terms are calculated in terms of averaged values, $\bar{n}_{DT}$, $\bar{T}_{DT}$, etc.

Thermalization of injected deuterons and of the fusion alpha particles is computed as a function of r from a model of a test particle slowing down in a multicomponent plasma. From this calculation the distribution of fast ion energy among the plasma components and the suprathermal fusion rate are determined. The thermalization model is described in Appendix A of Reference 1.

b. Transport Model

A multi-regime transport model is used to compute the confinement parameters, τ. At high collision frequencies, τ_{DT}^P and τ_e^E are computed from pseudoclassical theory and τ_{DT}^E is computed from neoclassical theory. It is assumed $\tau_\alpha^P = \tau_I^P = \tau_{DT}^P$. For electron-ion collision frequencies less than the

electron bounce frequency, τ_{DT}^{P} and τ_{e}^{E} are computed from pseudoclassical, trapped-electron mode or trapped-ion-mode theory, whichever yields the smalles τ; and τ_{DT}^{E} is computed from either neoclassical or trapped-ion-mode theory, whichever yields the least value of τ. The expressions used are consistent with Ref. 2, and are written here for the confinement parameter $n_{DT}\tau$.

(1) Pseudoclassical (Particles and Electron Energy)

$$(n\tau)_{P}^{PC} = \frac{1.8 \times 10^{8}\ I_{p}^{2}\bar{T}_{e}^{1/2}}{\bar{Z}_{eff}} ,$$

$$(n\tau)_{E}^{PC} = 0.3(n\tau)_{P}^{PC} . \qquad \text{(C-17)}$$

(2) Trapped Electron Mode (Particles and Electron Energy)

$$(n\tau)_{P}^{TEM} = \begin{cases} \dfrac{6.35 \times 10^{6}\ \tilde{A}^{3/2}}{\bar{Z}_{eff}}\ \bar{T}_{e}^{1/2} I_{p}^{2}\left[1 + \left(\nu_{ei}/\omega_{0}\right)^{2}\right] , & \text{if } \nu_{ei} < \omega_{-1} \\ 0 , & \text{otherwise} \end{cases}$$

$$(n\tau)_{E}^{TEM} = (n\tau)_{P}^{TEM} \Big/ \frac{3}{2}\,\tilde{A} . \qquad \text{(C-18)}$$

This is a combination, of the form given by Reference 3, which approaches the asymptotic limits given in Reference 2 for TEM-1 and TEM-2.

c. Trapped Ion Mode (Particles, Electron Energy, and Ion Energy)

$$(n\tau)_P^{TIM} = (n\tau)_E^{TIM}$$

$$= \begin{cases} \dfrac{2.05 \times 10^{-5}\ \beta_{pe}^2 I_p^4 \bar{Z}_{eff} B_{t0}^2 \tilde{A}^{5/2}}{\bar{T}_e^{11/2}} \left[1 + \left(\dfrac{\bar{T}_e}{\bar{T}_{DT}}\right)\right]^2, & \text{if } \nu_{ei} < \omega_{-1} \quad \text{(electrons)} \\ & \text{or } \nu_{ei} < \left(\dfrac{\bar{T}_{DT}}{\bar{T}_e}\right)^2 \omega_{-1} \text{ (ions)} \\ 0, & \text{otherwise .} \end{cases} \quad \text{(C-19)}$$

d. Neoclassical (Ion Energy)

$$(n\tau)_P^{NC} = \begin{cases} \dfrac{1.83 \times 10^7\ \bar{T}_{DT}^{1/2} \tilde{A}^2 I_p^2}{\bar{Z}_{eff}}, & \nu_{ei} > \left(\bar{T}_{DT}/\bar{T}_e\right)^2 \omega_{-2} \\ & \text{(collisional)} \\ \dfrac{9.95 \times 10^6\ \bar{T}_{DT}^{1/2} \tilde{A}^{1/2} I_p^2}{\bar{Z}_{eff}} \left[\dfrac{\nu_{ei}}{\left(\bar{T}_{DT}/\bar{T}_e\right)^2 \omega_{-1}}\right], & \left(\dfrac{\bar{T}_{DT}}{\bar{T}_e}\right)^2 \omega_{-1} < \nu_{ei} < \left(\dfrac{\bar{T}_{DT}}{\bar{T}_e}\right)^2 \omega_{-2} \\ & \text{(plateau)} \\ \dfrac{9.95 \times 10^6\ \bar{T}_{DT}^{1/2} \tilde{A}^{1/2} I_p^2}{\bar{Z}_{eff}}, & \nu_{ei} < \left(\dfrac{\bar{T}_{DT}}{\bar{T}_e}\right)^2 \omega_{-2} \\ & \text{(banana) ,} \end{cases} \quad \text{(C-20)}$$

where I_p is the plasma current, $\bar{T}_{DT}$ and $\bar{T}_e$ are the average ion and electron temperatures, $\tilde{A} = R/\tilde{a}$ is the average aspect ratio, R_0 is the major radius, $\tilde{a}$ is the average radius of the cross section,

$$Z_{eff} = \sum_{ions} n_j Z_j^2 \Big/ \sum_{ions} n_j Z_j$$

is the effective charge,

$$\nu_{ei} = \frac{1.6 \times 10^{-15}\ \bar{Z}_{eff}\bar{n}_{DT}}{\bar{T}_e^{3/2}}$$

is the electron-ion collision frequency,

$$\nu_{eff} = \frac{3}{2}\tilde{A}\ \nu_{ei}$$

is the effective collision frequency,

$$\omega_{\zeta} = \frac{0.19\ \bar{T}_e^{1/2} I_p}{\tilde{A}^{1/2} B_{t0} \tilde{a}^2}$$

is the frequency where TEM peaks, B_{t0} is the toroidal magnetic field at the center of the chamber,

$$\omega_{-1} = \frac{2.04\ \bar{T}_e^{1/2} I_p}{\tilde{A}^{1/2} \tilde{a}\ R_0 B_{t0}}.$$

is the frequency where the neoclassical plateau regime for electrons changes to the banana regime, and

$$\omega_{-2} = 1.84\ \tilde{A}^{3/2}\ \omega_{-1}$$

is the frequency where the neoclassical collisional regime for electrons changes to the plateau regime.

A graph of the confinement parameter for a case similar to the reference design is shown in Figure C-1.

2. MHD Equilibrium Model

The axisymmetric, ideal MHD equilibrium model used in this report is essentially that of Callen and Dory.[4] The equations used are the ideal MHD equilibrium equation

$$\nabla p = \vec{J} \times \vec{B} \qquad \text{(C-21)}$$

and the Maxwell equations

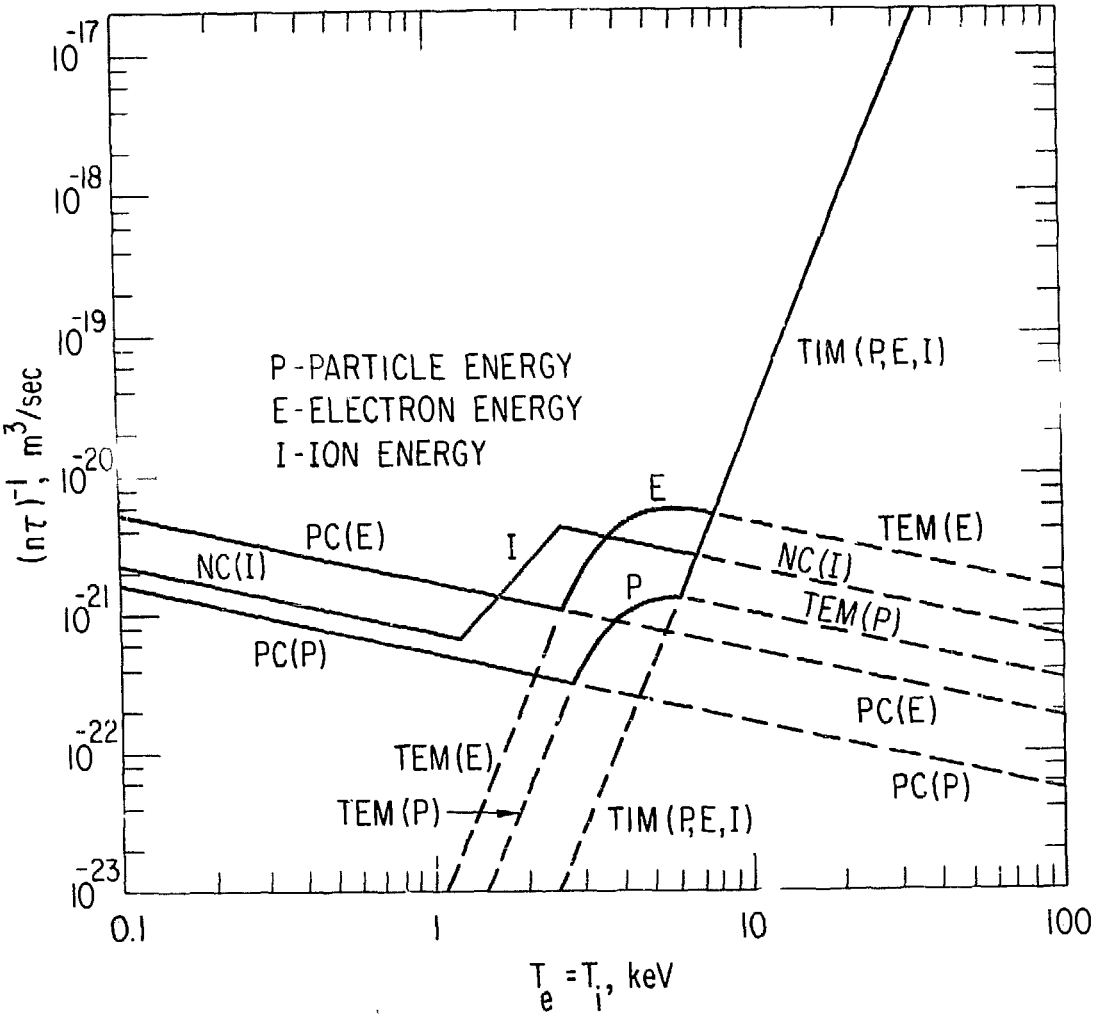

Figure C-1. Confinement versus temperature for an EPR plasma.

$$\nabla \cdot \vec{B} = 0 \tag{C-22}$$

$$\nabla \times \vec{B} = \mu \vec{J} \, . \tag{C-23}$$

For azimuthal symmetry [$(\partial/\partial\phi) = 0$], the magnetic field can be written

$$\vec{B} = \vec{B}_t + \vec{B}_p = B_t \hat{\phi} + \frac{\hat{\phi}}{2\pi R} \times \nabla\psi \, , \tag{C-24}$$

where $\psi = 2\pi R A_\phi$ is the flux function, and $\vec{A}$ is the vector potential. It can be shown that the poloidal field lines are tangent to the surfaces ψ = constant. The pressure, p, and the quantity $F \equiv RB_t$ must be constant on the flux surfaces,

$$p = p(\psi) \tag{C-25}$$

$$F = F(\psi) \, , \tag{C-26}$$

and the current flows in the flux surfaces. The components of the current density are:

$$J_p = -\frac{2\pi B_p}{\mu} \frac{dF}{d\psi} \tag{C-27}$$

$$J_t = -\frac{2\pi F}{\mu R} \frac{dF}{d\psi} - 2\pi R \frac{dp}{d\psi} \, . \tag{C-28}$$

The equilibrium equation for the flux function is:

$$\frac{\partial^2\psi}{\partial R^2} - \frac{1}{R}\frac{\partial\psi}{\partial R} + \frac{\partial^2\psi}{\partial Z^2} = -4\pi^2 \left[\mu R^2 \frac{dp}{d\psi} + F \frac{dF}{d\psi}\right] \, . \tag{C-29}$$

This equation is solved by specifying $p(\psi)$ and $F(\psi)$, then solving for $\psi(R,Z)$. The parametrization of p and F used in this report is:

$$p = p_0 \hat{\psi}^\alpha \tag{C-30}$$

$$F^2 = F_0^2 \left(1 - \delta\hat{\psi}^\beta\right) \, , \tag{C-31}$$

where

$$\hat{\psi} = \frac{\psi_\ell - \psi}{\psi_\ell - \psi_m}, \tag{C-32}$$

where ψ_ℓ and ψ_m are the values of ψ at the limiter and magnetic axis, respectively.

The definitions of the plasma current, I_p, the safety factor, q,[5] and the pressure ratios, β_p and β_t are given in terms of integrals around a poloidal flux line defined by a value, ψ, of the flux function:

$$\mu I_{enc}(\psi) = \oint_\psi B_p \, d\ell \tag{C-33}$$

$$\mu I_p = \oint_{\psi_\ell} B_p \, d\ell \tag{C-34}$$

$$q(\psi) = \frac{F(\psi)}{2\pi} \oint_\psi \frac{d\ell}{R^2 B_p} \tag{C-35}$$

$$\beta_p = \frac{2\mu \bar{p}}{\left\langle B_n^2 \right\rangle_{\psi_\ell}} \tag{C-36}$$

$$\beta_t = \frac{2\mu \bar{p}}{B_{t0}^2}, \tag{C-37}$$

where $\bar{p}$ is the average pressure over the plasma cross section, the flux line average is defined as:

$$\langle x \rangle = \oint_\psi x \, d\ell \Big/ \oint_\psi d\ell ,$$

and B_{t0} is the vacuum toroidal field at the center of the chamber. It should be noted that other definitions of β_p are in use. (The Shafranov limit[6] for the definition given above is $\beta_p < 1/2\ A$.)

It can be seen that if ψ is a solution of Eq. (C-29), then $\psi \to \psi' = \lambda\psi$ is a solution provided:

$$\vec{B}_p \rightarrow \vec{B}_p' = \lambda \vec{B}_p$$

$$I \rightarrow I' = \lambda I$$

$$p \rightarrow p' = \lambda^2 p$$

$$F_0 \rightarrow F_0', \text{ arbitrary}$$

$$F^2 \rightarrow F'^2 = F_0'^2 + \lambda^2 \int_{\psi_a}^{\psi} F'^2 \, d\psi$$

$$\beta_p \rightarrow \beta_p' = \beta_p$$

$$\frac{\beta_t}{F_0} \rightarrow \frac{\beta_t'}{F_0'} = \frac{\lambda^2 \beta_t}{F_0'}$$

$$\frac{q}{F_0} \rightarrow \frac{q'}{F_0'} = \frac{q}{\lambda F_0'} . \qquad \text{(C-38)}$$

Since p and F are known only as a function of ψ, but $\psi(R,Z)$ is not known, one cannot specify a quantity such as I_p or q *a priori*. Once a solution is known, however, it can be scaled to give the required value (provided F^2 stays non-negative). All of the solutions that vary only by scaling have the same magnetic axis, and if one does not have reversed toroidal currents, then none do.

Two methods are used in solving Eq. (C-29) in this report. In the fixed boundary method* the flux line at the outer perimeter of the plasma is specified in space. The solution is scaled to give, for example, the desired current or $q(\psi_m) = 1$, and the other quantities are determined for given α, β, and δ. The vector potential (and hence the flux function) due to the plasma loop alone is then calculated explicitly. The part of the flux function not supplied by the plasma loop must be supplied by the external coils. In addition to being the faster and easier of the two methods, the fixed boundary method gives the required external field for any equilibrium and has exactly the plasma

*The fixed boundary code used was based on an equilibrium code originally developed by R. A. Dory at Oak Ridge National Laboratory and substantially modified at Argonne National Laboratory.

cross section desired. In the free boundary method* the plasma current, maximum pressure, and position and currents for the external coils are given, along with the position(s) of a limiter(s). The position of the plasma edge is then determined along with the other quantities for a given α and β. This method gives the equilibrium that would be obtained with an actual placement of coils and also calculates the equilibrium field outside of the plasma. In cases where the boundaries are the same, the two methods give the same results for the same α and β.

3. Global Model Parameters

Plasma Pressure

In computing the plasma pressure, or equivalently β_t, not only the pressure of the thermalized particles but the fast alpha particles and deuterons from the beam which are in the process of thermalizing are included.

$$\beta_t = \frac{\overline{n_{DT}T_{DT}} + \overline{n_e T_e} + \overline{n_\alpha T_{DT}} + \sum \overline{n_I T_{DT}} + \frac{2}{3}\overline{n_\alpha E_\alpha} + \frac{2}{3}\overline{n_B^f E_B}}{B_{t0}^2/2\mu}, \qquad \text{(C-39)}$$

where the sum in the numerator is over impurities, E_α and E_B are the mean energies of the thermalizing alpha particles and deuterons, respectively, and n_α^f and n_B^f are the corresponding densities of such particles at any given instant. These latter quantities are computed from the general consideration that the number of particles in the process of thermalizing at any time is equal to the source rate times the thermalization time. The formulas are

$$n_\alpha^f = \overline{\left[p(1-p)\langle\sigma v\rangle_f n_{DT}^2 + fI_B\right]\tau_\alpha^{SD}}, \qquad \text{(C-40)}$$

and

$$n_B^f = \overline{I_B \tau_B^{SD}}, \qquad \text{(C-41)}$$

where τ^{SD} is the thermalization time defined in Appendix A of Ref. 1.

---

*The free boundary calculations used the Princeton free boundary code developed by S. Jardin and R. Grimm.

For the static global calculations, the value of β_t is determined from Eq. (C-37) for a given MHD equilibrium state, then Eq. (C-39) determines the upper limit on $\bar{n}_{DT}$, hence the maximum power.

Reactor Performance Parameters

The neutron power flux through the first wall is

$$P_w(MW/m^2) = 2.26 \times 10^{-18} J_w(n/m^2/s) , \tag{C-42}$$

where

$$J_w = \left[\overline{p(1-p)\langle\sigma v\rangle_f n_{DT}^2} + \overline{fI_B}\right] \frac{V_p}{A_w} ,$$

is the 14-MeV neutron current density at the first wall, A_w is the surface area of the first wall, and $V_p = 2\pi^2 a^2 \kappa R$ is the plasma volume. κ is the ratio of the cross-sectional area of a noncircular cross section to that of a circular cross section of the same width. The total power output is

$$P_T(MW) = 1.602 \times 10^{-22} E_{fus}\left[\overline{p(1-p)\langle\sigma v\rangle_f n_{DT}^2} + \overline{fI_B}\right] + \overline{I_B U_B} V_p + \bar{P}_\Omega , \tag{C-43}$$

where

$$E_{fus}(keV) = \left[14.1\ \varepsilon_{bkt} + 3.52\right] \times 10^3 , \tag{C-44}$$

with ε_{bkt} accounting for the energy enhancement in the blanket, and $\bar{P}_\Omega$ is the ohmic heating power,

$$\bar{P}_\Omega(MW) = 10^{-6}\ \eta \bar{J}^2 V_p = 5.6 \times 10^{-14} \frac{\gamma \bar{Z}_{eff} I_p^2 R}{\bar{a}^2 \kappa \bar{T}_e^{3/2}} , \tag{C-45}$$

where R is the major radius. The neutron power is

$$P_N = \varepsilon_{bkt} P_w A_w , \tag{C-46}$$

where ε_{bkt}, P_w and A_w have been defined above.

The radiation power is

$$P_R(MW) = 1.602 \times 10^{-22}\left(\bar{P}_{rad} + \bar{P}_c\right)V_p ,$$

where P_{rad} was defined in Appendix B, and P_c was defined in Section 1 of this appendix. The power loss by transport processes is

$$P_L(MW) = 1.602 \times 10^{-22}\left[\frac{3}{2}\frac{\overline{n_{DT}T_{DT}}}{\tau^E_{DT}} + \frac{3}{2}\frac{\overline{n_\alpha T_{DT}}}{\tau^P_{DT}} + \frac{3}{2}\frac{\overline{n_e T_e}}{\tau^E_e}\right]V_p . \qquad (C\text{-}47)$$

Additional Parameters

There are four additional parameters which are useful in characterizing the performance of the plasma in a tokamak (for that matter, in any reactor). The plasma Q_p is defined as the thermonuclear power generated by the plasma (including the blanket enharcement) divided by the total power put into the plasma from external sources. In a steady-state situation

$$Q_p \equiv \frac{P_T - \left(P_B + P_\Omega\right)}{P_B + P_\Omega} , \qquad (C\text{-}48)$$

where $P_B = P_{inj}V_p$ is the beam power injected into the plasma, and $P_{inj} = \bar{I}_B U_B$. The quantity, Q_p, becomes very large for devices approaching ignition and provides a measure of the gain when neutral beam injection is used to maintain the plasma in a subignition condition. It is used in the steady-state analyses of Chapter III. The definition of Q_p averaged over a burn cycle is

$$Q_p = \frac{\int_0^t \left(P_N + P_L + P_R\right) dt}{\int_0^t \left(P_B + P_\Omega\right) dt} - 1 . \qquad (C\text{-}49)$$

The ratio of the energy density of the injected deuterons to the plasma energy density is

$$\Gamma = \frac{\overline{I_B U_B \tau_B^{SD}}}{\left[\frac{3}{2}\left(\overline{n_{DT}T_{DT}} + \overline{n_e T_e} + \overline{n_\alpha T_{DT}} + \sum \overline{n_I T_{DT}}\right) + \overline{n^f_\alpha E_\alpha} + \overline{n^f_B E_B}\right]} , \qquad (C\text{-}50)$$

where the sum is over impurities.

The fractional burnup is

$$f_{bu} = \frac{2\left[\overline{p(1-p)\langle\sigma v\rangle_f n_{DT}^2} + \overline{fI_B}\right]}{2\left[\overline{p(1-p)\langle\sigma v\rangle_f n_{DT}^2} + \overline{fI_B}\right] + \left(\bar{n}_{DT}/\tau_{DT}^P\right)} . \tag{C-51}$$

The parameter ξ is defined as the ratio of the enhanced beam power to the alpha heating power

$$\xi = \frac{\overline{I_B G_B U_B}}{\overline{p(1-p)\langle\sigma v\rangle_f n_{DT}^2 U_\alpha}} . \tag{C-52}$$

4. Plasma Control Algorithms

Several simple control methods have been examined in connection with the burn cycle analysis. The controllable inputs to the plasma are assumed to be the external refueling current, $\bar{I}_c$, the tritium fraction of the refueling current, p_c, and the supplemental beam power, $\bar{P}_B$, if any. The only time the tritium fraction, p_c, must be varied is when and if the supplemental beam is present, so these two go together. (If there is no supplemental beam, $p_c = 0.5$.)

The control methods for $\bar{I}_c$ and $\bar{P}_B$ are based on the same goal, to maintain β_p as close to $\beta_p^{opt} = 1.7$ as possible, thereby maximizing the fusion power. The control scheme has been formulated as follows. An "error" signal in β_p is defined as the deviation of β_p from its allowed optimum value, i.e.,

$$\Delta\beta_p = \beta_p(t) - \beta_p^{opt} . \tag{C-53}$$

It is desired to reduce this error with a time constant "γ",

$$\left.\frac{d\beta_p}{dt}\right|_{desired} = -\frac{\Delta\beta_p}{\gamma} . \tag{C-54}$$

At any time, there is an actual value of $\dot{\beta}_p$. The difference between the actual

value and the desired value of $\dot{\beta}_p$ determines differential equations for the refueling current and/or the supplemental beam:

$$\frac{d\bar{I}_c}{dt} = -\left[\left.\frac{d\beta_p}{dt}\right|_{actual} - \left.\frac{d\beta_p}{dt}\right|_{desired}\right]\left(\frac{\partial \bar{n}_{DT}}{\partial \beta_p}\right)\left(\frac{\partial \bar{I}_c}{\partial \bar{n}_{DT}}\right), \tag{C-55}$$

$$\frac{d\bar{P}_B}{dt} = -\left[\left.\frac{d\beta_p}{dt}\right|_{actual} - \left.\frac{d\beta_p}{dt}\right|_{desired}\right]\left(\frac{\partial \bar{T}}{\partial \beta_p}\right)\left(\frac{\partial \bar{P}_B}{\partial \bar{T}}\right), \tag{C-56}$$

where

$$\bar{T} = \frac{\bar{T}_{DT} + \bar{T}_e}{2} \approx \bar{T}_{DT} .$$

The partial derivatives in Eqs. (C-55) and (C-56) must be evaluated from the analytical model of the plasma. Using this technique and a suitable differencing scheme, the value of $\bar{I}_c$, for example, becomes

$$\bar{I}_c(t + \Delta t) = \bar{I}_c(t) - \left.\frac{d\bar{n}_{DT}}{dt}\right|_t - \left(\frac{10^8\ I_p^2}{2a^2\bar{T}_{DT}}\right)\left[\frac{\bar{\Delta\beta}_p}{\gamma} + \left.\frac{d\beta_p}{dt}\right|_t\right] \tag{C-57}$$

subject to the restriction that $\bar{I}_c \geq 0$ and a technically imposed restriction that $\dot{\bar{I}}_c$ be less than some $\dot{\bar{I}}_c^{max}$. The information needed from the plasma to implement Eq. (C-57) would be the density, temperature, plasma current, and the poloidal beta itself. The same information is needed to compute the supplemental beam power.

The control scheme for the tritium fraction of the refueling current, p_c, seeks to maintain the tritium fraction, p, of the plasma at a value of 50% (thereby maximizing the fusion power). The algorithm for p_c is analogous to the others except that the "error" signal to be reduced is now the deviation of p from 0.5:

$$\Delta p = p(t) - 0.5 . \tag{C-58}$$

It then follows that:

$$\frac{dp_c}{dt} = -\left[\left.\frac{dp}{dt}\right|_{actual} - \left.\frac{dp}{dt}\right|_{desired}\right]\left(\frac{\partial p_c}{\partial p}\right), \qquad \text{(C-59)}$$

where

$$\left.\frac{dp}{dt}\right|_{desired} = \frac{-\Delta p}{\gamma}$$

subject to $p_c \leq 1$.

In the present analysis γ has been set to 1 sec. The control methods have been tested for a wide variety of conditions and appear to perform fairly well both singly and in combination. The plasma poloidal beta is held fairly closely to β_p^{opt} when the control algorithms are used. The variations in the control parameters dictated by the algorithms do not appear to be physically unreasonable.

5. Core-Corona Model

In order to represent a number of important phenomena which occur in the plasma edge, or corona, region, a model was devised in which separate particle and power balance equations are written for the core and corona regions. The core equations are as given above, except

$$\frac{n_{DT}}{\tau_{DT}^P}\left(1 - f_{DT}\right) \rightarrow \frac{S_{12}}{V_1}\Gamma_{DT12} \quad \text{in Eq. (C-1)},$$

$$\frac{3}{2}\frac{n_{DT}T_{DT}}{\tau_{DT}^E} \rightarrow \frac{S_{12}}{V_1}\left[\frac{3}{2}T_{DT1}\Gamma_{DT12} + q_{DT12}\right] \quad \text{in Eq. (C-2)},$$

and a term

$$-\frac{3}{2}\left(T_{DT1} - T_{DT2}\right)\frac{\partial n_{I1}}{\partial t}$$

is added to Eq. (C-2) when the impurity concentration is increasing, to represent power required to heat incoming impurities. (The overbar, indicating a spatial average over temperature and/or density profiles, is suppressed in

this and the following section.) Also,

$$\frac{n_\alpha}{\frac{P}{\tau_\alpha}}\left(1 - f_\alpha\right) \rightarrow \frac{S_{12}}{V_1}\Gamma_{\alpha 12} \quad \text{in Eq. (C-7)}$$

$$\frac{3}{2}\frac{n_e T_e}{\tau_e^E} \rightarrow \frac{S_{12}}{V_1}\left[\frac{3}{2}T_{e1}\Gamma_{e12} + q_{e12}\right] \text{ in Eq. (C-12)} ,$$

and Eq. (C-10) is replaced by

$$\dot{n}_{I1} = -\frac{S_{12}}{V_1}\Gamma_{I12} . \tag{C-60}$$

S_{12} is the area of the surface interfacing regions 1 (core) and 2 (corona), V_1 is the volume of the core, Γ_{12} and q_{12} are the net convection and conduction currents at the interface (with $1 \rightarrow 2$ being the positive sense).

The corresponding equations for the corona region are similar:

D-T Ions

$$\dot{n}_{DT2} = I_{B2}(1 - f) - 2p(1 - p)\langle\sigma v\rangle_f n_{DT2}^2 + I_{C2} + \frac{S_{12}}{V_2}\Gamma_{DT12} - \frac{S_{2w}}{V_2}\Gamma_{DT2w}\left(1 - f_{DT}\right) , \tag{C-61}$$

$$\frac{3}{2}\frac{d}{dt}\left(n_{DT2}T_{DT2}\right) = p(1 - p)\langle\sigma v\rangle_f n_{DT2}^2 U_\alpha f_{\alpha DT2} + G_B U_B I_{B2}\hat{f}_{BDT2} - K_{ie2}$$
$$+ \frac{3}{2}T_{DT2}\left[I_{B2}(1 - 2f) - 2p(1 - p)\langle\sigma v\rangle_f n_{DT2}^2\right] + \frac{S_{12}}{V_2}q_{DT12}$$
$$+ \frac{3}{2}\left(\frac{T_{DT1} + T_{DT2}}{2}\right)\frac{S_{12}}{V_2}\Gamma_{DT12} - \frac{S_{2w}}{V_2}q_{DT2w}$$
$$- \frac{3}{2}T_{DT2}\frac{S_{2w}}{V_2}\Gamma_{DT2w}\left[1 + \frac{\left(1 - \eta_{DT}\right)R_{DT}A_{cx}}{1 - R_{DT}A_{cx}} - \frac{\left(1 - \eta_{DT}\right)R_{DT}A_{cx}R_{DT}^E}{1 - R_{DT}A_{cx}}\right]$$

$$- F_{DT}^{ext} A_{cx}^{ext} \left[\frac{3/2\ T_{DT2}}{1 - R_{DT} A_{cx}} \left(1 - A_{cx} R_{DT} R_{DT}^{E} \right) - E^{ext} \right]$$

$$- \frac{3}{2} T_{DT2} \left[\Gamma_{\alpha 2w} \left(1 - \eta_{\alpha} \right) R_{\alpha} \left(1 - R_{\alpha}^{E} \right) \right.$$

$$\left. + \Gamma_{I2w} \left(1 - \eta_{I} \right) R_{I} \left(1 - R_{I}^{E} \right) \right] \frac{S_{2w}}{V_2} - \frac{3}{2} T_{DT2} Q_{I} \ , \qquad \text{(C-62)}$$

where

$$Q_{I} = p(1 - p) \left[\langle \sigma v \rangle_{f1} n_{DT1}^{2} \frac{V_1}{V_2} + \langle \sigma v \rangle_{f2} n_{DT2}^{2} \right] S_{n} + F_{wall}^{DT} S_{DT}$$

$$+ F_{wall}^{I} S_{I} + F_{wall}^{\alpha} S_{\alpha} \ , \qquad \text{(C-63)}$$

S_{2w} is the surface area of the external boundary of the corona, R^E is the fraction of the incident energy which a particle retains in being reflected from the wall ($R^E = 0$ in this report), and E^{ext} is the energy of the external D-T particle source. The last term in Eq. (C-62) represents the power lost in heating wall-sputtered impurities; the next-to-last term represents the power lost in heating recycling alphas and impurities; the third-to-last term represents the power loss associated with the charge-exchange of the refueling atoms; and the fourth-to-last term represents the D-T convective loss from the plasma edge — including charge-exchange effects.

Equation (C-5) determines the external source required to refuel the corona at a rate I_{c2} in the presence of charge-exchange. Equations (C-6) and (C-9) give the (ion + neutral) wall flux with the replacement $n/\tau \rightarrow \left(S_{2w}/V_{2w} \right) \Gamma_{2w}$.

Alpha Particles

$$\dot{n}_{\alpha 2} = p(1 - p) \langle \sigma v \rangle_{f} n_{DT2}^{2} + f I_{B2} + \frac{S_{12}}{V_2} \Gamma_{\alpha 12} - \frac{S_{2w}}{V_2} \Gamma_{\alpha 2w} \left(1 - f_{\alpha} \right) \ , \qquad \text{(C-64)}$$

where f_{α} is given by Eq. (C-8).

Electrons

The charge neutrality condition of Eq. (C-11) is imposed to determine the electron density in both core and corona. The power balance is:

$$\frac{3}{2}\frac{d}{dt}\left(n_{e2}T_{e2}\right) = p(1-p)\langle\sigma v\rangle_f n_{DT2}^2 U_f f_{ne} + G_B I_{B2} W_B \hat{f}_{Be} + K_{fe2} + \eta_2 J_2^2$$

$$- W_{R2} + \frac{S_{12}}{V_2} q_{e12} + \frac{S_{12}}{V_2}\frac{3}{2}\left(\frac{T_{e1}+T_{e2}}{2}\right)\Gamma_{e12} - \frac{S_{2w}}{V_2} q_{e2w}$$

$$- \frac{3}{2} T_{e2}\frac{S_{2w}}{V_2}\Gamma_{e2w} - W_{ion}^I\left(Q_I + F_{wall}^I R_I\right)$$

$$- \frac{S_{2w}}{V_2} q_{e2w} - \frac{3}{2} T_{e2}\frac{S_{2w}}{V_2}\Gamma_{e2w} - W_{ion}^I\left(Q_I + F_{wall}^I R_I\right)$$

$$- W_{ion} F_{wall}^n R_n - W_{ion}^{DT}\left\{\left[\frac{\left(1-A_{cx}\right)A_{cx}^{ext}}{1-R_{DT}A_{cx}} + \left(1-A_{cx}^{ext}\right)\alpha\right] F_{DT}^{ext}\right.$$

$$\left. + \frac{S_{2w}}{V_2}\Gamma_{DT2w}\left(1-\eta_{DT}\right)R_{DT}\frac{\left(1-A_{cx}\right)}{\left(1-R_{DT}A_{cx}\right)}\right\}, \qquad \text{(C-65)}$$

where

$$\alpha = \begin{cases} 1, & A_{cx}^{ext} \neq 0 \\ 0, & A_{cx}^{ext} = 0 \end{cases},$$

and W_{ion} is the ionization energy.

The convective and conductive losses from the corona to the wall are computed from

$$\frac{S_{2w}}{V_2}\Gamma_{e2w} = \frac{n_{e2}}{\tau_P^*}, \qquad \frac{S_{2w}}{V_2} q_{e2w} = \frac{3}{2}\frac{n_{e2}T_{e2}}{\tau_E^*},$$

where the particle (τ_ξ^P) and energy (τ_ξ^P) confinement times are computed as in Section A.1, but using the characteristic dimension, Δr_2, of the corona rather than the plasma radius, a. Thus, the prescriptions of Section A.1 are reduced by the factor, $(\Delta r_2/a)^2$, in computing the corona confinement.

The coupling between the core and corona is in terms of particle flows ($\Gamma_{\xi 12}$) and heat conduction ($q_{\xi 12}$). These quantities are represented as follows:

$$\frac{S_{12}}{V_1} q_{\xi 12} = \frac{\frac{3}{2}\left(T_{\xi 1} - T_{\xi 2}\right)}{\tau_\xi^E} \left(\frac{n_{\xi 1} + n_{\xi 2}}{2}\right), \tag{C-66}$$

with

$$\tau_\xi^E = \begin{cases} \tau_{\xi 12}^E, & T_{\xi 1} \geq T_{\xi 2} \\ \tau_{\xi 21}^E \dfrac{V_1}{V_2}, & T_{\xi 1} < T_{\xi 2} \end{cases},$$

$$\frac{S_{12}}{V_1} \Gamma_{\xi 12} = \frac{n_{\xi 1} - n_{\xi 2}}{\tau_\xi^P}, \tag{C-67}$$

with

$$\tau_\xi^P = \begin{cases} \tau_{\xi 12}^P, & n_{\xi 1} \geq n_{\xi 2} \\ \tau_{\xi 21}^P \dfrac{V_1}{V_2}, & n_{\xi 1} < n_{\xi 2} \end{cases},$$

where $\tau_{\xi 12}$ indicates that the quantity is evaluated with core parameters, and $\tau_{\xi 21}$ indicates that the quantity is evaluated with corona parameters.

When the electron-ion collision frequency in the corona is greater than the electron bounce frequency, the particle fluxes, $\Gamma_{\xi 12}$, across the core-corona interface are calculated from the multispecies Pfirsch-Schlüter theory developed in Reference 7. As long as $\tau_{\xi 2} \geq \tau_{\xi 2}$, the heat conduction across the core-corona interface is also computed from the multispecies Pfirsch-Schlüter theory.

6. Plasma Initiation Model

The model used to investigate the development of the plasma during the breakdown is similar to that used for the burn cycle calculations, with some modifications required by the special conditions of low plasma current and partially ionized plasma.

a. Electron, Ion, and Neutral Density

The densities of electrons, ions, and neutrals are determined by the relations

$$\frac{dn_e}{dt} = \frac{n_e}{\tau_{ion}} - \frac{n_e}{\tau_{conf}} - n_e f\left(B_Z, B_p\right) , \qquad n_{DT} = \frac{n_e}{1 + \sum_I \frac{n_I}{n_{DT}} Z_I} , \qquad \text{(C-68)}$$

where the sum is over all impurities,

$$\frac{dn_0}{dt} = -\left(V_{discharge}/V_{tank}\right) \frac{dn_e}{dt} + (\text{pulsed neutral gas}) ,$$

where $V_{discharge}$ is the volume of the plasma discharge, and V_{tank} is the volume of the toroidal vacuum chamber. The ionization time, τ_{ion}, has been determined experimentally and is a function of the electric field, $\vec{E}$, and the neutral pressure, P_0.[8] The confinement time, τ_{conf}, is essentially equal to the pseudo-classical confinement time, τ_E^{PC}, at large times.[2] Before the plasma current and rotational transform develop, the plasma is accelerating outwards due to the gradient in the toroidal magnetic field, and the confinement time is the time, $\tau_{\nabla B}$, required to drift to the wall. Because of particle reflection from the walls, shorting of the $E_{\nabla B}$ fields by the limiter, and eddy current stabilization of the plasma, one would expect that experimental data might show somewhat longer confinement. In order to duplicate the data of Dimock, et al.,[9] it is found necessary to increase $\tau_{\nabla B}$. By using a confinement time of the form

$$\tau_{conf} = \tau_E^{PC} + \left(\tau_{\nabla B}\right)^{0.75} , \qquad \text{(C-66)}$$

where

$$\tau_{\nabla B} = \frac{2a\left(\varepsilon_0 R_0 B_{t0}^2/q\right)}{n_e T_e} \qquad \text{(C-70)}$$

agreement with experimental data has been obtained. At small times $\tau_{conf} \propto (\tau_{VB})^{3/4}$, and at large times ($t > 3$ ms) $\tau \rightarrow \tau_E^{PC}$. This formulation attempts to reproduce the way in which the rotational transform increases the natural confinement as the current develops. Energy and particle confinement times are set equal, which is consistent with experimental data.[9]

The term $f(B_Z, B_p)$ is introduced to simulate plasma losses due to errors in the toroidal field. At zero current this term equals $V_{drift} B_Z/B_t$, which represents the rate of spiral drift of electrons out of the discharge due to a component, B_Z, of the field in the Z direction. The expression $f(B_Z, B_p)$ decreases as B_p/B_Z increases, becoming zero for $B_p \geq B_Z$.

The ion density is set equal to the electron density, and the density of neutrals, n_0, is determined by the constraint that the sum of neutrals and ions is a constant.

b. Electron and Ion Energy Balance

The electron and ion energies are determined by the relations

$$\frac{3}{2}\frac{d(n_e T_e)}{dt} = (P_{OH} - P_{ion} - P_{ie} - P_{impur} - P_{rad} - P_{eN}) - \frac{3}{2}\frac{n_e T_e}{\tau_{conf}} - n_e T_e f(B_Z, B_p) + P_{add} \quad \text{(C-71)}$$

and

$$\frac{3}{2}\frac{d(n_{DT} T_{DT})}{dt} = (P_{ie} - P_{ex}) - \frac{3}{2}\frac{n_{DT} T_{DT}}{\tau_{conf}} . \quad \text{(C-72)}$$

Electron energy is provided by ohmic heating power, P_{OH}, and lost by ionization of neutrals, P_{ion}, heating of ions, P_{ie}, line and recombination radiation due to impurities, P_{impur}, bremsstrahlung radiation, P_{rad}, elastic collisions with neutrals, P_{eN}, particle losses, and losses due to field errors. Additional power, P_{add}, due to rf heating or neutral beams, is allowed. Ion energy is provided by collisions with electrons and lost in charge-exchange collisions and particle losses. During breakdown the plasma resistivity is determined by the relation $\eta = \eta_{Spitzer} + \eta_{Boltzmann}$.

Impurity losses are calculated by looking at the equilibrium distributions of oxygen ions and calculating the amount of energy lost by electron interactions with each charge state, following the method of Büchs and Griem.[10] The total oxygen density is fixed at a fraction of the electron density. Although impurity recycling can be accommodated, no recyling is assumed in the first few milliseconds.

c. Plasma Current

The current is determined by the relation

$$d(LI)/dt = V_{loop} - IR \ , \tag{C-73}$$

where

$$L = \mu_0 R_0 [\ln(8R/a) - 1.75] \ ,$$

and

$$V_{loop} = M_{POH} \frac{dI_{OH}}{dt} + M_{PEF} \frac{dI_{EF}}{dt} \tag{C-74}$$

represents the combined effects of the ohmic heating and equilibrium field coils. Here, I_{OH} is the current in the OH coil, I_{EF} is the current in the EF coil, and M_{POH} and M_{PEF} are the mutual inductances between the plasma and each coil system. At very early times, when the charge density is very low, the current cannot rise as fast as $\left(V_{loop} - IR\right)/L$, so the current is limited to

$$\frac{dI}{dt} = q \, V_{drift} A \frac{dn_e}{dt} \ , \tag{C-75}$$

where A is the aspect ratio. The drift velocity, V_{drift}, is proportional to E/p for weakly ionized gases.

d. Runaway Electrons

Runaway electron production has been calculated using the formulae of Kulsrud, et al.[11] for completely ionized plasmas, and Gurevitch[12] for weakly ionized plasmas. These runaway production rates are not, however, used as inputs to other parts of the program because (a) runaway production is assumed to be small; and (b) comparisons of theory and experiment[11,13] have shown that the theoretical estimates are not very reliable.

Input data to this calculation consists of loop voltage, V_{loop}, discharge area, and total ion plus neutral density at specified times in the discharge. Interpolation is used to determine parameter values at any instant.

---

1. W. M. Stacey, Jr., "Tokamak Experimental Power Reactor Studies," Argonne National Laboratory Report ANL/CTR-75-2 (1975).

2. S. O. Dean, et al., "Status and Objectives of Tokamak Systems for Fusion Research," USAEC Report WASH-1295 (1974).

3. B. B. Kadomstsev and P. O. Pogutse, "Trapped Particles in Toroidal Magnetic Systems," *Nucl. Fusion*, 11, 67 (1971).

4. J. D. Callen and R. A. Dory, "Magnetohydrodynamic Equilibria in Sharply Curved Axisymmetric Devices," *Phys. Fluids*, 15, 1523 (1972).

5. A. I. Morozov and L. S. Solov'ev, "The Structure of Magnetic Fields," in *Reviews of Plasma Physics* (Consultants Bureau, New York, 1966), Vol. 2, p. 18.

6. V. S. Mukhovatov and V. D. Shafranov, "Plasma Equilibrium in a Tokamak," *Nucl. Fusion*, 11, 605 (1971).

7. C. D. Boley, E. M. Gelbard and W. M. Stacey, Jr., "Multispecies Transport in Collisional Tokamaks," Argonne National Laboratory Report ANL/CTR/TM-63 (1976).

8. A. Buffa, G. Malesani and F. Nalesso, "Measurement of Ionization Growth Rates in H_2 at High E/p," *Phys. Rev.*, 3A, 955 (1971).

9. D. L. Dimock, et al., "The Ontogeny of a Tokamak Discharge," *Nucl. Fusion*, 13, 271 (1973).

10. D. Düchs and H. R. Griem, "Computer Study of the Dynamic Phase of a Small θ Pinch," *Phys. Fluids*, 9, 1099 (1966).

11. R. M. Kulsrud, et al., "Runaway Electrons in a Plasma," *Phys. Rev. Letters*, 31, 690 (1973).

12. A. V. Gurevitch, "On the Theory of Runaway Electrons," *Sov. Phys. (JETP)*, 12, 904 (1961).

13. D. A. Sprong, J. F. Clarke and J. A. Rome, "Relativistic Electron Production in ORMAK Device," Oak Ridge National Laboratory Report ORNL-TM-4120 (1973).

APPENDIX D

STRUCTURAL SUPPORT SYSTEM*

Structural support systems must be developed simultaneously with the other EPR components in order to insure that efficient support is provided and potential constraints on the design are identified. This appendix summarizes a study using representative EPR input loads, geometry, room temperature support points, and component definition to establish a conceptual structural support for the EPR.

Two conceptual structural designs were developed and analyzed. The two concepts, a torque shell design and a torque frame design, both provide support for the blanket and shield, vacuum system, and poloidal and toroidal field coil magnets. Emphasis was placed on evaluating the advantages of each concept and identifying general structural support requirements. Either design concept is capable of providing the required support. At this point the torque shell design has tentatively been selected as the reference design. However, the final design approach must await more detailed design of the major EPR components and establishment of detailed maintenance requirements.

In developing these structural support concepts, alternate structural materials were evaluated, finite element analysis techniques were applied toward determining structural requirements and weights, access and maintenance requirements were considered and rough order of magnitudes (ROM) costs were determined. In addition, a scoping effort was undertaken to identify the required manufacturing lead time, approximate cost and recommendations on how to proceed with development of the structural support system.

1. Summary

Both the torque shell and the torque frame concepts developed in this study can provide adequate structural support for the EPR components. These concepts, shown in Figures D-1 and D-2 and described herein, differ primarily in the method of restraining the lateral forces induced on the TF coil. The eventual baseline concept selection will depend primarily on the TF coil support requirements and on the frequency that access is required to the blanket and shield.

---

* This work was performed by McDonnell-Douglas Astronautics Company - East in collaboration with Argonne National Laboratory. A more detailed description of the work is presented in reference 1.

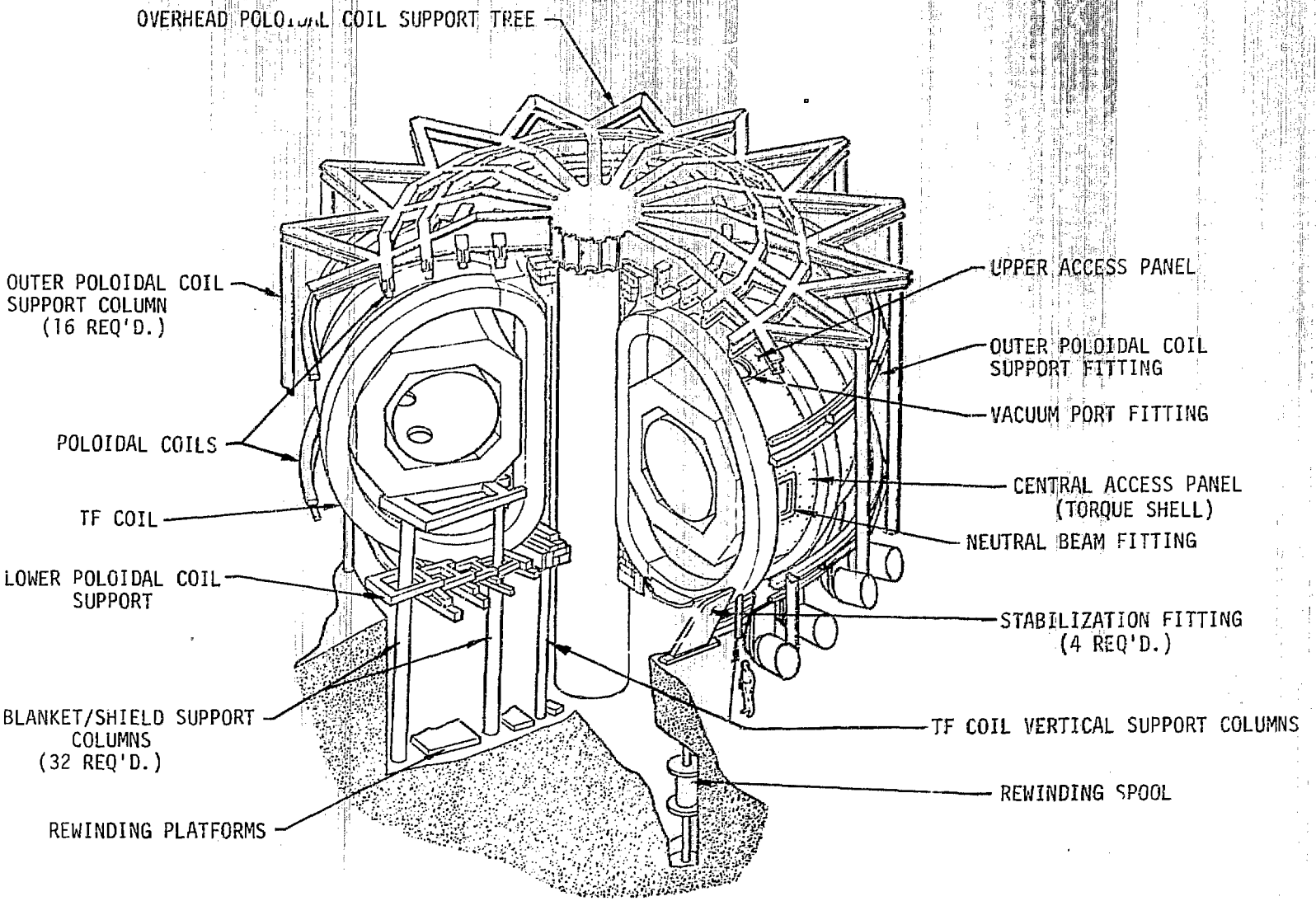

Figure D-1. Torque Shell Structural Support

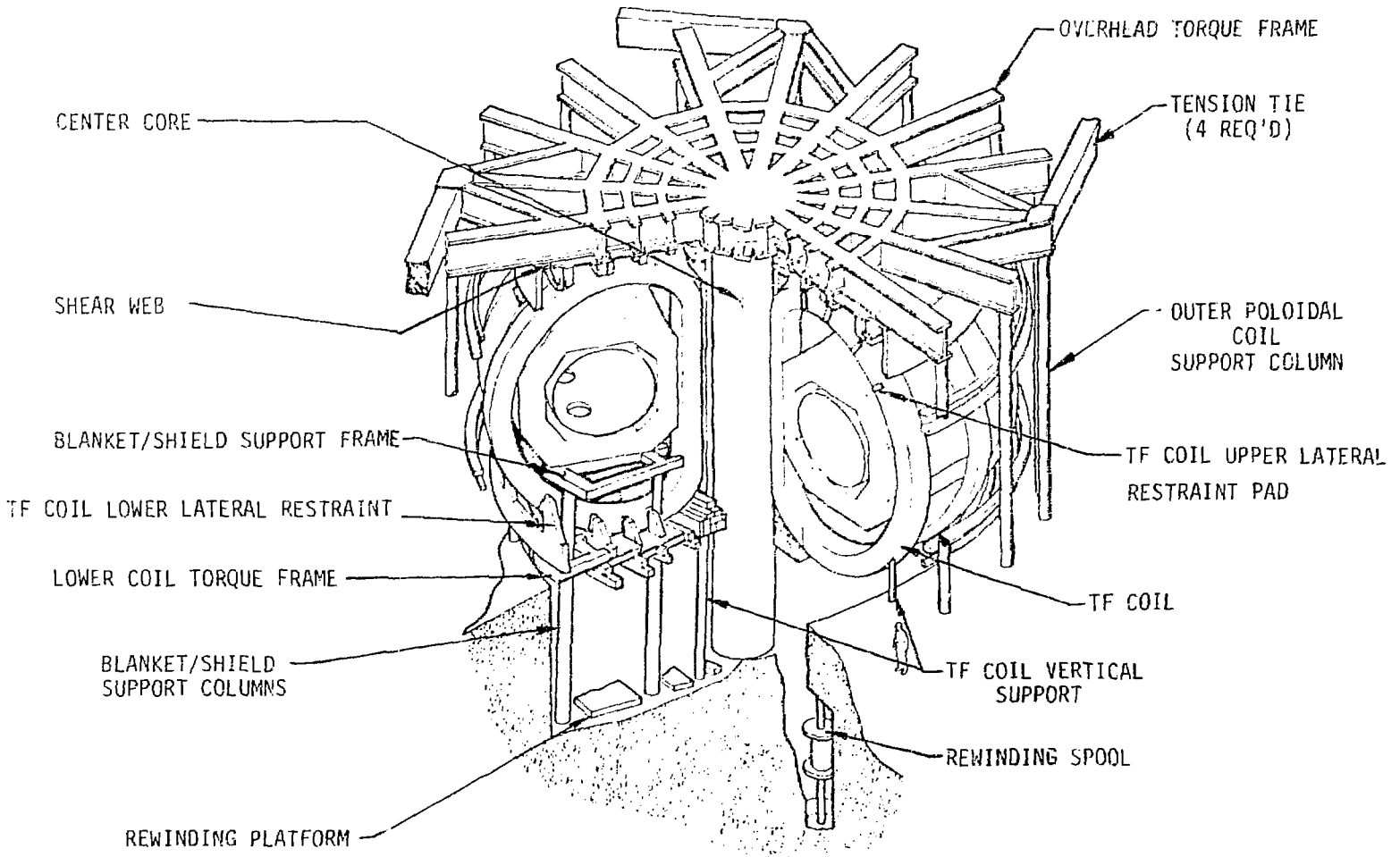

Figure D-2. EPR Torque Frame Structural Support

Both concepts provide blanket and shield access through an approximately 3 x 8 m opening between TF coils. All blanket and shield maintenance operations should be designed to be performed through this opening. Very little access, if any, will be available from above and below the TF coil because of required structure. Openings for vacuum ducts and instrumentation, however, can be provided through this structure. The floor area around the reactor will not be restricted by structural members with either concept, thereby providing ease of locating components such as neutral beam heaters and for freedom of movement for maintenance equipment. Except in the area of the lower poloidal coils, the structural support members can be moved easily to allow repair of any failed magnet coil. The outer and upper poloidal coils can be removed using their supporting structure as a lifting fixture. The lower poloidal coils are captivated by the various support columns and require in in-place repair/replacement facility.

Use of 7075-T6 aluminum alloy in a bolted structural support design results in a lighter and lower cost approach that can be achieved using welded stainless steel. Aluminum also offers the advantage of having a low activation and being a native material that will be available for commercial power reactors. The overall cost of designing, fabricating and erecting the structural support system will be about $6 million for either concept. Cost is not expected to be the decisive factor in selecting a baseline concept.

As the EPR component designs evolve, further iterations of this study will be required to assure compatibility. However, this study should serve to define structural support requirements and options and to allow the evaluation of the compatability of the EPR systems design and maintenance procedures with the structural support requirements.

2. EPR Definition

The EPR design defined in Reference 2 was used as a baseline in this study, except for a change in the blanket/shield design, changes in the location and number of equilibrium (EF) and ohmic heating (OH) coils and further definition of the toroidal field (TF) coil system.

In this study it is assumed that room temperature attachment points are provided on the coil cryostat to react the forces and weights of the magnet coils.

Induced electromotive forces and weights of the major components are shown in Figures D-3 and D-4. The induced forces used in this study were defined early in the EPR magnet design effort. Further analysis of these induced forces indicates worst case loading conditions may be 50-70% higher than those used. These increased loads will require an increase in the size of structural members to react the loads and will result in increased structural weight and material/fabrication cost. These changes are not expected to significantly change the available access, maintenance approach, structural configuration, or material selection.

3. Material Selection

Several stainless steel and aluminum alloys were evaluated for the EPR support structure primary material. These alloys were 304 and Nitronic 40 stainless steel and 2219, 7075, 5086, and 6061 aluminum alloys. This evaluation included consideration of the material strength, stiffness, cost, and fabrication techniques. Material costs, fabrication techniques, and fabrication costs are based on results of a survey of structural fabricators. Data for the materials are shown in Table D-1.

In comparing materials, three figures of merit (FOM) were used. The FOM's used were yield strength (YS), modulus of elasticity (E), fabrication costs, including material (cost) and weight (WT). The FOM's and their application criteria are shown below.

FOM	When Used
$\frac{YS}{WT}$	Lightweight structure
$\frac{YS}{(WT)(COST)}$	Low cost, lightweight structure
$\frac{(YS)(E)}{(WT)(COST)}$	Low cost, lightweight structure with maximum stiffness

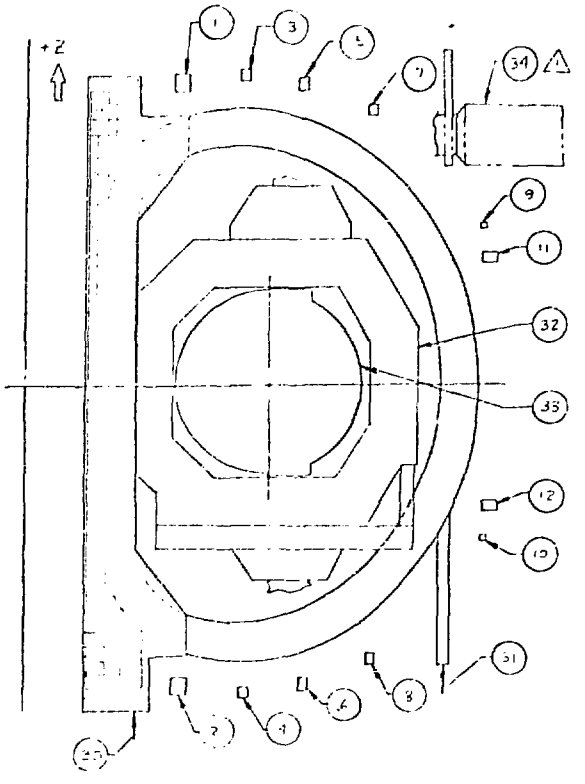

EPR COMPONENT VERTICAL LOADS

ITEM NUMBER	NAME	QUANTITY	WEIGHT (TONS)	INDUCED FORCE IN BURN (TONS)	INDUCED FORCE PRIOR TO START UP (TONS)
1	OH COIL	1	-35 ⚠2	-1811	-2578
2	OH COIL	1	-35	+1811	+2578
3	EQUIL. COIL	1	-31	-935	-
4	EQUIL. COIL	1	-31	+935	-
5	EQUIL. COIL	1	-40	-1070	
6	EQUIL. COIL	1	-40	+1070	-
7	EQUIL. COIL	1	-49	-443	-
8	EQUIL. COIL	1	-49	+443	-
9	OH COIL	1	-18	-1560	+286
10	OH COIL	1	-18	+1560	-286
11	EQUIL. COIL	1	-140	+1828	-
12	EQUIL. COIL	1	-140 ⚠2	-1828	-
30	CENTER CORE COMPOSITE	1	-3116 ⚠3		
31	OUTER TF SUPPORT	16	-131		
32	BLANKET/ SHIELD	1	-6600		
33	FIRST WALL	1	-200		
34	VACUUM SYSTEM	1	-390		

TOTAL WEIGHT (EXCLUDING SUPPORT STRUCTURE) 13,078 TONS

⚠1 OPTIONAL LOCATION

⚠2 APPROXIMATED BY SOLID COPPER WEIGHT FOR CONDUCTOR CROSS SECTION PLUS 20% FOR CRYOSTAT

⚠3 INCLUDES 10% ALLOWANCE FOR CRYOSTAT

Figure D-3. Vertical Forces on EPR Components

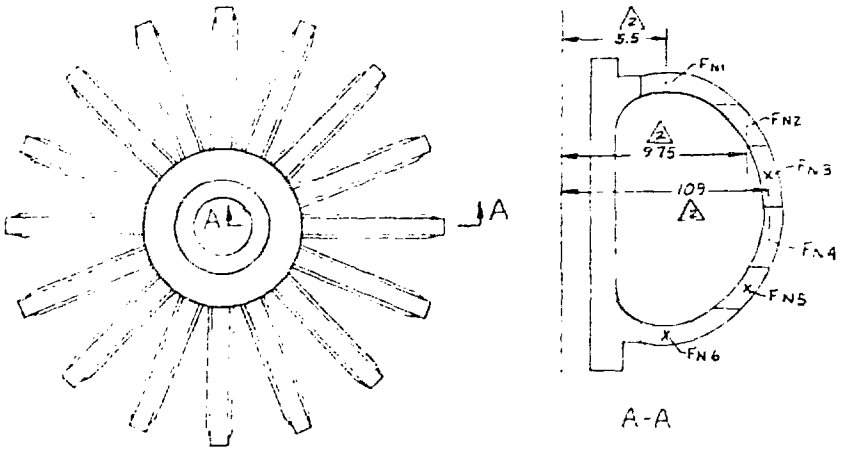

LATERAL LOAD PER TF COIL	UNIFORM LOAD (4) (LB/M)	TOTAL LOAD (LB)
FN1	$.76 \times 10^6$	3.04×10^6
FN2	$.47 \times 10^6$	2×10^6
FN3	$.33 \times 10^6$	-1×10^6
FN4	$.33 \times 10^6$	$+1 \times 10^6$
FN5	$.47 \times 10^6$	-2×10^6
FN6	$.76 \times 10^6$	-3.04×10^6

NOTE: 1. POSITIVE LOADS ARE IN A DIRECTION OUT OF THE PAPER IN VIEW A-A

2. LOCATION OF CENTER OF FORCE

3. LOADS GENERATED ON THE TF COIL IN THE CENTER CRYOSTAT ARE ASSUMED TO BE REACTED INTERNALLY

4. BASED ON TOTAL LOAD SUPPLIED BY ANL

Figure D-4. Induced Lateral Loads of TF Coil

MATERIAL/PROPERTIES	MATERIAL COST $/LB.	FABRICATION TECHNIQUE	COST OF FABRICATION (6)	FIGURES OF MERIT: YS X E / COST X WT.	FIGURES OF MERIT: YS / WT.	FIGURES OF MERIT: YS / WT. X COST
304 Stainless Steel Y.S. = 30,000 psi	.84	Weld	$3600-5200/Ton (2)	833	100	277
Nitronic 40 (1) (SS) Y.S. = 70,000 psi	1.23	Weld	$6000-8600/Ton (3)	1166	233	388
2219 Aluminum	.98					
Cond. T62 YS=19000 psi		Weld	$6300-8300 (5)	301	190	301
Cond. T87 YS=26000 psi		Weld	$6300-8300	412	260	412
Cond. T62 YS=42000 psi		Bolt	$6300-8300	666	420	666
Cond. T81 YS=51000 psi		Bolt	$6300-8300	809	510	809
7075-T6 Aluminum	.965					
YS=68,000		Bolt Only	$6300-8300	1070	680	1070
5086 Aluminum	.83					
YS=18,000 psi		Weld	$6000-8000	300	180	300
YS=30,000 psi		Bolt	$6000-8000 (5)	500	300	500
6061 Aluminum	.83					
Cond. T6 YS=18000 psi		Weld	$6000-8000	300	180	300
Cond. T6 YS=40000 psi		Bolt	$6000-8000	366	400	666

(1) Armco Steel

(2) Obtained from Mississippi Valley Structural Steel

(3) Scaled from (2) based on Nooter Corp. estimate

(4) Welding Aluminum Manual, American Welding Soc. - The Aluminum Assoc. Copyright 1967

(5) Obtained from Allied Industries, Houston, Texas

(6) Includes cost of raw material and is based on torque frame concept

Table D-1. Base Material/Fabrication Comparison

Stainless steel was considered to be joined only by welding since the weld strength is approximately equal to the base metal strength. Stainless steel must be used in the annealed condition because of the size limitation and because cold working causes loss of non-magnetic characteristics. As shown in Table D-1, 7075-T6 and Nitronic 40 stainless steel are comparable for stiffness applications, however if stiffness (E) is eliminated from the FOM, 7075-T6 is clearly superior. Stiffness is important in FPR only when structural buckling is the limiting factor such as in support columns.

The survey results indicate that the cost of welding an aluminum structure is approximately equal to the cost of bolting if the structure is tailored for the method of fabrication. The strength of aluminum is degraded by welding and can be upgraded by heat treatment after welding but this is not considered practical because of the large size of the structural elements. A small improvement in properties can be attained with local post-weld aging. The 7075-T6 aluminum alloy joined by bolting is superior to the other alloys and was selected as a baseline material for the structure. In conjunction with the bolted fabrication technique, extrusions and forgings can be used where desirable to simplify fabrication and since 7075-T6 has poor weld characteristics, other materials can be substituted locally if welding is necessary.

4. Structural Analysis Considerations

Analyses were conducted in order to establish the feasibility of suggested concepts and to provide a consistent basis for concept comparison. Structural analysis of support components was facilitated by use of finite element computer programs and computer graphics capabilities. NASTRAN (NASA Structural Analysis) was used to model the toroidal field magnets for deflections due to both the large out of plane magnet forces and the in-plane dead weight forces. This program was also used to model and analyze the torque shell structural support concept. The CASD (Computer Aided Structural Design) was used to model the torque frame structural support concepts.

Guidelines were established for allowable stress levels based on the Steel Construction Manual (Reference 3) as follows. Yield strength properties are based on Reference 4 values.

STRESS	ALLOWABLE
Tension	$0.6\ F_{ty}$
Shear	$0.4\ F_{ty}$
Compression	Buckling, $0.6\ F_{ty}$ Max.

The allowable stress levels were used in conjunction with induced magnet loads and dead weight loads without additional factors of safety. It should be noted however, that the factors of $0.6\ F_{ty}$ and $0.4\ F_{ty}$ result in a margin of ~ 1.7 on the ultimate and shear allowables of the 7075-T6 aluminum. The fatigue allowable (Reference 3), based on 10^6 cycles, is approximately the same as $0.6\ F_{ty}$ for 7075-T6 aluminum. Therefore, no further reductions in strength properties were applied in the study. Additional considerations need to be given, however, to other conditions such as upset and emergency conditions in the EPR design. Also, the codes (Reference 5) require that consideration be given to effects of impact loads and earthquake loads and that components be designed to minimize vibration.

5. Magnet Support Considerations

Studies were conducted to investigate various room temperature support configurations for reaction of the large lateral forces induced on the TF coils. Analyses for these studies were aided by a simple NASTRAN beam element model. Lateral bending stiffness for the TF coils was calculated based on the baseline one inch thick stainless steel liquid helium superconductor support case. Lateral loads, defined in Figure D-4 were applied and the resulting deflections and stresses examined for the three different configurations. Shown in Figure D-5 (a), (b) and (c), for each of three support arrangements, are resulting deflected shapes with maximum deflections and stresses included.

Shown in Figure D-5 (a) are deflections for a four point coil support configuration. The maximum deflections and bending stress in this case are 0.35 in. and 55,000 psi. respectively. The effect of additional support along the cryostat interface and the outer portion of the coil is shown in Figure D-5 (b). These additional supports reduce stresses and deflections

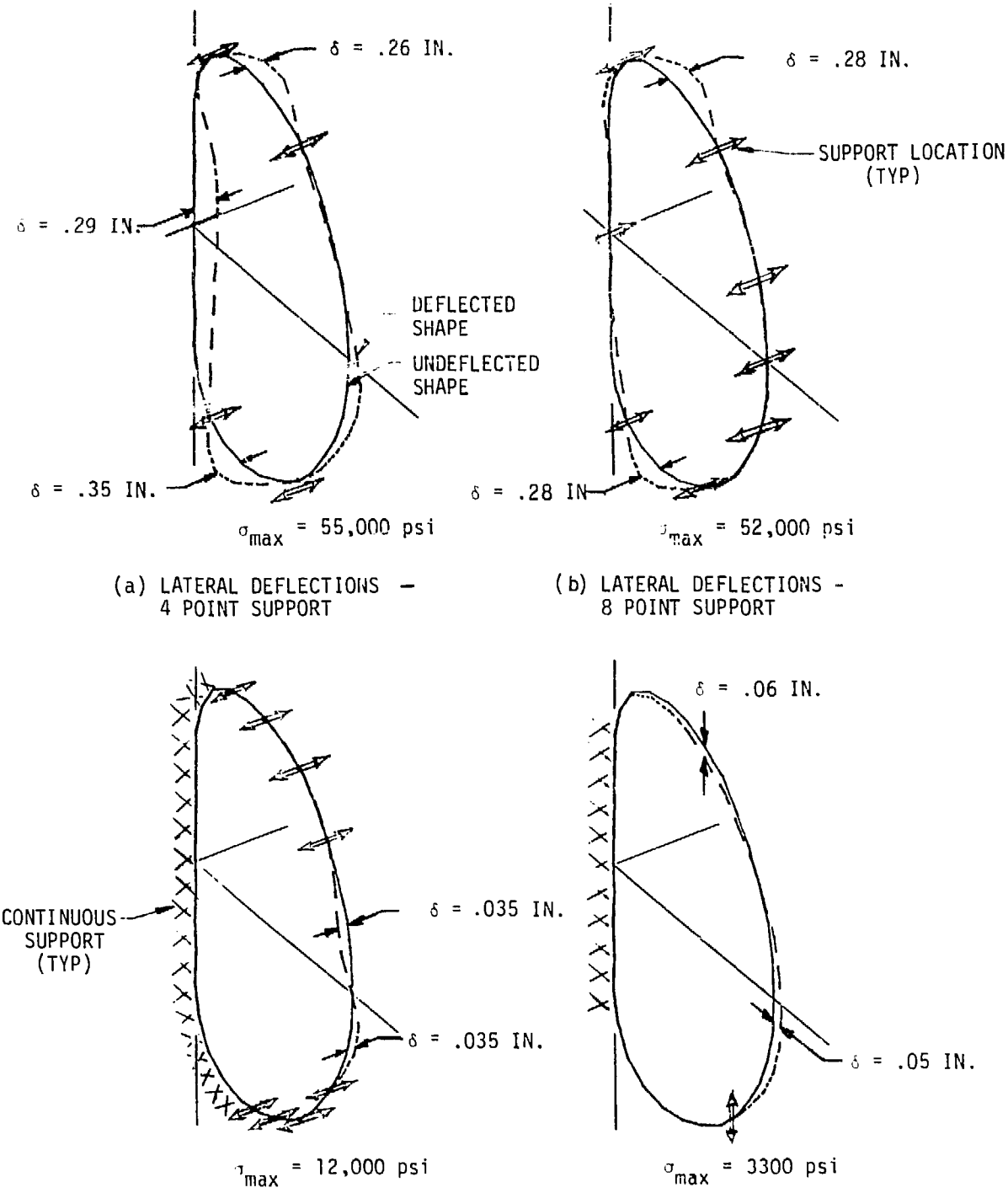

Figure D-5. TF Coil Response to Lateral and Dead Weight Loads

in the region of the supports; however, because these added supports are not located in the region of maximum lateral loading they have a minimal effect on maximum magnet deflections and bending stresses. Location of supports at the top and bottom of the coil in the region of maximum lateral loading, significantly reduces both deflections and bending stresses to maximums of 0.035 in., and 12,000 psi respectively, as shown in Figure D-5 (c). Although no specific criteria presently exists for allowable magnet deflections, the results obtained do not appear to be excessive, even with the conservative stiffness values (vacuum walls not accounted for). Based on these results, it appears that support of the TF coils at the top and bottom (Figure D-5 (c)) is the most suitable for purposes of minimizing coil stress and deflections. This support concept is also attractive because it provides maximum access to the blanket/shield.

In-plane deflections due to the coil dead weight were also obtained. The deflected shape for this condition and maximum deflection and bending stress are shown in Figure D-5 (d). Support for the in-plane loads is located along the center core interface and vertical support is provided at an outer point indicated in the figure. The magnet is allowed to deflect horizontally at this outer support point, however.

6. Design Development

Factors which drive the EPR design approach are: (1) the large lateral forces (toroidal injection) induced on the TF coil, (2) the requirement to remotely remove all components for repair, and (3) access requirements for maintenance. The lateral forces on the TF coil create a torque of approximately 1.8×10^9 ft-lb in a counterclockwise direction at the top of the coil and an equal and opposite torque at the bottom. To transmit these loads without excessive stresses or deflections require use of direct load paths. These load paths must allow adequate access for remote maintenance of reactor components. Structural members can be removed to attain access, but it is desirable to have direct access to components requiring frequent maintenance. This implies maximum access to the first wall and vacuum system with reduced accessibility to the magnet system. The EPR structural support concepts will be a compromise of maintenance, fabrication, cost, and risk factors.

In the present study two different concepts were developed for comparison purposes. The two concepts selected are referred to as: (1) the Torque Shell concept and (2) the Torque Frame concept. These concepts differ primarily in their manner of restraining the lateral forces developed by the TF coils and in the access provisions.

a. The Torque Shell

The torque shell concept uses shear webs located between each TF coil to provide continuous support for the coil. The shear webs transmit the large torques induced on the TF coil. This concept was shown in Figure D-1. Other major features include an overhead tree for support of the upper OH and EF coils, an outer support system for the large OH and EF coils, a lower OH and EF coil support frame with a built in rewinding facility and four lateral stabilization fittings which attach to the shear panels to provide stability for any unsymmetric loads.

(1) Shear Panel Definition

A cylindrically shaped shear panel assembly approximately 2.0 inches thick is located between each set of TF coils. It is attached at the center of the TF coil cross-section using 3-inch diameter threaded fasteners located on 9-inch centers. Each of these 16 assemblies consists of four panels and five fittings. Continuous fittings are used at each penetration (i.e. vacuum pump, neutral beam, etc.) to provide the necessary load carrying capability around the opening. These fittings are installed with the penetration equipment and can be left in place when shear panels are removed.

(2) Shear Panel Attachment

The shear panels attach to the TF coil cryostat through a flange that is butt welded to the TF coil cryostat. This flange is 2 inches thick, approximately 7 inches wide and is installed at an angle 78.5° with respect to the TF coil plane to provide a cylindrical surface for mounting the shear webb between adjacent TF coils. This flange can be segmented as required to assure proper location of the mounting plane during TF coil manufacture.

Fitting of the shear panels can be accomplished by the use of matched drilling during assembly. When the panels are removed, the TF coils will deflect and cause fastener misalignment of approximately 0.02 inches. Additional misalignment is expected from internal distortion of the TF coils during their manufacture. Tapered shear pins and fasteners in oversize holes can be used to draw the shear panel down and align the closer fitting fastener holes.

Eddy currents will be prevented from flowing through the TF coil to adjacent shear panels by insulating the attachment joint. The mating surface between the attachment flange and shear panel can be insulated using tapers or spacers (teflon, phenolic, etc.) having limited load carrying capacity. The bolt, however, must be insulated using material of high strength which can carry the necessary shear loads.

(3) Panel Installation and Removal

It is estimated that each bolt will require approximately 3 minutes to install and 2 minutes to remove. To minimize the impact on overall maintenance time, it is desirable to perform panel installation/removal in parallel with other maintenance operations or to develop a quick panel attachment design (latches, etc.). The level of radiation at the external surface of the shear panels is expected to be low enough to allow removal of the fasteners with a minimal amount of radiation protection if the blanket and shield are left intact.

Normal maintenance access is provided by removal of the central access panel. This requires removal of approximately 120 bolts and provides an access opening approximately 8.0 m x 2.8 m to the blanket/shield assembly. This panel can be removed in approximately 6 manhours without disconnecting the neutral beam injectors. The design may require that temporary supports be provided so that the TF coils do not have to be de-energized before removal of this panel.

As an option to the fully closed torque shell structure some areas could be left open to make the concept more attractive from a maintenance standpoint. This will not cause any significant change in calculated weights since adjacent panels and stiffeners will have to be beefed up to accommodate this approach.

Additional access can be provided for major repair operations by removing the upper and lower access panels. These panels can be removed from around the blanket/shield supports and vacuum pumps, however, little additional access is obtained unless the vacuum ports and the upper and lower poloidal coils are moved.

(4) Torque Shell Analysis

The torque shell support concept was modeled using shear panels and axial rod members. As shown in Figure D-6, the structure was assumed to be constrained for deflection in the vertical as well as the lateral (tangential to the shell) direction at the stabilization support fitting. In addition vertical constraints were imposed at the top and bottom of the model where the shell attaches to the center core. The shell was allowed to deflect tangentially at the shell/center core interface. Maximum lateral deflections at the top and bottom of the reactor are approximately 1.3 inch and 0.65 inch respectively. Applied loads result in small induced tension forces of approximately 200,000 lbs in the inner magnet leg and/or the center core structure. Shell thickness of 7075-T6 aluminum is approximately 1.0 inch based on the shear allowables of 0.4 F_{ty}. Some additional panel thickness and/or stiffeners will be required to preclude panel buckling, resulting in approximately a 10% in weight.

(5) Blanket/Shield Support

The blanket/shield and first wall are supported by a frame which is provided as part of the Primary Energy Conversion System (PECS). This frame is supported by a total of 32 columns each 40 feet long which attach to the reactor floor in the lower access pit. These columns have been sized as circular aluminum tubes 16 inches in diameter with a 1-inch thick wall to provide support for a combined dead weight/induced force load of 6955 tons. This total load is due to the 6600 tons PECS weight plus the lower torque frame and poloidal magnets. The columns provide sufficient margin against buckling.

(6) Overhead OH and EF Coil Support

The shear panel concept requires that a separate support be provided for the four upper OH and EF coils. This is provided through use of an aluminum support tree as shown in Figure D-6. The support tree consists

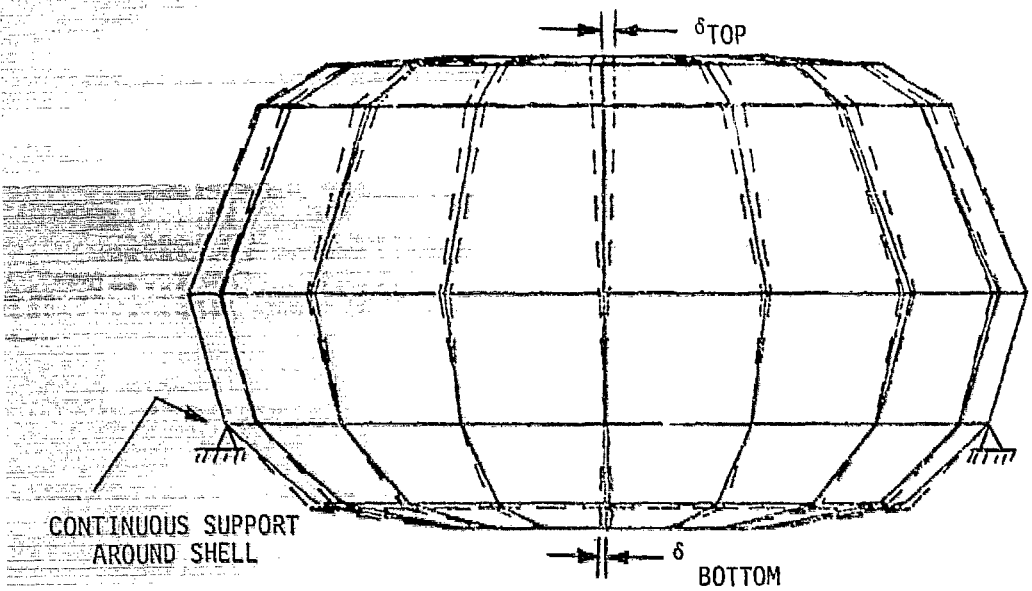

(a) SIDE VIEW

MATERIAL	δ_{TOP} (IN.)	δ_{BOT} (IN.)
304 SS	.20	.10
NITRONIC 40	.45	.22
7075-T6 AL	1.30	.65

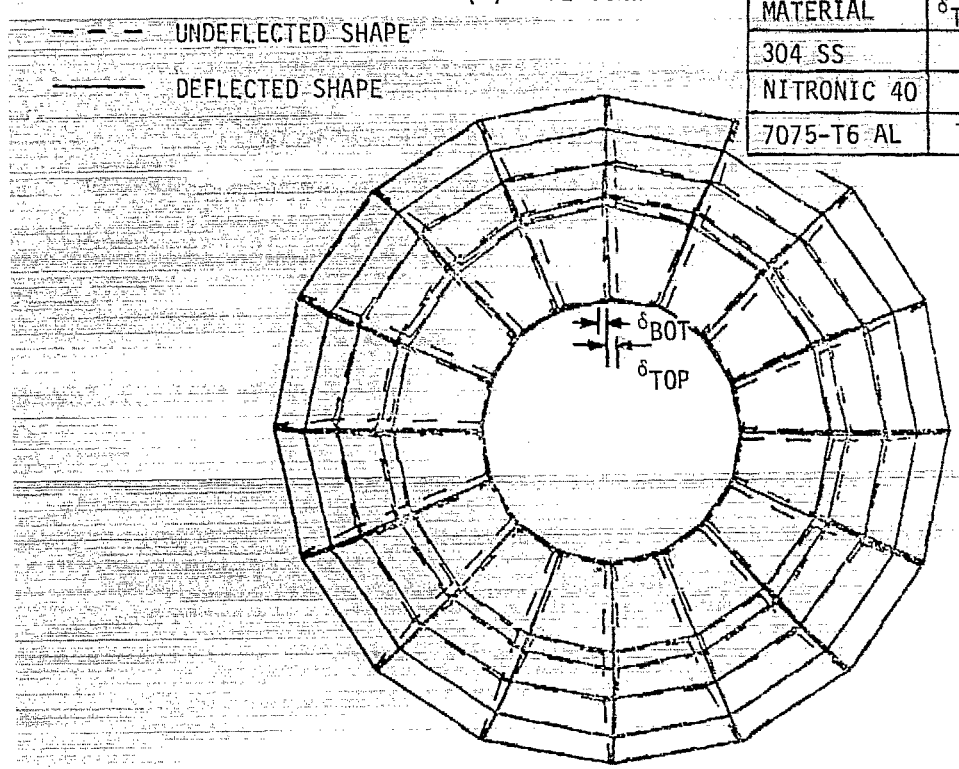

(b) TOP VIEW

Figure D-6. Torque Shell Finite Element Model and Deflected Shape

of sixteen (16) aluminum radial beams which span 12 m (40 ft) between the center core and the outer OH and EF coil support columns. Resulting compressive stresses of 1500 psi occur in the 9 foot diameter concrete center core which supports its' own dead weight (380 tons), the support tree (less than 245 tons) and 5211 tons of magnet weight and induced forces. The beams are centered between TF coils to provide clearance for the coil connections.

Each beam supports 4 cross members which provide continuous support for segments of the OH and EF coils. A gap is provided between the ends of adjacent cross members and the beams are separated with structural insulated joints in the center area to limit induced eddy current flow within the structural tree.

In addition to providing structural support for the poloidal coils, this support tree serves as a handling fixture for the 155 tons of coil weight. This coil weight combined with the 15 ton structural weight is significantly below the 400 ton polar crane capacity.

(7) Lower OH and EF Coil Support

For the torque shell concept the 4 lower OH and EF coils are supported by 16 beams attached to the blanket/shield support columns. These beams transfer the upward acting induced coil forces to the support columns during reactor operation as well as support the dead weight loads of the coils. These columns incorporate jacks to allow lowering of the support beams and coils for repair. The support beams provide continuous support for the coils through use of cross members. As with the overhead support tree, these cross members incorporate insulating features to limit induced eddy currents.

(8) Outer OH and EF Coil Support

The two sets of outer OH and EF coils are supported by fittings attached to the outer poloidal support columns. These fittings form a continuous support for the coils and incorporate insulated joints as required to limit eddy current flow. Each set of OH and EF coils have induced forces which act in opposite directions, thereby reducing the net load which must be supported by the support column.

Each column incorporates a set of jacks (elevators) which allow raising and lowering the outer coil support fittings for additional access. The fittings also serve as a handling fixture in that, the overhead crane can

be attached to pickup the assembly if coil removal is required for repair. As an alternate to overhead coil removal, a rewinding facility could be provided about the reactor centerline and the support columns integrated into a jacking system for raising and lowering these coils for repair.

(9) TF Coil Vertical Support

The 16 TF coils assemble into a common cryostat around the center column of the reactor. The requirements for in place repair of the OH and EF coils within the lower half of this cryostat prevents effective support of the cryostat from the center concrete column. Support for the cryostat has been provided by the use of 8 columns, 25 feet long. Each column is a 16 in. x 16 in. rectangular tube with a 1/2 inch wall. Access for repair of the center core coils is provided between these columns.

An additional vertical support located near the outer portion of the coil is provided as a part of the basic TF coil and requires a support pad which can carry approximately 131 tons/pad. The effect of this support on the magnet deflected shape was shown in Figure D-5 (d).

b. Torque Frame Concept

This concept uses a frame and shear panel combination to react both the large torque induced in the top of the TF coil and the large vertical forces induced in the upper OH and EF coils. A similar frame and shear panel structure is used to support the lower OH and EF coils and to react the torques induced at the bottom of the TF coil. These frames provide a total of eight support points for each TF coil. This support arrangement was based on an analysis of the TF magnet support requirements as described in Section 5. Support is provided for the vertical loads of the blanket/shield and TF coil using the same concepts as described for the torque shell. The outer OH and EF support is also similar to the torque shell except supports are not provided on the columns for the vacuum ports.

(1) Upper Torque Frame

The upper torque frame consists of a horizontal circular shear plate to which concentric rings are attached to provide continuous support for the upper ohmic and equilibrium coils. Four concentric rings of TF coil lateral restraint fittings extend from the shear plate down and attach to the side of the TF coil to react the TF magnet torque forces. Support for

the vertical loads is accomplished by radial beams which rest on the center concrete core and are supported around the periphery of the reactor by the outer support columns located at each TF coil. This support concept is similar to the support used for the torque shell.

Lateral TF coil forces are transferred into the torque frame, by the lateral restraint fittings, and are transferred by the torque frame to four primary tension members. These four members, each carry approximately 5×10^6 pounds tension force and are located in a horizontal plane approximately 50 feet above the floor extending 120 feet to the outer wall of the reactor building. These tension members are pinned to the upper torque frame and can be readily disconnected and placed in storage positions against the building wall. Normal maintenance operations (those requiring less than 50 feet overall height) canbe performed without removing these members.

Toroidal field coil lateral restraint fittings were analyzed to obtain material thickness for use in weight determination. Overturning moments due to the lateral magnet loads are reacted by adjacent panel structure and the lateral applied loads are transferred into the reacting torque frame above. Applied lateral loads were obtained from results of the magnet deflection studies.

Analysis of the upper torque frame was conducted using a CASD finite element model. This model idealized the structure as axial bars and shear panels as shown in Figure D-7. Only one quarter of the full model was required due to symmetry. The automatic resizing capability of the CASD program was utilized to size the shear panel thicknesses and axial bar areas to the specified stress levels. These results were then applied to structural weight calculations.

Vertical forces are applied to the torque frame beams due to a combination of poloidal magnet dead weight and in-burn poloidal magnet forces. Each of the sixteen radial beams was analyzed as a pinned-pinned simply supported member with vertical loads applied. Because no clearance requirements were identified these beams were allowed to be as deep as required and, to further minimize weight, beam cross sections were allowed to taper according to moment carrying requirements. The smaller circumferential beams which provide continuous support of the poloidal magnets were also analyzed as pinned-pinned

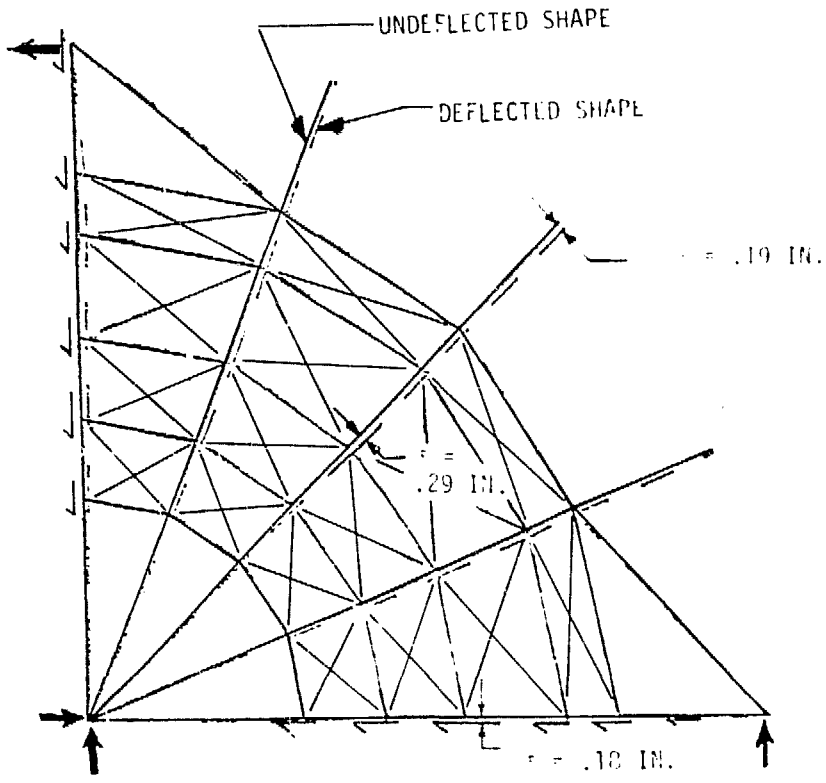

Figure D-7. CASD Finite Element Torque Frame Model and Deflected Shape

simply supported members, although a degree of fixity is recognized here. Weight contribution by these members is small in comparison to the weight of the radial beams.

(2) Support Columns

Sixteen columns around the reactor perimeter are needed to help support the overhead torque frame and two sets of OH and EF coils. These fifty foot tall columns must be capable of withstanding applied axial compression loads and the intermediate moments at the coil support locations. Column weights were calculated based on both stainless steel and aluminum material properties. Although the yield strength is greater for the aluminum, its lower modulus caused resulting weights to be approximately equal for both steel and aluminum since the columns are designed to preclude buckling

(3) Lower Torque Frame

The lower frame is similar to the upper frame except it is located between the TF coil and the lower OH and EF coil. This location allows lowering of individual magnets to the rewinding turntable without disassembly of the structural frame. The shear plate for this frame must be offset slightly to allow clearance of the TF and lower coils.

The structural rings directly above the OH and EQ coils provide continuous support for these coils. Four concentric rings of lateral support pads react the TF coil induced torques. These 4 rings are attached to the torque frame structure to allow the TF coil induced torques to be transmitted to the wall of the lower access pit. This frame is supported in the vertical direction by the blanket/shield support columns. By release of these support points, this frame assembly can be lowered to allow magnet repair. The vacuum pumps are supported by a removable bracket attached to the torque frame. Both the vacuum pump and brackets must be removed prior to lowering the magnets for repair.

Both the upper and lower torque frames are divided into segments by insulated joints to reduce the radial flow of eddy currents. Torque frame rings will also be isolated from the upper and lower OH and EF coils to prevent current flow through the frame into these coils.

7. Concept Comparison

Each of the concepts considered provides structual support for the TF coil components. Support requirements for the magnets must be further evaluated and integrated into an optimum overall design considering the various loading conditions which may occur, the magnet deflection criteria, access and maintenance requirements, weights, and costs. In this section, advantages and disadvantages of the torque shell and torque frame structural support concepts will be discussed. In addition data will be presented on the concept weights and construction costs for different materials.

a. TF Coil Support

The primary difference between the torque frame and torque shell concept is in the method of supporting the lateral loads induced in the toroidal field coils. The torque shell concept provides more continuous support for the TF coil which will probably allow use of thinner TF coil cryostat structural walls and result in less eddy current heating.

b. Overhead Support Frames

The radial beams used for overhead poloidal coil support were shown in different locations for the torque frame and torque shell concept to show the effect of TF coil electrical connector location on structure design. The torque frame concept uses a straight beam aligned with the TF coils and outer support column and requires relocation of the TF coil connector but results in a straightforward design. The torque shell concept locates the radial beam between adjacent TF coils to clear the TF coil connector in its present location. However this requires splitting the beam ends to span to the support columns. Either of these beam locations can be used without significant effect on overall weight, although the split beam will increase fabrication cost slightly.

c. Access/Maintenance

All normal maintenance of the blanket and shield will be accomplished from the side of the reactor. Both concepts provide equivalent access to the magnets and blanket/shield components. The torque frame concept with the overhead tension ties allows direct access for normal maintenance. In comparison, the torque shell concept requires removal of 1 to 16 central access

shear panels depending on the amount of access required. Each panel requires approximately four manhours for removal and six manhours for reinstallation. It is anticipated that panel removal can be accomplished during blanket and shield cooldown and therefore may not increase downtime. Reactor start-up will be delayed, however, for panel reinstallation.

For both support concepts, the upper poloidal coils can be removed for repair by lifting the overhead support structure with the reactor polar crane. Direct access can be provided for TF coil removal by raising the upper poloidal coils, removing or lowering the outer poloidal coils and removing the required outer support column.

Failure of the lower poloidal coils could require disassembly of the entire reactor unless in-place repair provisions are provided. The concept developed for this repair operation was shown previously in Figure D-1. It consists of a system of jacks built into the blanket/shield support columns which can be used to lower the support frame and coils to a turntable. Once the coil is placed on the turntable the support frame is raised and shielding installed to allow direct access to the magnets. The turntable can then revolve about the reactor center column to allow rewinding of superconductor through the openings between support columns. As an option to this in situ rewinding facility, depending upon magnet reliability and cost compared to the cost of the rewinding facility, the installation of spare magnets in the access pit during initial reactor assembly may be used. Provisions for accessing and repairing the lower coils are included in both structural support concepts.

d. Weight Comparisons

Weight of the structural support system components is important when it affects the cost of material, cost of fabrication, or handling equipment requirements. As shown previously in Table D-1, both the cost of material and cost of fabrication are based upon weight, for comparable shapes and fabrication techniques. A summary of the structural support system weights is shown in Table D-2 for 7075-T6 aluminum, 2219-T87 aluminum and 304 stainless steel. These weights are based on the structural sizing of components as determined during the study.

The only place where weight has significant impact on handling equipment is the overhead support tree in the shear panel concept and the upper

Table D-2. Weight and Cost Comparison

CONCEPT	TORQUE SHELL			TORQUE FRAME		
MATERIAL AND FABRICATION TECHNIQUE	ALUMINUM		STAINLESS STEEL	ALUMINUM		STAINLESS STEEL
	Bolt 7075-T6	Weld 2219-T87	Weld 304	Bolt 7075-T6	Weld 2219-T87	Weld 304
TOTAL WEIGHT (TONS)	240	437	722	358	684	1552
COST (MILLIONS)						
Material & Fabrication	$1.8 - 2.4M	$3.3 - 4.4M	$3.1 - 4.5M	$2.2 - 3.0M	$4.3 - 5.7M	$5.6 - 8.1M
Erection	$0.5 - 0.8M	$0.5 - 0.8M	$0.5 - 0.8M	$0.5 - 0.8M	$0.5 - 0.8M	$0.5 - 0.8M
Design	$2.7M	$2.7M	$2.7M	$2.7M	$2.7M	$2.7M
Total	$5.0 - 5.9M	$6.5 - 7.9M	$6.3 - 8.0M	$5.4 - 6.5M	$7.5 - 9.2M	$8.8 - 11.6M

torque frame in the torque frame concept. Because the four poloidal coils weight 155 tons, the structure must be limited to a maximum of 245 tons to keep from exceeding the 400 ton overhead crane capacity. Only aluminum used in a bolted fabrication falls within this limit for the torque frame concept while any of the materials shown easily fall within the limit for the torque shell concept. It is desirable to stay well below the limit to allow margin for increased weight due to increased loads or to allow use of heavier but lower cost fabrication techniques.

c. Cost Comparisons

The total cost of the structural support system will consist of cost of design, material/fabrication, and erection. A summary of total concept weights and costs are shown in Table D-2. The lowest cost is achieved using 7075-T6 aluminum and is approximately $6 M for the torque frame design and $5.5 M for the torque shell design.

Several fabricators were contacted to obtain estimates of material and fabrication cost for aluminum and stainless steel alloys using the overhead torque frame as a basis. These estimates were then scaled to the torque shell concept based on a Mississippi Valley Structural Steel estimate of a 20% increase for complexity. The estimates were shown previously in Table D-1.

Costs for 304 stainless steel, 2219-T87 welded aluminum and for bolted 7075-T6 aluminum are shown in Table D-3 for the torque frame concept along with an estimate by Mississippi Valley Structural Steel of the erection cost for either concept.

Table D-3. Cost Estimate for Torque Frame Materials

Material	Stainless Steel	Aluminum	
Material Type	304	2219-T87	7075-T6
Fabrication Technique	Welded	Welded	Bolted
Material & Fabrication	$ 3600	$ 6300-8300	$ 6300-8300
Erection	$ 600-1000/ton	$ 600-1000/ton	$ 600-1000/ton

1. C. A. Trachsel, "Development and Evaluation of TEPR Support Structure Concepts," McDonnell Douglas Astronautics Company - East, Contract 31-109-38-3391, Argonne National Laboratory (May 1976).

2. Weston M. Stacey, Jr., et al., "Tokamak Experimental Power Reactor Studies," Argonne National Laboratory, Report ANL-CTR-75-2, Argonne, Illinois (June 1975).

3. Manual of Steel Construction, American Institute of Steel Construction, Seventh Edition.

4. MIL-Handbook 5, Metallic Materials and Elements for Flight Vehicle Structures, Department of Defense, (August 1975).

5. Rules for Construction of Nuclear Power Plant Components, ASME Boiler and Pressure Vessel Code, Section III, Div. 1, Subsection NF, 1974 edition.

6. H. C. Mantz, "Structural Support/Thermal Isolation of Superconducting Magnets," Task I and III of CCP No. 1 Contract No. 31-109-38-3391, Argonne National Laboratory, (May 1976).

APPENDIX E

MATERIALS CONSIDERATIONS FOR THE PRIMARY ENERGY CONVERSION SYSTEM

The materials in the primary energy conversion system will be exposed simultaneously to the severe radiation, thermal, mechanical, and environmental conditions imposed by an operating fusion reactor. As a result, materials problems present one of the major technological constraints to the successful operation of a fusion power reactor, and the proper selection of materials will have a major influence on the attainment of the EPR objectives. As stated previously, the primary objectives of the EPR are the production of megawatt quantities of thermonuclear power and the conversion of this power to sensible heat, which may be used to produce electricity. The minimum risk approach for enhancing the attainment of these two objectives in the suggested time period severely limits the materials alternatives for the EPR. In particular, the absence of a tritium-breeding blanket in EPR alters the priorities for materials selection in the primary energy conversion system relative to a demonstration or commercial-scale reactor. The strong incentive to utilize available materials technology in order to meet scheduled design objectives places further restraints on the materials selection. It will be necessary to utilize materials in EPR that are probably not optimal for commercial-power reactor applications, since time and economic restrictions prohibit the satisfactory development of an advanced materials technology for the EPR. As a result, the materials considerations for EPR are strongly influenced by available materials technology.

The major components of the primary energy conversion system are the first-wall system, the blanket, and the shield. The primary function of the first-wall system is to provide a region of appropriate geometry and sufficiently pure environment that satisfactory plasma performance can be achieved. The first-wall system consists of (1) the toroidal vacuum vessel that surrounds the plasma region, (2) a current breaker to minimize the ohmic heating of the vacuum wall, (3) coolant panels to shield the more permanent vacuum wall from intense photon and charged-particle radiation eminating from the plasma, (4) a low-Z liner for control of high-Z impurities in the plasma, (5) all penetrations of the primary vacuum vessel

such as vacuum-, auxiliary heating-, and diagnostic-ports, and (6) plasma diagnostics and instrumentation located within the vacuum vessel. Since the first-wall system serves as the first physical barrier that isolates the plasma from the remainder of the reactor system, the materials of these components are subjected to the most severe radiation environment in the reactor. Since EPR does not include a tritium-breeder blanket, the materials considerations for the blanket/shield region relate primarily to neutronic properties (see Chapter IX).

The materials considerations for the primary energy conversion system are discussed according to the primary function, viz., structural, low-Z liner, electrical insulator, and neutronic shield. Structural materials are used for the vacuum vessel, coolant panels, coolant piping, and blanket support. Low-Z liner materials, which shield the plasma from the high-Z structural materials, are needed for impurity control. Electrical insulators are required for current breakers, rf coil support and diagnostics. Shield materials protect the superconducting magnets from the high-energy neutrons. In the following sections the properties of candidate materials for the various applications are summarized as they relate to EPR applications.

1. Structural Materials

The structural materials must maintain their mechanical integrity and dimensional stability for extended periods under the severe conditions imposed by a fusion reactor environment. Primary considerations for the selection of structural materials are fabricability, elevated-temperature mechanical properties, resistance to radiation damage, induced activity, coolant compatibility, resource availability, and economic impact. A number of candidate alloys have been evaluated with respect to these property requirements.[1] Austenitic stainless steel appeared to be adequate for the limited EPR design requirements; however, vanadium-base alloys were considered to have greater long-term potential for commercial reactor applications. The overriding considerations in this assessment were the established fabrication technology and available data base for stainless steel. The following assessment of the property data for the candidate structural materials, primarily stainless steel, provide a data base for determining the operating limitations of the materials in EPR.

a. Austenitic Stainless Steel

The properties of annealed Types 304 and 316 stainless steel and 20% cold-worked, Type 316 stainless steel are reviewed for the temperature range 23 to 550°C. Emphasis is placed on the physical, mechanical, and radiation properties; however, other properties relating to compatibility, magnetic fields, and weld-metal are discussed briefly.

(1) Physical Properties

The temperature dependence of the physical properties for Types 304 and 316 stainless steel is well documented.[2] Table E-1 summarizes the relevant physical property data for the two steels at room temperature and 500°C. The differences in properties between Types 316 and 304 stainless steel are quite small. There is no experimental evidence that radiation significantly alters these physical properties at the fluences expected in EPR.

(2) Mechanical Properties

(a) Tensile Properties

The nominal tensile properties of the austenitic stainless steels, which are well documented,[3] are listed in Table E-1 at 23° and 500°C. The tensile strength of stainless steel remains fairly uniform to temperatures of 600°C, where it begins to decrease significantly. However, extensive fission reactor irradiation data indicate that neutron irradiation substantially affects the strength and ductility of stainless steel.[4-13] Data obtained from post-irradiation fission reactor tests at temperatures of 480 to 540°C were used in Figures E-1 through E-4 to show the effects of neutron radiation on the strength and ductility of stainless steel at ∿ 500°C. The error bars show the range of uncertainty in the data. Only a small amount of information exists for irradiations above 20 dpa (equivalent to a fission reactor flux of ∿ 4×10^{22} n/m^2, E > 0.1 MeV),[4] so that the curves are of limited accuracy at the higher fluences. The curves indicate that the strength and ductility differences in these materials become smaller with irradiation. At fluences above ∿ 40 dpa, the yield and ultimate tensile strengths approach ∿ 80 ksi, and the uniform and total elongations approach 0.5 and 1%, respectively. Annealed Type 316 stainless steel maintains the largest ductility up to at least 20 dpa. The limited data taken above 20 dpa indicate that a saturation

Table E-1. Properties of Austenitic Stainless Steels[2,3]

Property	Annealed 304		Annealed 316		316 20% CW	
	23°C	500°C	23°C	500°C	23°C	500°C
Specific Heat (cal/g-°K)	0.090	0.097	0.107	0.137	0.107	0.137
Thermal Conductivity (cal/s-cm-°K)	0.0375	0.053	0.0315	0.0475	0.0315	0.0475
Thermal Diffusivity (cm^2/s)	0.0385	0.0460	0.0370	0.0450	0.0325	0.0430
Thermal Expansion ($\times 10^{-6}$/°C)	16.7	20.2	16.7	20.2	16.7	20.2
Density (g/cm^3)	8.02	7.82	7.95	7.77	7.95	7.77
Electrical Resistivity (Ω-cm $\times 10^{-6}$)	70	105	76	104	76	104
Young's Modulus ($\times 10^6$ psi)	28.1	23.2	28.1	22.9	28.1	22.9
Uniform Elongation (%)	35	22	33	25	14	7.5
Total Elongation (%)	40	25	39	28	21	8
0.2% Yield Strength ($\times 10^3$ psi)	30	16	30	17	92	74
Ultimate Tensile Strength ($\times 10^3$ psi)	75	54	75	60	119	99

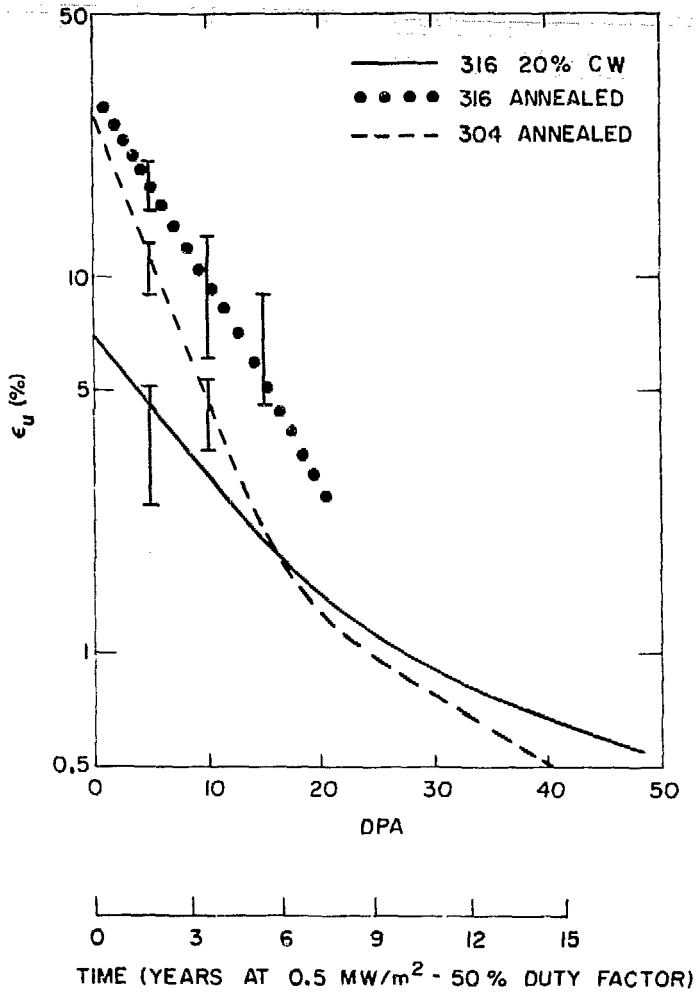

Figure E-1. Uniform elongation of annealed 304, annealed 316, and 20% cold-worked 316 stainless steel at 500°C as a function of radiation damage and time in EPR[3-13]

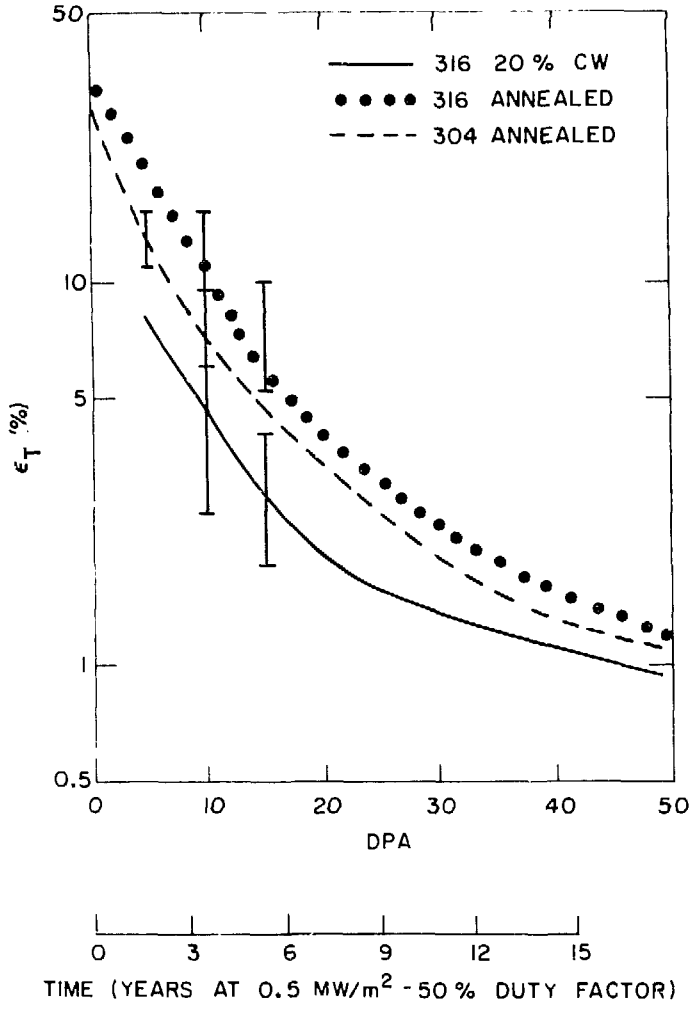

Figure E-2. Total elongation of annealed 304, annealed 316, and 20% cold worked 316 stainless steels at 500°C as a function of radiation damage and time in EPR.[3-13]

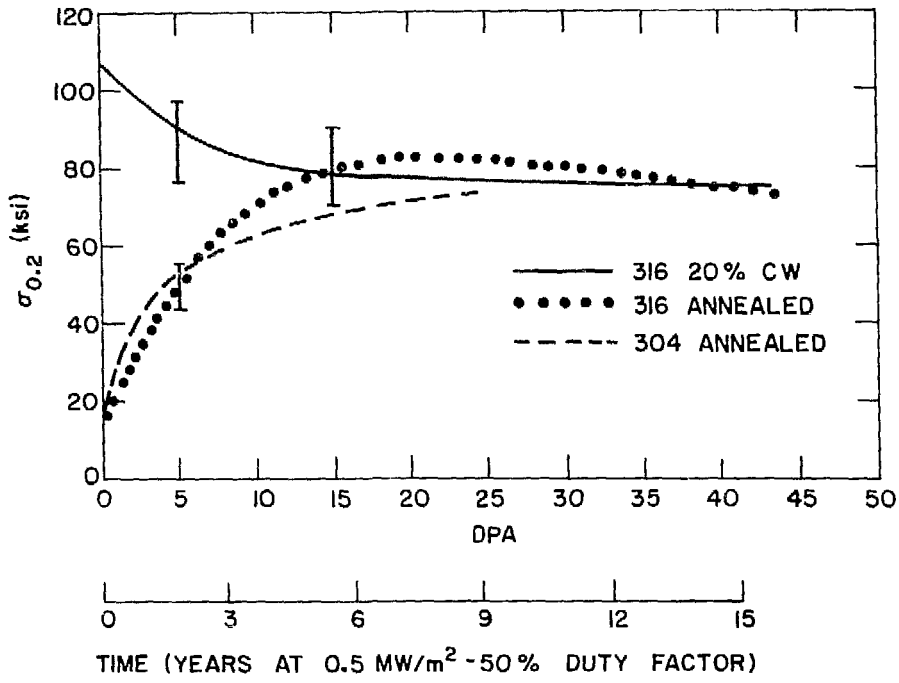

Figure E-3. 0.2% yield strength of annealed 304, annealed 316, and 20% cold worked 316 stainless steels at 500°C as a function of radiation damage and time in EPR.[3-13]

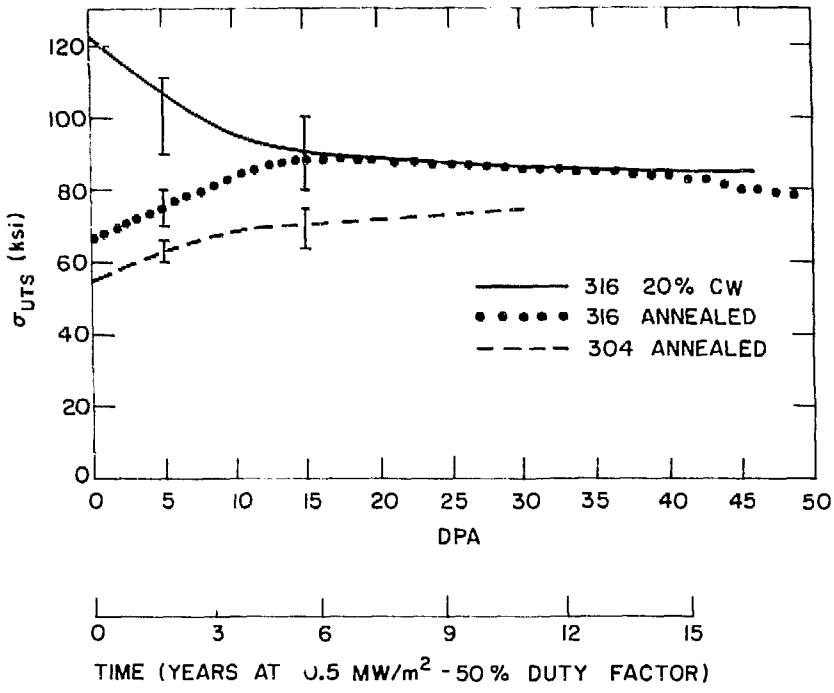

Figure E-4. Ultimate tensile strength of annealed 304, annealed 316, and 20% cold worked 316 stainless steels as a function of radiation damage and time in EPR. 3-13

level may be reached above which the deterioration of the tensile properties slows or stops;[5] however, lack of data between 20 and ∿ 60 dpa precludes the determination of this saturation point. Also shown in Figures E-1 to E-4 are the changes in strength and ductility with time that correspond to a wall loading of 0.5 MW/m^2 and 50% duty factor.

Substantial amounts of helium, which will be generated in stainless steel by the 14-MeV fusion neutrons, will further degrade the residual ductility of the steel. Helium generated in the matrix by (n, α) reactions segregates into bubbles along grain boundaries. Under an applied stress, the bubbles grow and coalesce to initiate cracks, which produce an intergranular fracture and a sharp decrease in ductility. The potential effects of large concentrations of helium on the ductility of Type 316 stainless steel has recently been investigated.[5] At 600°C, ∿ 60 dpa, and ∿ 4000 appm He, the total elongation in annealed Type 316 stainless steel was reduced to 0.8%, compared to a value of 0.2% for 20% cold-worked Type 316 stainless steel. At 680°C, the total elongation was practically zero for both materials under similar irradiation conditions. This ductility loss due to the presence of helium dominates the fracture process above 600°C, and severely limits the permissible operating temperatures of stainless steel structural components. Experimentally, the presence of helium will begin to significantly reduce ductility above 500°C.[14] To avoid excessive helium embrittlement, the operating temperatures of structural components in EPR will be limited to temperatures ≤ 500°C.

The radiation hardening increases the strength of the annealed material at elevated temperature while the strength of the cold-worked material decreases slightly due to aging (see Figure E-3 and E-4). After irradiation to > 10 dpa at 500°C, the effect of prior history on the tensile properties of austenitic stainless steel is not critical.

(b) Creep

Creep is the time-dependent plastic flow of metals under the conditions of constant stress. Two forms of creep will occur under EPR conditions, viz., thermal and radiation creep. Thermal creep depends sensitively on both temperature and stress. For the case of austenitic stainless steels, thermal creep is negligible below 500°C; however, it becomes significant at substantially

higher temperatures.[15] This rapid increase in the thermal creep rate will be a factor in limiting the operating temperatures in EPR. The effects of irradiation on creep properties have been measured in two ways, by in-reactor creep tests and by post-irradiation creep-rupture tests. The in-reactor creep behavior of stainless steel is not well characterized. There have been relatively few experiments performed, and most of the experiments were performed at low fluences. Post-irradiation creep-rupture tests indicate that radiation damage can substantially alter the creep rate and creep strain at fracture. The total time to fracture can be reduced because of either an increased creep rate or decreased ductility.[5,7,11,14,16-18]

The effects of radiation on creep are estimated from equations developed from test data.[3,19,20] Figure E-5 indicates that, at 10 ksi, radiation creep dominates the creep process under EPR conditions such that after 10 years of operation radiation creep may reach $\sim$ 1.5%. It should be emphasized that the radiation creep equation was formulated using low fluence ($\sim$ 5 dpa) data and that the influence of high helium production and significant void swelling on creep was not taken into account. Therefore, the extent of radiation creep indicated by Figure E-5 is probably not conservative. The 100,000-hour post-irradiation rupture stress for annealed Type 316 stainless steel is shown in Figure E-6[20] as a function of displacement damage at 500, 550, and 600°C. The rupture stress first decreases with fluence, passes through a minimum, and then begins to increase. As the steel is irradiated, both the creep rate and ductility decrease. The loss of ductility, which can be reduced to below 1%,[14] dominates the creep rupture process at low fluences and results in a decreased rupture time. At high fluences the creep rate is greatly reduced due to irradiation hardening, which results in an increased rupture time even though the ductility remains low. Figure E-6 indicates a minimum creep rupture stress of $\sim$ 17 ksi at 500°C.

One variable which has not been thoroughly studied, but which will likely be important in fusion reactor applications, is the effect of high helium concentrations on the creep-rupture properties. Helium tends to promote intergranular fracture at high temperatures and low strain rates. Small concentrations of helium have been shown to significantly affect creep properties of stainless steel at temperatures above 550°C;[18] however, little

data exist on the effect of high helium concentrations (> 100 appm) at lower temperatures. A recent investigation on Type 316 stainless steel indicates that the combination of high helium concentration and appropriate neutron damage may substantially reduce the creep-rupture life below that caused only by neutron damage.[5] Another major deficiency in the available data relates to the fact that most mechanical property data are obtained from post-irradiation tests rather than during irradiation, which is more desirable.

(c) Fatigue

Mechanically or thermally induced cyclic loading can lead to fatigue failure of structural components. The allowable fatigue lifetimes of the materials are generally expressed in terms of cycles to failure as a function of strain range. Considerable elevated temperature baseline data, primarily in the low-cycle fatigue regime, have recently been obtained on austenitic stainless steel for fission reactor applications.[21,22] Although the fatigue lifetimes of annealed Types 304 and 316 stainless steel in air do not differ significantly, factors such as prior history (cold-work), strain rate, temperature, and test environment can substantially affect the fatigue properties of stainless steel. Figure E-7 gives elevated temperature fatigue data for annealed Type 316 tested in air. Also shown in Figure E-7 is the elevated temperature fatigue design curve established by ASME code case 1331-8 for 18 Cr - 8 Ni stainless steel (this includes both Type 304 and 316 stainless steel). Appropriate adjustments to the design curve must be made to account for variations such as loading (hold-time), mean stress, and environment. Only limited data exist on the effect of neutron radiation on the austenitic stainless steels. Representative data for irradiated Type 316 stainless steel, which are shown in Figure E-8, indicate a moderate decrease in fatigue life caused by irradiation. A smaller effect of radiation was observed for annealed Type 304 stainless steel; however, the fatigue lifetime of cold-worked material was lower than that of annealed Type 316 stainless steel. The effects of combined neutron damage with high helium concentrations have not been evaluated.

(3) Radiation Swelling

Significant swelling of austenitic stainless steel has been observed after irradiation in fission reactor environments to high fluences (> 10^{21} n/cm^2)

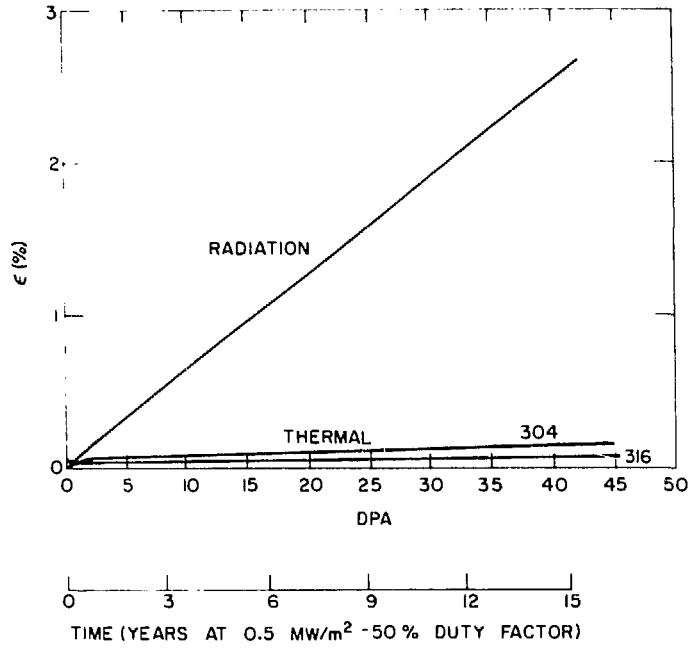

Figure E-5. Thermal and radiation creep in 304 and 316 stainless steels at 500°C and 10 KSI as a function of radiation dose and time in EPR. 3-19

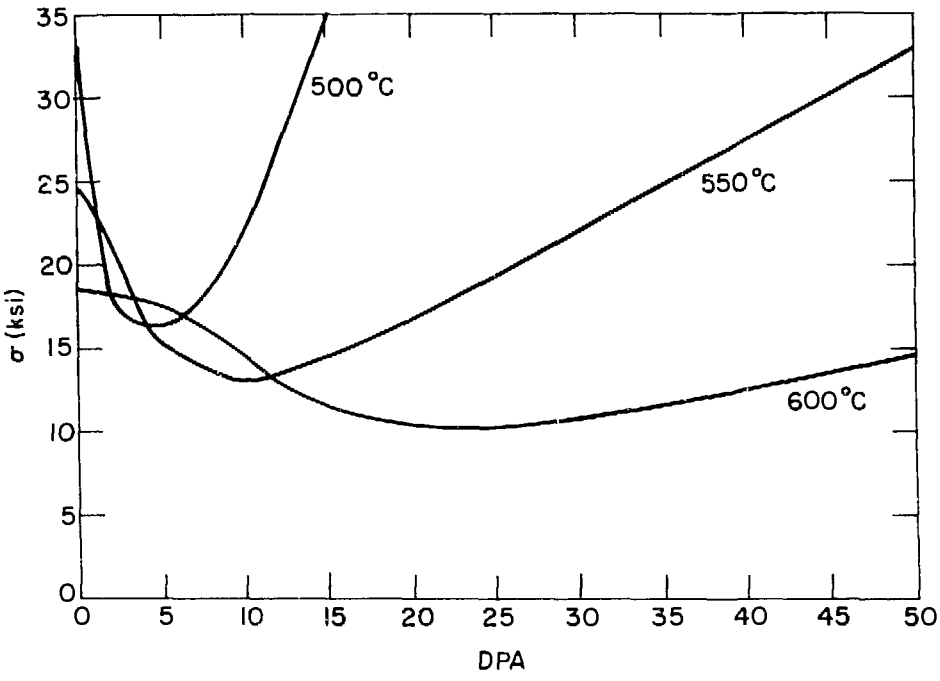

Figure E-6. 100,000 hour creep rupture stress in 316 stainless steel at 500, 550, and 600°C as a function of radiation damage.[20]

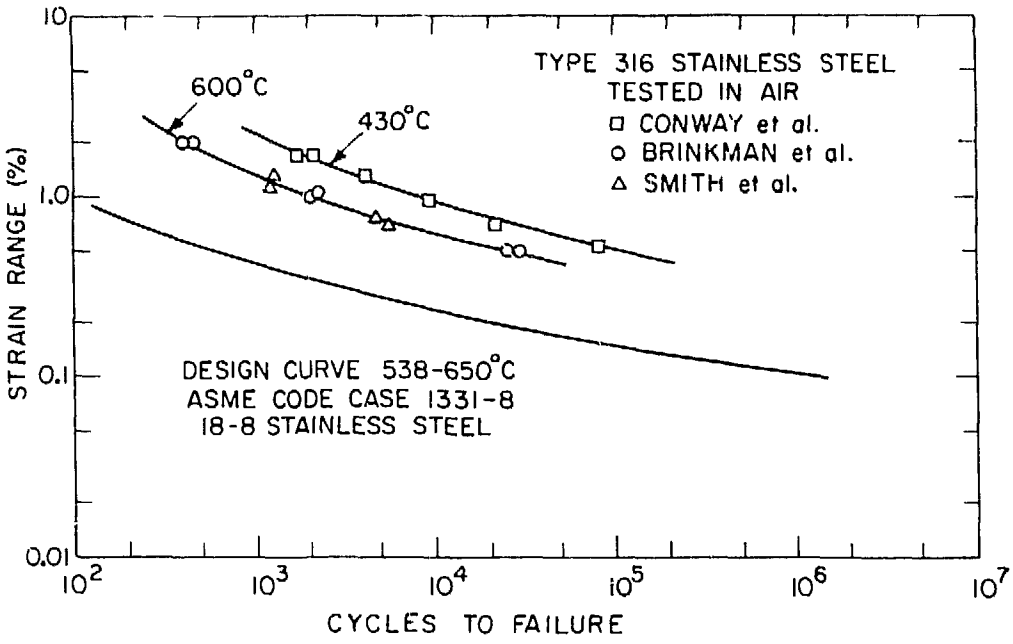

Figure E-7. Fatigue life of annealed 316 stainless steel at 593°C under various test conditions ($\dot{\varepsilon} = 4 \times 10^{-3} s^{-1}$). 23-25

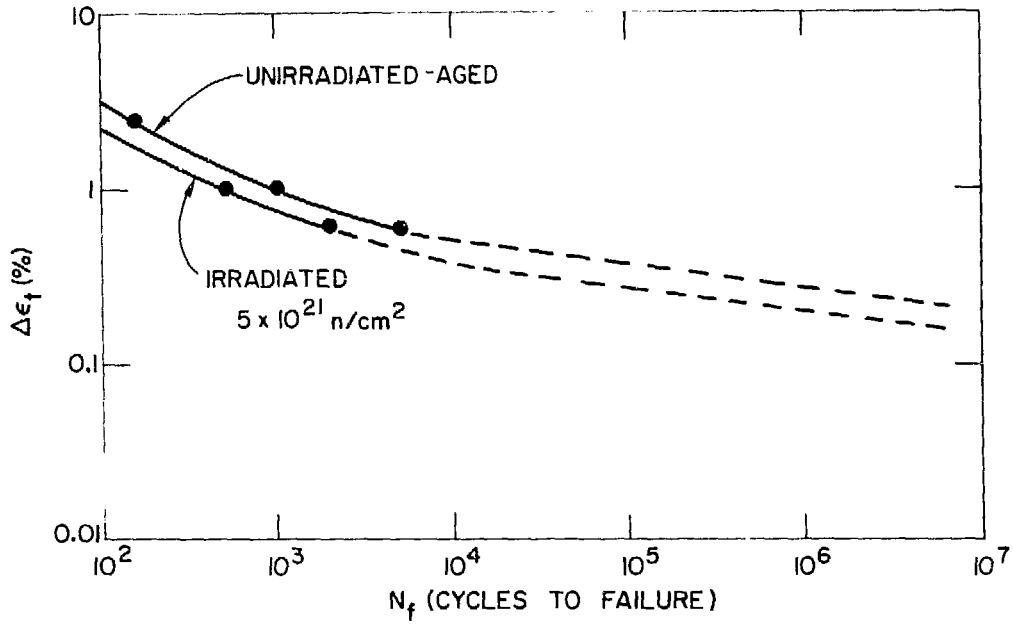

Figure E-8. Effect of radiation on the fatigue life of annealed 316 stainless steel at 700°C ($\dot{\varepsilon} = 8 \times 10^{-4} s^{-1}$).[26]

The swelling is caused primarily by the segregation of radiation produced vacancies into voids during high temperature irradiation. Normally, swelling occurs between 0.3 to 0.5 of the absolute melting temperature, which corresponds to temperatures of 250 to 575°C for stainless steel. Several factors, including temperature, neutron flux, total radiation dose, prior history, grain size, impurity concentration, and the presence of helium, influence the degree of swelling.[27] Swelling data from fission reactors have been used to formulate empirical equations that relate temperature and neutron fluence to the amount of swelling in stainless steels.[3,28] The peak swelling predicted by these equations is given in Figure E-9 for Types 304 and 316 stainless steel. The neutron fluence, ϕt, has been converted to displacements per atom, dpa, using the relation 50 dpa $\sim 10^{23}$ n/cm^2 (E > 0.1 MeV).[4] The swelling versus time in EPR at a wall loading of 0.5 MW/m^2 and a 50% duty factor is also indicated. All three materials show swelling of $\leq$ 5% after 10 years with 20% cold-worked Type 316 stainless steel showing the lowest swelling. These results do not allow for effects caused by the high helium production rates expected in fusion reactor applications. However, recent experiments indicate that large concentrations of helium do not appreciably alter the extent of peak swelling, but rather the helium tends to broaden the temperature range where peak swelling is observed.[29] Because of this peak-broadening effect, peak swelling should be assumed in EPR over a wider range of temperatures.

(4) Effects of Weldments

A large amount of welding will be required in the construction of an EPR. Since much of the weldments will be exposed to the same severe environment as the bulk metal, the integrity of both the weld-metal and the heat-affected-zones is critical. Only limited data are available with which to evaluate the reliability of welds in a fusion reactor environment. Variations in properties of weldments and heat-affected zones are caused by differences in chemical composition and microstructure from the base metal. For example, significant ferrite phase is intentionally included in weld-metal to minimize embrittlement.[30] Thermally induced residual stresses in weld regions can also affect the behavior of welds.

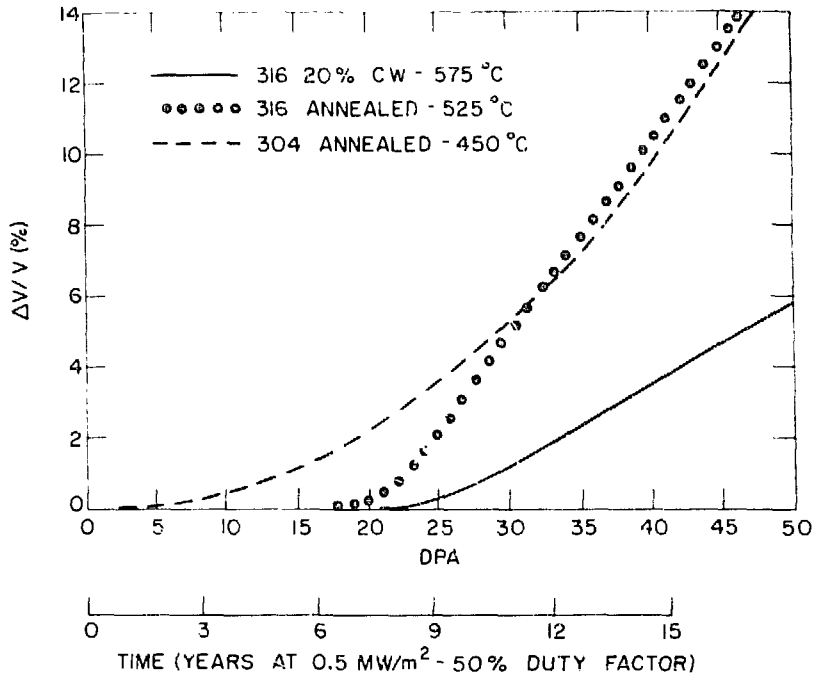

Figure E-9. Peak swelling in annealed 304, annealed 316, and 20% cold-worked 316 stainless steels as a function of radiation damage and time in EPR.[3,28]

The mechanical properties of weld material may be substantially different from the parent material.[31] For the case of Type 316 stainless steel at elevated temperatures, the tensile properties of the weld material are quite close to those of the parent material in a 7-8% cold-worked condition. Creep rupture tests on Type 316 weld-deposited metal indicate that the rupture life is approximately the same as the parent metal. Fatigue life of welded structures can be reduced from weld free structures, because the weld itself creates a point of stress concentration where fatigue cracks can originate.[32] The long life fatigue stress limit of weld joints appears to vary from 40 to 90% of the parent metal with most reported values in the range of 55 to 65%.[32]

The effects of radiation on weld-deposited stainless steel are similar to those in the parent metal. From the limited data available, there is an indication that the property change threshold for annealed weld metal occurs at a somewhat lower fluence than for the wrought alloy.[31] Considerable development will be required to reliably predict the behavior of the extensive weldments in EPR.

(5) Coolant Compatibility

The extensive pressurized-water coolant technology developed for fission reactor and conventional energy conversion applications provides a substantial data base for the EPR application.[33] However, two major concerns relating to coolant compatibility in the fusion reactor environment remain. The first involves stress corrosion cracking caused by a combination of a corrosive (oxidizing) environment and stress in the structural material, which can lead to premature cracking and failure. Since weld regions are particularly susceptible to this phenomenon, the sensitivity is increased because of the extensive welding required in the EPR. Problems relating to limitations of water chemistry control may be encountered because of the presence of tritium in the water. Hydrogen overpressures, which are typically used to control the oxygen levels in pressurized-water systems, may not be acceptable in the presence of substantial tritium inventories. The second problem relates to radioactive mass transfer of corrosion products from the high-flux regions of the reactor to areas outside the high-level shield. Further analysis is necessary to assess the impact of this effect on the shielding requirements.

(6) Magnetic Effects

The effects of the strong magnetic field on the significant amounts of ferrite present in the stainless steel have not been evaluated; however, they are of potential concern. Weldments of austenitic stainless steel normally contain 5-10% ferrite.[30] This contribution may be substantial because of the extensive welding that will be required in EPR. Irradiation of stainless steels at elevated temperatures will also induce ferrite formation in bulk material.[34] The ferrite particles that formed were calculated to be of the order of 20 Å in diameter, and the concentration of ferrite depended on the irradiation temperature and the heat treatment following irradiation. Simple aging at elevated temperatures can also contribute to ferrite formation. The importance of small quantities of ferrite in stainless steel on the magnetic field, and effects of the magnetic field on the steel components, should be resolved.

b. Alternate Structural Materials

Austenitic stainless steel appears to be an adequate structural material for the limited objectives of EPR; however, alternate materials will probably be required for more advanced designs. Major limitations of austenitic stainless steel for advanced applications include (1) relatively low-temperature operation ($\leq$ 500°C) limited by radiation embrittlement, swelling, and strength properties; (2) excessive swelling at high neutron fluences; (3) high induced activity; and (4) excessive corrosion by lithium at high temperatures. Stainless steel also has a relatively high thermal-expansion coefficient and relatively low thermal conductivity, both of which enhance thermal stress problems. Low-swelling stainless steels (Ti or Si modified), which tend to alleviate the swelling problem, have been proposed as an alternative to the standard stainless steels. However, they do not circumvent many of the other disadvantages of standard steels.

The refractory metals, niobium, molybdenum, vanadium and their alloys, have been suggested as possible structural materials for fusion devices. These materials all have a body-centered cubic structure and high melting temperatures (1900°C < T_m < 2600°C). In the temperature range of 0.2 to 0.5 T_m, the strength of pure refractory metals is relatively independent of temperature, and the ductility is high. Interstitial impurities (oxygen,

nitrogen, carbon) usually increase the strength and decrease the ductility substantially.[35] These metals also exhibit a ductile to brittle transition temperature (DBTT) below which they fracture in a brittle mode. Their major disadvantages for fusion applications relate to the lack of fabrication technology, of materials property data and of experience under reactor conditions. However, the refractory metals possess many attractive properties that are discussed below.

Although niobium (Nb-1Zr), molybdenum (TZM) and vanadium-base alloys are considered to be the prime candidates, vanadium-base alloys possess the most favorable properties.[1] The major advantages of vanadium-base alloys compared to niobium- and molybdenum-base alloys relate to lower induced activity, less effect on breeding ratio and better radiation swelling properties. In comparison with stainless steels, the vanadium-base alloys also result in much lower induced activity. Radiation swelling in pure refractory metals occurs to about the same degree as in stainless steels, but the peak swelling temperature is higher in refractory metals.[36,37] Interstitial impurities can alter the radiation swelling properties substantially and are responsible for the formation of an ordered array of voids, known as the void lattice.[36,38] Substitutional alloys often show reduced swelling. The principle example is vanadium-titanium alloys, which show almost no swelling at relatively high fluences.[37] At low temperatures, radiation affects the mechanical properties of refractory metals by increasing the strength and decreasing the ductility.[39] Radiation also increases the DBTT. In molybdenum, the DBTT can be raised to 500°C by irradiation.[40] Helium embrittlement also occurs in refractory metals, but the onset of embrittlement occurs at higher temperatures than in stainless steel.[41] Selected vanadium-base alloys maintain much higher ductility after irradiation than does stainless steel.[36] Since the thermal expansion is less and the thermal conductivity is greater for vanadium than for stainless steel, thermally-induced stresses would be considerably reduced for a given heat flux.[2] Vanadium, as well as other refractory metals, possesses good compatibility with high-purity lithium.[42] The refractory metals probably can not be used with water or helium coolants at the required temperatures.

The basic conclusion to be drawn from this information is that refractory metals in general, and vanadium-base alloys in particular, are potentially capable of withstanding higher radiation doses, temperatures, heat fluxes, and neutron wall loadings than stainless steels. Vanadium-base alloys with a composition of V-(10-15)Cr - (0.3 - 1.0)Ti are presently considered to be the best choice for advanced application.

2. Insulators

Ceramic insulators are generally ionicly-bonded brittle materials with high melting points. They include metal oxides, nitrides, carbides, phosphides, silicides, and sulfides. Their bulk properties are not only a function of material composition, but vary over a wide range with fabrication methods. Variables such as porosity, grain size, and surface condition can have a great influence on ceramic properties.

The primary use of ceramic insulators in EPR is as electrical insulation. Current breakers in the first wall and flux breakers in the blanket require low voltage insulator materials, while the rf coils, if installed, would require high voltage insulation. As with stainless steel, the insulation should maintain its mechanical integrity over the lifetime of the reactor. The mechanical property requirements are minimal, however, since the insulatio will not be used for structural purposes. The basic properties of candidate ceramics for use in EPR are reviewed in this section. Interpretation of available information is complicated by the large number of ceramics that have been tested and the large amount of scatter in the data. Because of the difficulty of evaluating individual materials, the properties of ceramics are discussed primarily in general terms. Reviews of the properties of insulator materials for use in fusion reactors, which recently have been published, contain additional information.[43,44]

a. Electrical Properties

Electrical conductivity is very low in most ceramic materials.[43] The conductivity of these materials at low to moderate temperatures is typically 10^{-14} to 10^{-12} Ω^{-1} cm^{-1}, increasing rapidly with temperature to 10^{-6} to 10^{-4} Ω^{-1} cm^{-1} at 1000°C. The activation energy for the conduction process at elevated temperature is often close to that of atomic self diffusion.

The physical mechanisms for conduction can be complex because of the ionic nature of the lattice. Conduction may be either ionic or electronic depending on the temperature and valence considerations. Since the conductivity is low, small amounts of impurities and the surface environment can play a significant role in the conduction process. Such variables as environment, heat treatment, purity, fabrication history, microstructure, and measurement technique are responsible for the large scatter of experimental data (up to 7 orders of magnitude). Typical values for the electrical conductivity of several candidate materials are shown in Table E-2.

There is a similar wide variation in the dielectric properties of insulators. The dissipation factor (tan δ) and dielectric constant (ε') are also dependent on impurities, environment and fabrication. In general, tan δ is lower and ε' is higher as the purity increases. Single-crystal and sputtered insulators are superior to sintered insulators. The tan δ increases and ε' decreases rapidly with frequency at temperatures above $\sim$ 300°C. At room temperature very little change occurs with frequency.

Radiation can significantly alter the electrical properties of insulators. Neutron irradiation can increase the conductivity by 10^2-10^3, and ion bombardment can increase the conductivity by as much as 10^5. These changes are usually temporary, and the pre-irradiation conductivity normally returns either after irradiation ceases or after suitable heat treatment following irradiation. It is difficult to predict what permanent changes might occur in insulators at the high fluence levels expected in EPR since the experiments that have been performed have all been done only at low fluence levels. In addition, there is a large amount of data scatter, and experimental difficulties in measuring electrical properties in a radiation field limit the accuracy of the data. Further experimentation will be required before the effect of radiation on the electrical properties of insulators can be properly evaluated.

b. Radiation Swelling

Studies of radiation swelling in insulators have all been made at low fluences ($< 10^{22}$ n/cm^2). Even at these low fluences, volume changes of several percent have been observed. The volume changes are usually anisotropic, except in certain cubic insulators such as MgO.[43,45] The mechanisms

Table E-2. Representative Values of the Bulk Properties of Ceramic Materials at ~500°C[43,44,52]

Material	Density (g/cm^3)	Melting Point (°C)	Electrical Conductivity (Ω^{-1}-cm^{-1})	Young's Modulus (× 10^6 psi)	Thermal Conductivity (cal/s-cm-°K)	Thermal Expansion (× 10^{-6}/°C)	Specific Heat (cal/g-°C)	Bend Strength (× 10^3 psi)
Al_2O_3	3.9	2050	10^{-9}	55	0.026	7.9	0.27	55
BeO	3.0	2550	10^{-8}	50	0.185	10.3	0.35	35
MgO	3.3	2800	10^{-9}	45	0.033	11.6	0.29	30
Y_2O_3	5.0	2410	10^{-9}	17	0.0054	7.5	0.13	57
CrO_3	3.1	2265	10^{-2}			7.0	0.19	
BN	2.2	2400 (SUB)	10^{-10}	7	0.069	3-8	0.54	10
AlN	2.6	2500 (SUB)	10^{-9}	50	0.057	4.8	0.27	35
Si_3N_4	3.0	1900 (SUB)	10^{-9}	20	0.020	3-4	0.25	10-100

for radiation swelling in insulators are significantly different from those of metals. Volume changes can be caused by lattice parameter changes produced by lattice defects, by defect agglomeration and dislocation loop formation, by crack formation, and by gas bubble formation.[43,45] Void formation may occur in these materials,[46] but voids have not been identified as major contributors to swelling as they have in metals. As with other properties, radiation swelling is influenced by the fabrication process and amount of pre-existing porosity in the material. The effect of impurities on radiation swelling has not been systematically investigated; however, a small concentration of lithium has been shown to reduce the radiation damage observed in MgO.[47]

c. Mechanical Properties

The brittle nature of ceramics determines to a large extent their response to an applied stress. At low to moderate temperatures, very little plastic deformation occurs, and a crack, once initiated, will propagate rapidly through the material. Generally, the limiting mechanical property is the low tensile strength. It is usually specified in a statistical manner since repetitive tensile tests under presumably similar experimental conditions do not yield similar results. The scatter in test results is due to the dispersion of flaws, e.g., surface scratches on the specimens. When a sufficient stress is applied, one or more of these flaws will grow into a crack. Fracture is likely because there is no plastic deformation to blunt the crack tip.[44] Porosity and grain size, which can be treated as flaws, can influence the strength of insulators.[48] A large porosity can also alter the elastic moduli of ceramics.[49] These materials typically show some plasticity at elevated temperatures (> 1000°C), and a few insulators show increased strength at temperatures where plastic deformation occurs.[44] Representative mechanical properties of candidate ceramic materials are given in Table E-2.

Radiation can, at low doses, increase the rupture stress of ceramics by reducing the residual strain caused by anisotropic thermal expansion during fabrication or by impeding dislocation movement. Radiation can also degrade the mechanical properties of insulators by introducing defects in the lattice that can act as flaws for crack initiation. A large increase in the number of flaws will increase the statistical probability of fracture under an applied

stress. Microcracking that results from radiation swelling leads to a marked reduction in the modulus of rupture. The degree of microcracking with radiation depends on temperature, grain size, fabrication method, and the amount of anisotropy in radiation swelling.[45] The onset of significant microcracking will generally set the upper limit to the mechanical lifetime of an insulator in a radiation environment.

d. Physical Properties

Thermal expansion and thermal conductivity are generally less in insulators than in metals. One notable exception to this rule is BeO which has a thermal conductivity greater than that of many metals. A comparison of the thermophysical properties of insulators is given in Table E-2. Most of these properties, specifically thermal expansion and specific heat, are not expected to be effected by porosity,[50,51] however, thermal conductivity will decrease significantly with an increase in the amount of porosity.[50] Neutron irradiation also reduces the thermal conductivities of ceramics. The effect of radiation is greater at lower irradiation temperatures.[43] At the low fluences used in experiments ($< 10^{22}$ n/cm^2), the thermal conductivity decreases from 25 to 50%. The effect of high neutron fluences on the thermophysical properties has not been investigated.

3. Low-Z Liner Materials

The use of low-Z materials in the form of a thin coating on the interior of the first wall has been proposed for plasma impurity control in EPR.[1] Candidate materials for the first wall coatings include Be, B_4C, BeO, BeC, SiC, BN, C, and B. Surface radiation properties of these materials and some technological considerations relating to the coating concept are discussed in Appendix B. Reference 43 gives a good review of the state of coating technology and Reference 44 is a recent review of low-Z ceramic materials for fusion reactor applications. Representative values of the physical properties of the candidate low-Z materials are given in Table E-3. The physical properties of these materials as coatings will depend to a large extent on the fabrication process and the final microstructure of the coatings. The microstructures typical of plasma spray coatings differ substantially from those of monolithic cast or sintered material. Therefore, property values given in the table should be used only as a general

Table E-3. Representative Values of Bulk Properties of Low-Z Materials at 500°C[2]

Material	Density (g/cm^3)	Melting Point (°C)	Thermal Conductivity (cal/s-cm-°K)	Thermal Expansion ($\times 10^{-6}$/°C)	Specific Heat (cal/g-°C)	Vapor Strength (Torr)
Be	1.86	1285	0.26	11.2	0.66	$<10^{-9}$ (est.)
B_4C	2.4	2430	0.043	6.5	0.37	
BeO	3.0	2570	0.14	8.8	0.44	$<10^{-10}$ (est.)
Be_2C	1.9	2100		9.4	0.51	$<10^{-9}$ (est.)
SiC	3.2	2830	0.175	5.5	0.28	
BN	2.25	2300	0.07	8.5	0.37	
C	1.5-2.0	3500 (SUB)	0.34	4.0	0.18	$<10^{-10}$ (est.
B	2.5	2037	0.043		0.50	$<10^{-9}$ (est.)

guideline. Thermal conductivity can be substantially affected by significant porosity or microcracking of the structure. In general, high melting point, thermal conductivity and specific heat are desirable for the coating material, and low vapor pressure and low thermal-expansion coefficients are regarded as beneficial.

4. Blanket and Shield Materials

The materials in the blanket and shield have been chosen primarily because of their neutronic properties. The bulk properties of these materials, with the exception of stainless steel, are discussed below. Since the materials that are likely to be the most seriously affected by the radiation environment are boron carbide and graphite, their properties are explored in greater detail. Since both of these materials have been used extensively in existing fission reactors, a considerable amount of information on radiation effects is available.

a. Boron Carbide

Boron carbide is a brittle material with a high melting point. Like other refractory materials, the bulk properties are sensitive to the method of fabrication and the degree of porosity. Typical values for the bulk properties are shown in Table E-4. The thermal conductivity and the elastic moduli will decrease with increasing porosity,[49,53] however, the effects of fabrication variables on the mechanical properties are not quantitatively defined.

Much of the boron carbide radiation damage is caused by the formation of large amounts of helium produced by (n, α) reactions with ^{10}B. The insoluble gas forms into bubbles with high internal pressures, which produce swelling, internal cracking, and a loss of strength. The effect of radiation can be divided into three temperature regimes. At irradiation temperatures less than 500°C, plate-like defects containing helium form, but no bubble growth occurs. At temperatures between 500 and 1000°C, cavities form and collect helium to high internal pressures. Denuding of cavities near grain boundaries is evident. At temperatures greater than 1000°C, large bubbles will form and result in increased swelling. The denuded zones will also increase in size at the higher temperatures.[53] In samples irradiated at

Table E-4. Representative Values of the Bulk Properties of Blanket and Shield Materials[44,56,67,68]

Material	Density (g/cm^3)	Melting Point (°C)	Electrical Conductivity (Ω^{-1}-cm^{-1})	Young's Modulus ($\times 10^{-6}$ psi)	Thermal Conductivity (cal/s-cm-°K)	Thermal Expansion ($\times 10^{-6}$/°C)	Specific Heat (cal/g-°C)	Tensile Strength ($\times 10^3$ psi)
B_4C (500°C)	2.4	2430	—	58	0.043	6.5	0.37	22
Graphite (23°C)	1.5-2.0	3500 (SUB)	7×10^2	5	0.34	4.0	0.18	12
Lead Mortar (23°C)	2.4	—	—	6.9	0.0081	3.5	0.297	0.40
Al (23°C)	2.7	660	4×10^5	10	0.55	24	0.215	10

650 to 730°C, the platelets were accompanied by large strain fields. These strains were eliminated by annealing at or above 1450°C.[53] The high pressure helium bubbles can cause fracture in B_4C. Both powder and bulk B_4C have been observed to break up after neutron irradiation.[53,54] At 430 and 700°C after a 3% burnup of ^{10}B, 98% dense pellets showed extensive transgranular fragmentation. Less cracking was observed in 90% dense pellets under the same conditions.[53] Neutron irradiation also decreases the thermal conductivity of B_4C.[55] Samples of 91% and 77% theoretical density were irradiated at 300°C to a fluence of 3.3×10^{19} n/cm^2. Little change in the thermal conductivity of the 91% dense material was observed, however, a factor of five decrease in the thermal conductivity of the 77% dense samples occurred. Annealing at 1000°C returned the thermal conductivity to the unirradiated value. Reduced effects of helium are expected with material depleted in ^{10}B.

b. Graphite

Graphite is unique among materials in that it can be manufactured in many forms, and its bulk properties can be varied over a wide range. Graphite is available as whiskers, fiber, cloth, foil, and coatings, as well as in bulk form. It has a hexagonal structure with an atomic spacing of 1.4 Å in the a direction and with an atomic spacing of 3.3 Å in the c direction. In crystalline form, its properties are highly anisotropic due to the variation of atomic bonding between the a and c directions.[56] This atomic arrangement leads to an anisotropy of two orders of magnitude in measured values of the thermal conductivity and thermal expansion. The various forms of graphite are usually described in terms of their anisotropy, density, and crystalline size distribution.

The mechanical properties of graphite show a brittle behavior at low temperatures, but plasticity and creep occur at elevated temperatures, and the strength increases at elevated temperatures as plasticity increases.[57] The various types of graphite show a wide range of strengths with pyrolytic carbon being significantly stronger than commercial pitch-coke graphites. Representative values of the properties of graphite are given in Table E-3.

Radiation damage in graphite is fundamentally different from that observed in metals. Transmission electron microscopy has revealed that visible

radiation damage occurs in the form of dislocation loops.[58] At irradiation temperatures below 650°C, the loops are all interstitial in character, and above 650°C, small vacancy loops begin to form in the immediate vicinity of the interstitial loops. It is believed that interstitial atoms are produced randomly by radiation and diffuse easily along the basil plane where they form small groups of atoms. These small groups, moving slowly, amalgomate to form stable loop nuclei. Vacancies are assumed to be stationary at lower temperatures and only begin to move above 650°C.

The volume changes of graphite with neutron irradiation are well documented because of its use as a neutron moderator. Although the reaction of graphites to radiation varies over a large range, several trends emerge. Elevated temperature irradiation first induces an initial volume contraction followed by a turnaround and rapid expansion.[59] Graphite will typically densify 5-10%, return to 0% volume change after being irradiated to $\sim 10^{22}$ n/cm^2 (E > 0.18 MeV), and swell without limit at higher fluences.[60] The densification rate is greatest in the range from 800-1200°C, and low density graphites (< 1.6 g/cm^3) densify at a faster rate than high density material. Measurements of crystallite dimension changes show that shrinkage occurs in the basal plane and expansion occurs along the c direction.[59] Many bulk graphites show large anisotropic swelling. Certain forms of graphite have a greater resistance to dimensional changes than others. Generally, the strongest and most isotropic materials show the best dimensional stability.[61,62]

Radiation can promote creep in graphite.[63] At 550°C the observed creep is approximately linear with fluence and occurs at approximately constant volume. Approximately 2% creep strain is observed in bulk graphite after irradiation at 550°C to a fluence of $\sim 10^{22}$ n/cm^2. Graphite coatings also show high creep strains.[64] Coatings irradiated between 750-1000°C exhibited creep strains as high as 5%.

Other properties that can be effected by radiation include thermal expansion which decreases with irradiation at elevated temperatures,[62] Young's modulus, which increases with irradiation,[62,65] fracture stress, which generally increases with irradiation,[65] and thermal conductivity, which decreases with irradiation.[66] Since the available data on these properties are limited to fluence levels below 10^{22} n/cm^2 i.e., below the

onset of rapid radiation swelling, their behavior at high damage levels cannot be reliably assessed.

c. Lead Mortar and Aluminum

Lead mortar and aluminum, used in the outer shield, will not be subjected to high neutron fluences or elevated temperatures, and therefore their bulk properties are not expected to change with time. Property values for these materials are included in Table E-4.

---

1. W. M. Stacey, Jr., et al, "Tomamak Experimental Power Reactor Studies," ANL/CTR-75-2, Argonne National Laboratory (1975).

2. Y. S. Touloukian, ed., Thermophysical Properties of High Temperature Solid Materials, The MacMillian Company, New York, (1967)

3. Nuclear Systems Materials Handbook, Vol. 1, Design Data.

4. G. L. Kulcinski, R. G. Brown, R. G. Lott, and P. A. Sang, "Radiation Damage Limitations in the Design of the Wisconsin Tokamak Fusion Reactor," Nucl. Tech. 22, 20 (1974).

5. E. E. Bloom and F. W. Wiffen, "The Effects of Large Concentrations of Helium on the Mechanical Properties of Neutron-Irradiated Stainless Steel," J. Nucl. Mater. 58, 171 (1975).

6. D. Kramer, H. R. Brager, C. C. Rhodes, and A. G. Pard, "Helium Embrittlement in Type 304 Stainless Steel," J. Nucl. Mater. 25, 121 (1968).

7. E. E. Bloom, "Correlation of Structure and Ductility of Irradiated Stainless Steel, Irradiation Embrittlement and Creep in Fuel Cladding and Core Components, Brit. Nucl. Energy Soc. 93, (1972).

8. K. R. Garr, C. G. Rhodes, and D. Kramer, "Effects of Microstructure on Swelling and Tensile Properties of Neutron Irradiated Type 316 and 405 Stainless Steels," Effects of Radiation on Substructure and Mechanical Properties of Metals and Alloys, ASTM-STP 529, 109 (1973).

9. J. M. Steichen, "Effect of Irradiation on the Strain Rate Dependence of Type 304 Stainless Steel Mechanical Properties," Nucl. Tech., 16, 308 (1972).

10. D. Fahr, E. E. Bloom, and J. O. Steigler, "Post Irradiation Tensile Properties of Annealed and Cold-Worked Type 316 Stainless Steel," Irradiation Embrittlement and Creep in Fuel Cladding and Core Components, Brit. Nucl. Energy Soc. 167 (1972).

11. R. L. Fish, A. J. Lovell, H. R. Brager, J. J. Holmes, "Tensile and Creep Behavior of Cold-Worked 316 Stainless Steel After EBR-II Irradiation," Irradiation Embrittlement and Creep in Fuel Cladding and Core Components," Brit. Nuc. Energy Soc., 187, (1972).

12. P. Soo and J. McAndrew, Type 304 and Type 316 Stainless Steel Data for High Temperature Design, WARD-3045T2C-3, (1972).

13. R. L. Fish, G. W. Hunter, J. D. Watrous, and J. J. Holmes, "Test Temperature and Notch Effects on the Tensile Behavior of Highly Irradiated EBR-II Duct Thimble Material," HEDL-TME 75-23-UC-79b, p HEDL-18, (1975)

14. J. J. Holmes, A. J. Lovell, R. L. Fish, "Ductility of Irradiated Stainless Steel," Effects of Radiation on Substructure and Mechanical Properties of Metals and Alloys, ASTM-STP-529, 383 (1973).

15. P. Greenfield, Creep of Metals at High Temperatures, Mills and Boon, Ltd., London, (1972)

16. N. K. Shamardin, S. N. Votinov, and V. I. Prochorov, "Effects of Irradiation on the Different Stages of Creep," Irradiation Embrittlement and Creep in Fuel Cladding and Core Components, Brit. Nucl. Energy Soc. 117 (1972).

17. E. R. Gilbert, D. G. Kaulitz, J. J. Holmes, and T. T. Claudson, "Fast Reactor Induced Creep in 20% Cold-Worked 316 Stainless Steel," Irradiation Embrittlement and Creep in Fuel Cladding and Core Components, Brit. Nucl. Energy Soc., 239 (1972).

18. E. E. Bloom and J. O. Stiegler, "Effects of Irradiation on the Microstructure and Creep-rupture Properties of Type 316 Stainless Steel," Effects of Radiation on Substructure and Mechanical Properties of Metals and Alloys, ASTM-STP-529, 360 (1973).

19. W. N. McElroy, R. E. Dahl Jr., and E. R. Gilbert, "Neutron Energy-Dependent Damage Function for Analysis of Austenitic Steel Creep Data," *Nucl. Eng. Des.*, 14, 319 (1970).

20. A. J. Lovell, "Post Irradiation Rupture Life of Annealed 316 Stainless Steel," HEDL-TME 72-21, CU-79b, (1972).

21. A. D. Tetelman and A. J. McEvily, Jr. Fracture of Structural Materials, John Wiley and Sons, Inc., New York, NY 377 (1967).

22. R. W. Weeks, D. R. Diercks, and C. F. Cheng, "ANL Low-Cycle Fatigue Studies Program, Results, and Analysis," ANL-8009, Argonne National Lab. (1973).

23. J. B. Conway, R. H. Stentz, and J. T. Berling, "Fatigue, Tensile, and Relaxation Behavior of Stainless Steels," Technical Information Center, Office of Information Services, USAEC TID-26135.

24. C. R. Brinkman, G. E. Korth, and R. R. Hobbins, "Estimates of Creep-Fatigue Interaction in Irradiated and Unirradiated Austenitic Stainless Steels," *Nucl. Tech.*, 16, 297 (1972).

25. L. Smith, K. Natesan, T. F. Kassner, and G. J. Zeman, "Effects of Sodium on the Low Cycle Fatigue Behavior of Austenitic Stainless Steel," ASME Symp. on Structural Materials for Service at Elevated Temperatures in Nuclear Power Generation, MPC-1, 290 (1975).

26. C. R. Brinkman, G. E. Korth, and J. M. Beeston, "Influence of Irradiation on the Creep-Fatigue Behavior of Several Austenitic Stainless Steels and Incoloy 800 at 700°C," Effects of Radiation on Substructure and Mechanical Properties of Metals and Alloys, ASTM-STP-529, 473 (1973).

27. W. G. Johnston, T. Lauritzen, J. H. Rosolowski, A. M. Turkalo, "The Effect of Metallurgical Variables on Void Swelling," G. E. Information Series, 76CR0019, (1976)

28. F. A. Garner, G. L. Guthrie, and T. K. Bierlein, "Evaluation of 20% Cold-Worked Swelling Correlation," R. A. Garner, T. K. Bierlein, "Development of Solution Annealed 316 Swelling Correlation," Semi-Annual Progress Report, Irradiation Effects on Reactor Structural Materials, HEDL-TME-75-23, UC-79b, HEDL-95 to 114, (1975).

29. F. W. Wiffen, E. E. Bloom, "Effect of High Helium Content on Stainless-Steel Swelling," *Nucl. Tech.* 25, 113, (1975).

30. Joining of Stainless Steels, American Society for Metals, Metals Park, Ohio, (1967).

31. A. L. Ward, "Thermal and Irradiation Effects on the Tensile and Creep-Rupture Properties of Weld-Deposited Type 316 Stainless Steel," *Nucl. Tech.* 24, 201 (1974).

32. T. R. Gurney, Fatigue of Welded Structures, Cambridge University Press, Cambridge, (1968).

33. S. H. Bush, "Structural Materials for Nuclear Power Plants," *ASTM J. of Testing and Evaluation*, 2, 435 (1974).

34. J. T. Stanley and K. R. Garr, "Ferrite Formation in Neutron Irradiated Type 316 Stainless Steel," *Met. Trans.* 6A, 531 (1975).

35. J. H. Bechtold, E. T. Wessel, and L. L. France, "Mechanical Behavior of Refractory Metals," Refractory Metals and Alloys, M. Semchyshen, J. J. Harwood, eds., ASME Metallurgical Society Conferences, Vol. 11, Interscience Publishers, New York, N. Y., 25, (1961).

36. F. W. Wiffen, "The Effect of Alloying and Purity on the Formation and Ordering of Voids in BCC Metals," Radiation Induced Voids in BCC Metals, Proc. of Int. Conf., 386, (1971).

37. A. T. Santhanum, A. Taylor and S. D. Harkness, "Changed Particle Simulation Studies of Vanadium and Vanadium Alloys," Defects and Defect Clusters in BCC Metals and Their Alloys, R. J. Arsenault, ed., 302 (1973).

38. B. A. Loomis, A. Taylor, and S. B. Gerber, "Void Swelling of Nb and Nb-1% Zr by $^{58}Ni^{+}$ Bombardment," *J. Nucl. Mater.*, 56, 25 (1975).

39. J. Moteff, "Irradiation Effects on the Mechanical Properties of BCC Metals," Fusion First Wall Materials, WASH-1206, 46 (1971).

40. T. H. Webster, B. L. Eyre and E. A. Terry, "The Effect of Fast Neutron Irradiation on the Structure and Tensile Properties of Molybdenum and TZM," in Irradiation Embrittlement and Creep in Fuel Cladding and Core Components, British Nuc. Energy Soc., 61 (1972).

41. D. Kramer, "Helium Embrittlement" Fusion Reactor First Wall Materials, WASH-1206, 50 (1971).

42. D. L. Smith and K. Natesan, "Influence of Nonmetallic Impurity Elements on the Compatibility of Liquid Lithium with Potential CTR Containment Materials," *Nucl. Tech.* 22, 392 (1974).

43. A. A. Bauer and J. Bates, "An Evaluation of Electrical Insulators for Fusion Reactors," BMI-1930, Battelle Columbus Laboratory (1974).

44. L H. Rovner and G. R. Hopkins, "Ceramic Materials for Fusion," *Nucl. Tech.* 29, 274 (1976).

45. R. S. Wilkes, "Neutron-Induced Damage in BeO, Al_2O_3, and MgO - A Review," *J. Nucl. Mater.*, 26, 137 (1968).

46. R. W. Clinard, Jr., J. M. Bunch, and W. A. Ranken, "Neutron Irradiation Damage in Al_2O_3 and Y_2O_3," LA-UR-75-1840, Los Alamos Sci. Lab. (1975).

47. Y. Chen and M. M. Abraham, "Evidence for Suppression of Radiation Damage in Li-Doped MgO," *J. Am. Cer. Soc.* 59, 101, (1976).

48. A. M. Alper, ed., High Temperature Oxides, Academic Press, New York, 41, (1970).

49. J. K. MacKenzie, "The Elastic-Constants of a Solid Containing Spherical Holes," *Proc. Phys. Soc.*, (London) 63B, 2 (1950).

50. F. Euler, "Simple Geometric-Model for the Effect of Porosity on Material Constants," *J. App. Phys.* 28, 1342 (1957).

51. A. J. Walter and A. R. Trowell, "The Thermal Conductivity of Porous Copper," *J. Mater. Sci.* 6, 1044, (1971).

52. Engineering Properties of Selected Ceramic Materials, compiled by Battelle Memorial Institute, Columbus Laboratories, American Ceramic Society, Columbus, Ohio, (1966).

53. G. L. Copeland, R. G. Donnelly, and W. R. Martin, "Irradiation Behavior of Boron Carbide," *Nucl. Tech.* 16, 226 (1972).

54. A. Jostons, C. K. H. DuBose, G. L. Copeland, and J. O. Stiegler, "Defect Structure of Neutron Irradiation Boron Carbide," *J. Nucl. Mater.* 49. 136 (1973/74).

55. T. Iseli, M. Ito, H. Suzuki, "Effect of Neutron Irradition on the Thermal Conductivity, Electrical Resistivity, and Thermal Expansion of Boron Carbide," *J. Nucl. Sci. Tech.* 10, 632 (1970).

56. R. T. Dolloff and J. T. Meers, "Status and Future of Graphite and Refractory Compounds," High Temperature Materials, II, Interscience Publishers. N.Y.. 387 (1963).

57. W. V. Kotlinsky and H. E. Martens, "Tensile Properities of Pyrolytic Graphite to 5000°F," High Temperature Materials, II, Interscience Publishers, N.Y. 403 (1963).

58. P. A. Thrower, "The Study of Defects in Graphite by Transmission Microscopy," Chemistry and Physics of Carbon, Vol. 5, P. L. Walder, Jr., ed., Marcel Decker, Inc., N. Y., 217, (1969).

59. P. A. Thrower, "The Structure of Reactor Graphites and Its Relation to High Temperature Irradiation Dimensional Stability." *Carbon* 9, 265 (1971).

60. G. B. Engle, "Irradiation Behavior of Nuclear Graphites at Elevated Temperatures," *Carbon* 9, 539 (1971).

61. G. B. Engle, "Relationship Between Crystal Structure and Properties and Irradiation Behavior of Reactor Graphites," *Carbon* 12, 291 (1974).

62. A. L. Pitner, "Irradiation Behavior of Poco Graphites," *Carbon*, 9, 637 (1971).

63. W. J. Gray, "Constant Stress Irradiation-Induced Compressive Creep of Graphite at High Fluence," *Carbon*, 11, 383 (1973).

64. J. L. Kaae and J. C. Bokros, "Irradiation-Induced Dimensional Changes and Creep of Isotropic Carbon," *Carbon*, 9, 111 (1971).

65. J. L. Kaae, "Effect of Irradiation on the Mechanical Properties of Isotropic Pyrolytic Carbons," *J. Nucl. Mater.*, 46, 121 (1973).

66. M. R. Everette, L. W. Graham, R. Manzel and R. Blackstone, "Dimensional and Physical Property Changes of High Temperature-Reactor Graphites, Pyrocarbons and Fuel Bodies Irradiated at Temperatures in the Range 600-1200°C," *Carbon* 9, 417 (1971).

67. Metallic Mortars, Chemtree Corp., Document 13.8 Ch.

68. Metals Handbook, Vol. 1, Metals Handbook Comittee, American Society for Metals, Metals Park, Ohio (1961).

APPENDIX F

MAGNETICS

1. Normal Metal Flux Shield for Toroidal Field Coils

The TF coils can be shielded from the time-varying field of the poloidal field coils and plasma if they are enclosed by a good conductor. Eddy currents induced in the conducting shield will produce a magnetic flux which opposes the change in flux inside the shield. For a change of flux parallel to the TF coil, we can treat the shield as a long solenoid, with uniform induced flux within.

Consider the shield as an ac circuit driven by an emf $\dot{\phi}_{App}$ from the changing applied flux. A length ℓ of the shield has resistance R and inductance L given approximately by

$$R\ell = \rho p/X \tag{F-1}$$

$$L\ell = \gamma \mu_o A \tag{F-2}$$

where p and A are respectively the cross sectional perimeter and enclosed area of the shield, ρ is the electrical resistivity, $\mu_o = 4\pi \times 10^{-7}$ H/m. The current depth X is determined by the smallest of three lengths: the shield thickness t, the skin depth δ, and the so-called mean hydraulic depth A/p. The numerical factor γ is nearly unity in the interesting cases $p\delta \ll A$ or $pt \ll A$.

For a sinusoidal time variation of the applied flux, we can write

$$\phi_{App} = B_o A \exp(j\omega t)$$

$$\dot{\phi}_{App} = j\omega B_o A \exp(j\omega t) \quad .$$

The current will also be sinusoidal and obey

$$\dot{I} = j\omega I \quad .$$

The circuit equation

$$\dot{\phi}_{App} = L\dot{I} + RI$$

or

$$\dot{\phi}_{App} = L\ell \frac{\dot{I}}{\ell} + R\ell \frac{I}{\ell}$$

has a solution

$$\frac{I}{\ell} = \frac{j\omega B_o A \exp(j\omega t)}{j\omega L\ell + R\ell} \quad . \tag{F-3}$$

The average power dissipated per unit length is

$$\frac{\overline{P}}{\ell} = 1/2 \left|\frac{I}{\ell}\right|^2 R\ell = \frac{R\ell\omega^2 B_o^2 A^2}{2(\omega^2 L^2 \ell^2 + R^2 \ell^2)} \quad . \tag{F-4}$$

When Equation (F-5) and (F-6) are substituted into Equation (F-8), we obtain

$$\frac{\overline{P}}{\ell} = \frac{X\ \omega^2 B_o^2 A^2}{2\ \rho p\ [1 + (\gamma\omega\mu_o\ AX/\rho p)^2]} \quad . \tag{F-5}$$

In the limits of low conductivity and high conductivity, Equations (F-3) and (F-5) simplify to give the following:

Low Conductivity Limit: $R >> \omega L$

$$I/\ell = j\omega B_o\ AX \exp(j\omega t)/\rho p \tag{F-6}$$

$$\overline{P}/\ell = X\omega^2 B_o^2 A^2/2\rho p \tag{F-7}$$

High Conductivity Limit: $R << \omega L$

$$I/\ell = B_o \exp(j\omega t)/\gamma\mu_o \tag{F-8}$$

$$\overline{P}/\ell = \rho p B_o^2/2\ X\ \gamma^2\mu_o^2 \quad . \tag{F-9}$$

Equations (F-6 to F-9) always give an over-estimate of the current and power, but unless $R \sim \omega L$ one or the other limit gives results close to the exact expression.

Equation (F-9) can be used in the low conductivity limit, if we replace X by

$$X' = p^2\delta^4/4A^2X \quad . \tag{F-10}$$

If the time-varying field is perpendicular to the axis of the shield, the general eddy-current problem does not have an analytic solution. For a circular cross section shield of radius a in the high conductivity limit with $\gamma = 1$, the power is given by

$$\begin{aligned} P_\perp/\ell &= 4\ \pi\ aB_o^2\rho/2\ X\mu_o \\ &= \rho p B_o^2/X\mu_o^2 \\ &= 2\ (\overline{P}_{\parallel}/\ell) \quad . \end{aligned} \tag{F-11}$$

Although Equation (F-11) is derived for a circular shield, it is expected to hold for any convex shield with aspect ratio not much different from unity.

From Equation (F-9) and (F-11) we can obtain the power lost in the shield of a TF coil in a sinusoidally-varying flux, if the high-conductivity limit applies

$$\overline{P} = (\rho p/X\mu_o^2) \oint (B_{o\perp}^2 + 1/2\ B_{o\parallel}^2)\ d\ell\ . \qquad \text{(F-12)}$$

If the time variation is not sinusoidal, but given by the Fourier series

$$B(t) = B_o \sum_{n=0}^{\infty} a_n \cos 2\pi nt/\tau\ ,$$

with τ the period, and if $X = \delta_n = (2\rho/\mu_o\omega_n)^{1/2} = \sqrt{n}\ \delta_1$, then Equation (F-12) becomes

$$\overline{P} = (\rho p/\delta_1\mu_o^2) \oint (B_{o\perp}^2 + 1/2\ B_{o\parallel}^2)\ d\ell \sum_{n=1}^{\infty} \sqrt{n}\ a_n^2\ . \qquad \text{(F-13)}$$

Equation (F-13) is used in Chapter IV to calculate the power lost in a normal metal shield.

2. Eddy Current Effects in the Subdivided Blanket and Shield

Although placing the equilibrium field coils outside the blanket and shield is helpful from the points of view of maintenance and protection from radiation damage, the time-varying equilibrium field must penetrate the blanket and shield if it is to act on the plasma. The flux from the EF coils will induce eddy currents in the metal blanket and shield, which in turn will serve to exclude the flux, or at least retard its penetration. The eddy currents and their effects can be lessened by subdividing the blanket and shield. In the following we develop equations to calculate eddy current effects in the blanket and shield with various degrees of subdivision.

a. Unsegmented Blanket and Shield

If the construction of the blanket and shield prevents radial currents, it can be approximated by a toroidal shell, with toroidal and poloidal currents only. Furthermore, unless the aspect ratio is too low, the toroidal shell can in turn be replaced by a cylindrical shell, with the toroidal and poloidal currents replaced by axial and azimuthal currents.

If the equilibrium field B_o is vertical and perpendicular to the axis of the cylindrical blanket and shield, then when the equilibrium field changes, there will be, in the low conductivity limit, an axial current with density

$$J = - \sigma a \sin \theta \dot{B}_o , \qquad \text{(F-14)}$$

where σ is the electrical conductivity of the blanket and shield material, a is the radius of the cylindrical shell, the dot designates the time derivative, and θ is the azimuthal angle. This current will produce a field in the plasma

$$B_{in} = - \frac{\mu_o}{2} h a \sigma \dot{B}_o , \qquad \text{(F-15)}$$

where h is the thickness of the cylindrical shell.

The results of the calculations are given in Chapter IV, but it is appropriate to state here that the induced field at the plasma as calculated by Equation (F-15) is more than the applied field. This non-physical result would not actually occur; the induced fields would induce additional currents which in turn would produce fields, limiting the net induced field to a value sufficient to cancel the applied field. Two conclusions follow about what will happen if the blanket and shield are unbroken.

(1) The induced field is large (comparable to the applied field).

(2) Fields induced by the induced field are significant.

Consequently, it appears that the blanket and shield must be divided into pieces small enough so that:

(1) The induced field at the plasma is negligible.

(2) Fields induced by the induced field are negligible.

b. Blanket and Shield Segmented Toroidally

If the cylinder is broken into segments of length 2ℓ which is small compared with the diameter, the current density has components

$$J_\theta = \sigma y \cos\theta \dot{B}_o \qquad \text{(F-16)}$$

$$J_y = \frac{-\sigma}{2a} (\ell^2 - y^2) \sin \theta \dot{B}_o \qquad \text{(F-17)}$$

where y is measured axially from the center of the segment. The field on axis a distance y_o along the axis is given by

$$B_{in} = \frac{\mu_o \sigma h a}{8} \dot{B}_o \left[\frac{y\,(a^2 + y_o^2 - c^2)}{a^2 \sqrt{a^2 + y^2}} - \ln\left(\sqrt{a^2 + y^2} + y\right) \right]_{y = -c - y_o}^{y = c - y_o} \qquad \text{(F-18)}$$

For 16 segments and an applied field of 4.2 kG, the induced field at the plasma is calculated by Equation (F-18) to be 390 G; for 32 segments, it is reduced to 97 G, or 2.3 percent of the applied field. Plasma physics considerations suggest that even this value is uncomfortably large; it seems safest to try to further reduce the eddy currents. To do so requires either segmenting even more or making the blanket and shield of blocks weighing a few tons each.

c. Subdivided Blanket and Shield Represented by a Brick Model

The induced magnetic field due to eddy currents is given by the Biot-Savart Law:

$$\vec{B}_{in} = \frac{\mu_o}{4\pi} \int \frac{\vec{J} \times \vec{r}}{r^3}\, dV \qquad \text{(F-19)}$$

where B_{in} is the induced field, J is the eddy current density, and r is the displacement from the source point (x, y, z) to the field point (x_o, y_o, z_o). The eddy current density is determined by the conditions:

$$\vec{J} \cdot \vec{n} = 0 \text{ on the conductor surface} \qquad \text{(F-20)}$$

$$\text{div } \vec{J} = 0 \qquad \text{(F-21)}$$

$$\text{curl } \vec{J} = -\sigma \dot{\vec{B}} = \sigma \left(\dot{\vec{B}}_a + \dot{\vec{B}}_{in}\right) \qquad \text{(F-22)}$$

where n is a unit vector normal to the conductor surface, σ is the electrical conductivity, B_a is the applied field, and the dot designates differentiation with respect to time. Solution of Equations (F-19 to F-22) is a difficult problem, and no general algorithm for their solution exists.

Let us make sufficient assumptions that the equations have convenient analytic solutions. Limitations on the applicability of the model due to these assumptions are discussed below.

(1) The conductivity is sufficiently low that the induced field is small relative to the applied field. Thus $\dot{\vec{B}}_a + \dot{\vec{B}}_{in}$ may be replaced in Equation (F-22) by $\dot{\vec{B}}_a$.

(2) All conductors can be represented as rectangular solids aligned parallel to the coordinate axis. Let a conductor be centered at the origin and have length 2a, 2b, 2c in the x, y, z directions respectively.

(3) The field B_a is everywhere in the z direction; consequently J is everywhere parallel to the x-y plane.

(4) The field B_a varies across a rectangular conductor according to

$$B_a = B_o \left(1 - \frac{x^2 + y^2}{a^2 + b^2}\right) . \qquad \text{(F-23)}$$

Under the above assumptions, Equations (F-20 to F-22) are satisfied by a current density J with components

$$J_x = \sigma \dot{B}_o y \frac{a^2 - x^2}{a^2 + b^2} \qquad \text{(F-24)}$$

$$J_y = -\sigma \dot{B}_o x \frac{b^2 - y^2}{a^2 + b^2} . \qquad \text{(F-25)}$$

Equation (F-19) then has a z component which can be written

$$B_{in} = \frac{\sigma \dot{B}_o}{a^2 + b^2} \iiint [(y_o - y)y(a^2 - x^2) + (x_o - x)\, x\, (b^2 - y^2)]/\, r^3\, dy\, dz . \qquad \text{(F-26)}$$

Substituting:

$$u = x - x_o,\ v = y - y_o,\ w = z - z_o ,$$

and carrying out the integration, we find the following equation for the z component parallel to B_a:

$$\begin{aligned} B_{in} = -\frac{\mu_o}{4\pi} \frac{\sigma}{a^2 + b^2} \dot{B}_o \Big[& \tan^{-1} \frac{uv}{wr} \{1/2\, w^2 (x_o^2 - a^2 + y_o^2 - b^2) - w^4/6\} \\ & + \tan^{-1} \frac{uw}{vr} \{vy_o(a^2 - x_o^2) + 1/2\, v^2(a^2 - x_o^2 + y_o^2 - b^2) + v^3 y_o + 1/2\, v^4\} \\ & + \tan^{-1} \frac{vw}{ur} \{ux_o(b^2 - y_o^2) + 1/2\, u^2(b^2 - y_o^2 + x_o^2 - a^2) + u^3 x_o + 1/2\, u^4\} \\ & + \ln (r + u) \{wv(b^2 - y_o^2 - 2v^2/3) - wy_o(a^2 - x_o^2 + 3v^2/2) - 1/2\, w^3 y_o\} \\ & + \ln (r + v) \{wu(a^2 - x_o^2 - 2u^2/3) - wx_o(b^2 - y_o^2 + 3u^2/2) - 1/2\, w^3 x_o\} \\ & + \ln (r + w) \{uy_o(u^2 + x_o^2 - a^2) + vx_o(v^2 + y_o^2 - b^2) + 2x_o y_o(u^2 + v^2)\} \\ & + r \{uvw/6 + 1/2\, x_o vw + 1/2\, y_o uw + 2x_o y_o w\}\Big] \end{aligned} \qquad \text{(F-27)}$$

where σ is the electrical conductivity, $r = (u^2 + v^2 + w^2)^{1/2}$, and u, v, and w are evaluated at their upper and lower limits $\pm a - x_o$, $\pm b - y_o$, and $\pm c - z_o$ respectively.

To use the model to calculate the effects of subdividing the blanket and shield, each piece of the blanket and shield is represented by a rectangular stainless-steel brick. A FORTRAN program, BRICK, was written to establish the vertices of the bricks in one segment, to translate and rotate the bricks to represent the other segments, and to calculate the induced field at a specified point by Equation (F-27).

The torque on a horizontal block due to the toroidal field can readily be found from Equation (F-24 and F-25):

$$N = \iiint J_x y B_t dV = 16\, \hat{B}_o \sigma B_t a^3 b^3 c / 9(a^2 + b^2) \ , \qquad \text{(F-28)}$$

where N is the torque and B_t the toroidal field.

d. Limitations to the Model Due to Assumptions

Let us look at the consequences of the four assumptions listed above. For the type of application intended, subdividing the conductor to control the effects of eddy currents, assumption (1) holds by definition in that the conductor is not adequately subdivided unless the assumption holds. Depending upon the degree of subdivision required, assumption (2) may or may not hold. In some cases, a more detailed treatment may be needed for nearby conductors, and the model used for more distant conductors. There is a class of problems for which assumption (3) is good, but certainly the model would be improved by including all three components of J and B. Assumption (4) is the most questionable; if the field B_a were actually uniform and equal to B_o, then the above expression would probably underestimate B_{in}, but by less than one third.

If we relax the condition that the field must vary across a brick according to Equation (F-28), which was imposed so that the current density would obey the simple expressions Equation (F-24 and F-25) and if instead we allow fifth-power terms in the expressions for current, we get

$$J_x = \sigma \hat{B}_o y \left[a^2 - x^2 + \left\{a^2b^2 (a^2 - b^2) + (a^4 - a^2b^2 + b^4)\, x^2 + 2a^2b^2y^2 - 2\, b^2x^2y^2 - a^2x^4\right\} / \left\{a^4 + 5a^2b^2 + b^4\right\}\right] / (a^2 + b^2) \qquad \text{(F-29)}$$

$$J_y = -\sigma \dot{B}_o x \left[b^2 - y^2 + \{ a^2b^2(b^2 - a^2) + (a^4 - a^2b^2 + b^4)y^2 + 2\, a^2b^2x^2 - 2\, a^2x^2y^2 - b^2y^4 \} / \{a^4 + 5\, a^2b^2 + b^4\} \right] / (a^2 + b^2) \tag{F-30}$$

$$B_a = B_o \left[1 - \frac{a^2x^4 + 6\, x^2y^2 (a^2 + b^2) + b^2y^4}{(a^2 + b^2)\,(a^4 + 5\, a^2b^2 + b^4)} \right] \tag{F-31}$$

Equations (F-29 and F-31) obey the conditions expressed by Equations (F-19 and F-22). Moreover, Equation (F-31) approximates $B_a = B_o$ over much more of the conductor volume than Equation (F-23) does. When Equations (F-29 and F-30) are substituted into Equation (F-19) and the integration carried out, an analytical expression for B_{in} results, involving the same functions as the simpler expression in Equation (F-27). When calculations with that expression are compared with those described above, the limitations of assumption (4) can be understood.

e. Phase Delay and Time Delay

All of the induced fields considered above will lag behind the applied field, because of their $\dot{B}_o$ dependence. Thus they will contribute a phase delay and time delay to the total field B_o and B_{in}. If we take the applied field to have the time variation

$$B_o(t) = \frac{1}{2} B_{oo} - \frac{1}{2} B_{oo} \cos \pi t/\tau ,$$

then the induced field will vary with time as

$$B_{in}(t) = - B_{in\ max} \sin \pi t/\tau$$

The combined field can be written

$$B_o + B_{in} = \frac{1}{2} B_{oo} - B' \cos (\pi t/\tau - \phi)$$

with the phase delay ϕ given by

$$\phi = \tan^{-1} 2B_{in\ max}/B_{oo} \tag{F-32}$$

The phase delay ϕ can also be put in terms of a time delay t_o

$$\cos (\pi t/\tau - \phi) = \cos \pi(t - t_o)/\tau \tag{F-33}$$

with $t_o = \phi\tau/\pi$

APPENDIX G

NEUTRONICS PENETRATION ANALYSIS

In Section A of Chapter IX, the penetrations for neutral beam injection and vacuum pumping were treated for the reference design. This appendix is intended as a supplement to the penetration analysis. Results presented here represent a scoping study carried out for earlier iterations of the reference design. However, these results are of general nature and bring out many of the important aspects involved in the design of penetrations and their special shields.

1. General Considerations

The blanket/shield system in EPR, and in future tokamak fusion reactors as well, is required to accommodate a variety of penetrations including those for vacuum pumping, neutral beam and/or radio frequency (rf) heating, and experimental and maintenance access. These penetrations occupy typically 5 to 10% of the blanket/shield volume. Penetrations such as those for vacuum pumping and neutral beam heating represent large void regions (0.5 - 1 m^2 in cross-sectional area) which extend from the first wall (directly visible to the plasma neutrons), radially through the blanket/shield, and on out between the toroidal-field (TF) coils. The functional requirements of the neutral beam ducts exclude any possibility of introducing any significant bends in the duct. Sharp bends in the evacuation ducts greatly reduce the efficiency of vacuum pumping and they force the designer to increase the size of the ducts.

The need to guard against the potential problems that can be created by radiation streaming through such penetrations, or streaming assisted by the presence of these penetrations, is obvious. The blanket/shield system provides, in general, about six orders of magnitude attenuation of nuclear radiation in order to protect the TF coils and auxiliary systems located on the exterior of these coils from excessive radiation damage, nuclear heating, and induced-activation. The volume fraction of the major penetrations indicate that these penetrations would cause more than 1% of the neutrons to escape into the exterior of the primary (bulk) shield. Thus the additional special penetration shield will have to provide roughly four orders of magnitude of attenuation for neutrons streaming in the presence

of penetrations. Therefore, the special shields for penetrations represent a very significant part of the shielding system in EPR and are expected to remain equally important in future tokamak reactors. The design of a penetration shield is more difficult, however, than the design of the primary bulk shield in two respects: (1) treatment of penetrations requires three-dimensional neutronics analysis, and (2) the geometry of the reactor imposes severe restrictions on the availability of space for penetration shields, above and beyond the space restrictions on the bulk shield. Moreover, as will be shown later in this appendix, the neutral beam ducts can be shielded on the sides only. Thus, there is always a straight-through path for the neutrons, a path leading to the beam injector and on to the exterior of the reactor.

The penetrations in a tokamak reactor can be classified, in general, into two types: (1) major penetrations, and (2) normal penetrations. The major penetrations are those penetrations that are large in size and their functional requirements do not permit substantial modifications in their shape. These major penetrations include, for example, the evacuation, neutral beam, and rf ducts. On the other hand, the normal penetrations are small and are amenable to substantial shaping of their path inside the blanket/shield. Among the penetrations in this category are, for example, the coolant channels, clearances between shield blocks, and some of the small penetrations for diagnostics. This classification is of great importance with respect to the development of a strategic procedure for the design of a reactor. The effects of normal penetrations can be regarded as moderate perturbations on the performance of the system. Thus, although the impact of these normal penetrations should be anticipated qualitatively in the early stages of the design, their detailed design and analysis can be deferred until later stages of the overall reactor design process without much penalty. On the other hand, the effects of the major penetrations and their special shields on many of the reactor components is so great that these effects must be factored into the design as early as possible. By treating the major penetrations and their special shields as an integral part of the reactor system many of the trade-offs and conflicts can be resolved at early stages of the design. To do otherwise may result in a need for costly modifications in more advanced phases of the design.

2. Calculational Model

Any penetration analysis depends to a great extent on many specific details of the reactor geometry and characteristics. The preliminary reference design for EPR documented in references 1 and 2 was used for the initial parts of the penetration scoping study. This reference design has a major radius, R, of 625 cm and a circular plasma cross section with a minor radius, a, of 210 cm. There are 16 TF coils; each has a D-shaped vertical cross section with a horizontal bore of 7.7 m and a vertical bore of 11 m. A horizontal cross section of a TF coil is 0.60 m thick and 0.90 m wide. The blanket and primary shield consist of alternating zones of stainless steel (SS) and boron carbide (B_4C). A small segment of the blanket/shield at the inner side of the torus is 1.0 m thick while the rest of the blanket/shield is 1.31 m thick. In the reference design, as in any tokamak reactor, the inner segment of the blanket/shield cannot be utilized for placement of any major penetrations. These are generally accommodated on the top, bottom, and outer side of the torus. Therefore, the specific details of the inner segment of the blanket/shield will be ignored for the purpose of this work, and the blanket/shield is assumed to surround the plasma with a uniform thickness of 1.31 m. The dimensions and material disposition of the blanket/shield are shown in Table G-1. The inner radius of the first wall is 2.40 m. There are 32 vacuum ducts in the design, and each is cylindrical with an 0.85 m diameter. Two vacuum ducts are located at the top and bottom of the torus, equally spaced between each pair of the TF magnets. A cylindrical neutral beam duct with an 0.85 m diameter is located between each pair of TF magnets, centered around the midplane, and its axis is nearly tangential to the toroidal magnetic axis. In order to make the discussions of the geometric models clear in the rest of this appendix, a schematic reference of toroidal geometry is given in Figure G-1.

Most of the neutronics analyses were carried out using a three-dimensional geometric model with the continuous energy Monte Carlo Code VIM[3] and nuclear data from ENDF/B-IV.[4] Three-dimensional geometries are best treated at present with the Monte Carlo method. These calculations are inherently machine- and man-time consuming, making a thorough 3-D analysis of the full reactor geometry very costly. Therefore, a somewhat simplified 3-D geometric model, which is less costly but incorporates the basic features of the reactor

TABLE G-1 Dimensions and Material Composition of a Reference Blanket/Shield for a Scoping Study of Major Penetrations.

Zone	Outer Radius cm	Thickness cm	Material Composition
1	210	210	Plasma
2	240	30	Vacuum
3	241	1	Stainless Steel
4	256	15	Stainless Steel
5	261	5	Boron Carbide
6	276	15	Stainless Steel
7	281	5	Boron Carbide
8	291	10	Stainless Steel
9	301	10	Boron Carbide
10	311	10	Stainless Steel
11	321	10	Boron Carbide
12	331	10	Stainless Steel
13	340	9	Boron Carbide
14	351	11	Stainless Steel
15	361	10	Boron Carbide
16	371	10	Stainless Steel
17	430	59	Vacuum
18	490	60	Magnet

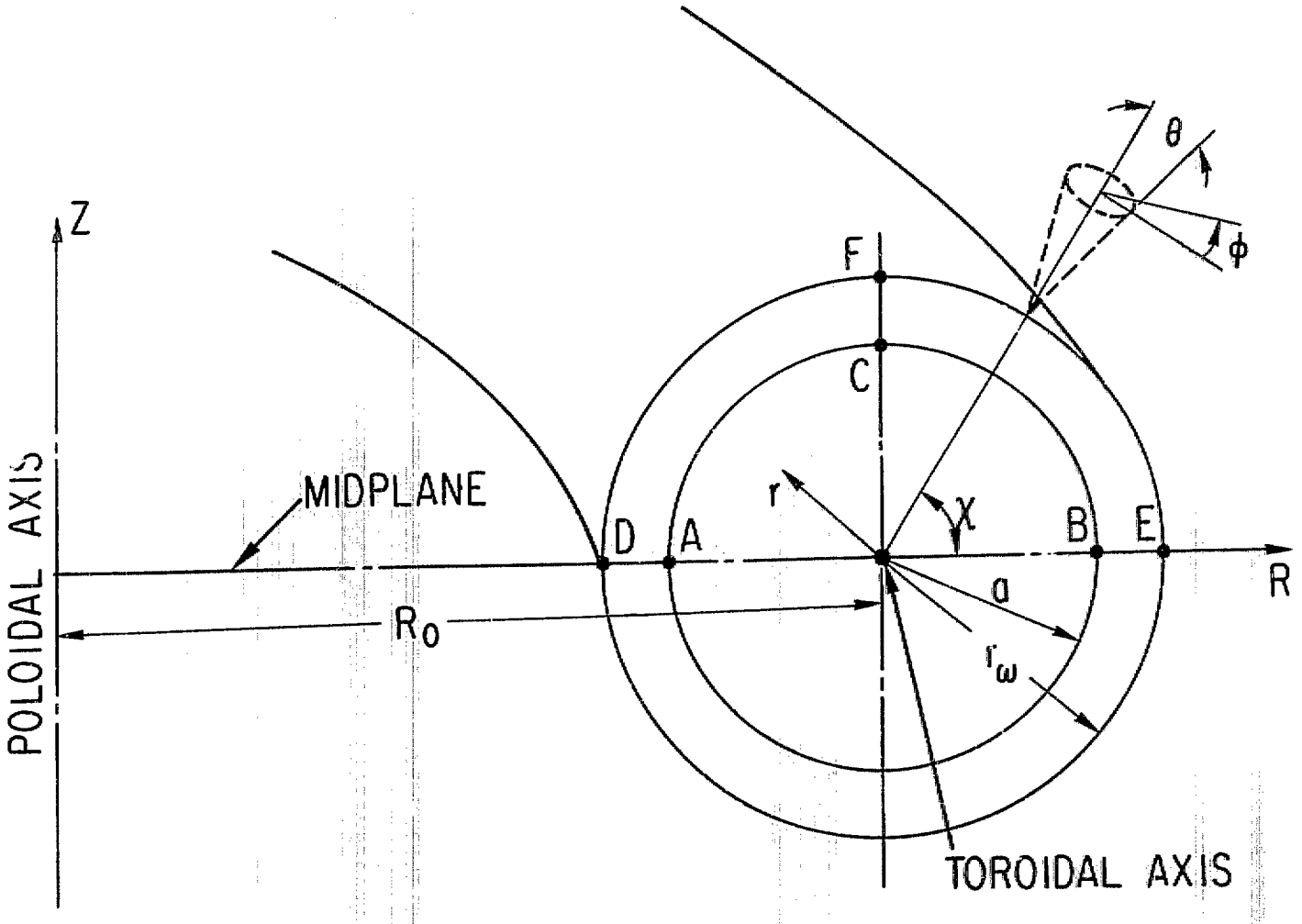

Figure G-1. A Schematic Reference of Toroidal Geometry

geometry and accounts for all first-order effects of penetrations, was developed as follows: (1) Since the torus consists of 16 segments that are essentially identical, only one segment needs to be analyzed. The segment is defined as the entire reactor region bounded by two planes which intersect at the poloidal axis (see Figure G-1) and each plane divides a TF magnet into two symmetric halves. A periodic boundary condition is applied at both planes. (2) It is assumed that the interaction of perturbations due to various types of penetrations is a second order effect and can be ignored in a scoping study on first-order effects of penetrations. Therefore, the evacuation ducts are analyzed in the absence of neutral beam ducts and vice versa. This makes it possible to identify the effects of each individual type of penetration. For any one particular type of penetration, the interface of ducts with one another is accounted for, however, by virtue of the periodic boundary conditions specified in item 1 above. (3) In order to avoid explicit toroidal calculations, the toroidal curvature is ignored, but the dimensions of the segments are adjusted to produce correct volumes, and correct spacing of regions in the vicinity of the penetrations under considerations. The effect of toroidal curvature on local fluxes is small, as shown in Chapter IX. However, the toroidal geometry causes the spacing between the TF magnets to vary from almost zero at the inside, to a fraction of a meter at the top and bottom, and a few meters on the outside. In order to account for the correct relative positions of the penetrations, penetration shields, and magnets, the spacing between the TF magnets in the neighborhood of the specific penetration under consideration is employed. Note also that the outward shift of the magnetic flux surfaces which causes an outward shift of the plasma neutron source strength will enhance radiation streaming through penetrations located at the outer side of the torus. This shift in the neutron source is not accounted for here, and a uniformly distributed neutron source in the plasma region is assumed. (4) Since the exact position of the (nearly tengential) neutral beam axis relative to the toroidal axis cannot be reproduced in the geometric model discussed above, an inclination angle θ_b is assumed. The sensitivity of the results to this angle is examined in a later section of this appendix.

Figure G-2 shows a schematic of the geometric representation for analysis of the vacuum ducts and their shields. If the toroidal magnetic axis is assumed to be a straight line, then Figure G-2 represents a cross section in the x-z plane where the z-axis is taken along the toroidal magnetic axis and the x-axis is parallel to the poloidal axis and passes through the plasma centerline. The system is symmetric around the midplane. A cross-section view in the x-y plane would show the blanket and the bulk shield as a set of concentric circles surrounding the circular plasma and scrape-off regions with one cylindrical vacuum duct at the top and another at the bottom. Figure G-3 shows a schematic of the geometric representation for the analysis of the neutral beam ducts and their shields. A set of orthogonal coordinate system (x,y,z) is also used here. The z-axis, as in Figure G-2, represents the toroidal magnetic axis, but the x-axis is in the midplane and the y axis is parallel to the poloidal axis. The neutral beam duct is 0.85 m in diameter. The axis of the beam duct is in the midplane (x-z plane) and makes an angle θ_b with the x-axis. Note that in both Figures G-2 and G-3 the minor radius, r, for a point, is simply $r = \sqrt{x^2 + y^2}$.

In Figures G-2 and G-3 some spatial zones are identified by numbers that will be useful in later discussions. Zone 1 represents the plasma region and Zone 2 for the scrape-off region. Zones 3 through 16 and 31 through 44 constitute the blanket-bulk shield. The wall of the penetration duct is represented as 1-cm thick tube of stainless steel that extends from the first wall to the exterior of the TF coils. The portion of the penetration duct inside the blanket and bulk shield is defined as Zone 21 and the corresponding portion of the duct wall is Zone 23. The part of the penetration duct outside the blanket-bulk shield is Zone 22 and the corresponding portion of the duct wall is Zone 24. The neutral beam and evacuation duct extend far beyond the TF coils in a detailed design. A neutral beam duct generally extends $\sim$ 2-5 meters beyond the TF coils and leads to the large size chamber of the beam injector. Many components are located inside the beam injector, such as the neutralizer, bending magnets, cryosorption panels, ion source and accelerator. An evacuation duct leads to a vacuum pump. An evacuation duct can be bent before it is connected to a vacuum pump, but at the expense of a reduction in the pumping efficiency. If the vertical bore of the magnet is large enough, the vacuum duct can be bent external to the bulk shield and

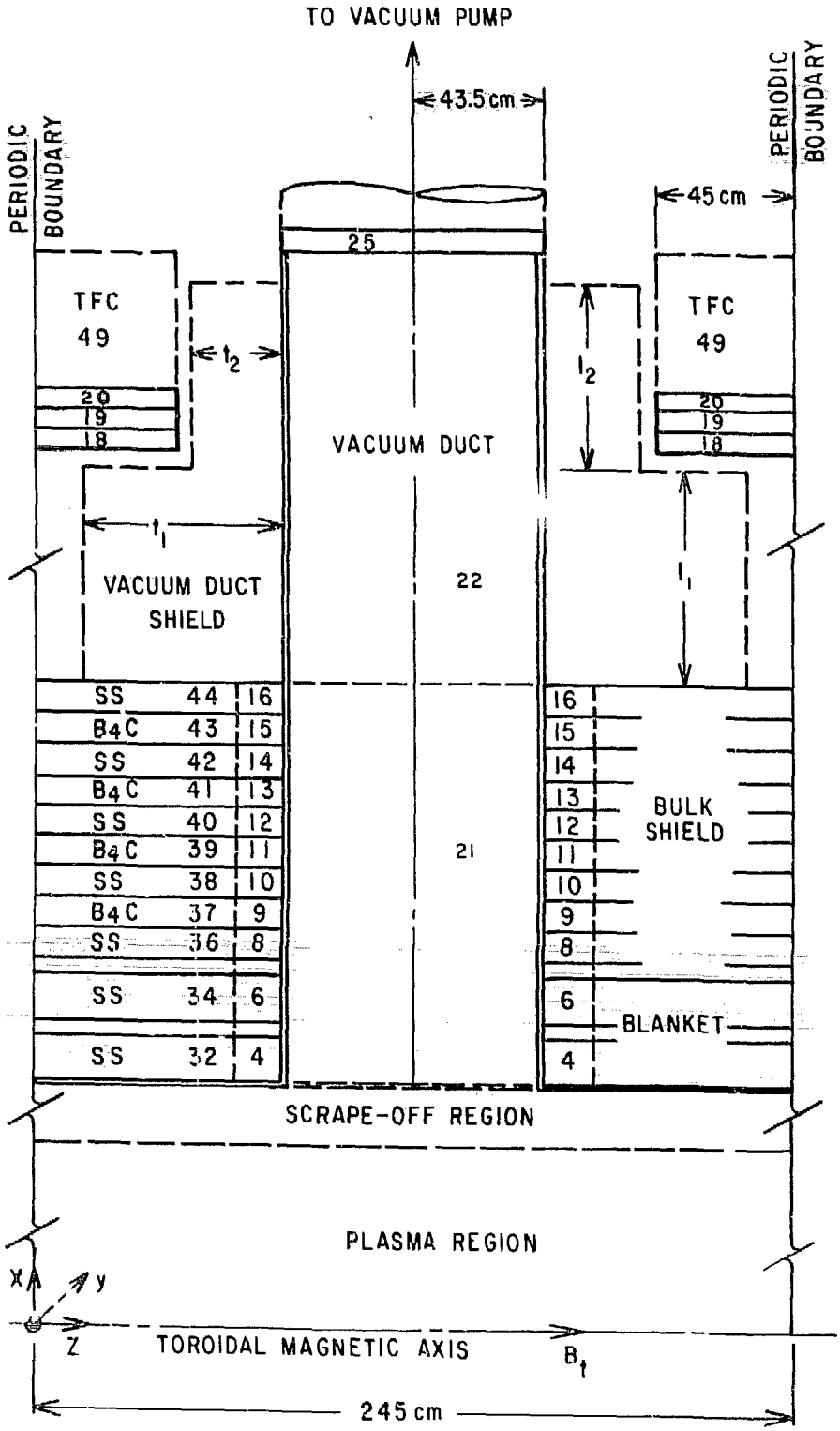

Figure G-2. Schematic of Geometrical Representation for Analysis of Vacuum Ducts and Their Shields

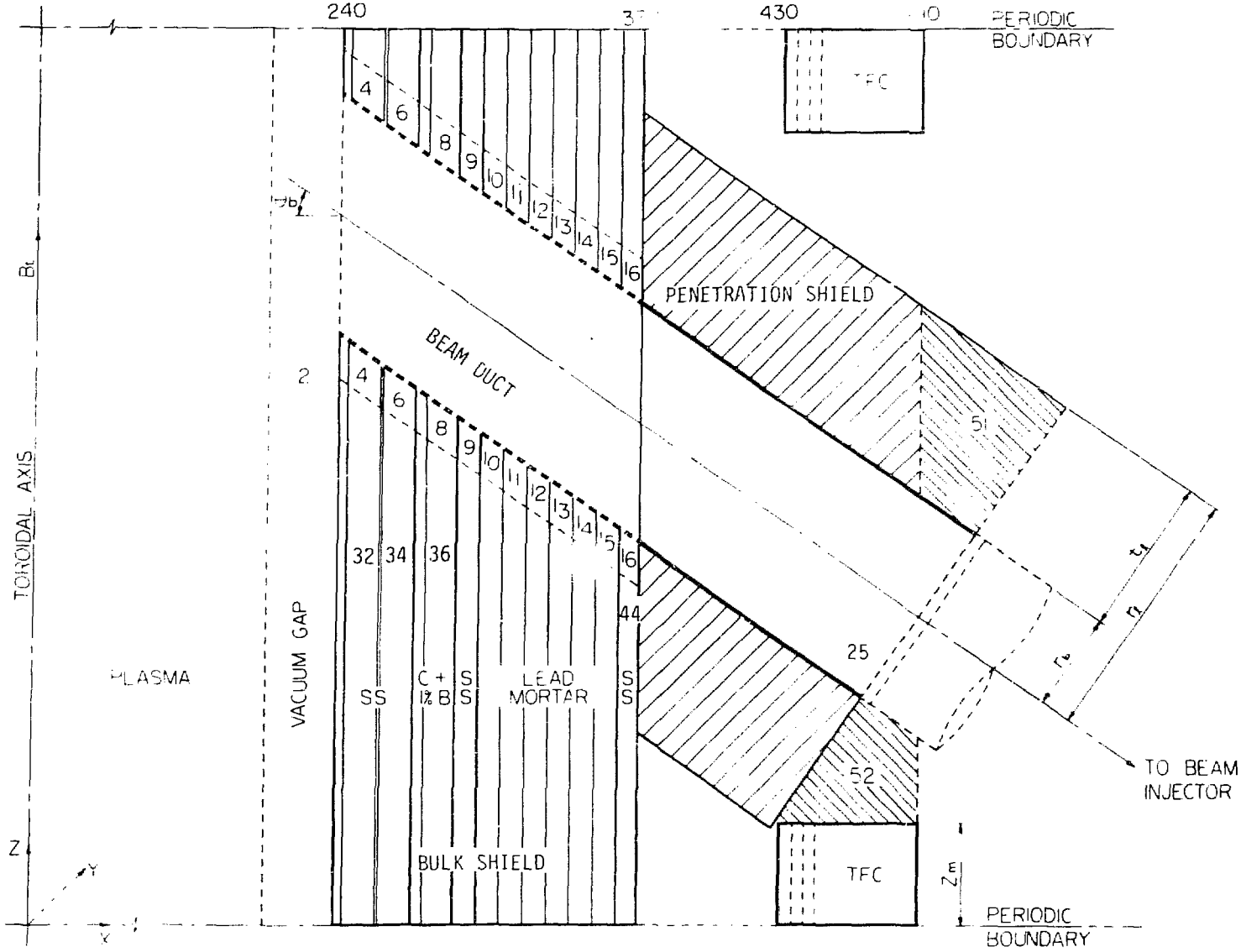

Figure C-3. Schematic of Geometry Representation for Analysis of Neutral Beam Penetrations and Their Shields

before it reaches the TF coils. In this study, no effort was made to model the beam injectors or the vacuum pumps. This avoided excessive computational cost involved in tracking the histories of particles in very large volumes beyond the exterior of the TF coils. Particles crossing a surface external to the TF coils were tallied in a leakage bin. However, in order to quantify the level of radiation streaming into the beam injectors and vacuum pumps, a 5-cm thick stainless steel disc was placed as an "end cap" on the penetration duct and is shown as Zone 25 in Figures G-2 and G-3.

As will be shown later in this appendix, the presence of penetrations causes a strong redistribution of neutrons in the blanket-bulk shield and the TF coils. In order to show this effect, the blanket/shield and the TF coils are divided into zones according to locations with respect to the penetration duct. For the blanket-bulk shield, each concentric poloidal ring is divided into two zones. One zone close to the penetration duct is bounded by the cylindrical wall of the duct, and by another cylinder with an axis coinciding with the duct axis and a radius that is 0.15 m larger than that of the penetration duct. The other zone spans the rest of the volume of the poloidal concentric ring. An example of such two zones are Zones 6 and 34, respectively. The TF coils composition is homogenized as 50% SS + 50% cu. These coils are divided into poloidal concentric rings, each is 5 cm thick (depth). Each ring is divided into two zones. One zone is bound between two planes located at $y = -100$ and $y = +100$ and the other zone constitutes the rest of the ring. The first 5-cm ring consists of Zones 18 and 28 and the second 5-cm ring consists of Zones 19 and 29 with Zones 18 and 19 as the regions closer to the penetration duct.

3. Analysis of Unshielded Penetrations

Calculations for seven design sets, A-G were made. Each set examines one or more aspects of the penetrations and their shield. This section is devoted to an analysis of the unshielded penetrations. Although it is clear that special shielding has to be provided to counteract the penetration effects, this analysis of unshielded penetrations is useful in providing insight into the requirements of such special shielding. Various schemes for shielding the penetrations are examined in the next section.

Design set A includes three cases (1, 2, and 3), all of which have no penetrations, i.e. the blanket-bulk shield is solid and continuous everywhere. The variable parameter here is the blanket-bulk shield thickness, which is 131, 111, and 91 cm for cases 1, 2, and 3, respectively. The blanket and bulk shield composition for case 1 is that shown in Table G-1 and referred to here as composition C1. Cases 2 and 3 are obtained by eliminating outer parts of the shield with the appropriate thickness. The innermost radius of the TF coils in all cases is 430 cm. Table G-2 shows the total neutron fluxes (normalized to 1 MW/m^2 neutron wall loading) at several key locations and the neutron leakage per DT neutron. In Table G-2 and other tables in this appendix, the percentage values in parentheses below each flux or leakage value represent the statistical error (i.e. the standard deviation) as estimated by VIM. These results show that increasing the thickness of the bulk shield by 20 cm reduces the level of nuclear radiation at the TF coils by a factor of > 15. The tolerable level of nuclear radiation at the TF coils is generally determined from a trade-off study of the conflicting requirements of the various reactor components and an optimization procedure to minimize the overall cost of the reactor per unit power output.[2,5] One constraint that cannot be violated, however, is that the radiation level at the TF coils must not exceed a level that permits the components of the superconducting magnet to function properly without excessive radiation damage and nuclear energy deposition. The magnet protection criteria were summarized in Chapter IX and were examined in more detail in references 2 and 5. These magnet protection criteria depend on the design of the magnet and the specific superconducting and stabilizing materials. The radiation levels of cases 1 and 3 cover the range of acceptable levels for tokamak reactor designs that are of practical interest at present.

Design set B consists of cases 4, 5, and 6, which are similar to designs 1, 2, and 3, respectively, except for incorporating a cylindrical penetration duct that is 0.85 m in diameter, as shown in Figure G-2. Results for cases 4, 5, and 6 are shown in Table G-3. Comparison of results in this table with results shown in Table G-2 for design set A shows that: (1) The presence of penetrations causes a strong spatial variation of the TF coil neutron fluxes in the poloidal direction (i.e. along the circumference of the D-shape). The

TABLE G-2 Neutron Fluxes Normalized to a Neutron Wall Loading of 1MW/m^2 at Key Locations for Designs in Design Set A (no penetrations)

Case No.	1	2	3
Code No.[a]	MC004	MC005	MC006
Composition of Bulk Shield	C1	C1	C1
Thickness of Bulk Shield	131 cm	111 cm	91 cm
Diameter of Penetration Duct	none	none	none
Orientation of Penetration	-	-	-
Penetration Shield Composition (if any)	-	-	-
Dimensions of Penetration Shield	-	-	-
Number of Histories	20,000	16,000	16,000
ϕ_{18}	9.93(6) (±18%)	1.85(8) (±14%)	3.19(9) (±13%)
ϕ_{19}	7.28(6) (±18%)	1.23(8) (±15%)	2.20(9) (±14%)
ϕ_{28}	9.93(6) (±18%)	1.85(8) (±14%)	3.19(9) (±13%)
ϕ_{29}	7.28(6) (±18%)	1.23(8) (±15%)	2.20(9) (±14%)
ϕ_{25}	9.90(6) (±18%)	1.85(8) (+14%)	3.20(9) (±13%)
Neutron Leakage per DT Neutron	1.16(-7) (±14%)	1.91(-6) (±13%)	2.93(-5) (±11%)

[a] Code No. refers to a particular computer run and is used only for convenience in documentation.

TABLE G-3 Total Neutron Fluxes Normalized to a Neutron Wall Loading of 1MW/m^2 at Key Locations for Designs in Design Set B

Case No.	4	5	6
Code No.	MC003	MC111	MC091
Composition of Bulk Shield	C1	C1	C1
Thickness of Bulk Shield	131 cm	111 cm	91 cm
Diameter of Penetration Duct	85 cm	85 cm	85 cm
Orientation of Penetration	perpendicular[a]	perpendicular	perpendicular
Penetration Shield Composition (if any)	none	none	none
Dimensions of Penetration Shield	-	-	-
Number of Histories	20,000	10,000	10,000
ϕ_{18}	4.08(12) (±9%)	6.19(12) (±17%)	1.03(13) (±9%)
ϕ_{19}	2.67(12) (±11%)	4.13(12) (±19%)	7.77(12) (±8%)
ϕ_{28}	3.42(11) (±7%)	7.11(11) (±8%)	1.14(12) (±14%)
ϕ_{29}	1.90(11) (±11%)	4.00(11) (±13)	6.84(11) (±16%)
ϕ_{21}	1.59(14) (±3%)	4.59(14) (±4%)	1.50(14) (±6%)
ϕ_{22}	2.22(13) (±6%)	2.16(13) (±11%)	2.37(13) (±8%)
ϕ_{23}	1.48(14) (±3%)	1.50(14) (±4%)	1.27(14) (±5%)
ϕ_{24}	1.63(13) (±8%)	1.47(13) (±10%)	1.83(13) (±9%)
ϕ_{25}	1.19(13) (±10%)	1.14(13) (±17%)	1.83(13) (±12%)
Neutron Leakage per DT neutron	1.97(-2) (±6%)	2.54(-2) (±8%)	3.18(-2) (±8%)

[a] axis of penetration duct perpendicular to the toroidal axis as shown in Fig. G-2.

ratio of the neutron flux in region 18, ϕ_{18}, to that in region 28, ϕ_{28}, is $\sim$ 12. The penetrations also cause large variations in the toroidal direction (in the Z directions; see Figure G-2) across the TF coils. (2) The penetrations increase the neutron flux in the TF coils by several orders of magnitude. (3) Increasing the bulk thickness of the blanket-bulk shield from 0.91 m to 1.31 m reduces the neutron flux at the magnet by a factor of $\sim$ 300 in the absence of penetrations but by only a factor of $\sim$ 3 when penetrations are present. (4) The large-size penetrations assist a greater number of neutrons at high energy to reach the TF coils. This causes the increase in the transmutation, atomic displacement, and nuclear heating rates at the TF coil due to the presence of penetrations to be generally higher than the increase in the total neutron flux. (5) The neutron leakage per DT neutron in the presence of penetrations is $\sim$ 2 to 3%, while in the absence of penetrations it varies from 1.2×10^{-7} for the 1.31 m bulk shield (case 1) to 3×10^{-5} for the 0.91 m bulk shield (case 3). (6) The neutron flux at the end cap, Zone 25, is $\sim 1.2 \times 10^{13}$ n/cm^2 sec. (For comparison, the neutron flux at the first wall is 7.6×10^{14}.) This means that auxiliary systems located at the end of the penetration duct receive a significantly high dose of radiation.

The large-size penetrations enable a large number of neutrons and photons to reach the magnets in two ways: (1) by creating possible direct line-of-sight from the plasma region to the magnets, and (2) increasing the population of the neutrons and photons in the blanket/shield regions in the vicinity of the void penetration where they can travel into the magnets through short paths in the blanket/shield. This second effect, generally called penetration-assisted radiation streaming, becomes more dominant as the size of the void penetration is decreased and the line-of-sight streaming is reduced. But both direct and assisted streaming are sensitive to the size of penetration for a given reactor configuration, as shown next.

Table G-4 shows the neutron fluxes and leakage for cases 7 and 8 compared with case 4 discussed above. The diameter of the cylindrical penetration is varied from 0.85 m in case 4 to 0.42 m in case 7, and to 0.20 m in case 8. The results in Table G-4 show that the neutron fluxes at the TF coils are reduced by more than an order of magnitude when the cross section area of the

TABLE G-4 Total Neutron Fluxes Normalized to a Neutron Wall Loading of $1MW/m^2$ at Key Locations for Designs in Design Set C (size of penetration)

Case No.	4	7	8
Code No.	MC003	MC061	MC062
Composition of Bulk Shield	C1	C1	C1
Thickness of Bulk Shield	131 cm	131 cm	131 cm
Diameter of Penetration Duct	85 cm	42 cm	20 cm
Orientation of Penetration	perpendicular	perpendicular	perpendicular
Penetration Shield Composition (if any)	none	none	none
Dimensions of Penetration Shield	-	-	-
Number of Histories	20,000	20,000	50,000
ϕ_{18}	4.08(12) (±9%)	3.51(11) (±18%)	1.10(10) (±56%)
ϕ_{19}	2.67(12) (±11%)	1.85(11) (±25%)	8.04(9) (±70%)
ϕ_{28}	3.42(11) (±7%)	2.56(10) (±34%)	2.50(9) (±65%)
ϕ_{29}	1.90(11) (±11%)	1.86(10) (±32%)	2.03(9) (±79%)
ϕ_{21}	1.59(14) (±3%)	1.24(14) (±6%)	8.65(13) (±7%)
ϕ_{22}	2.22(13) (±6%)	6.18(12) (±24%)	7.62(11) (±65%)
ϕ_{23}	1.48(14) (±3%)	1.14(14) (±7%)	8.65(13) (±7%)
ϕ_{24}	1.63(13) (±8%)	3.61(12) (±27%)	5.16(11) (±64%)
ϕ_{25}	1.19(13) (±10%)	4.30(12) (±43%)	5.35(11) (±100%)
Neutron Leakage per DT neutron	1.97(-2) (±6%)	1.81(-3) (±20%)	8.26(-5) (±45%)

void penetration is reduced by a factor of 4. From the very limited number of cases in Table G-4, it can be tentatively concluded that the total neutron flux at the TF coils is roughly proportional to the square of the cross section area of the void penetration. Thus the neutron flux at the TF coils is approximately proportional to d^4, where d is the characteristic dimension of the penetration cross section (e.g. d is the diameter of a circular cross section or the side length of a square cross section). These correlations are brought up here only to demonstrate qualitatively the great dependence of radiation streaming on the size of penetrations. The geometry of the system and the shape of the penetration are also important. For example, a penetration with a rectangular cross section with one side much larger than the other side is likely to result in less radiation streaming than another penetration with the same cross section area but with a square or circular cross section. Both direct and assisted streaming are strongly dependent on the size and shape of the penetration.

Comparing ϕ_{23} as well as ϕ_{24} for the three cases in Table G-4 shows that the neutron fluxes along the walls of the penetration vary also with the penetration size. The neutron fluxes in the portion of the duct walls inside the blanket-bulk shield increase by $\sim$ 30% when the diameter of the duct is doubled. The variation in the neutron fluxes in the portion of the duct walls outside the blanket-bulk shield with the size of the duct is much more pronounced. These results indicate that the spatial variation in response rates such as gas production and nuclear heating along the duct walls depends on the size of penetration and is generally stronger for smaller size penetrations.

In Table G-4, as well as in other tables in this appendix, the number of neutron histories run for each case is given. This number represents the number of primary (DT) neutrons and does not include the multiplicative effect of neutron splitting. The number and locations of splitting surfaces used in the Monte Carlo computation was changed from one problem to another according to a rough expectation of the spatial distribution of the neutron population. A limitation of VIM and many other present Monte Carlo codes is that the splitting surfaces have to be surfaces of concentric bodies. When these bodies are taken as the concentric cylinders in the blanket-bulk shield with their common axis as the z-axis (see Figure G-2) a difficulty is encountered. If the number of splitting surfaces is kept small, then the

number of neutrons that travel mostly in the blanket-bulk shield and reach the TF coils is severely underestimated because of the very large degree of attenuation ($\sim 10^6$ to 10^8) involved. On the other hand, if the number of splitting surfaces is greatly increased extremely large numbers of histories are generated by splitting those neutrons traveling only in the void ducts. This causes the computer storage capacity to be rapidly exceeded. For unshielded large-size penetrations, a reasonably small number of splitting surfaces suffices, as the major contribution to the radiation level in the exterior of the bulk shield comes from the void duct and the neighboring region where radial attenuation is very weak. The situation is more difficult, however, for smaller size penetrations, as can be seen clearly from comparing the number of neutron histories and the associated statistical errors in cases 4, 7, and 8 in Table G-4. For example, 20,000 neutron histories are sufficient to calculate the neutron flux at the end-cap, ϕ_{25}, to within 10% accuracy when the penetration diameter is 0.85 m, but 50,000 neutron histories are not sufficient to calculate ϕ_{25} to better than 100% accuracy when the penetration diameter is 0.20 m. These difficulties are compounded when an exterior penetration shield is employed, as shown in the next section. A capability of handling general splitting surfaces that permits less splitting in the void duct and its vicinity and more splitting in regions where strong attenuation takes place is believed to be an important tool in any Monte Carlo code to be used in this type of penetration analysis.

4. Shielding of Major Penetrations

The effects of major void penetrations can be classified into two categories. The first category includes the effects on reactor components external to the bulk shield due to a dramatic enhancement of radiation streaming. The effects on the penetration walls and blanket-bulk shield in the vicinity of the penetrations are included in the second category. Effects in the second category were covered in Section A of Chapter IX. Effects in the first category can be guarded against by incorporating efficient penetration shields, as examined in this section.

There are several shielding schemes which might be used to protect reactor components external to the bulk shield from enhanced radiation streaming caused by large-size penetrations. These are:

(1) Moveable Shield Plug — If the functional requirements of a penetration permit that the penetration be closed during the plasma burn, then a shield plug can be moved at the beginning of each pulse to close completely the penetration region embedded in the bulk shield.

(2) Local Component Shield -- Reactor components affected by radiation can be surrounded by a shield capable of reducing the radiation level in the component to a tolerable level.

(3) Bulk Shield Extension — The bulk shield can be extended into and in between the TF coils, and on to the outside as necessary.

(4) Local (exterior) Penetration Shield -· Each penetration is surrounded as it emerges from the bulk shield by an appropriate local shield. This shield must suffice to reduce the radiation level at the TF coils and at all other auxiliary systems located in the reactor building to a permissible level.

Each of these shielding approaches has its own merits and disadvantages. The movable shield plug is the easiest to define in terms of nuclear requirements, since it needs to have the same dimensions as the penetration itself and it can be of a composition similar to that of the blanket-bulk shield. The most important advantage of the movable shield plug is that, in contrast to all other approaches, it completely eliminates the penetration effects and restores the effectiveness of the bulk shield. It also requires the smallest inventory of shielding materials of the four options. Whether a movable shield plug is less costly and is more favorable than the other shielding schemes has yet to be determined from detailed studies including engineering and reliability considerations. A movable shield plug weighs several thousands of kilograms for the size of penetration discussed in this work. It also requires incorporating mechanical and electrical components as well as automatic control system, all of which must have high quality performance. Moreover, failure of these components has to be anticipated and the consequences must be assessed and factored into the design. There is a finite probability that the movable shield plug will fail to close the penetration before initiation of the plasma burn. In such situations, a significant number of neutrons and photons would stream through the penetration.

Repair of a major failure in the shield plug would have to be made remotely and would involve a down time period for the reactor. However, in view of many disadvantages associated with other shielding schemes, a movable shield plug has to be considered as a serious candidate for penetration shielding. A movable shield plug should be considered only, of course, for penetrations whose functional requirements permit that they can always be closed during the entire duration of the plasma burn, i.e. at all times when the fusion probability is greater than zero. This immediately eliminates, for example, a movable shield plug as a viable approach for neutral beam ducts in beam-driven devices and for divertors.

This study does not find the movable shield plug to be a viable approach for the neutral beam ducts for several reasons. One specific reason for near-term devices up to and including the tokamak EPR is that these machines may have to be operated in a beam-driven mode, either to offset subignition confinement or to prolong burn pulses. In this case, the beam duct cannot be closed during the time of plasma burn. For future tokamaks beyond EPR's the movable shield plug does not appear atractive for the neutral beam ducts for reasons that include the following:

(1) During the plasma heating phase, the neutral beam is injected for a finite period of time and the fusion power increases steadily. The total energy of the neutrons emitted during the beam injection phase depends on the characteristics of the design but it is generally significant. Thus radiation streaming during the plasma heating phase when the shield plug cannot be used is very likely to be intolerable. The same problem arises when the beam is used to extend the burn pulse.

(2) The neutral beam ducts have to provide a straight-through path from the neutralizer to the plasma chamber. Thus, the mechanical movements of the shield plug to close the neutral beam duct will involve rotational as well as displacement movements. This will involve time delay in closing the beam duct with the plasma already in the ignition phase. Moreover, complicated patterns of movements for placing the shield plug inside the beam duct will magnify the risk of failure that will always be associated with periodic mechanical movements of massive weights on a short time scale.

The second approach for penetration shielding is local shielding of components that are affected by radiation. This approach can be easily rejected as the primary approach on the ground of the large volumes of reactor components that have to be shielded; it is, however, a useful supplemental shielding method for some small-size equipment that is overly sensitive to nuclear radiation.

Simple extension of the bulk shield is not an efficient technique for reducing radiation levels. As shown in the previous section, increasing the thickness of the bulk shield by 0.40 m reduces the high level of radiation streaming by only a factor of 3. Of course, in principle the bulk shield can be extended much further, into the spaces between TF coils and out beyond these coils if necessary, to protect the magnet and other auxiliary systems. Unfortunately, the volumes of materials involved in this approach are so large that the cost is very high.

The local penetration shield approach takes full advantage of the specific shapes of penetrations, and of the fact that the penetrations may be located relatively long distances apart. In this approach, each penetration is surrounded as it emerges from the bulk shield by local shielding. The shapes and compositions of the local shields can be carefully adjusted so as to conserve space and minimize cost. With this local penetration shield approach, the dimensions of the bulk shield, for a given material composition, should be no greater than the minimum required for the protection of the TF coils in regions far away from the penetrations (i.e. in the complete absence of any penetration effects). The local penetration shield approach requires extensive nuclear analysis to determine the appropriate material composition and the optimum geometrical shape for each particular type of penetration. In this study, a modest attempt is made to examine the gross features of a local penetration shield.

Because of constraints on available space for local penetration shields it is important to find an effective shield material which is not unduly expensive. Such a composition was found in references 2 and 5 for typical fusion reactor spectra to be a mixture of stainless steel and boron carbide. Design set D in Table G-5 allows for a penetration shield whose composition

TABLE G-5 Total Neutron Fluxes Normalized to a Neutron Wall Loading of 1MW/m^2 at Key Locations for Designs in Design Set D

Case No.	9	10	11
Code No.	MC215	MC51	MC52
Composition of Bulk Shield	C1	C1	C1
Thickness of Bulk Shield	131 cm	131 cm	131 cm
Diameter of Penetration Duct	85 cm	85 cm	85 cm
Orientation of Penetration	perpendicular	perpendicular	perpendicular
Penetration Shield Composition (if any)	50%SS+50%B_4C	SS	B_4C
Dimensions of Penetration Shield	t_2=t_1=30cm $\ell_1+\ell_2$=119cm	t_2=t_1=30cm $\ell_1+\ell_2$=119cm	t_2=t_1=30cm $\ell_1+\ell_2$=119cm
Number of Histories	30,000	10,000	10,000
ϕ_{18}	9.69(10) (±20%)	1.93(12) (±13%)	7.08(11) (±19%)
ϕ_{19}	6.04(10) (±23%)	1.27(12) (±23%)	3.30(11) (±20%)
ϕ_{28}	9.97(9) (±18%)	1.78(11) (±12%)	1.67(10) (±25%)
ϕ_{29}	7.37(9) (±22%)	1.14(11) (±21%)	1.67(10) (±27%)
ϕ_{21}	1.68(14) (±3%)	1.72(14) (±4%)	1.55(14) (±4%)
ϕ_{22}	3.37(13) (±5%)	4.53(13) (±8%)	2.32(13) (±8%)
ϕ_{23}	1.53(14) (±3%)	1.56(14) (±6%)	1.39(14) (±4%)
ϕ_{24}	2.88(13) (±5%)	-	-
ϕ_{25}	1.67(13) (±7%)	2.25(13) (±11%)	1.17(13) (±17%)
Neutron Leakage per DT neutron	4.04(-3) (±7%)	1.10(-2) (±8%)	4.44(-3) (±12%)

is 50% SS + 50% B_4C in case 9, all stainless steel in case 10, and all B_4C in case 11. The geometry of the system is as shown in Figure G-2, with the inner radius of the TF coils as 4.30 m. The penetration shield is 0.30 m thick and extends from the bulk shield to the end cap. The results in Table G-5 show that the B_4C penetration shield is more effective than the SS penetration shield in reducing neutron fluxes at the TF coils. The reason is that the B_4C absorbs a larger fraction of the low energy neutrons. Boron carbide, on the other hand, is much less effective than SS in slowing down the high energy neutrons. Therefore, the 50% SS + 50% B_4C penetration shield in case 9 gives much better overall attenuation than we find in cases 10 and 11. Comparing cases 9 and 11 shows that the 50% SS + 50% B_4C penetration shield lowers the radiation level at the TF coils and other components on the side of the shield by about a factor of 7 compared with the all-B_4C penetration shield. However, the radiation level in both cases is essentially the same at the open ends. The problem is just that - open ends. Some neutrons, travelling in the void duct, strike the penetration shield adjacent to the side of the duct, but others do not; many neutrons scatter from the side penetration shield into the duct where they can travel for a long path before they can make another collision on the side shield. Thus, the attenuation of neutron fluxes outward in the void duct will tend to be weak. This effect, as will be seen shortly, persists regardless of the thickness of the penetration shield. The attenuation of the neutron fluxes along the duct could perhaps be affected significantly by a perfect absorber penetration shield. Such an absorber, which would also effectively attenuate neutrons of all energies traveling in the direction of the TF coils, does not exist. However, the possibility of optimizing the composition and material disposition of the penetration shield needs to be examined thoroughly in future studies.

Comparing case 9 in Table G-5 with case 4 in Table G-3 shows that the use of a 0.30 m thick penetration shield results in a factor of 40 reduction in the neutron fluxes at the TF coils. However, in reference to case 1 in Table G-2, the penetration shield needs substantial improvement to provide an additional four orders of magnitude in attenuation in order to completely eliminate the penetration effects at the TF coils. Design set E in Table G-6 examines the effects of the penetration shield thickness and length. In cases 12, 13 and 14, only the first 15 cm of the magnet depth are included

TABLE G-6 Total Neutron Fluxes Normalized to a Neutron Wall Loading of 1MW/m^2 at Key Locations for Designs in Design Set E

Case No.	12	13	14	9
Code No.	201	202	212	215
Composition of Bulk Shield	C1	C1	C1	C1
Thickness of Bulk Shield	131 cm	131 cm	131 cm	131 cm
Diameter of Penetration Duct	85 cm	85 cm	85 cm	85 cm
Orientation of Penetration	Perpendicular	Perpendicular	Perpendicular	Perpendicular
Penetration Shield Composition (if any)		50% SS + 50% B_4C		
Dimensions of Penetration Shield	t_1=30cm ℓ_1=55cm t_2=ℓ_2=0	t_1=75cm ℓ_1=55cm t_2=ℓ_2=0	t_1=75cm ℓ_1=59cm t_2=34, ℓ_2=15cm	t_1=t_2=30cm ℓ_1+ℓ_2=119cm
Number of Histories	20,000	30,000	30,000	30,000
ϕ_{18}	2.17(11) (±21%)	1.31(11) (±12%)	1.32(9) (±79%)	9.69(10) (±20%)
ϕ_{19}	2.13(11) (±23%)	1.80(11) (±16%)	1.08(9) (±85%)	6.04(10) (±23%)
ϕ_{28}	2.11 (10) (±26%)	4.84(8) (±41%)	2.44(6) (±100%)	9.97(9) (±18%)
ϕ_{29}	1.06(10) (±34%)	3.14(8) (±42%)	NS*	7.37(9) (±22%)
ϕ_{21}	1.58(14) (±4%)	1.52(14) (±3%)	1.58(14) (±2%)	1.68(14) (±3%)
ϕ_{22}	2.46(13) (±5%)	2.48(13) (±5%)	2.91(13) (±5%)	3.37(13) (±5%)
ϕ_{23}	1.44(14) (±4%)	1.38(14) (±3%)	1.41(14) (±3%)	1.53(14) (±3%)
ϕ_{24}	2.02(13) (±6%)	2.09(13) (±5%)	2.36(13) (±5%)	2.88(13) (±5%)
ϕ_{25}	1.23(13) (±10%)	1.14(13) (±8%)	1.28(13) (±7%)	1.67(13) (±7%)
Neutron Leakage per DT neutron	9.60(-3) (±6%)	9.18(-3) (±6%)	8.80(-3) (±5%)	4.04(-3) (±7%)

*NS = no score = No neutrons reached this region in the histories run.

in the calculation in order to eliminate the computer time consumed in tracking particles traveling inside the TF coils (i.e. in region 49 in Figure G-2). Case 9 of Table G-5 is also shown in Table G-6 for comparison purposes. All penetration shields in cases 12, 13, 14 and 9 have a 50% SS + 50% B_4C composition. The penetration shield in case 12 is 0.30 m thick and covers only 0.55 m of the duct length external to the bulk shield. The penetration shield in case 13 has the same length as that of case 12 but is 0.75 m thick. The penetration shield in case 14 is 0.75 m thick in the region between the bulk shield and inner surface of the magnet then narrows down to fully occupy the 0.34 m thick region between the TF coils. Note that a cylindrical penetration shield region that is 0.75 m thick and has a length of 0.59 m ($\ell_1 = r_2 - r_1 = 4.30 - 3.71 = 0.59$ m where r_2 is the inner radius of the magnet and r_1 the outer radius of the bulk shield) interfaces with the TF coils (this can be viewed in an x-y view of Figure G-2). Regions of interface were excluded from the penetration shield.

Results for cases 12 and 9 in Table G-6 show that removing the portion of the penetration shield between the TF coils increases the neutron fluxes at the TF coil by a factor > 2. Increasing the thickness of the penetration shield to 0.75 m without shielding the penetration segment which lies between the TF coils is an inefficient approach, as can be seen on comparing the TF coil fluxes for cases 13 and 9. The results in Table G-6 show that increasing the thickness of the penetration shield from 0.30 m in case 9 to 0.75 m in case 14 (with the penetration covered from the outer surface of the bulk shield to in between the TF coils) reduces the neutron fluxes at the magnets by a factor of $\sim$ 70. There is an important difference between the penetration shields in cases 9 and 14 beside the different thickness. In case 9 the penetration shield covers the penetration fully, i.e. it extends to the end cap. In case 14, however, the penetration shield covers only those portions of the penetration which lie between the bulk shield and the TF coils, and extends in between the TF coils for only 0.15 m. Thus, the portion of the TF coils (0.15 m depth) included in the calculation is protected from direct line-of-sight exposure of any region inside the penetration duct (note that a vacuum boundary condition is applied at the

outermost surfaces) in both cases. However, in case 14 the portion of the duct beyond the TF coils is left bare. This causes the neutron leakage in case 14 to be about twice that in case 9. A comparison of the neutron fluxes in Zone 25, ϕ_{25}, and the neutron leakage for cases 9 and 14 reaffirms an important conclusion obtained earlier in this section. Regardless of how thick the penetration shield is made to be, extending the penetration shield to surround the portions of the void duct beyond the TF coils is necessary in order to protect auxiliary systems and equipment located external to the TF coils.

On comparing the results for cases 14 and 1 one sees that the attenuation obtainable with thick penetration shield in case 14 (0.75 m thick and tapered off to 0.34 m in between the TF coils) needs to be improved by an additional two orders of magnitudes in order to completely eliminate the penetration effects at the TF coils. The inadequacy of this relatively thick penetration shield may be surprising at first glance, but should seem more plausible when the characteristics of the problem at hand are examined more closely. The neutron flux at the first wall, in the problems examined so far, is $\sim 7.6 \times 10^{14}$ n/cm^2, sec. The results for case 1 (see Table G-2) shows that the 1.31 m thick bulk shield provides an overall attenuation in the neutron fluxes of $\sim 10^8$. The results of case 4 (see Table G-4) shows that the 0.85 m diameter duct allows ~ 0.02 of the neutrons to stream out. Thus, to completely restore the effectiveness of the shield system, the penetration shield is required to provide 10^6 attenuation. Previous results[2] show that in typical fusion spectra the 50% SS + 50% B_4C mixture provides a factor of 10 attenuation for about every 17 cm. Thus, the penetration shield needs to be, very qualitatively, greater than 1 m thick. Comparing ϕ_{18} for cases 14 and 4 shows that the 0.75 m thick penetration shield provides an attenuation of $\sim 4 \times 10^3$, which is consistent with the expected attenuation if the fact that a portion of the penetration shield in case 14 is only 0.34 m is accounted for. Comparing the results of case 14 in Table G-6 with Case 3 in Table G-2 shows that if the magnet protection criteria are satisfied by the attenuation provided by the 0.91 m thick blanket-bulk shield in the absence of penetrations, then the penetration shield specified in case 14 is adequate to eliminate the penetration effects at the TF coils. Thus, the size of the penetration shield, as expected, depends strongly on the tolerable radiation level at the TF coils.

In cases 1 to 14 the width of the repeating segment, W_s, which is the distance along the Z-axis between the two symmetry planes shown in Figure G-2 was taken as 2.45 m. The inner radius of the magnet, r_m, was taken in these cases to be 4.30 m. If the outer minor radius of the bulk shield is r_o, then the radial clearance, Δ_{sm}, between the bulk shield and the toroidal field coils is given as $\Delta_{sm} = r_m - r_o$. Obviously, the penetration effects and the design of the penetration shield should depend on W_s and Δ_{sm} in addition to the dependence on other parameters discussed earlier in this section and the previous section. The value of W_s depends on the major radius, the spacing between each pair of TF coils, and the coil width in the vicinity of penetration. For a given r_o, the value of Δ_{sm} depends on the actual shape of the toroidal-field coils, and on the location of the penetration. For a D-shaped TF coil, Δ_{sm} is larger on the top and bottom of the torus than on the outside at midplane. Conversely, W_s is smaller on the top and bottom of the torus than on the outside at midplane. This introduces a basic difference between the geometric representation of the evacuation ducts and that of the neutral beam ducts, in addition to the difference in orientation of the ducts. It will be recalled that the axis of the evacuation duct is perpendicular to the magnetic axis, while the neutral duct axis is almost tangential to the magnetic axis. In the following, the differences in the neutronics effects of the two types of penetrations are examined.

In the EPR design given in Reference 1, and used for guidance in geometric representation of this penetration scoping study, each TF coil has a D-shaped vertical cross section with a horizontal bore of 7.7 m and a vertical bore of 11 m. Thus, for the evacuation ducts located at the top and bottom of the torus, W_s = 2.45 m and Δ_{sm} = 1.79 m. Design set F in Table G-7 includes three cases; 15, 16 and 17 for the evacuation ducts. Case 15 is for unshielded evacuation duct. It should be noted that case 15 is similar to case 4 in Table G-3 except that Δ_{sm} is 0.59 m in case 4 and 1.79 m in case 15. Comparing the results for these two cases shows that extending the vertical bore of the TF coils actually increases the neutron fluxes at the coils while the neutron leakage remains approximately the same. Case 16 in Table G-7 incorporates a penetration shield that is 0.75 m thick and extends 0.60 m beyond the outer surface of the bulk shield. Thus case 16 is

TABLE G-7 Total Neutron Fluxes Normalized to a Neutron Wall Loading of 1MW/m^2 at Key Locations for Designs in Design Set F

Case No.	15	16	17
Code No.	401	405	406
Composition of Bulk Shield	C1	C1	C1
Thickness of Bulk Shield	131 cm	131 cm	131 cm
Diameter of Penetration Duct	85 cm	85 cm	85 cm
Orientation of Penetration	perpendicular	perpendicular	perpendicular
Penetration Shield Composition (if any)	none	50%SS+50%B_4C	50%SS+50%B_4C
Dimensions of Penetration Shield	--	ℓ_1=60 cm	ℓ_1=100cm
	--	t_1=75 cm	t_1=75 cm
	--	$\ell_2=t_2=0$	$\ell_2=t_2=0$
Number of Histories	20,000	20,000	20,000
ϕ_{18}	4.87(12) (±10%)	1.79(12) (±11%)	8.93(11) (±9%)
ϕ_{19}	3.61(12) (±10%)	1.31(12) (±15%)	5.61(11) (±12%)
ϕ_{28}	9.44(11) (±7%)	2.60(11) (±9%)	1.13(11) (±10%)
ϕ_{29}	6.12(11) (±6%)	1.44(11) (±9%)	6.86(10) (±11%)
ϕ_{21}	1.55(14) (±3%)	1.60(14) (±4%)	1.51(14) (±4%)
ϕ_{22}	1.58(13) (±7%)	1.62(13) (±7%)	1.90(13) (±7%)
ϕ_{23}	1.34(14) (±3%)	1.43(14) (±4%)	1.32(14) (±4%)
ϕ_{24}	1.12(13) (±6%)	1.23(13) (±7%)	1.48(13) (±7%)
ϕ_{25}	6.69(12) (±14%)	5.47(12) (±12%)	6.02(12) (±13%)
Neutron Leakage per DT neutron	1.99(-2) (±5%)	8.94(-3) (±7%)	7.05(-3) (±8%)

essentially the same as case 13 except that Δ_{sm} is 1.79 m in case 16 and 0.59 m in case 13. Again, a larger number of neutrons can reach the TF coils when the magnet vertical bore is increased if the penetration shield is not extended to reach in between the coils. Case 17 in Table G-7 is the same as case 16, except that the penetration shield length is increased from 0.60 m in case 16 to 1.0 m in case 17. This increase of 0.40 m in the penetration shield length reduces the neutron fluxes at the TF coils by only a factor of 2. Although the volume of the penetration shield in case 17 is more than 60% larger than that in case 14, the radiation level at the TF coils in case 17 is about a factor of 670 greater than that in case 14. This again is due to the fact that a portion of the evacuation duct near and in between the TF coils is left "bare" in case 17. A significant conclusion to be drawn, therefore, is that, for all practical purposes, increasing the bore of the TF coils cannot eliminate the need for effective shielding surrounding the evacuation duct in the regions where it passes between the TF coils. This is unfortunate since to make room for such shielding, it is necessary that the clearance space beteeen a pair of TF coils be $\geq d + 2t_{ps}$, where d is the duct diameter and t_{ps} is the thickness of the penetration shield. To satisfy this requirement for a given major radius, d, t_{ps}, and TF coil width, the number of TF coils has to be reduced. The resulting increase in the magnetic field ripple then leads to enhancement of particle diffusion from the plasma. To avoid this situation, it seems that the vertical bore of the TF coils has to be increased, and the increase should be utilized in a different approach. If the increase in the magnet vertical bore is such that Δ_{sm} is significantly larger than $d + t_{ps}$ then the evacuation duct can be bent as it emerges from the bulk shield. Thus, the vacuum pumps can be moved so that they will no longer be visible to neutrons in the primary portion of the evacuation ducts, and at the same time both branches of the duct can be completely surrounded on all sides with penetration shield in order to protect the TF coils.

Cases 18 through 21 in Table G-8 examine some of the neutronics aspects of the neutral beam ducts with the geometric representation shown in Figure G-3 and discussed earlier in Section 2 of this appendix. The width of the repeating segment, W_s, in all these cases is 3.90 m, which leaves 3.0 m

TABLE G-8 Total Neutron Fluxes Normalized to a Neutral Wall Loading of 1MW/m^2 at Key Locations for Designs in Design Set G.

Case No.	18	19	20	21
Code No.	501	502	504	505
Composition of Bulk Shield	C1	C1	C1	C1
Thickness of Bulk Shield	131 cm	131 cm	131 cm	131 cm
Diameter of Penetration Duct	85 cm	85 cm	85 cm	85 cm
Orientation of Penetration	θ_b=0	θ_b=35°	θ_b=35°	θ_b=35°
Penetration Shield Composition (if any)	none	none	50%SS+50%B_4C	50%SS+50%B_4C
Dimensions of Penetration Shield	--	--	Thickness = 50 cm	Thickness = 70 cm
Number of Histories	20,000	20,000	40,000	40,000
ϕ_{18}	7.54(11) (±11%)	9.62(11) (±12%)	1.69(9) (±62%)	1.35(8) (±68%)
ϕ_{19}	5.97(11) (±12%)	5.83(11) (±16%)	2.06(9) (±67%)	3.41(8) (±65%)
ϕ_{28}	1.18(11) (±13%)	1.13(11) (±17%)	2.20(9) (±59%)	6.11(7) (±64%)
ϕ_{29}	7.30(10) (±17%)	7.78(10) (±18%)	9.2(7) (±75%)	3.43(7) (±79%)
ϕ_{25}	1.45(13) (±12%)	8.21(12) (±20%)	9.19(12) (±11%)	9.92(12) (±9%)
Neutron Leakage per DT neutron	1.45(-2) (±6%)	9.45(-3) (±6%)	3.92(-3) (±6%)	4.00(-3) (±6%)

clearance between each pair of TF coils. The inner radius of the magnet, r_m, is 4.30 m in all cases. Cases 18 and 19 incorporate no penetration shield. In cases 19, 20 and 21 the axis of the beam duct makes a 55° angle with the toroidal magnetic axis, i.e. $\theta_b = 35°$ (see Figure G-3). For comparison, the axis of the beam duct in case 18 has a $\theta_b = 0°$, i.e. this duct is perpendicular to the toroidal magnetic axis. Thus, case 18 is similar to case 4 except that W_s is 3.90 m in case 18 and 2.45 m in case 4. When the neutron fluxes in both cases are normalized to the same neutron wall loading, the results for the two cases provide a useful comparison between the effects of a penetration located at the top (or the bottom) of the torus and another that is located on the outside centered around the midplane. The neutron flux at the end cap, ϕ_{25}, is approximately the same in both cases (the difference is within the statistical uncer inty in the Monte Carlo calculations). Since the penetration size is the same in the two cases but W_s is substantially different, it can be concluded that the neutron flux inside the void penetration is fairly independent of the ratio of the void penetration volume to that of the blanket-bulk shield. The dependence on the penetration size was shown earlier in Section 3 to be very strong. Comparing ϕ_{18}, ϕ_{19}, ϕ_{28}, and ϕ_{29} for cases 4 and 18, one finds that the radiation level at the TF coils in case 18 is about a factor of 5 smaller than that in case 4. This means simply that increasing the clearance between the TF coils reduces the number of neutrons streaming into the TF coils. Thus, increasing the clearance between the TF coils should lead to an increase in the neutron leakage. When the neutron leakage per DT neutron is renormalized so that the DT neutron current at the first wall is the same in cases 4 and 18, the neutron leakage in case 18 is found to be indeed 30% higher than that in case 4.

With $\theta_b = 0°$ in case 18 and $\theta_b = 35°$ in case 19, the results for the two cases should provide an indication of the sensitivity of the neutronics effects of the beam duct to the orientation of the beam duct axis with respect to the magnetic axis. The differences in the neutron fluxes for the two cases as shown in Table G-8 are found to be near the limits of the statistical uncertainty. Additional computation to reduce the statistical error was found unwarranted as these results already indicate that the neutronics effects of the beam ducts are not overly sensitive to the orientation of the beam axis with respect to the magnetic axis. There are many compensating and counteracting effects that tend to reduce the dependence on θ_b.

A penetration shield of 50% SS + 50% B_4C surrounds the beam duct in both cases 20 and 21 and extends from the outer bulk-shield boundary to the end cap. The beam duct shield is 0.50 m thick in case 20 and is 0.70 m thick in case 21. The 0.50 m-thick beam duct shield provides a factor of $\sim$ 570 reduction in the maximum neutron flux, ϕ_{18}, at the TF coils. The 0.70 m thick beam duct shield reduces ϕ_{18} by a factor of 12 relative to that with the 0.50 m thick shield. Comparing the results for case 21 with those for case 1 shows that the 0.70 m thick beam duct shield needs to be improved further in attenuation effectiveness by about a factor of 13 in order to reduce the maximum neutron flux at the TF coil to that in the absence of the beam duct. On the other hand, if the radiation level at the TF coils obtainable in case 2 is acceptable, then the 0.70 m thick beam duct shield is sufficient to protect the superconducting coils against radiation streaming caused by the neutral beam ducts. Note, however, that the neutron fluxes at the end cap and the neutron leakage obtainable with the 0.70 m thick beam duct shield are still very high.

Effects of penetrations on the blanket-bulk shield regions in the vicinity of penetrations were found to be very significant as discussed in detail in Chapter IX. The radiation damage indicators and energy deposition in the walls of the penetration were also examined in Chapter IX.

---

1. W. M. Stacey, Jr., et al., "Tokamak Experimental Power Reactor Studies," ANL/CTR-75-2, Argonne National Laboratory (June 1975).

2. Mohamed A. Abdou, "Nuclear Design of the Blanket/Shield System for a Tokamak Experimental Power Reactor," *Nuclear Technology*, 29, 7-36 (April 1976).

3. E. M. Gelbard and R. E. Prael, "Monte Carlo Work at Argonne National Laboratory," Proceedings of the NEACRP Meeting of a Monte Carlo Study Group, ANL-75-2 (1974); also R. E. Prael and L. J. Milton, "A User's Manual for the Monte Carlo Code VIM," an ANL internal memorandum FRA-TM-84 (1976).

4. D. Garber, C. Dunford, and S. Pearlstein, "Data Formats and Procedures for the Evaluated Nuclear Data File, ENDF," Brookhaven National Laboratory, BNL-NCS-50496 (ENDF 102), also TID-4500 (October 1975).

5. M. A. Abdou and C. W. Maynard, "Nuclear Design of the Magnet Shield for Fusion Reactors," Proc. of the 1st Topical Meeting on the Tech. of Controlled Nuclear Fusion, CONF-740402-P1 (April 1974).

APPENDIX H

FIRST WALL STRESS ANALYSIS

The structural design and analysis of the EPR first wall is based on two general guidelines -- (1) "minimum mass" design within the constraints of the required geometric configuration and the applied mechanical and thermal loads; and (2) maximum first wall lifetime for the prescribed cyclic thermal loading and irradiation-induced changes of material properties.

Minimum mass design is analogous to minimum weight design in the aerospace industry, where the payoff is in reduction of propulsion plant requirements. For the EPR, decreasing the mass of the first wall structure reduces the radiation it absorbs, which is accompanied by a reduction of temperature gradients, thermal lag between parts of the structure during thermal cycling, and thermal stresses. Consequently, the size and complexity of the coolant system required for the first wall can be reduced. Moreover, because the structural functions of the first wall require that its maximum allowable temperature be less than that for the blanket, heat removed from the first wall is less useful from consideration of power plant economics. Decreasing the mass of the first wall also reduces its volume, leaving more room for the blanket and shield within the toroidal field coils. However, minimum mass design also involves trade-offs with fabrication and analysis costs, since it is likely to involve more complex structural configurations and increased hazard of buckling instability.

A number of types of structural failure must be considered in assuring an adequate lifetime for a first-wall structure. Plastic strains resulting from a combination of sustained and cyclic mechanical loads can result in immediate stress failure or low cycle fatigue failure. A sustained mechanical load accompanied by cyclic thermal strains can result in thermal ratcheting, which leads to plastic instability failure or low cycle fatigue failure. High temperature operation under sustained loads can cause creep deformation, resulting in loss of structural function or creep failure. High cycle fatigue failure may result from low amplitude, high frequency strain variations accompanying thermal cycling. Atmospheric pressure acting on the evacuated first wall structure may cause short-time mechanical buckling or, at elevated

temperatures, creep buckling. The long term failure mechanisms are influenced by the effects of strain history and irradiation and thermal environment on material properties. A suitable choice of design restrictions and structural configurations can eliminate some failure mechanisms from consideration, and others can be designed against by a proper choice of structural dimensions and configurations and coolant system specifications.

The general considerations discussed above contribute to a number of decisions and restrictions for the first wall structural design. In addition, design decisions for other EPR components also affect the first wall structural configuration. Analyses providing quantitative information on the sensitivity of stress levels to structural configurations and dimensions are summarized in subsequent sections of this appendix. Some general conclusions and design decisions pertaining to or following from stress analysis of the EPR first wall are:

- The first wall should not be supported directly by the blanket, since temperature differences between the two structures or shifting of the massive blanket blocks could result in failure of the thin-walled vacuum vessel. Support should be provided by struts or hangers with a minimum of constraint to avoid excessive stresses from non-uniform thermal expansion of the vessel and support structure.
- A ring-reinforced thin-walled vacuum vessel is preferable to a thicker uniform-wall shell from minimum mass design considerations for vessels of EPR size.
- Reinforcing rings can be made significantly smaller for a given stress level if the vessel is supported from the sides rather than from the top or bottom.
- Buckling can be prevented by proper design of the vessel wall and its reinforcing rings and stringers. However, further analytical and experimental work is required in this area to assure a reliable design because of the structural complexity of the EPR vacuum vessel. The wall thickness is sized primarily from buckling considerations; therefore, an improvement in the

accuracy of the calculation of the buckling load could result in a reduction in the applied safety factor and a significant decrease in first wall mass.

- Detachable coolant panels should be located inside the vacuum vessel on sliding supports to avoid thermal ratcheting failure and assure a long cyclic fatigue lifetime. The vacuum vessel supports the atmospheric pressure load and the weight of the vessel, detachable coolant panels, and its own coolant system. The detachable coolant panels absorb the brunt of the plasma thermal cyclic load. Thermal ratcheting is caused by the superposition of a sustained mechanical load and a cyclic thermal load which combine to produce plastic strain in the same direction in each cycle and subsequent failure. The separation of coolant panels and vacuum vessel prevents thermal ratcheting of either structure since sustained mechanical loads are not transferred from the vacuum vessel to the coolant panels through the sliding supports and cyclic thermal loading of the vacuum vessel is minimized. Sliding supports also reduce the cyclic thermal strain levels in the detachable coolant panels and thus increase their expected fatigue lifetimes.

- The EPR vacuum vessel is composed of truncated circular shell sections supported by circular rings. The circular cross-section components are easier to fabricate and analyze than a true toroidal shell, but the beveled corners at the joints between shell sections present stress problems which should be analyzed in detail.

- The EPR vacuum vessel and its support structure are designed to equilibrate all mechanical loads by elastic stresses to avoid any failure mechanisms involving plastic strain. Some plastic deformation of the coolant panels from thermal loads will be permitted since they perform no structural function.

- The maximum allowable operating temperature for the first wall structural material (Type 316 stainless steel) is set at 500°C to avoid thermal creep problems.

- The allowable design stress for structural components analyzed in subsequent sections of this appendix is set at two-thirds of the yield stress to allow a margin in the elastic range to cover stress concentrations and design features not included in the initial analyses. It is customary[1] to set allowable stress limits of $\sigma_m < \frac{2}{3}\sigma_y$ and $\sigma_m + \sigma_b < \sigma_y$, where σ_m, σ_b, and σ_y are primary membrane stress, primary bending stress, and yield stress, respectively; this assumes plastic shakedown of secondary stresses will occur in the first few load cycles in regions of stress concentration, so that subsequent cycles are elastic. However, the EPR first wall is subjected to cyclic variations from both the burn cycle and the reactor start-up shut-down procedure. The more conservative design assumption of $\sigma_m + \sigma_b < \frac{2}{3}\sigma_y$ is used here to lessen the likelihood of low-cycle fatigue failure aggravated by the severe thermal and radiation environment. It also provides a design margin to allow for features not covered in the analyses described in this appendix and to allow for some of the approximating assumptions used here. As more detailed analyses are performed, it will be possible to reduce some of the conservatism in the specification of design stress.

In the sections that follow, θ is the angular coordinate measured around the circumference of the vessel cross-section and x is the axial coordinate measured along the plasma axis. The components $\sigma_{\theta m}$, $\sigma_{\theta b}$, σ_{xm} and σ_{xb} denote membrane and bending stresses in the circumferential and axial directions. Membrane stresses are uniform across the wall thickness; bending stresses vary linearly across the thickness, being equal and opposite on the inner and outer surfaces. The upper and lower signs in expressions of the form $\sigma_{\theta b} = \pm f$ denote stress values on the outer and inner surfaces of the shell wall, respectively. Table H-1 gives values of frequently used parameters.

Table H-1. First Wall Structural Parameters

R_o, major radius of toroidal shell	6.25 m
R_s, radius of first wall cross section	2.40 m
E, elastic modulus	22.6×10^6 psi
ν, Poisson's ratio	0.3
$E_o = E/(1-\nu^2)$	25×10^6 psi
$\mu = [3\ (1-\nu^2)]^{-1/4}$	0.778
α, coefficient of thermal expansion	1.03×10^{-5}/°F
σ_y, yield stress	17,000 psi
σ_a, allowable stress	10,000 psi
γ, specific weight	0.28 lbs/in.^{3}

The toroidal vacuum vessel is approximated by a straight circular cylindrical shell in many of the following analyses. Implications of this approximation for various loading conditions have been discussed elsewhere.[2]

1. Effect of Constraints on First Wall Thermal Stresses

Stresses in the vacuum vessel resulting from the temperature difference between it and its support structure will be discussed here, and those resulting from the weight of the vessel and atmospheric pressure will be included in later sections.

Let the toroidal vacuum vessel be approximated by a straight circular cylindrical shell having the same cross section and having a uniform wall thickness. Assume the shell is connected at N equally spaced locations around its circumference to supporting structure which is at a different average temperature. Then, making use of results in Reference 3, the stresses in the shell at the supports are given by

$$\sigma_{\theta m} = -\frac{E_o \alpha h^2}{6R^2} \Delta T\ f(\beta)\ \cos\beta,$$
$$\sigma_{\theta b} = \mp \frac{E_o \alpha h}{R\beta} \Delta T\ f(\beta)\ (\sin\beta - \beta\cos\beta), \qquad \text{(H-1)}$$

where

$$\beta = \pi/N,$$

$$f(\beta) = \beta \sin\beta \left[\left(1 + \frac{h^2}{12\ R^2}\right)\beta(\beta + \sin\beta\cos\beta) - 2\sin^2\beta \right], \quad \text{(H-2)}$$

and ΔT is the average temperature of the vessel minus the average temperature of its supports. As the supports become continuous around the circumference of the shell, i.e., as $N \to \infty$,

$$\begin{aligned} \sigma_{\theta m} &\to E_o \alpha \Delta T, \\ \sigma_{\theta b} &\to 0, \end{aligned} \quad \text{(H-3)}$$

independently of the wall thickness.

Figure H-1 shows $\sigma_{\theta m}/\Delta T$, $\sigma_{\theta b}/\Delta T$, and their sum as functions of number of support locations, N, for a wall thickness, h, of 2 cm. Continuous curves are shown, but only integer values of N are physically realistic. As the number of supports become large, $\sigma_\theta/\Delta T$ becomes approximately 250 psi/°F, i.e., a 100°F temperature difference between the vacuum vessel and its support structure would produce a stress of about 25,000 psi, not including the stress due to vessel weight and atmospheric pressure. Therefore, supporting the first wall continuously by the blanket would present significant design problems in controlling the temperatures of first wall, blanket, and vacuum and beam ducts to avoid excessive thermal stresses in the thin-walled vacuum vessel. For simple hanger supports, i.e., N = 1, the thermal stresses due to support constraints vanish.

Consequently, the support system for the first wall should constrain the vacuum vessel as little as possible to avoid excessive thermal stresses during reactor start-up and operation.

The temperature drop δT through the first wall produces a bending stress given by

$$\sigma_{\theta b} = \pm \frac{E\alpha}{2(1-\nu)}\ \delta T \quad \text{(H-4)}$$

so that varying the wall thickness affects this stress component only insofar as it affects the temperature drop.

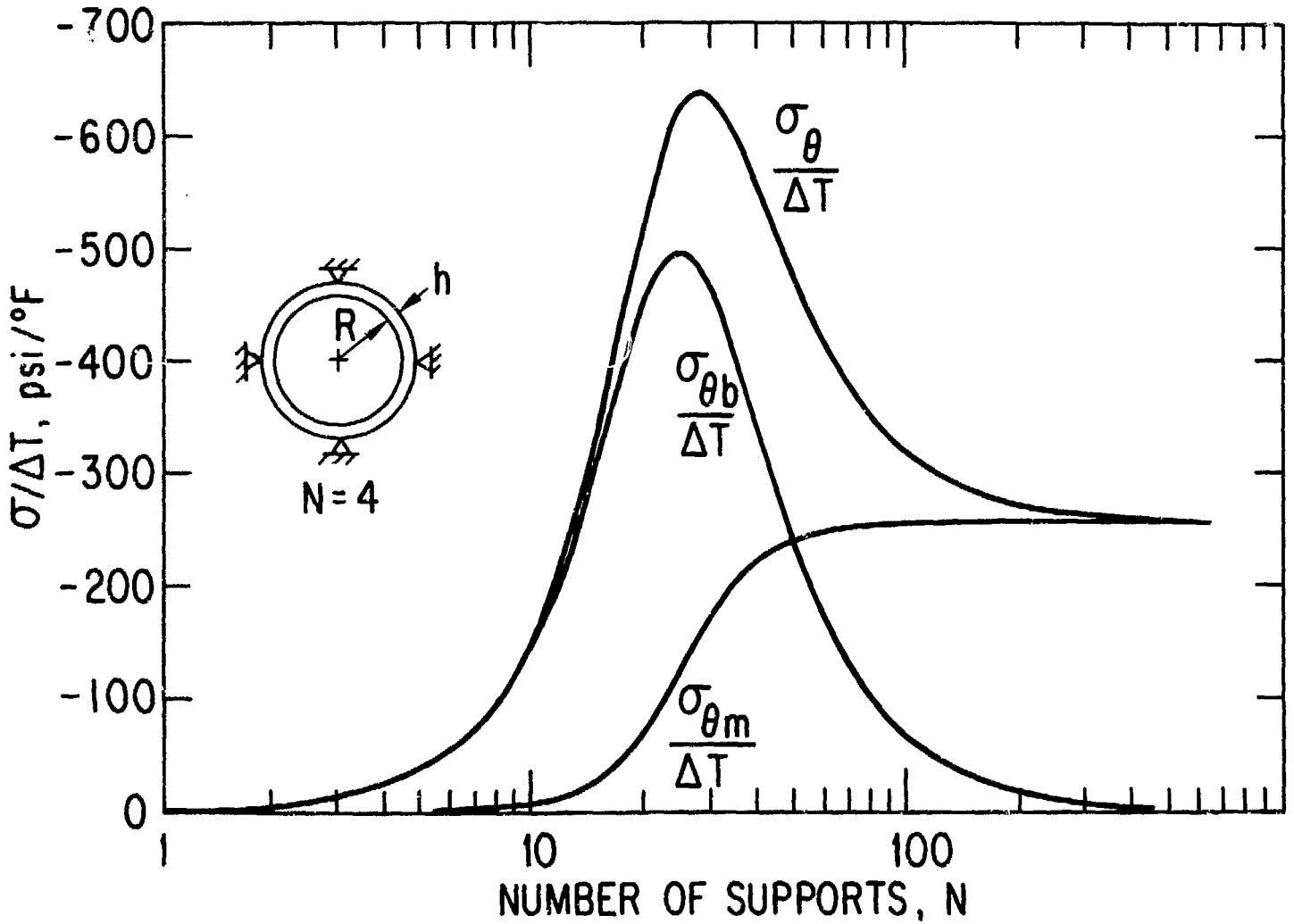

Figure H-1. Thermal Stress in Shell as a Function of Number of Support Locations

2. Stress in Uniform-Thickness Wall

The feasibility of using a uniform-thickness vacuum vessel to sustain the atmospheric, gravitational, and thermal loadings is investigated in this section.

a. Solid Wall

For uniform external pressure p, the circumferential and axial membrane stresses in a toroidal shell with circular cross sections are[4]

$$\sigma_{\theta m} = - \frac{pR}{2h} \frac{(2R_o + R \sin\theta)}{(R_o + R \sin\theta)} ,$$

$$\sigma_{xm} = - \frac{pR}{2h} . \qquad \text{(H-5)}$$

The corresponding stresses in a straight circular cylindrical shell with the same cross-sectional dimensions and capped ends are

$$\sigma_{\theta m} = - \frac{pR}{h} ,$$

$$\sigma_{xm} = - \frac{pR}{2h} . \qquad \text{(H-6)}$$

Figure H-2 shows the stresses produced by atmospheric pressure as a function of angular position for h = 2 cm. Approximating the toroidal shell by a straight shell is non-conservative at $\theta = -90°$ and conservative at $\theta = +90°$; the solutions agree at the top and bottom of the shells. Since the maximum stresses caused by the weight of the shell occur at the top and bottom and are considerably larger than those produced by atmospheric pressure, the use of cylindrical shell solutions for the vacuum vessel analysis appears reasonable. However, the reliability of this procedure requires further investigation.[2]

Consider a shell hung from a rigid beam at the top. The circumferential bending stress distribution resulting from the weight of the shell is given by[3]

$$\sigma_{\theta b} = \pm \frac{6\gamma R^2}{h} \left[1 + \frac{1}{2} \cos\theta - (\pi - \theta) \sin\theta\right] , \qquad \text{(H-7)}$$

and the sag at the bottom is

$$\Delta D = 3 (\pi^2 - 8) \frac{\gamma R^4}{E_o h^2} . \qquad \text{(H-8)}$$

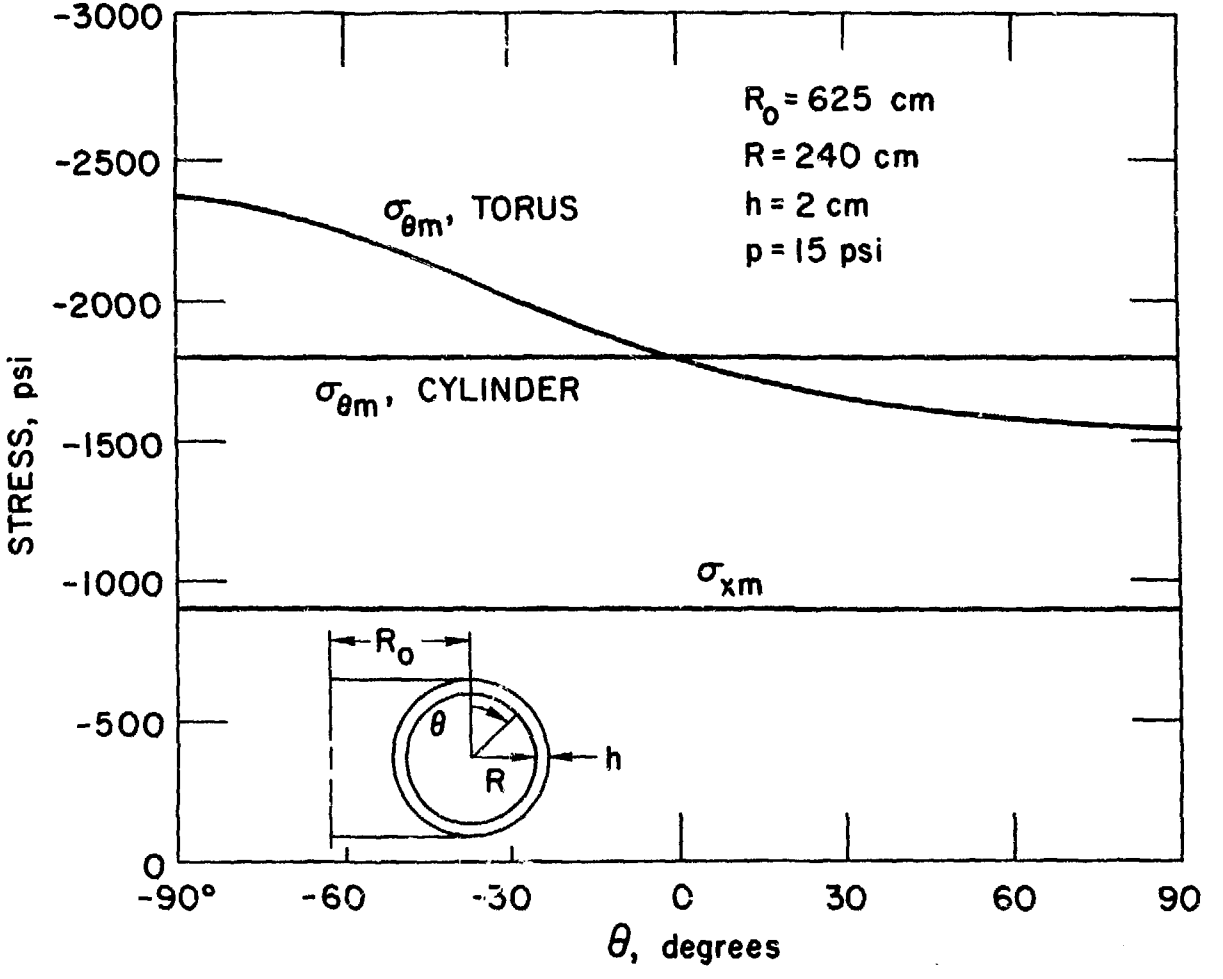

Figure H-2. Membrane Stress Distributions in a Toroidal Shell and Circular Cylindrical Shell.

The circumferential membrane stress resulting from the weight is negligible compared to the bending stress.

In general, the stress distribution in the shell results from support constraint against thermal expansion, atmospheric pressure, and the shell weight. The support constraint is zero for this case (N = 1 in Figure H-1). The maximum stress from the other two loadings occurs at the inside surface at the top of the shell and is found by adding $\sigma_{\theta m}$ from Equation H-6 to $\sigma_{\theta b}$ from Equation H-7 for $\theta = 0$. The result is shown in Figure H-3 as a function of wall thickness, along with the sag at the bottom. A wall thickness of about 6 cm would be required to satisfy the design stress value of 10,000 psi. A solid wall of this thickness would be difficult to cool evenly.

Supporting the shell at several points around its circumference was studied also. A significant reduction in wall thickness is then theoretically possible. However, the analysis is quite sensitive to the proper distribution of the shell weight among the supports, so that design and fabrication difficulties make this support configuration impractical.

b. Sandwich Wall

Another design concept that was investigated was using sandwich wall construction for the shell. Consider a shell wall of thickness h composed of two stainless steel cover plates of thickness h_o connected by a core which is k percent stainless steel. Since the core provides the shear connection between the cover plates, it must be securely attached to them and strong enough to cause the sandwich wall to bend as a unit. The maximum bending stress produced by the shell weight occurs at the top and is given by

$$(\sigma_b)_{max} = \pm \frac{9\gamma R^2 h}{2h_o} \left[\frac{2(1-k)h_o + kh}{h_o^2 + 3\,(h - h_o)^2} \right] \qquad \text{(H-9)}$$

The sag at the bottom is

$$\Delta D = \frac{\pi^2 - 8}{3} \frac{R^2}{E_o h} \left| (\sigma_b)_{max} \right| \quad . \qquad \text{(H-10)}$$

Figure H-4 shows the maximum stress from the shell weight and atmospheric pressure as a function of wall thickness for various wall constructions. For a design stress of 10,000 psi, the savings in mass to absorb radiation

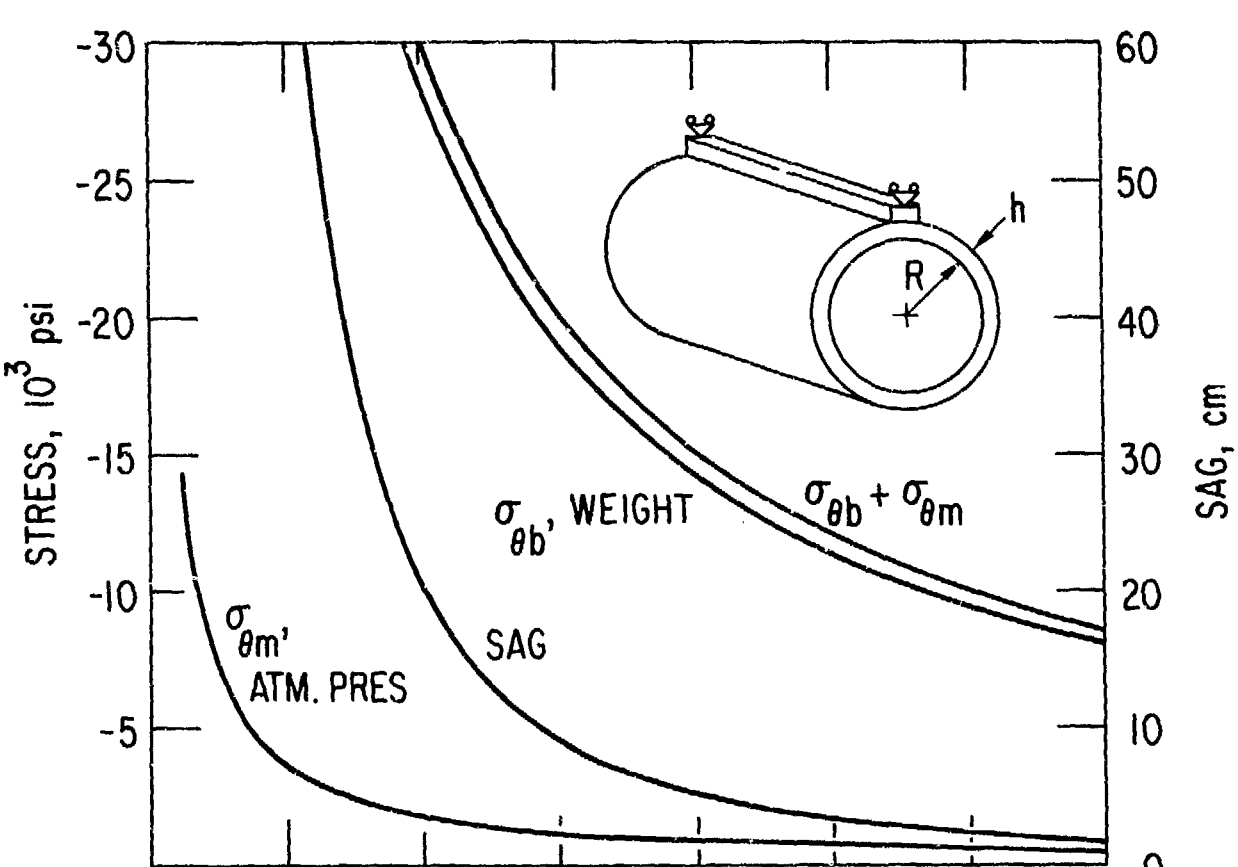

Figure H-3. Maximum Stress and Sag for Uniform Thickness Shell Supported from Top.

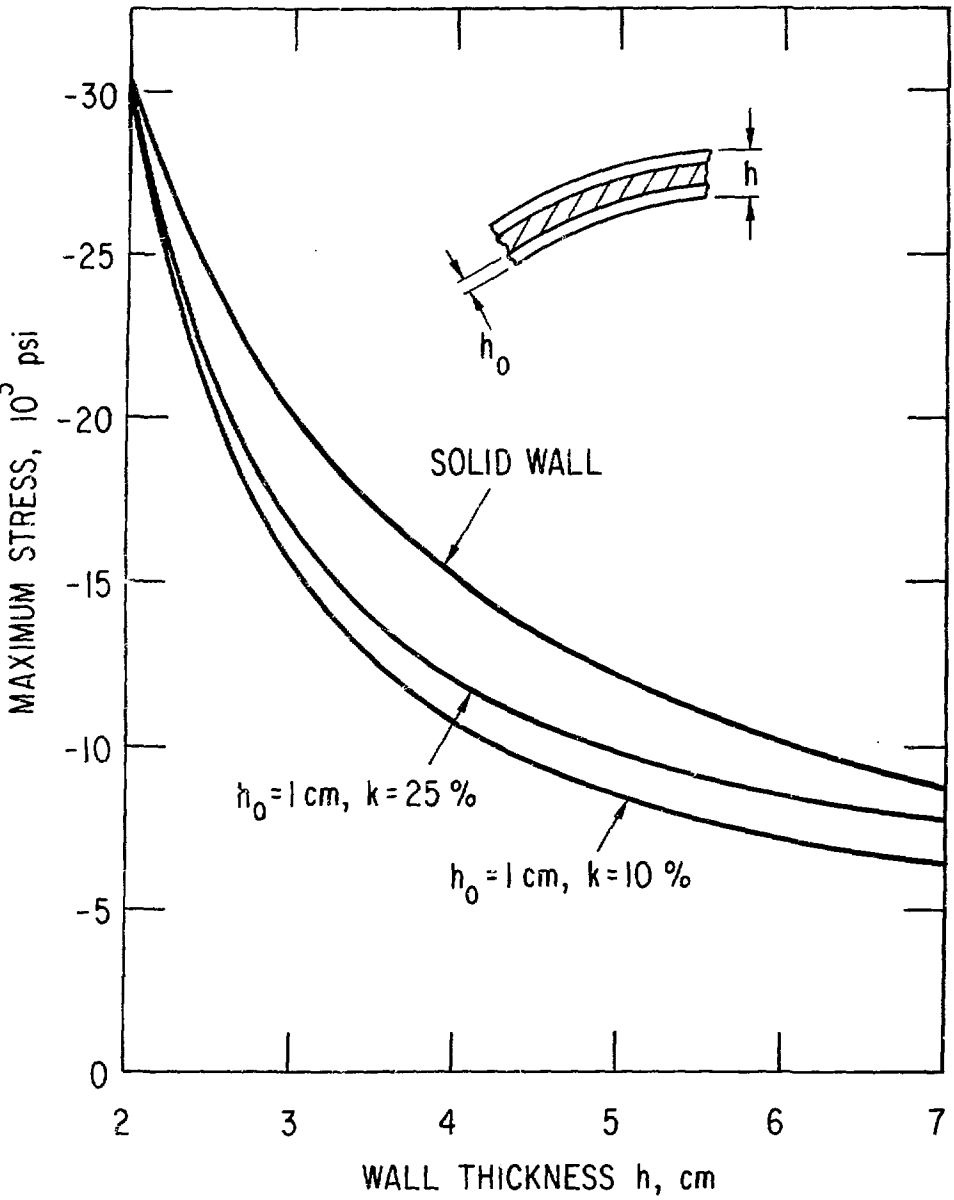

Figure H-4. Maximum Stress for Sandwich-Wall Shell Supported from Top

and require cooling is significant compared to a solid wall, as is shown in Table H-2.

Table H-2. Shell Mass Comparison for Sandwich Wall*

Configuration	h, cm	Mass per unit axial length kg/m
Solid wall	6	7030
h_o = 1 cm, k = 25%	5	3220
h_o = 1 cm, k = 10%	4.25	2610

* for maximum stress of 10,000 psi.

The major drawback of the sandwich wall is fabrication; fastening the core to the cover plates with sufficient rigidity to prevent crushing of the cross section in bending would require a difficult and expensive welding operation. The ring supported uniform shell construction discussed in the next section is comparable to the sandwich wall construction in weight and is much easier to fabricate.

3. Stress in Ring-Stiffened Shell

From Figure H-3 it is apparent that the main contribution to the stress in a uniform-wall shell hung from the top is the distortion of the cross section caused by the shell weight. Reinforcing rings reduce this distortion and result in thinner wall, lighter weight construction for a given peak stress. Because of the numerous penetrations of the first wall for vacuum and injection ports, there are not many locations suitable for continuous reinforcing rings. Rings spaced about one meter apart and straddling the vacuum ports clear the injection ports and can provide adequate support for the vacuum wall and its coolant system.

a. Effect of Ring Weight, Shell Weight, and Pressure Differential on Ring Dimensions

Consider stainless steel reinforcing rings of width c, depth b, and spacing L connected by sections of thin-walled, circular cylindrical shell of radius R and thickness h (see Figure H-5). Assume the rings

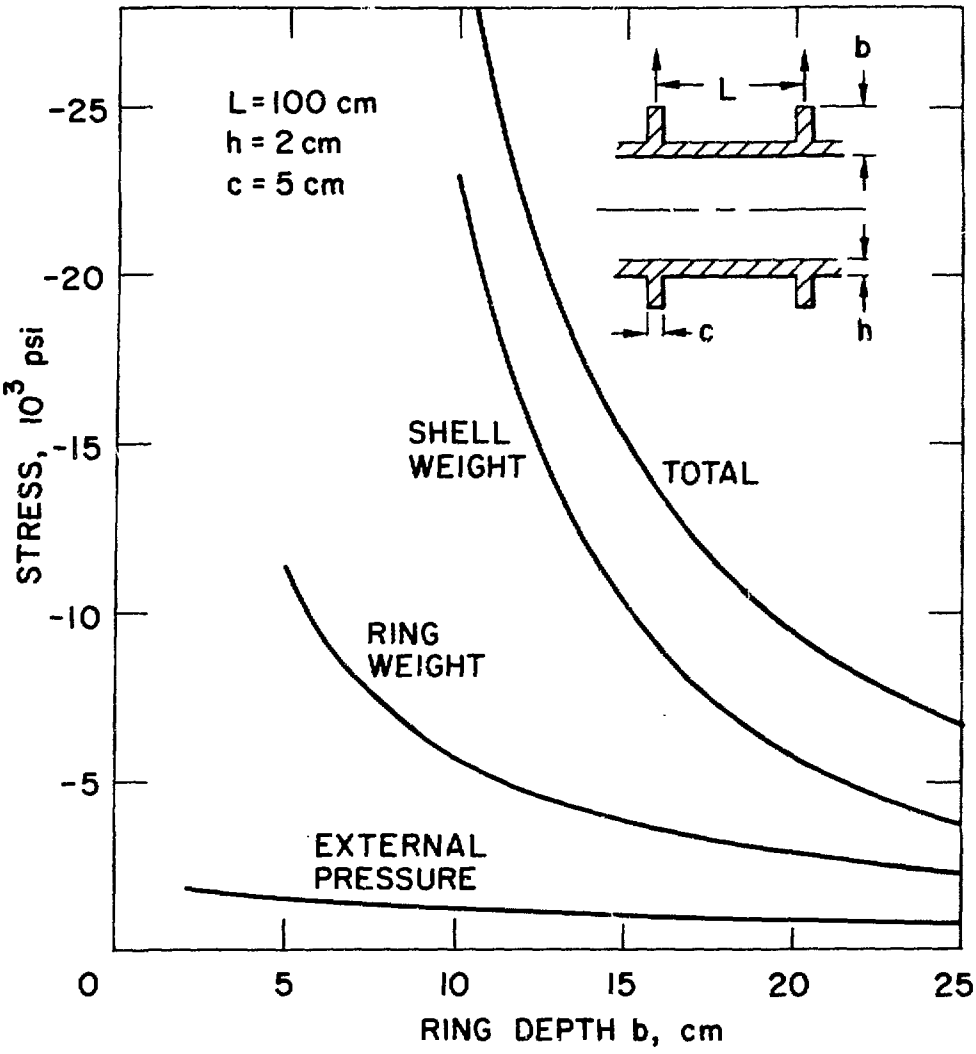

Figure H-5. Maximum Stress in Reinforcing Ring Resulting From Various Loads.

are hung from the top. The bending stress in the ring resulting from the weight of the shell which it supports is[3]

$$\sigma_{\theta b} = + \frac{6\gamma_s h R^2 (L-c)}{cb^2} \left[1 + \frac{1}{2}\cos\theta - (\pi-\theta)\sin\theta\right] . \qquad \text{(H-11)}$$

The bending stress in the ring from its own weight is[3]

$$\sigma_{\theta b} = + \frac{6\gamma_r R^2}{b} \left[1 + \frac{1}{2}\cos\theta - (\pi-\theta)\sin\theta\right] . \qquad \text{(H-12)}$$

The circumferential membrane stresses for both these loadings are negligible compared to the bending stresses. The membrane stress in the ring from atmospheric pressure p acting on the evacuated ring and shell structure is[3]

$$\sigma_{\theta m} = - pR \left[\frac{2\alpha\sqrt{hR} + c}{2\alpha h\sqrt{hR} + cb}\right] , \qquad \text{(H-13)}$$

where α is defined in Table H-1. The total circumferential stress is the sum of the components given by Equations H-11, H-12, and H-13; its maximum occurs at the inside surface at the top ($\theta = 0$). Figure H-5 shows the three components and their total as a function of ring depth b, for L = 1 m, c = 5 cm, h = 2 cm and parameters given in Table H-1. (This value of h is based on the buckling analysis described in the next section.) For a design stress of 10,000 psi, Figure H-5 indicates that a ring depth of about 19 cm would be required. If the ring width is increased to 10 cm, the required ring depth is reduced to about 15 cm.

The average mass of these ring and shell structures per unit axial length of shell are 3340 kg/m and 3870 kg/m for the 5 cm and 10 cm width rings, respectively. These contrast with 7030 kg/m for the uniform wall shell.

The ring dimensions determined above would not be considered unreasonable for most structural applications of the size of the first wall torus; however, for an EPR design, rings of these sizes might be difficult to cool, interfere with the blanket, or cause assembly problems. Consequently, methods were investigated for reducing the size of the rings while maintaining a design stress of 10,000 psi and the 1 m ring spacing.

b. Effect of Support Location on Ring Dimensions

One way by which smaller rings could be utilized is by moving the support location away from the top or bottom of the ring. Consider symmetric supports located at an angle β from the top of the ring. The bending stress in the ring resulting from the weight of the shell which it supports is[3]

$$\sigma_{\theta b} = \pm \frac{6\gamma h R^2 (L-c)}{cb^2} K(\theta,\beta), \tag{H-14}$$

and the bending stress in the ring from its own weight is

$$\sigma_{\theta b} = \pm \frac{6\gamma R^2}{b} K(\theta,\beta) . \tag{H-15}$$

In the above, K is defined by

$$\begin{aligned} K(\theta,\beta) &= \cos\beta - (\pi-\beta)\sin\beta + (\tfrac{1}{2} + \sin^2\beta)\cos\theta + \theta\sin\theta, \quad 0 \le \theta \le \beta; \\ K(\theta,\beta) &= \cos\beta + \beta\sin\beta + (\tfrac{1}{2} + \sin^2\beta)\cos\theta - (\pi-\theta)\sin\theta, \quad \beta \le \theta \le \pi. \end{aligned} \tag{H-16}$$

Figure H-6 shows K as a function of θ for several values of β. The maximum stress occurs where $|K|$ is a maximum; let θ_{max} denote this location for a given support location. Table H-3 gives θ_{max} and $K(\theta_{max},\beta)$ for various β.

Table H-3. Maximum Stress Location for Ring-Reinforced Shell

β	θ_{max}	$K(\theta_{max},\beta)$
0°	0°	1.50
22.5°	22.5°	0.619
45°	90°	-0.308
67.5°	67.5°	0.175
90°	66.8°, 113.2°	±0.0917

Figure H-7 shows the maximum circumferential stress in a ring supported at various locations as a function of ring depth b for a ring width c of 5 cm and a shell thickness h of 2 cm. This maximum stress is the sum of the bending stresses given by Equations H-14 and H-15, with K being given in Table H-3, plus the membrane stress resulting from atmospheric pressure

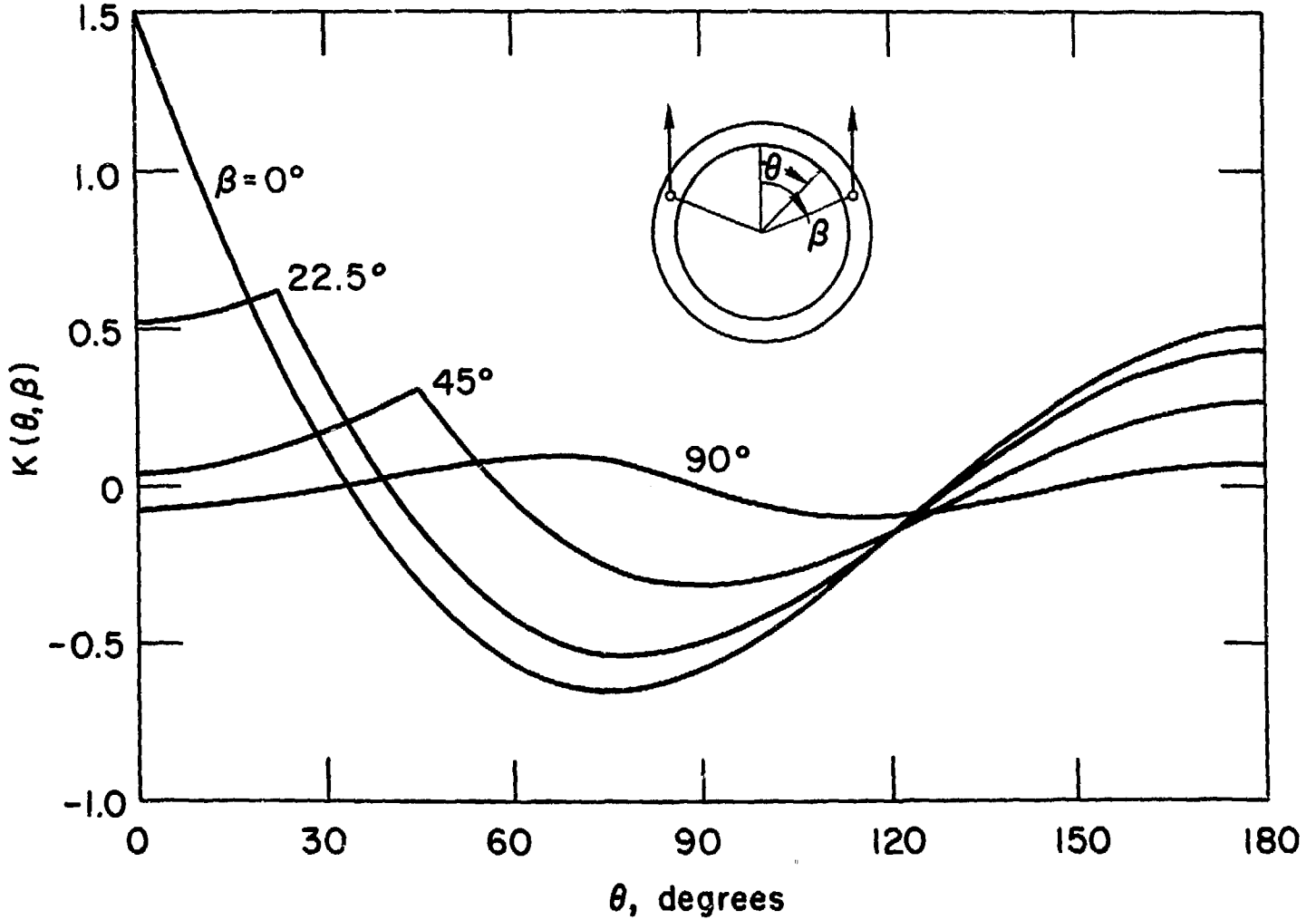

Figure H-6. $K(\theta, \beta)$ for Various Values of Support Location β.

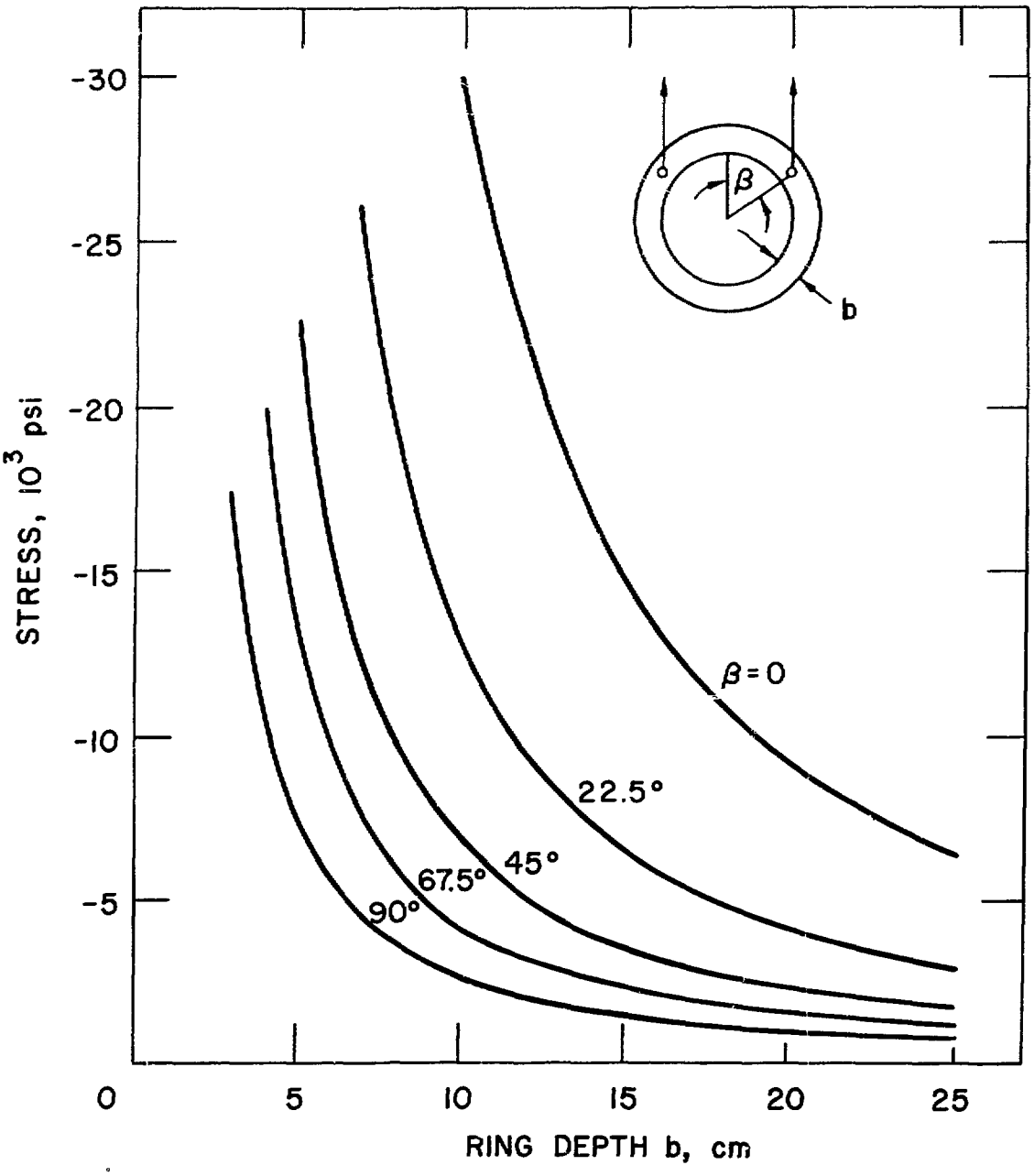

Figure H-7. Maximum Stress in Reinforcing Ring Supported at Various Locations.

given by Equation H-13. A significant reduction in ring depth is possible for a given maximum stress if the supports are moved away from the top of the ring. This occurs because the ring tends to distort less under a distributed weight if the supports are moved out. Table H-4 gives ring dimensions and vessel mass per unit axial length for various shell constructions. For the thinner ring configurations, the rings account for only about 10% of the total mass, so further mass reduction would have to come primarily from a decrease in the shell wall thickness h; this thickness is determined by buckling considerations, as discussed in Section 4 of this Appendix.

Table H-4. Shell Mass Comparison for Various Vessel Designs*

Configuration	h, cm	$\bar{\theta}$	c, cm	b, cm	Mass per Unit Length, kg/m
Uniform Wall	6	0°	-	-	7030
Ring-Reinforced	2	0°	5	19	3340
Ring-Reinforced	2	0°	10	15	3870
Ring-Reinforced	2	22.5°	5	12	2930
Ring-Reinforced	2	45°	5	8	2690
Ring-Reinforced	2	67.5°	5	6	2580
Ring-Reinforced	2	90°	5	4.5	2490

* for maximum stress of 10,000 psi.

c. Tapered Rings

Another technique for reducing the dimensions of a reinforcing ring is to vary the depth of the ring around its circumference. Since the stress varies around the circumference of a uniform ring as shown in Figure H-6, a more uniform stress state would be achieved by reducing ring dimensions in lightly loaded regions. Because the maximum stress in a ring supported at the top is at the top, its depth at the sides can be reduced by about one-third. The rings would then not intrude as far into the inner blanket region where space is at a premium. A similar reduction would not be possible for a ring supported away from the top because the maximum stress location then moves toward the side of the ring. A tapered ring would be more expensive to design and fabricate than a uniform ring. On the other hand, if the ring is supported at the top it might

be easier to combine its support structure with the vacuum port support structure and thereby result in less interference with blanket assembly and disassembly than a ring supported at the sides.

d. Effect of Coolant Panel Weight on Ring Dimensions

In the analyses described in subsections (1) and (2) above, the weight of the coolant panels and other coolant system hardware supported by the vacuum vessel was not included in sizing the reinforcing rings. Let the weight of the coolant panels, vacuum vessel coolant channels, and associated piping, manifolding, and supports be equivalent to an additional thickness h* of stainless steel shell. The circumferential bending stress in the ring corresponding to this additional weight is

$$\sigma_{\vartheta b} = \pm \frac{6\gamma h^* R^2 L}{cb^2} K(\vartheta,\beta), \qquad \text{(H-17)}$$

where K is again defined by Equation H-16. Figure H-8 shows the maximum stress in the ring resulting from the weight of the shell (Equation H-14), the weight of the ring (Equation H-15), the pressure differential across the vacuum wall (Equation H-13), and the weight of the first wall coolant system (Equation H-17) for a 5-cm-wide ring supported from the top. Figure H-9 gives the maximum stress if the supports are moved to a 45° location. For the EPR design, h* is approximately 2 cm. The design stress of 10,000 psi then corresponds to ring depths of 26 cm and 11 cm for these support cases. Increasing the ring widths to 10 cm results in a decrease of required ring depths to 19 cm and 8 cm for $\beta = 0°$ and $\beta = 45°$, respectively.

e. Stress Concentrations

The geometric discontinuity in wall thickness at the junction of ring and shell results in the portion of shell near the relatively stiffer ring being more highly stressed then the remainder of the shell.[5] The stress concentrations caused by the pressure differential across the vacuum vessel wall and by the average difference between shell temperature and ring temperature are described here.

The axial bending stress in the shell near the ring resulting from the external atmospheric pressure p is (H-18)

$$\sigma_{xb}(x) = \pm\frac{3pR}{h}\,\frac{\mu^2 c\,(b-h)}{2\mu h\,\sqrt{Rh} + bc}\,\exp\left(-\frac{x}{\mu\sqrt{Rh}}\right)\left[\cos\left(\frac{x}{\mu\sqrt{Rh}}\right) - \sin\left(\frac{x}{\mu\sqrt{Rh}}\right)\right]$$

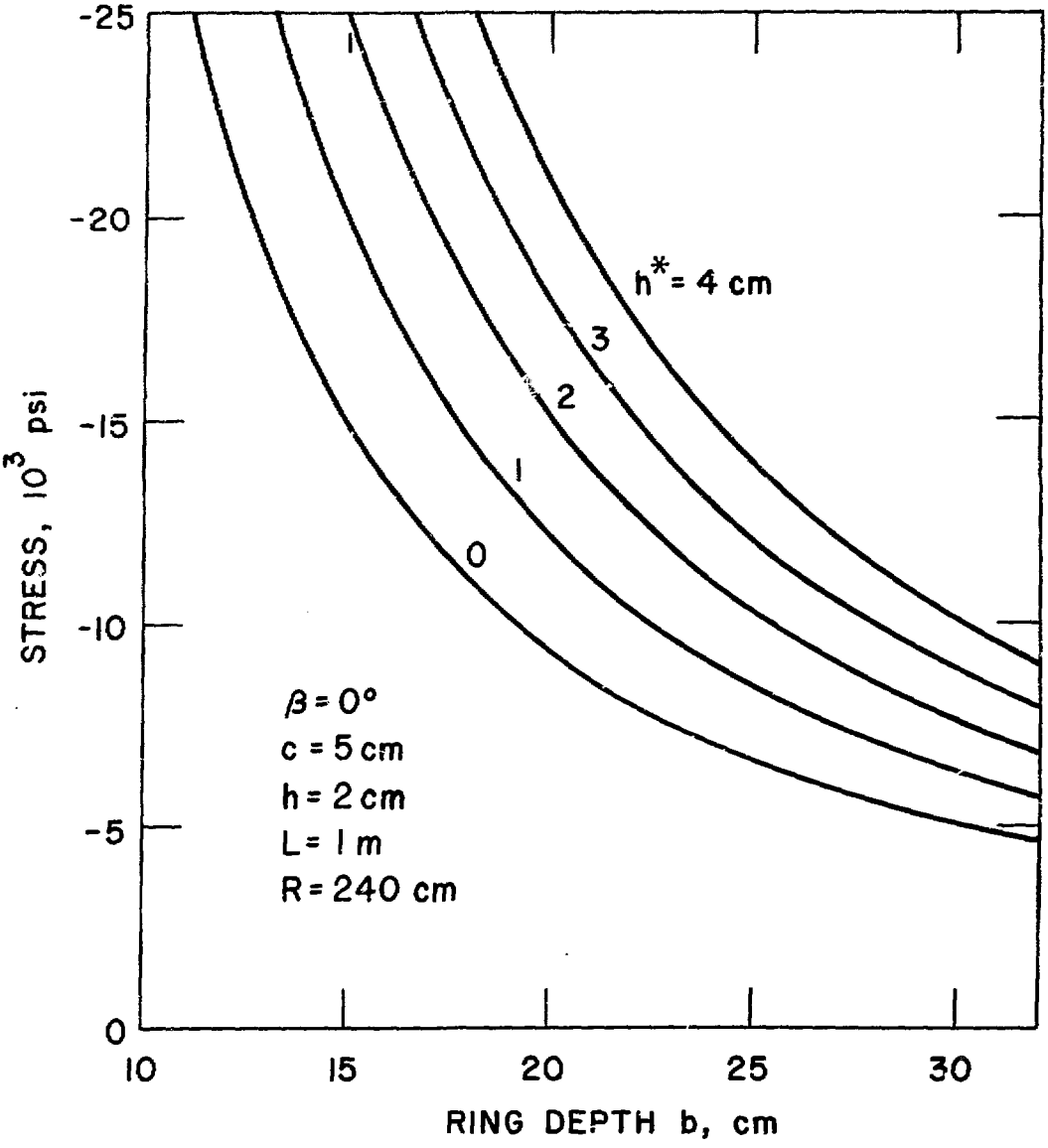

Figure H-8. Effect of Coolant Panel Weight on Reinforcing Ring Depth; Support at Top

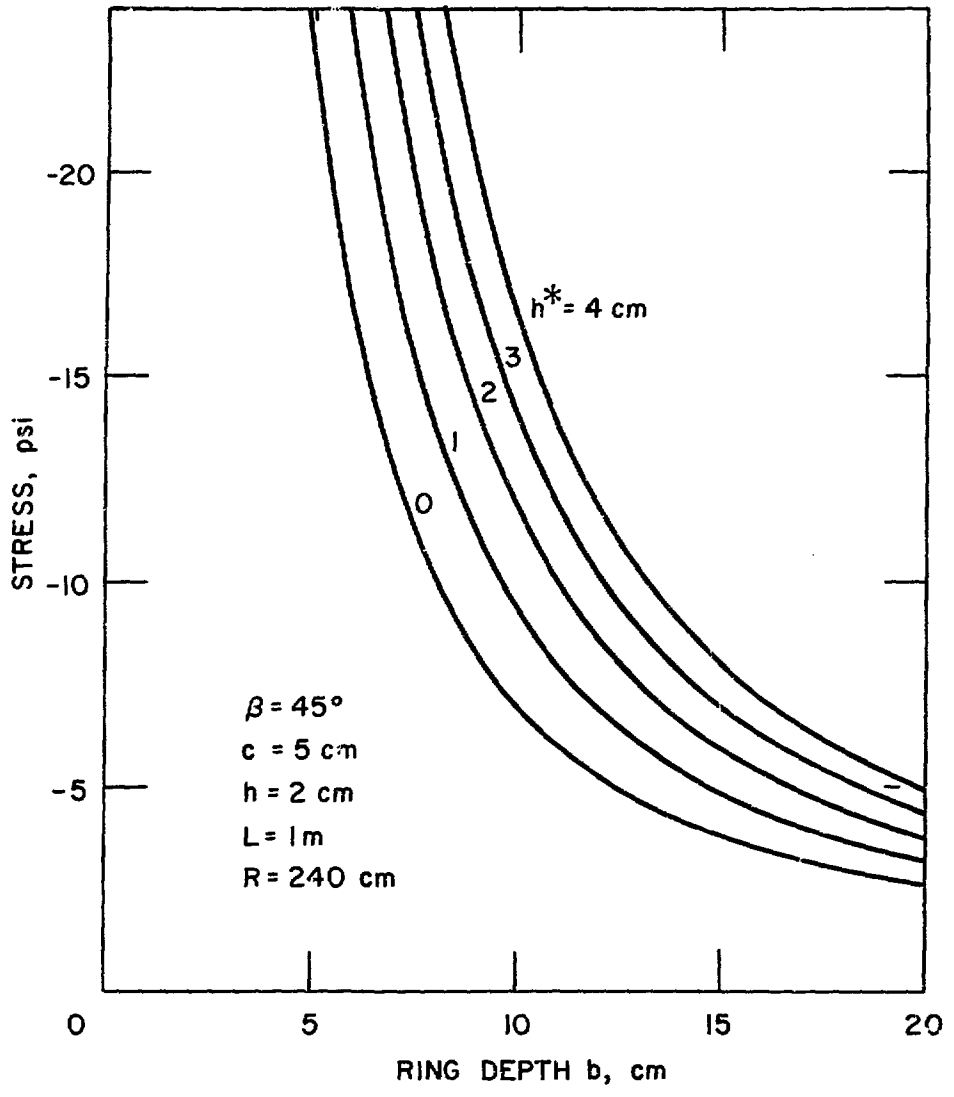

Figure H-9. Effect of Coolant Panel Weight on Reinforcing Ring Depth; Support at 45°

The circumferential membrane stress $\sigma_{\theta m}$ in the shell at the ring is equal to the corresponding stress in the ring as given by Equation H-13; it decays with the same exponential behavior as σ_{xb} to $-pR/h$ as x increases. Figure H-10 shows the stress components σ_{xb} and $\sigma_{\theta m}$ in the shell at the ring as a function of ring depth. For the ring sizes treated here, the discontinuity stresses are less than 2000 psi.

If the ring is at an average temperature T_r and the shell is at an average temperature T_s, the axial bending stress and circumferential membrane stress in the shell at the ring are

$$\sigma_{xb}(0) = \pm \frac{3\mu^2 cb\, E\alpha\, (T_r - T_s)}{2\mu h\, \sqrt{Rh} + bc}\ ,$$

$$\sigma_{\theta m}(0) = \frac{bc\, E\alpha\, (T_r - T_s)}{2\mu h\, \sqrt{Rh} + bc}\ . \qquad \text{(H-19)}$$

The variation with x is similar to that in Equation H-18. The corresponding circumferential membrane stress in the ring is

$$\sigma_{\theta m} = -\frac{2\mu\, \sqrt{Rh}\, E\alpha\, (T_r - T_s)}{2\mu h\, \sqrt{Rh} + bc}\ . \qquad \text{(H-20)}$$

The stress components resulting from the temperature difference $T_r - T_s$ are shown in Figure H-11. For rings of the size considered here, the shell stresses are approximately 200 psi/°F, so reasonably uniform temperature distributions must be provided by the structural coolant system to avoid large localized thermal stresses.

4. Buckling

A detailed buckling analysis of the EPR vacuum vessel composed of a ring and stringer reinforced polygonal shell of an approximate toroidal shape would be beyond the scope of the current design effort. Buckling loads for some simpler idealized structural configurations were determined to provide a basis for sizing the vacuum wall thickness.

Consider first a uniform-wall shell without reinforcing rings or stringers. Sobel and Flügge[6] give buckling pressures for thin-walled toroidal shells as a function of the ratios of major to minor radius, R_o/R, and minor radius to wall thickness, R/h. Their results are shown

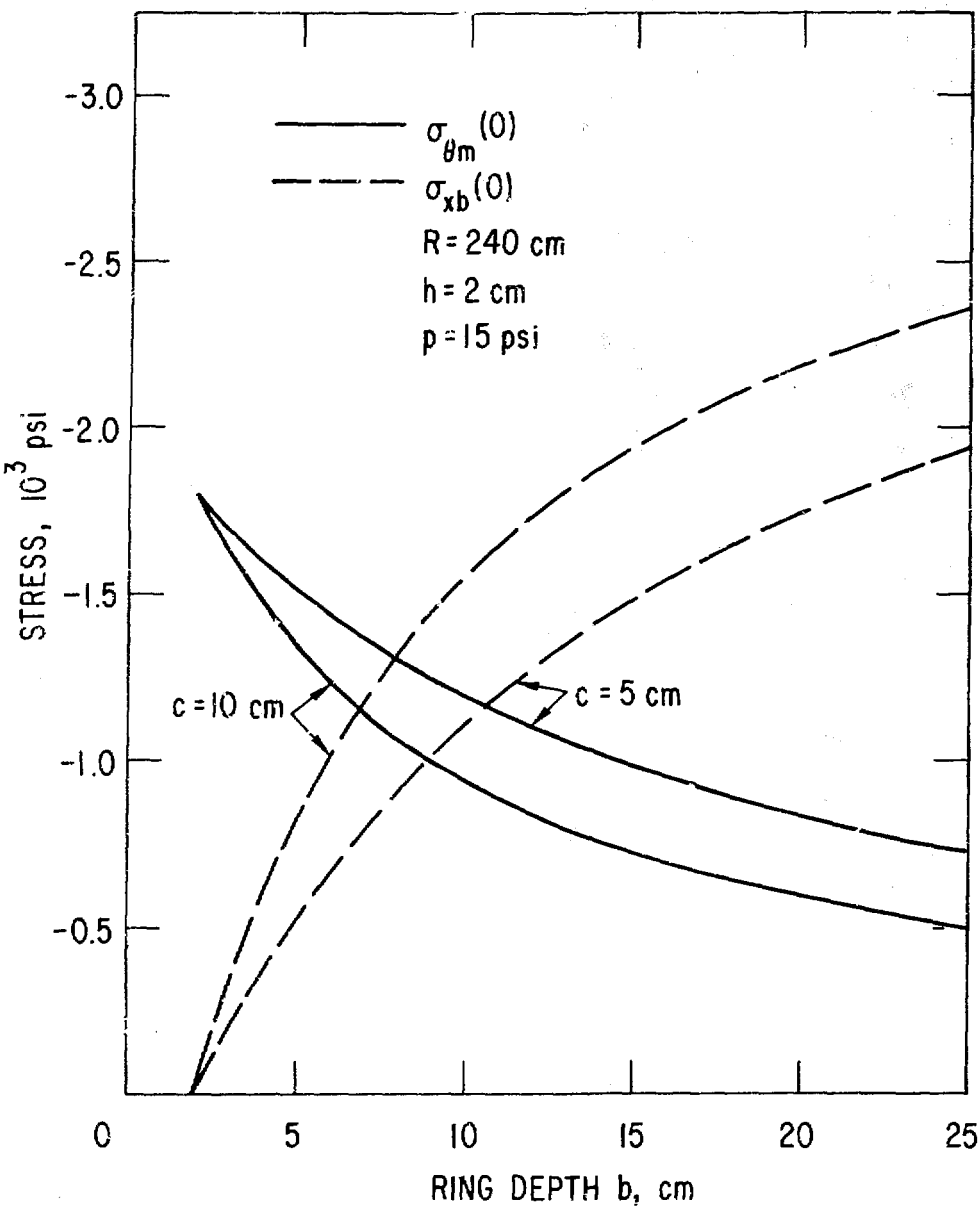

Figure H-10. Discontinuity Stresses at Shell-Ring Intersection Resulting from Vacuum Load.

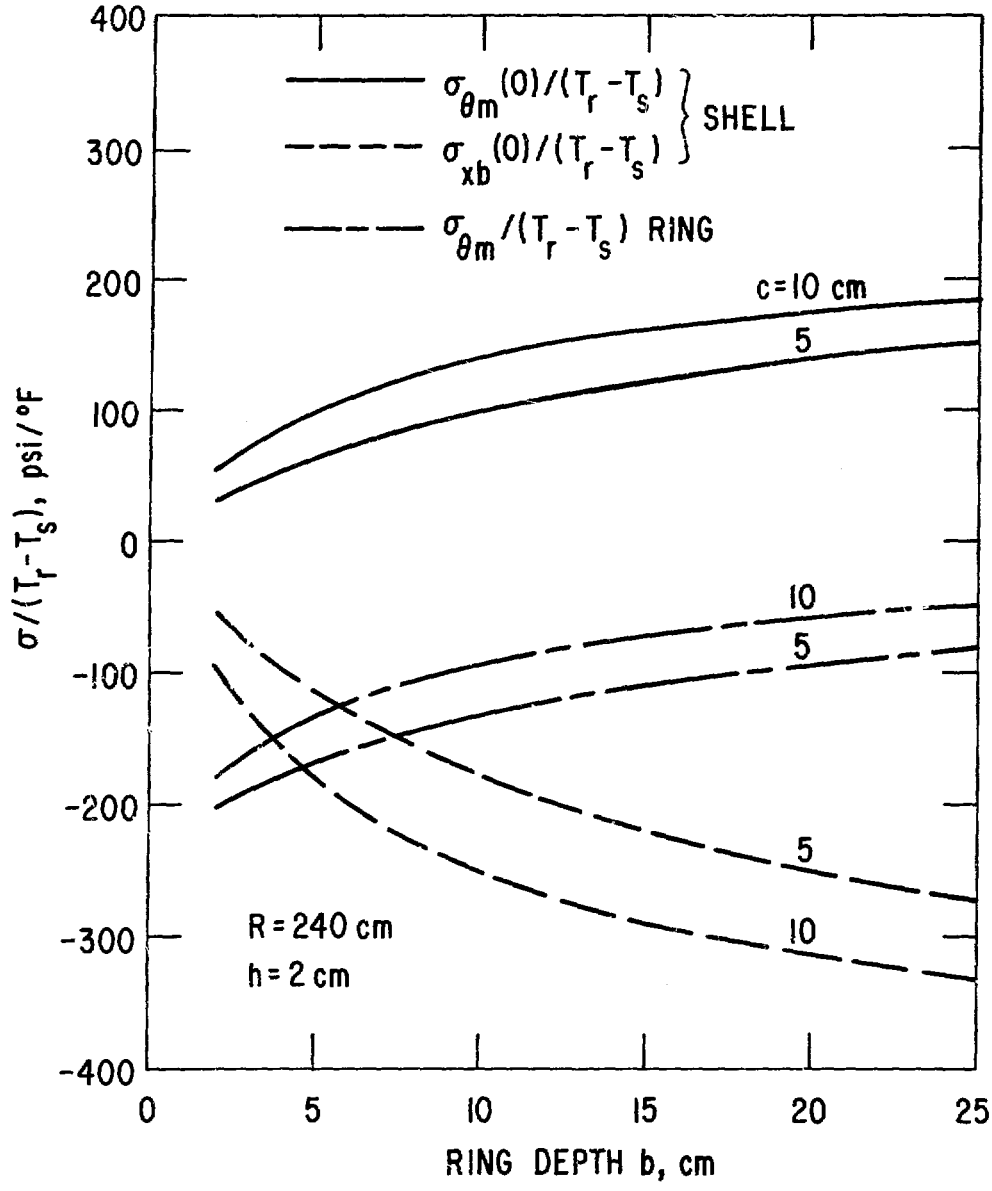

Figure H-11. Discontinuity Stresses at Shell-Ring Intersection Resulting from Temperature Difference.

in Figure H-12 as a function of wall thickness for R_o = 6.25 m and R = 2.4 m. For comparison, the buckling pressure of a long cylindrical shell of radius R is shown also; it is given by[3]

$$(p)_{buck} = \frac{E_o h^3}{4R^3} \quad . \tag{H-21}$$

The toroidal shell can withstand a considerably higher pressure because of the double curvature of its wall. The polygonal EPR vessel is composed of truncated sections of cylindrical shells. Although it lacks the double curvature of the toroidal shell, its beveled joints should provide a stiffening effect. Consequently, the results for a polygonal vessel should lie between those for toroidal and cylindrical vessels. The buckling mode configuration for a toroidal shell are quite complex; moreover, for EPR dimensions, Sobel and Flügge show that the buckling pressures for the three lowest modes almost coincide. In commenting on these results, Baker, Kovalevsky, and Rish[7] state, "For values of [R_o/R] less than 6.3, the buckling pressure should be verified by test." The ratio R_o/R for the EPR vessel is 2.6, and the buckling modes corresponding to its polygonal shape are probably more complex than those for the ideal toroidal shell.

Figure H-12 also shows buckling pressures for reinforced cylindrical shells. For short sections of cylinder between rigid reinforcing rings spaced a distance L apart, the buckling pressure is[3]

$$(p)_{buck} = \frac{2Eh}{R(2+q^2)} \left[\frac{q^4}{n^2 (1 + q^2)^2} + \frac{n^2 h^2 (1 + q^2)^2}{12 (1-\nu^2) R^2} \right] \tag{H-22}$$

where

$$q = \frac{\pi R}{nL} \tag{H-23}$$

and the mode number n is the integer which gives the lowest value for p for each combination of R, h, and L. The results shown in Figure H-12 are for L = 1 m and show that the buckling pressure for a ring reinforced cylindrical shell is much higher than that for an unreinforced cylinder. The EPR rings are too thin to be considered rigid, but the stringers between the rings also provide some stiffening for the shell.

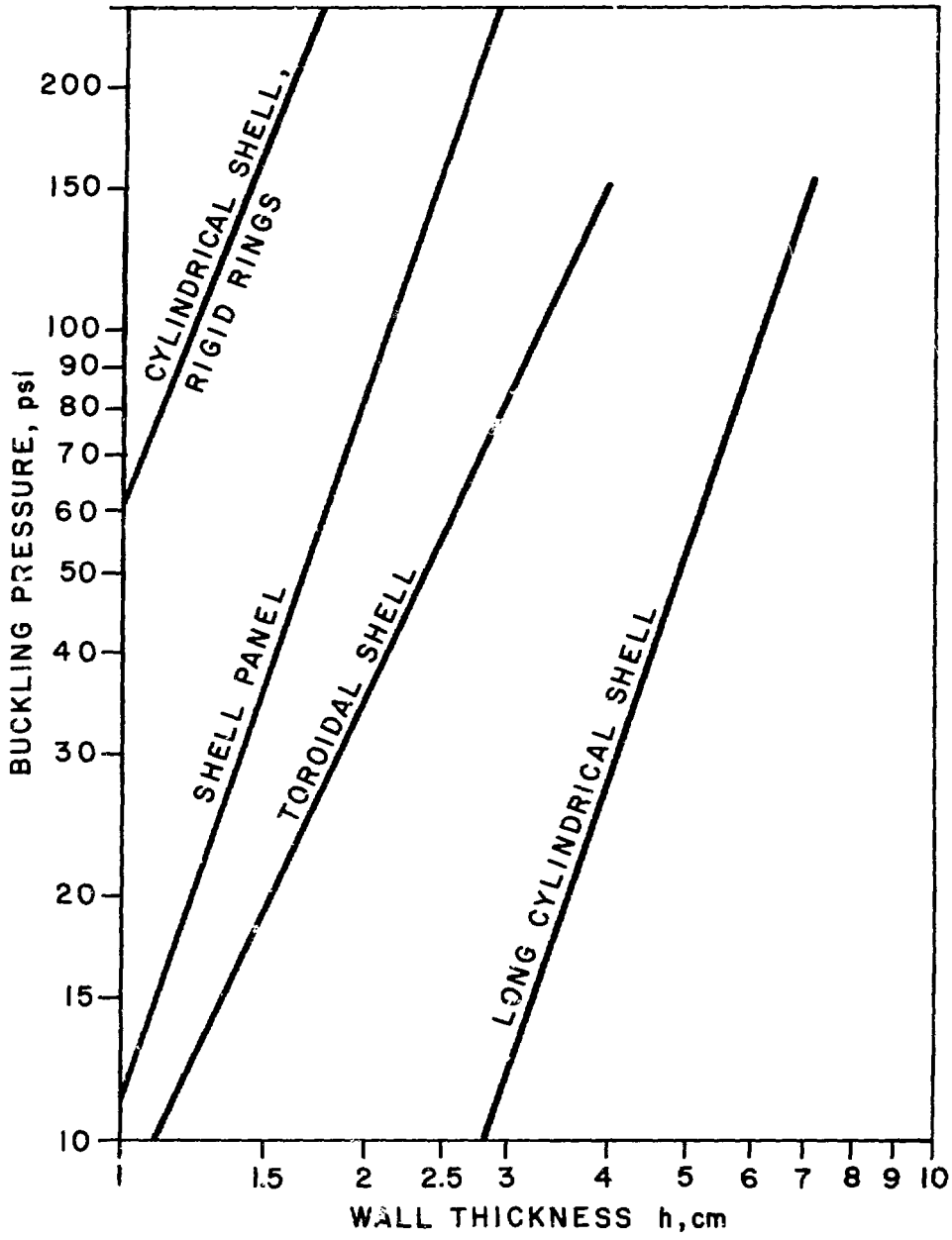

Figure H-12. Buckling Pressures for Various Shell Structures

The last curve on Figure H-12 shows buckling pressure for a cylindrical shell panel between rigid stringers, given by[3]

$$(p)_{buck} = \frac{kE_o h^3}{R^3} \qquad \text{(H-24)}$$

where k = 6.1 for stringers at 30° intervals. The reinforcement again adds significant buckling resistance to a cylindrical shell. The stiffening effect of the rings has been neglected here; on the other hand, the stringers are too thin to be treated as rigid.

Because of the flexibility of the reinforcing members, the buckling mode for the EPR polygonal shell probably involves combined deformations of the rings, stringers, and shell wall. A choice of h = 2 cm gives a large factor of safety over atmospheric pressure for the buckling pressures shown in Figure H-12 for the two types of shell reinforcement. Even though these cases both involve elements of non-conservatism, the factor of safety should be large enough to assure a safe design. However, a more detailed investigation should be performed to verify this and to provide a reliable basis for reducing the wall thickness.

5. Strain Cycling of Coolant Panels

The coolant panels are subjected to two types of thermal cycling, the burn cycle of approximately one minute duration and the reactor start-up/shut-down cycle of widely variable duration. Figure H-13 shows idealized temperature variations in the hottest EPR coolant panel during a typical burn cycle of duration Δt (see Chapter VIII-C); $T_i(t)$ is at the interface with the coating, $T_o(t)$ is at the outer surface exposed to the coolant, and

$$\Delta T(t) = T_i(t) - T_o(t) \ . \qquad \text{(H-25)}$$

The strain range for the burn cycle depends on the difference between the maximum and minimum values of ΔT, and the strain range for the reactor start-up/shut-down cycle (hereafter referred to as the ON-OFF cycle) is a function of the average value of ΔT during the burn cycle. Two support configurations will be considered here: (a) the panel is constrained against bending and expansion by supports at a constant temperature T_s during the burn cycle (fixed supports); (b) the panel is constrained against bending but not expansion (sliding supports). The later support

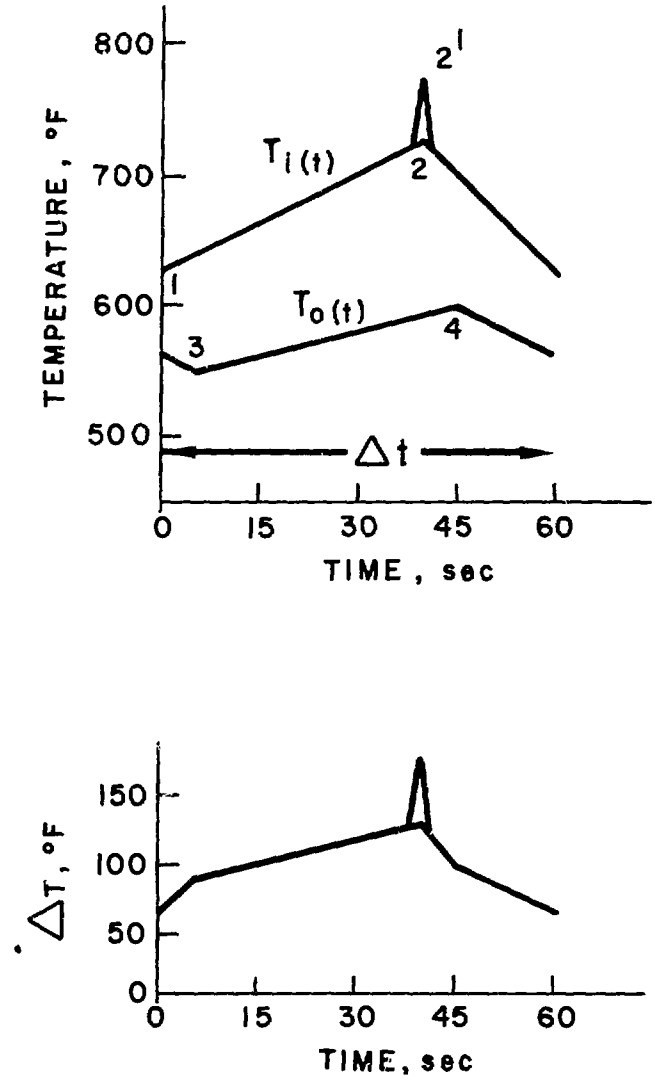

Figure H-13. Idealized Temperature Variation in Hottest Coolant Panel During Burn Cycle

configuration is the one chosen for the EPR design since it corresponds to a significantly longer fatigue lifetime for the coolant panels.

a. Fixed Supports

It is assumed here that no sustained mechanical loads from the weight of the structure or external pressure are transferred through the supports to the coolant panels. Such loads could lead to thermal ratcheting, where the mechanical loads provide a bias so that thermal cycling results in plastic strain accumulation in one direction and failure. Since the coolant panels are nearly as stiff as the vacuum wall, it is difficult to design fixed supports which do not transfer a portion of the mechanical loads to the panels; consequently, the sliding supports treated later would be preferable.

For fixed supports and approximately linear temperature variation through the panel thickness, the strains ε_i and ε_o at the coating interface and cooled surface, respectively, are

$$\varepsilon_i(t) = -\frac{\alpha}{1-\nu}\left[T_i(t) - T_s\right],$$
$$\varepsilon_o(t) = -\frac{\alpha}{1-\nu}\left[T_o(t) - T_s\right] \qquad \text{(H-26)}$$

From Figure H-13, the variation of the strain ε_i at the interface is more severe than the variation of ε_o.

Let ε_i^* be the average value of ε_i during the burn cycle assuming no stress relief has occurred previously. Then,

$$\varepsilon_i^* = -\frac{\alpha}{1-\nu}\left[(T_i)_{avg} - T_s\right], \qquad \text{(H-27)}$$

where

$$(T_i)_{avg} = \frac{1}{\Delta t}\int_{\Delta t} T_i(t)\,dt \approx \frac{1}{2}(T_2 + T_1). \qquad \text{(H-28)}$$

The strain range during the burn cycle is

$$(\varepsilon_i)_{rng} = \left|(\varepsilon_i)_{max} - (\varepsilon_i)_{min}\right|_{\Delta t} = \frac{\alpha}{1-\nu}(T_2 - T_1) \qquad \text{(H-29)}$$

Take the support temperature T_s = 450°F, which is about the average of the coldest and hottest panels. Using temperature values from Figure H-13,

$$\varepsilon_i^* = -0.0032, \qquad (\varepsilon_i)_{rng} = 0.0021 \qquad \text{(H-30)}$$

For the coldest panel, ε_i^* would have about the same magnitude but the opposite sign.

A mean strain alters the number of fatigue cycles to failure for a given strain range, with a mean tensile strain decreasing the lifetime and a mean compressive strain increasing it. However, the mean strain during a burn cycle may not equal the average value ε_i^* computed above because of stress relief during the operating cycle of the reactor, resulting from self-annealing of the average thermal stresses at reactor temperatures.[1] Figure H-14 shows an idealized reactor operating history. The ON and OFF phases are assumed to be approximately equal in duration and to be very long compared to the burn cycle duration Δt. The average interface strain in the hottest panel as it varies during the operating cycle is shown in Figure H-14; i.e., during the ON phase $(\varepsilon_i)_{avg}$ is the average value over the burn cycle Δt allowing for stress relief during the operating cycle, and during the OFF phase $(\varepsilon_i)_{avg}$ is the strain allowing for stress relief. It is assumed that the supports and panels come to a common temperature during the OFF phase, which may be T_s, room temperature, or somewhere in between. If no stress relief occurs (Case A) then $(\varepsilon_i)_{avg} = \varepsilon_i^*$ (Equation H-27) during the ON phase and $(\varepsilon_i)_{avg} = \varepsilon_i = 0$ during the OFF phase. If only the temperature in the ON phase is high enough to cause stress relief (Case B), then stress relief will occur during the first ON phase when the panel is permanently shortened but not in later ON phases when the strain is zero; since the panel is shortened, a residual tensile strain occurs in the OFF phases. If the OFF phase temperature is also high enough to cause stress relief (Case C), then the average strain decays during each ON and OFF phase. All these phenomena depend on temperature, material history, radiation history, and operating cycle variations.

Both strain range and mean strain are important in determining the number of cycles to failure. Table H-5 lists these quantities for the

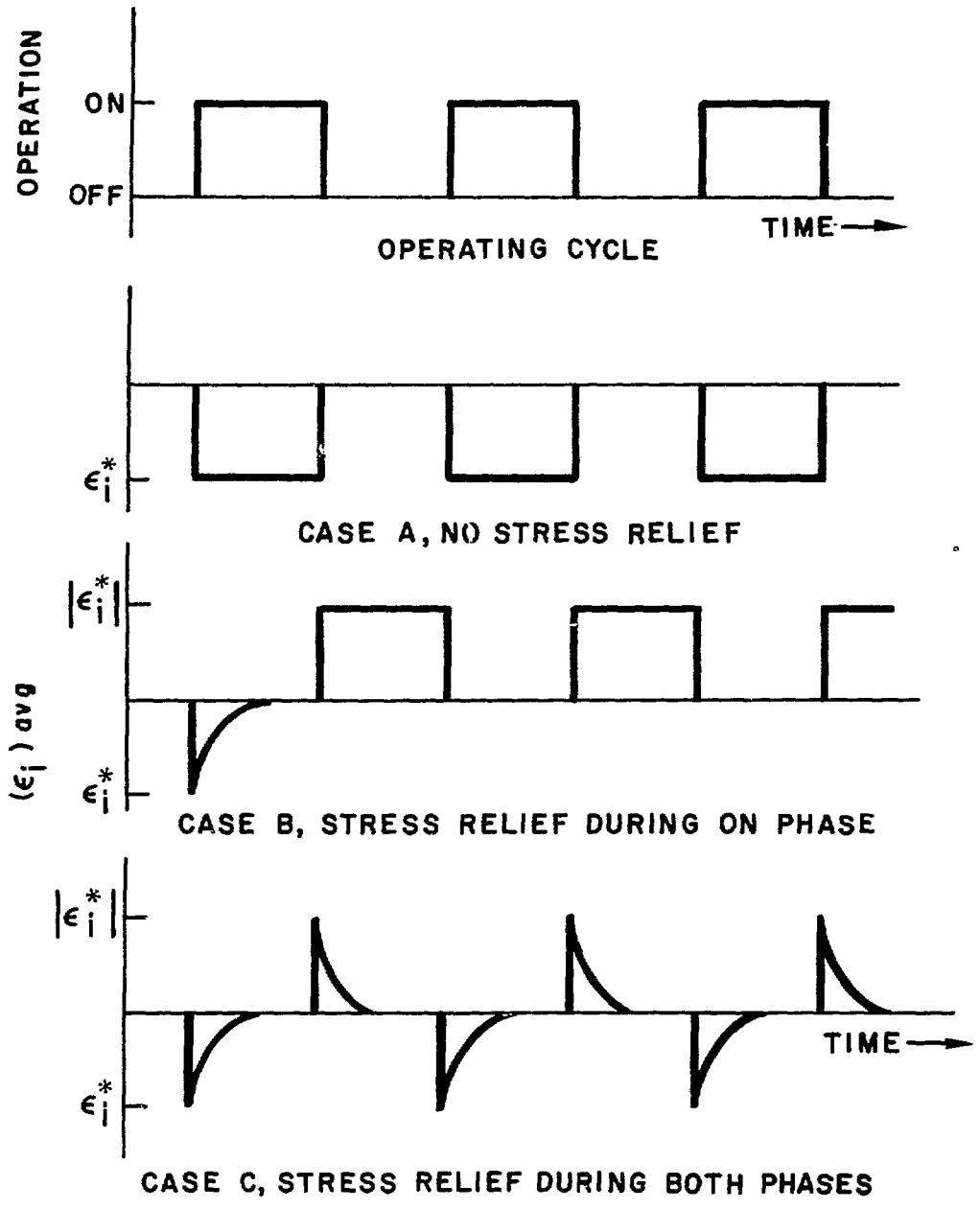

Figure H-14. Effect of Stress Relief During Operating Cycle on $(\epsilon_i)_{avg}$

Table H-5. Strain Combinations in Hottest Panel

	Burn Cycle			Operating Cycle		
Stress Relief Case	A	B	C	A	B	C
Strain Range	$(\varepsilon_i)_{rng}$	$(\varepsilon_i)_{rng}$	$(\varepsilon_i)_{rng}$	$\lvert\varepsilon_i^*\rvert$	$\lvert\varepsilon_i^*\rvert$	$2\ \lvert\varepsilon_i^*\rvert$
Mean Strain	ε_i^*	0 (After first ON phase)	Between 0 and ε_i^*	$-\frac{1}{2}\ \lvert\varepsilon_i^*\rvert$	$\frac{1}{2}\ \lvert\varepsilon_i^*\rvert$	0

hottest panel for both the burn cycle and operating cycle and for each of the stress relief cases A, B, and C shown in Figure H-14.

Figure VIII-8 shows expected cycles to fatigue failure as a function of strain range for zero mean strain. This most closely matches Case C. The expected lifetime is 10^4 burn cycles or 300 operating cycles, whichever comes sooner, for the hottest panel with fixed supports. The coldest panel would have a similar lifetime, and intermediate panels would survive longer.

b. Sliding Supports

The supports here as assumed to keep the panel flat but not to prevent expansion or transmit any structural load to the panel.

The strain variations at the interface and cooled surface are

$$\varepsilon_i(t) = - \frac{\alpha}{2\,(1-\nu)}\,\Delta T(t),$$
$$\varepsilon_o(t) = + \frac{\alpha}{2\,(1-\nu)}\,\Delta T(t), \qquad \text{(H-31)}$$

The strains ε_i and ε_o have the same magnitude and opposite signs.

Again letting ε_i^* be the average value of ε_i during the burn cycle for no previous stress relief, then

$$\varepsilon_i^* = - \frac{\alpha}{2\,(1-\nu)}\,(\Delta T)_{avg}, \qquad \text{(H-32)}$$

where

$$(\Delta T)_{avg} = \frac{1}{\Delta t}\int_{\Delta t} \Delta T(t)\,dt. \qquad \text{(H-33)}$$

The strain range during the burn cycle is

$$(\varepsilon_i)_{rng} = \left|(\varepsilon_i)_{max} - (\varepsilon_i)_{min}\right|_{\Delta t}$$
$$= \frac{\alpha}{2\,(1-\nu)}\left[(\Delta T)_{max} - (\Delta T)_{min}\right]. \qquad \text{(H-34)}$$

For the hottest panel (Figure H-13)

$$(\Delta T)_{avg} \sim 100°F$$
$$(\Delta T)_{max} \sim 180°F \text{ (at } t_2) \qquad \text{(H-35)}$$
$$(\Delta T)_{min} \sim 60°F \text{ (at } t_1);$$

for these values

$$\varepsilon_i^* = -0.0071, \qquad (\varepsilon_i)_{rng} = 0.00085 \qquad \text{(H-36)}$$

Table H-5 still pertains. but the values of ε_i^* and $(\varepsilon_i)_{rng}$ are much lower than those for the fixed support configuration.

Again assuming that stress relief case C is appropriate, Figure H-15 shows the expected number of burn cycles to failure as a function of $(\Delta T)_{max} - (\Delta T)_{min}$ and expected number of operating cycles to failure as a function of $(\Delta T)_{avg}$ for sliding supports. The fatigue lifetime data are based on Figure VIII-8. For the temperature differences given in Equation H-35, the expected lifetime for coolant panels on sliding supports is more than 10^6 burn cycles or 10^5 operating cycles, whichever comes sooner.

---

1. D. Burgreen, Design Methods for Power Plant Structures, C. P. Press, (1975).

2. H. Chung, "Stress and Buckling Analyses of Toroidal Shells," ANL/CTR/TM-69 (1976).

3. R. J. Roark and W. C. Young, Formulas for Stress and Strain, McGraw Hill, 5th Edition, (1975).

4. W. Flügge, Stresses and Shells, Springer-Verlag, 2nd Edition, (1973).

5. S. Timoshenko and S. Woinowsky-Krieger, Theory of Plates and Shells, McGraw-Hill, 2nd Edition, (1959).

6. L. H. Sobel and W. Flügge, "Stability of Toroidal Shells under Uniform External Pressures," *AIAA Journal*, 5, 425, (1967).

7. E. H. Baker, L. Kovalevsky, and F. L. Rish, Structural Analysis of Shells, McGraw-Hill, (1972).

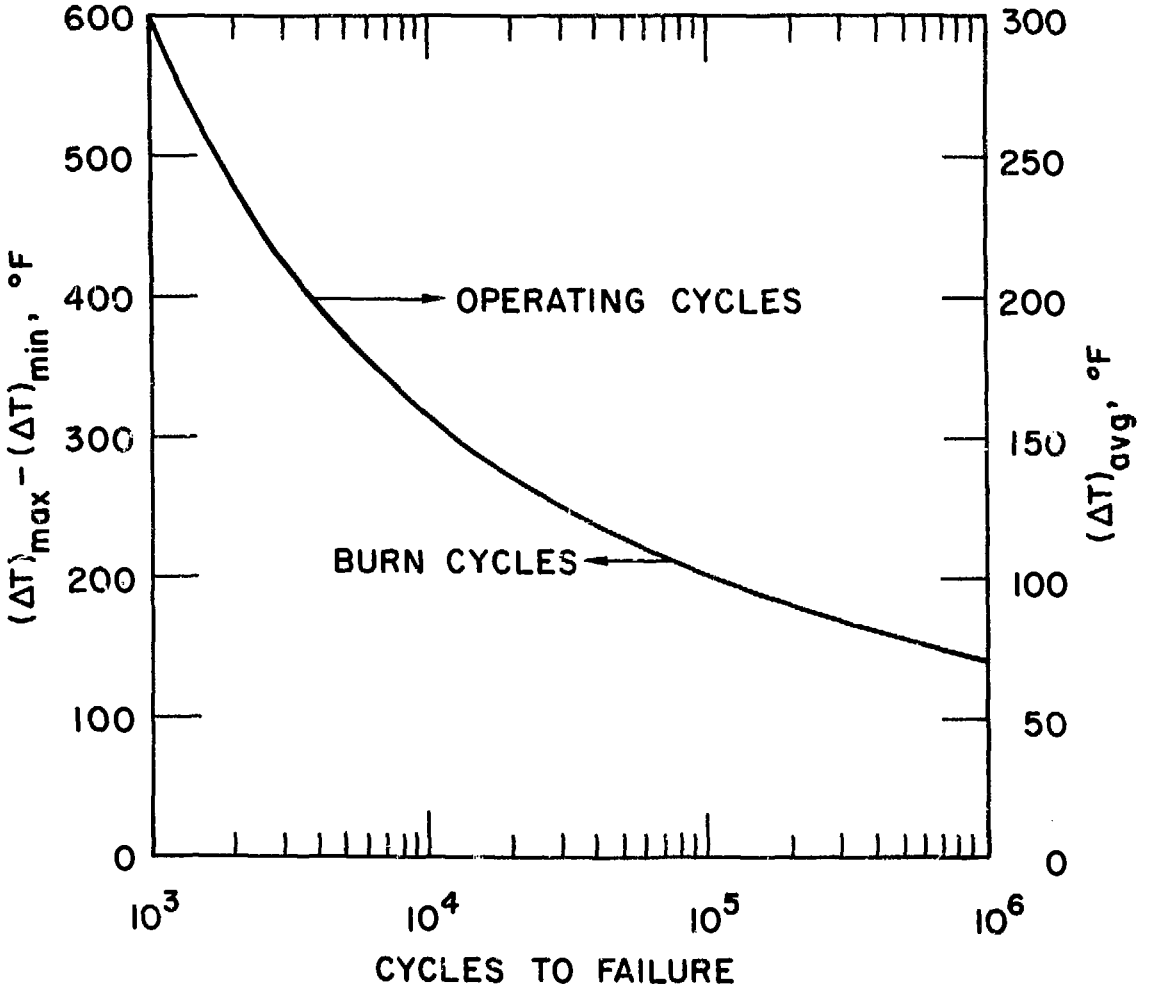

Figure H-15. Burn Cycle and Operating Cycle Lifetimes for Coolant Panels on Sliding Supports.

APPENDIX I

ENRICHMENT OF ISOTOPES OF HYDROGEN BY CRYOGENIC DISTILLATION

The estimated fuel burnup rate during a typical fueling cycle for presently-conceived tokamak-type D-T fusion reactors is of the order of a few percent of the injected species (an equimolar mixture of D and T); hence, based on economic considerations alone, it is essential that the spent fuel mixture be recycled. However, the contaminants produced in the plasma chamber (by sputtering, transmutation, permeation, chemical reaction, etc.) must be removed from the spent fuel mixture before the fuel can be reinjected. While removal of the high molecular weight contaminant atoms appears to present no serious problem, the purification of the hydrogen isotopes (H_2, HD, HT, D_2, DT and T_2) into reinjectable forms may prove to be more formidable. Not only must the protium atoms be removed from the fuel "ash", but the tritium and deuterium atom fractions must be properly adjusted for both cold fuel and neutral beam reinjection. Of the several enrichment schemes that are under consideration, isotope separation by cryogenic distillation seems to be the most promising. An examination of the composition of the spent gases and the purity and composition of the injected fuel shows that a relatively complex separation scheme involving upwards of six distillation columns, arranged in cascade, would be needed. Before a complex enrichment scheme can be adequately analyzed, the basic computational tools must be developed. The mathematical formulation for the analysis of equilibrium stage distillation processes and the solution of the resultant equations using the IBM System 370/195 is described below.

1. Development of the Computer Program

A variety of analytical techniques[1,2,3] have been used in the design of multi-component distillation columns. While most of these methods are adequate to fulfill the needs of the chemical process industries, the exact method of solution by matrix algorithm appears most suitable for isotope separations. (The inaccuracies inherent in empirical schemes and trial-and-error solutions make these methods largely incapable of achieving the level of

accuracy required in isotopic fuels analysis.) Hence, at the outset, it was decided to proceed with analyses based on an exact method of solution of the governing equations, in order to insure that the accuracy of the analytical results are limited only by the accuracy of the thermodynamic and phase equilibrium data.

a. General Considerations

A complex distillation column may contain many feeds, side streams, and other special features. The feed compositions may vary widely and may be introduced at any stage (or plate). Development of the computer simulation for a single distillation column was based on the general features shown in Figure I-1. Once the basic computer program that contained the essential characteristics of a single column was developed, other special features were added by appropriately modifying the mathematical model. Several simplifying assumptions, of necessity, were made before the development of the mathematical model was carried out. The ideal equilibrium stage concept in conjunction with the laws of conservation of mass and energy may be utilized to describe the functional relations among the various components. These assumptions may be stated briefly as follows:

(1) The pressure drop across the column is negligible so that the column may be assumed to operate at a constant pressure.

(2) Heat losses are small so that the column may be assumed to be operated adiabatically.

(3) Molar heats of vaporization of all components are the same so that constant molar vapor flow may be assumed. (This is not a very restrictive assumption because the differences among the molar heats of vaporization of the six isotopic species of hydrogen are small.)

(4) The vapors and liquids of the isotopes form ideal mixtures. This is not an unrealistic assumption for isotopes of the same element, especially at low pressures. Also, this assumption assures the

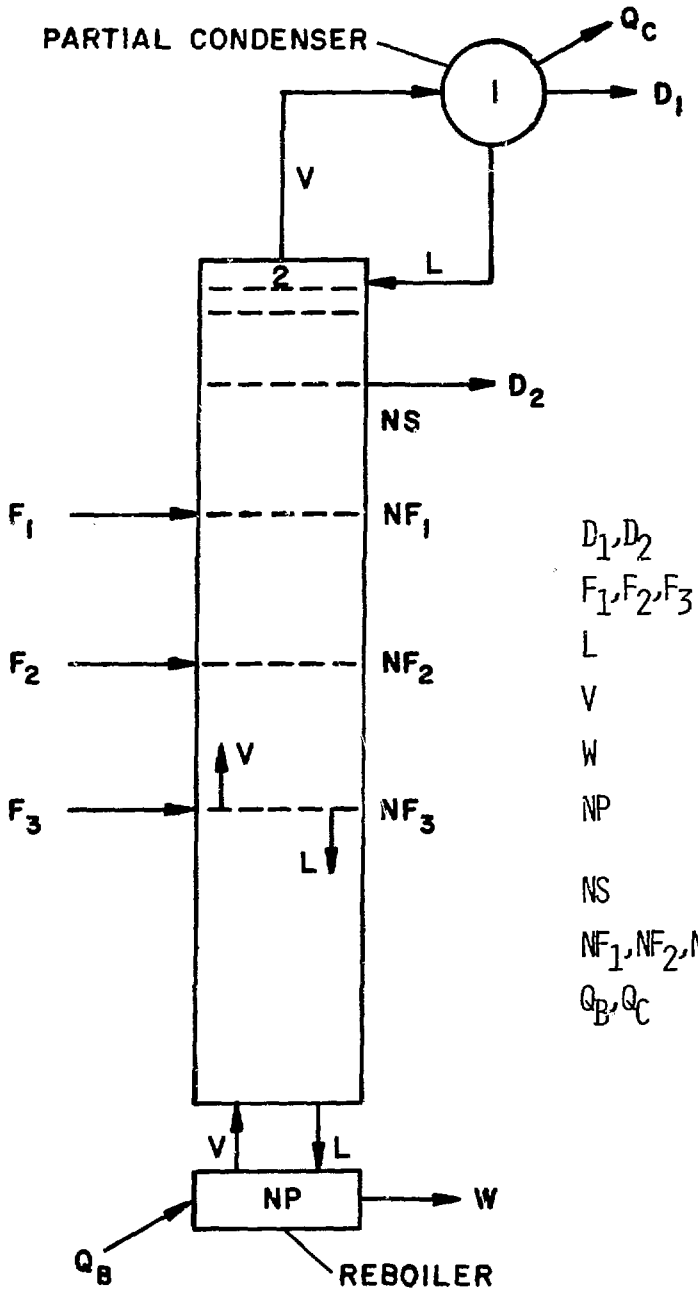

D_1, D_2	DISTILLATE RATES
F_1, F_2, F_3	FEED RATES
L	LIQUID FLOW RATE
V	VAPOR FLOW RATE
W	BOTTOM PRODUCT RATE
NP	NUMBER OF THEORETICAL STAGES
NS	SIDE STREAM LOCATIONS
NF_1, NF_2, NF_3	FEED PLATE LOCATIONS
Q_B, Q_C	HEAT RATES FOR REBOILER AND PARTIAL CONDENSER, RESPECTIVELY

Figure I-1. Complex Distillation Column: Schematic

validity of the laws of Raoult and Dalton; thus, the equilibrium relationship between the vapor mole fraction and liquid mole fraction may be represented by:

$$y_i = k_i x_i \tag{I-1}$$

$$k_i = \frac{p_i}{P} \tag{I-2}$$

where

y_i = mole fraction of component i in vapor phase
x_i = mole fraction of component i in liquid phase
k_i = equilibrium relation for component i between the two phases
p_i = partial pressure of component i
P = total pressure of the system

b. Mathematical Formulation

The composition of the feeds and the rates of the feeds, the distillates, and the side streams are assumed to be known. For a given number of equilibrium stages (NP), assumed feedplate (NF_1, NF_2) and side stream (NS) locations, and reflux ratio (L/D), the functional relationship between the various components across the distillation column can be expressed mathematically. For component i, of a total of NC components, the law of conservation of mass and phase equilibrium leads to NP (NP = number of theoretical stages) equations, each containing NP terms. By denoting the plate number as j and component number as i, the following set of NP equations may be written (in FORTRAN to simplify the subscript notation):

$$-A(1,1)\cdot X(1,I) + A(1,2)\cdot X(2,I) + 0 + 0 + \ldots = B(1,1) \tag{I-3-1}$$

$$A(2,1)\cdot X(1,I) - A(2,2)\cdot X(2,I) + A(2,3)\cdot X(3,I) + 0 + 0 + \ldots = B(2,1) \tag{I-3-2}$$

$$0 + A(3,2)\ X(2,I) - A(3,3)\cdot X(3,I) + A(3,4)\cdot X(4,I) + 0 + \ldots = B(3,1) \tag{I-3-3}$$

$$\vdots$$

$$0 + 0 + \ldots + A(NP,NP-1)\cdot X(NP-1,I) - A(NP,NP)\cdot X(NP,I) = B(NP,1) \tag{I-3-NP}$$

The above set of NP equations may be expressed in matrix algebra as follows:

$$AX = B \tag{I-4}$$

where

A = NP x NP square matrix

X = NP x 1 column matrix

B = NP x 1 column matrix

The nature of the physical problem is such that it leads directly to the tridiagonal matrix represented by equations (I-3-1), (I-3-2) ... (I-3-NP). It should be noted that there are NC sets of independent equations (one for each component) of the type represented by matrix equation (I-4). For a physical problem, since the determinant of the NP x NP square matrix is non-singular, the solution of equation (I-4) is given by

$$X = A^{-1}B \tag{I-5}$$

where A^{-1} is the inverse of matrix A. Hence, the solution of equation (I-4) results in NP values of component i, one value corresponding to each equilibrium stage. Similarly, the solution of the remaining sets of equations of type (I-4) gives the mole fractions of the other components in the liquid mixture. Thus, the mole fractions of all components at each equilibrium stage are determined simultaneously.

c. Convergence Criteria

The correct solution is obtained when the following criterion is satisfied (with an acceptable degree of tolerance) simultaneously at each stage.

$$\sum_{1}^{NC} y_i = 1 = \sum_{1}^{NC} k_i x_i \tag{I-6}$$

From this brief discussion, it is apparent that successful solution of the above set of equations depends on development of reliable convergence criteria. For ideal mixtures, the equilibrium constant, k, may be represented as a function of pressure and temperature. Since the column is assumed to operate at a constant pressure, the equilibrium constant is dependent on temperature only. Existing vapor pressure data[4] for the six

hydrogen isotopes were used to calculate the equilibrium constants. For a typical spent gas mixture, the vapor pressure data for the range from 20 to 30°K were found to be adequate to cover the entire range of interest. For component i, k_i may be represented by an n^{th} degree polynomial:

$$k_i = C_{0,i} + C_{1,i}T_j + C_{2,i}T_j^2 + \ldots + C_{n,i}T_j^n \qquad \text{(I-7)}$$

where $C_{0,i}$, $C_{1,i}$, etc., are constants, and T_j is the temperature of the liquid mixture at plate j. Since the operating temperature range for the column at pressures in the range from 500 to 2000 torr is quite limited, a fourth degree polynomial was found to adequately represent the data. A subroutine was written to obtain the polynomial fit coefficients for each component by least squares methods.

Before proceeding with the calculations, initial values for the end temperatures of the column were assumed, guided by the saturation temperature corresponding to the composition of the feed mixture. Additionally, the temperature drop across the column was assumed to be a linear function of the number of theoretical stages so that a set of starting values for the equilibrium constants could be estimated. To accelerate the convergence, Newton-Raphson interpolation techniques were applied to estimate a set of new temperatures for each plate during the successive iterative steps.

The solution of a set of linear equations for a typical component involves very large numbers. For example, the determinant of a 30 x 30 square matrix for most of the hydrogen isotopes represented by equation (I-4) is of the order of 10^{33}. To reduce the round-off errors, the main program as well as all of the subroutines were written in double precision. Thus, the propagation of round-off errors that are inherent in conventional iterative solutions is minimized. In order to ascertain the validity of the matrix inversion method adopted in solving equation (I-4), the solution vectors were back substituted to see whether the original constant vectors would be obtained. For all the cases considered, no error in the computational techniques could be found.

d. Description of the Computer Code

A detailed description of the main computer code, including FORTRAN listings, the supporting subroutines, data input and ouput options is given in Reference 5. The versatility of the computer code may be demonstrated by analysis of a number of cases as summarized below.

e. General Features of the Analytical Results

In order to study how enrichment of the spent fuel proceeds across a distillation column, a number of simplified cases with only a single feed and no side stream draw-off, were analyzed. The composition of the feed (spent fuel) was assumed to be representative of presently conceived tokamak-type reactors such as the ANL Experimental Power Reactor (ANL/EPR). Several cases were analyzed by varying the number of theoretical stages, reflux ratio, feed plate location, and operating pressure in order to (1) study the behavior of distillation columns handling isotopes of hydrogen, and (2) detect any anomalous behavior of the computer code such as failure to converge. Some of these results are summarized in Table I-1, and the detailed operating characteristics (in the form of computer printouts) are given in Tables I-2 through I-17.

All of the pertinent operating characteristics of the column, the composition of the feed, temperature of the liquid at each equilibrium stage, and summation of the liquid composition at each equilibrium stage are listed in the tables. In addition, the tables show the composition of the six isotopes of hydrogen and the atom percentage of the three species of hydrogen. Since the distillation column has been assumed to contain a partial condenser, the composition of the vapor leaving the column as distillate and the composition of the liquid returning to the column as reflux are shown under Plate No. 1. An examination of the plate temperatures shows that, for most cases, the difference between the bottom plate temperature and the top plate temperature is less than 1°K. The summations of the liquid mole fractions approach 1 after about 10 iterations, although the tables show computed values after 15 iterations (for conservatism). A slight difference in summary of data as shown in Table I-1 and the detailed computer printout may be noticed for a few cases. This is due to the fact that Table I-1 data are based on analytical results after 20 iterations whereas Tables I-2 to I-17 represent computer printouts after 15 iterations. The following observations may be made from the summary of the computer results:

(1) Effect of Number of Theoretical Stages

As the number of the theoretical stages is increased, separation of the lighter fractions from the heavier fractions is enhanced (see Tables

Table I-1. Summary of Operating Parameters and Analytical Results of Cryogenic Enrichment for ANL/TEPR

Parameter	Column Pressure	No. of Plates	Feed Plate Location	Reflux Ratio	Atom % Top Product H	Atom % Top Product D	Atom % Top Product T	Atom % Bottom Product H	Atom % Bottom Product D	Atom % Bottom Product T
Effect of Reflux Ratio	1000 Torr	30	15	5	6.8	72.4	20.8	0.08	38.9	61.0
				10	7.0	80.0	13.0	0.02	35.6	64.3
				15	7.0	83.2	9.8	~0	34.4	65.6
				20	7.0	84.7	8.3	~0	33.8	66.2
				25	7.0	85.5	7.5	~0	33.4	66.6
Effect of Feed Plate			10	15	7.0	81.7	11.3	~0	35.0	65.0
			15		7.0	83.2	9.8	~0	34.7	65.3
			20		7.0	83.0	10.0	0.02	34.4	65.5
Effect of No. of Plates		25	12		7.0	81.1	11.9	0.01	35.2	64.8
		20	10		6.9	78.7	14.4	0.02	36.2	63.8
		15	8		6.9	75.4	17.7	0.06	37.6	62.3
Effect of Pressure	500 Torr	30	15	15	7.0	86.2	6.8	~0	32.6	67.4
	1000 Torr				7.0	83.2	9.8	~0	34.4	65.6
	1500 Torr				7.0	81.0	12.0	~0.01	35.3	64.7
	2000 Torr				7.0	79.4	13.6	~0.02	36.0	64.0
	2500 Torr				6.9	78.1	15.0	~0.03	36.5	63.4

[a]Input Composition = 2.10% H, 48.95% D, 48.95% T

Table I-2. Study of the Effect of Theoretical Stages

CRYOGENIC DISTILLATION OF HYDROGEN ISOTOPES FOR ANL/TEPR, .. B.MISRA.. ..NOVEMBER, 1975

ISOTOPIC SEPARATION AT PT= 1.000D 03 TORR, AFTER NUMBER OF ITERATIONS= 15
NUMBER OF THEORETICAL STAGES= 15 REFLUX RATIO L/D1= 1.500D 01
SIDE STREAM LOCATION= 6 1ST FEED PLATE LOCATION= 5 2ND FP LOCATION= 6 3RD FP LOCATION= 7
FEED RATES: 0.0 0.0 1.00D 02 PRODUCTS: 3.00D 01 0.0 BOTTOMS: 7.00D 01

FEED COMP. N-H2	HD	HT	N-D2	DT	N-T2	APH	APD	APT
2.000000D-03	2.700000D-02	1.100000D-02	2.620000D-01	4.280000D-01	2.700000D-01	2.100D 00	4.895D 01	4.895D 01

EQUILIBRIUM STAGE TEMPERATURES, DEG.K.. (FROM L TO R IN ASCENDING ORDER OF PLATE NUMBER)

2.477319D 01	2.487590D 01	2.495381D 01	2.502059D 01	2.508023D 01	2.513521D 01
2.518683D 01	2.521978D 01	2.525210D 01	2.528545D 01	2.532088D 01	2.535924D 01
2.540122D 01	2.544735D 01	2.549799D 01			

SUMMATION OF LIQUID MOLE FRACTIONS..... (FROM L TO R IN ASCENDING ORDER OF PLATE NUMBER)

1.000000D 00	1.000000D 00	1.000000D 00	1.000000D 00	1.000000D 00	1.000000D 00
1.000000D 00	1.000000D 00	1.000000D 00	1.000000D 00	1.000000D 00	1.000000D 00
1.000000D 00	1.000000D 00	1.000000D 00			

PLATE NO.	N-H2	HD	HT	N-D2	DT	N-T2	APH	APD	APT
1	6.666650D-03	8.935635D-02	3.473226D-02	5.704631D-01	2.683498D-01	3.043165D-02	6.871D 00	7.493D 01	1.820D 01
1	1.872457D-03	5.868936D-02	2.759073D-02	5.530886D-01	3.154035D-01	4.335529D-02	4.501D 00	7.401D 01	2.149D 01
2	5.992456D-04	3.884902D-02	2.170680D-02	5.230572D-01	3.569591D-01	5.882867D-02	3.088D 00	7.210D 01	2.482D 01
3	2.662392D-04	2.642653D-02	1.709466D-02	4.863351D-01	3.927862D-01	7.709124D-02	2.203D 00	6.959D 01	2.820D 01
4	1.791891D-04	1.880053D-02	1.358423D-02	4.466621D-01	4.224737D-01	9.830028D-02	1.637D 00	6.673D 01	3.163D 01
5	1.556160D-04	1.417278D-02	1.096376D-02	4.065291D-01	4.456580D-01	1.225207D-01	1.272D 00	6.364D 01	3.508D 01
6	1.483106D-04	1.137592D-02	9.033045D-03	3.676089D-01	4.621231D-01	1.497107D-01	1.035D 00	6.044D 01	3.853D 01
7	1.451986D-04	9.677710D-03	7.621953D-03	3.309934D-01	4.718504D-01	1.797113D-01	8.795D-01	5.718D 01	4.194D 01
8	4.322422D-05	6.530006D-03	6.120371D-03	3.109938D-01	4.866271D-01	1.898883D-01	6.368D-01	5.576D 01	4.361D 01
9	1.279560D-05	4.365423D-03	4.859011D-03	2.888100D-01	4.998286D-01	2.021242D-01	4.625D-01	5.409D 01	4.545D 01
10	3.765951D-06	2.888100D-03	3.808334D-03	2.647910D-01	5.107890D-01	2.177192D-01	3.352D-01	5.216D 01	4.750D 01
11	1.101449D-06	1.887250D-03	2.941802D-03	2.392639D-01	5.186347D-01	2.317713D-01	2.416D-01	4.995D 01	4.981D 01
12	3.198421D-07	1.214380D-03	2.232114D-03	2.125808D-01	5.223129D-01	2.416595D-01	1.724D-01	4.743D 01	5.239D 01
13	9.202388D-08	7.657623D-04	1.656631D-03	1.851358D-01	5.206423D-01	2.917994D-01	1.211D-01	4.458D 01	5.529D 01
14	2.608299D-08	4.694496D-04	1.194910D-03	1.573760D-01	5.123954D-01	3.285642D-01	8.322D-02	4.138D 01	5.854D 01
15	7.144257D-09	2.758488D-04	8.290309D-04	1.298015D-01	4.964215D-01	3.726721D-01	5.524D-02	3.782D 01	6.213D 01

Table I-3. Study of the Effect of Theoretical Stages

CRYOGENIC DISTILLATION OF HYDROGEN ISOTOPES FOR ANL/TEPR, .. B.MISRA.. ..NOVEMBER, 1975

ISOTOPIC SEPARATION AT PT= 1.000D 03 TORR, AFTER NUMBER OF ITERATIONS= 15
NUMBER OF THFORETICAL STAGES= 20 REFLUX RATIO L/D1= 1.500D 01
SIDE STREAM LOCATION= 6 1ST FEED PLATE LOCATION= 6 2ND FP LOCATION= 8 3RD FP LOCATION= 10
FEED RATES: 0.0 0.0 1.000D 02 PRODUCTS: 3.000D 01 0.0 BOTTOMS: 7.000D 01

FEED COMP. N-H2	HD	HT	N-D2	DT	N-T2	APH	APD	APT
2.000000D-03	2.700000D-02	1.100000D-02	2.620000D-01	4.280000D-01	2.700000D-01	2.100D 00	4.895D 01	4.895D 01

EQUILIBRIUM STAGE TEMPERATURES, DEG.K.. (FROM L TO R IN ASCENDING ORDER OF PLATE NUMBER)

2.470881D 01	2.479932D 01	2.486817D 01	2.492601D 01	2.497762D 01	2.502546D 01
2.507095D 01	2.511488D 01	2.515773D 01	2.519971D 01	2.522659D 01	2.525229D 01
2.527822D 01	2.530522D 01	2.533399D 01	2.536512D 01	2.539918D 01	2.543670D 01
2.547813D 01	2.552384D 01				

SUMMATION OF LIQUID MOLE FRACTIONS.....(FROM L TO R IN ASCENDING ORDER OF PLATE NUMBER)

1.000000D 00	1.000000D 00	1.000000D 00	1.000000D 00	1.000000D 00	1.000000D 00	
1.000000D 00	1.000000D 00	1.000000D 00	1.000000D 00	1.000000D 00	1.000000D 00	
1.000000D 00	1.000000D 00	1.000000D 00	1.000000D 00	1.000000D 00	1.000000D 00	
1.000000D 00	1.000000D 00					

PLATE NO.	N-H2	HD	HT	N-D2	DT	N-T2	APH	APD	APT
1	6.666653D-03	8.877237D-02	3.573771D-02	6.311466D-01	2.224230D-01	1.425404D-02	6.942D 00	7.872D 01	1.433D 01
1	1.893866D-03	5.988235D-02	2.885771D-02	6.224724D-01	2.661959D-01	2.069784D-02	4.626D 00	7.855D 01	1.632D 01
2	6.128838D-04	4.030463D-02	2.311224D-02	5.998789D-01	3.073995D-01	2.869174D-02	3.232D 00	7.737D 01	1.939D 01
3	2.737968D-04	2.786282D-02	1.853671D-02	5.690617D-01	3.457646D-01	3.850044D-02	2.347D 00	7.559D 01	2.207D 01
4	1.841127D-04	2.009533D-02	1.499048D-02	5.335829D-01	3.807664D-01	5.038075D-02	1.773D 00	7.340D 01	2.483D 01
5	1.596754D-04	1.529554D-02	1.228955D-02	4.958733D-01	4.118071D-01	6.457486D-02	1.395D 00	7.094D 01	2.766D 01
6	1.521913D-04	1.234027D-02	1.025583D-02	4.576531D-01	4.383016D-01	8.129496D-02	1.145D 00	6.830D 01	3.056D 01
7	1.491199D-04	1.051333D-02	8.734945D-03	4.201494D-01	4.597471D-01	1.007061D-01	9.773D-01	6.553D 01	3.349D 01
8	1.472216D-04	9.368042D-03	7.600606D-03	3.842266D-01	4.757489D-01	1.229087D-01	8.632D-01	6.268D 01	3.646D 01
9	1.456665D-04	8.630713D-03	6.753258D-03	3.504728D-01	4.860760D-01	1.479216D-01	7.838D-01	5.976D 01	3.943D 01
10	1.442308D-04	8.136076D-03	6.116492D-03	3.192590D-01	4.906744D-01	1.754548D-01	7.271D-01	5.687D 01	4.241D 01
11	4.288593D-05	5.492676D-03	4.930948D-03	3.021328D-01	5.051272D-01	1.822734D-01	5.255D-01	5.574D 01	4.373D 01
12	1.269529D-05	3.683297D-03	3.942277D-03	2.833550D-01	5.186820D-01	1.903248D-01	3.825D-01	5.445D 01	4.516D 01
13	3.741330D-06	2.452406D-03	3.123747D-03	2.631902D-01	5.309484D-01	2.002814D-01	2.792D-01	5.299D 01	4.673D 01
14	1.097445D-06	1.619916D-03	2.450502D-03	2.418735D-01	5.413683D-01	2.126867D-01	2.036D-01	5.134D 01	4.846D 01
15	3.203082D-07	1.060147D-03	1.900274D-03	2.196343D-01	5.492237D-01	2.281812D-01	1.481D-01	4.948D 01	5.037D 01
16	9.297316D-08	6.860322D-04	1.453532D-03	1.967122D-01	5.536452D-01	2.475029D-01	1.070D-01	4.739D 01	5.251D 01
17	2.681387D-08	4.376243D-04	1.093377D-03	1.735663D-01	5.536326D-01	2.714701D-01	7.655D-02	4.504D 01	5.488D 01
18	7.668370D-09	2.738729D-04	8.053265D-04	1.498824D-01	5.480960D-01	3.009424D-01	5.396D-02	4.241D 01	5.754D 01
19	2.162290D-09	1.668121D-04	5.770507D-04	1.265766D-01	5.359272D-01	3.367524D-01	3.719D-02	3.946D 01	6.050D 01
20	5.897455D-10	9.748465D-05	3.980946D-04	1.037939D-01	5.161048D-01	3.796058D-01	2.478D-02	3.619D 01	6.379D 01

Table I-4. Study of the Effect of Theoretical Stages

CRYOGENIC DISTILLATION OF HYDROGEN ISOTOPES FOR ANL/TFPR, .. B.MISRA.. ..NOVEMBER, 1975

ISOTOPIC SEPARATION AT PT= 1.000D 03 TORR, AFTER NUMBER OF ITERATIONS= 15
NUMBER OF THEORETICAL STAGES= 25 REFLUX RATIO L/D1= 1.500D 01
SIDE STREAM LOCATION= 6 1ST FEED PLATE LOCATION= 8 2ND FP LOCATION= 10 3RD FP LOCATION= 12
FEED RATES: 0.0 0.0 1.00D 02 PRODUCTS: 3.00D 01 0.0 BOTTOMS: 7.00D 01

FEED COMP. N-H2	HD	HT	N-D2	DT	N-T2	APH	APD	APT
2.000000D-03	2.700000D-02	1.100000D-02	2.620000D-01	4.280000D-01	2.700000D-01	2.100D 00	4.895D 01	4.895D 01

EQUILIBRIUM STAGE TEMPERATURES, DEG.K..(FROM L TO R IN ASCENDING ORDER OF PLATE NUMBER)

2.466774D 01	2.475099D 01	2.483139D 01	2.486541D 01	2.491170D 01	2.495469D 01
2.499579D 01	2.503580D 01	2.507520D 01	2.511428D 01	2.515317D 01	2.519192D 01
2.521429D 01	2.523489D 01	2.525499D 01	2.527527D 01	2.529627D 01	2.531839D 01
2.534205D 01	2.536765D 01	2.539564D 01	2.542646D 01	2.546059D 01	2.549847D 01
2.554049D 01					

SUMMATION OF LIQUID MOLE FRACTIONS.....(FROM L TO R IN ASCENDING ORDER OF PLATE NUMBER)

1.000002D 00	1.000002D 00	1.000002D 00	1.000002D 00	1.000002D 00	1.000002D 00
1.000002D 00	1.000002D 00	1.000002D 00	1.000002D 00	1.000001D 00	1.000001D 00
1.000001D 00	1.000001D 00	1.000001D 00	1.000001D 00	1.000001D 00	1.000001D 00
1.000001D 00	1.000001D 00	1.000001D 00	1.000001D 00	1.000001D 00	1.000001D 00
1.000001D 00					

PLATE NO.	N-H2	HD	HT	N-D2	DT	N-T2	APH	APD	APT
1	6.666577D-03	8.993561D-02	3.623749D-02	6.742710D-01	1.848949D-01	7.996440D-03	6.975D 00	8.117D 01	1.186D 01
1	1.907656D-03	6.058847D-02	2.356933D-02	6.723207D-01	2.238600D-01	1.175387D-02	4.699D 00	8.145D 01	1.385D 01
2	6.217724D-04	4.121839D-02	2.395509D-02	6.558098D-01	2.619763D-01	1.651878D-02	3.321D 00	8.074D 01	1.594D 01
3	2.787687D-04	2.879355D-02	1.944046D-02	6.302204D-01	2.937601D-01	2.250673D-02	2.440D 00	7.940D 01	1.816D 01
4	1.873670D-04	2.095434D-02	1.590231D-02	5.989408E-01	3.240659D-01	2.994923D-02	1.862D 00	7.764D 01	2.049D 01
5	1.623633D-04	1.605479D-02	1.317380D-02	5.642926D-01	3.572258D-01	3.909062D-02	1.478D 00	7.559D 01	2.293D 01
6	1.547686D-04	1.300260D-02	1.109140D-02	5.279535D-01	3.926172D-01	5.018046D-02	1.220D 00	7.333D 01	2.545D 01
7	1.517382D-04	1.109441D-02	9.511702D-03	4.911691D-01	4.296107D-01	6.346231D-02	1.045D 00	7.090D 01	2.805D 01
8	1.499211D-04	9.886308D-03	8.315994D-03	4.548742D-01	4.676136D-01	7.915933D-02	9.251D-01	6.836D 01	3.071D 01
9	1.484423D-04	8.902620D-03	7.409451D-03	4.197674D-01	4.661104D-01	9.746130D-02	8.404D-01	6.574D 01	3.342D 01
10	1.470708D-04	8.574433D-03	6.718210D-03	3.863594D-01	4.796933D-01	1.185016D-01	7.793D-01	6.305D 01	3.617D 01
11	1.457439D-04	8.199463D-03	6.185848D-03	3.550063D-01	4.881167D-01	1.423459D-01	7.339D-01	6.032D 01	3.895D 01
12	1.444440D-04	7.916460D-03	5.769961D-03	3.259351D-01	4.912601D-01	1.689738D-01	6.988D-01	5.755D 01	4.175D 01
13	4.304071D-05	5.365583D-03	4.685554D-03	3.120278D-01	5.050711D-01	1.728069D-01	5.069D-01	5.672D 01	4.277D 01
14	1.277946D-05	3.618504D-03	3.782182D-03	2.966841D-01	5.186358D-01	1.772066D-01	3.713D-01	5.578D 01	4.385D 01
15	3.781277D-06	2.428163D-03	3.034341D-03	2.801253D-01	5.318224D-01	1.825861D-01	2.735D-01	5.472D 01	4.500D 01
16	1.114922D-06	1.620982D-03	2.418596D-03	2.625326D-01	5.443827D-01	1.890439D-01	2.021D-01	5.355D 01	4.624D 01
17	3.275509D-07	1.076112D-03	1.914144D-03	2.440697D-01	5.559585D-01	1.969812D-01	1.495D-01	5.226D 01	4.759D 01
18	9.586432D-08	7.099757D-04	1.502873D-03	2.248940D-01	5.660764D-01	2.068166D-01	1.107D-01	5.083D 01	4.906D 01
19	2.794227D-08	4.650869D-04	1.169215D-03	2.051644D-01	5.741429D-01	2.195084D-01	8.172D-02	4.925D 01	5.067D 01
20	8.108402D-09	3.020935D-04	8.999084D-04	1.850461D-01	5.794197D-01	2.343122D-01	6.010D-02	4.749D 01	5.245D 01
21	2.341274D-09	1.941762D-04	6.837413D-04	1.647149D-01	5.811279D-01	2.532802D-01	4.390D-02	4.559D 01	5.442D 01
22	6.720928D-10	1.231340D-04	5.112853D-04	1.443603D-01	5.792587D-01	2.767406D-01	3.172D-02	4.336D 01	5.661D 01
23	1.914300D-10	7.660707D-05	3.746578D-04	1.241886D-01	5.698174D-01	3.059426D-01	2.257D-02	4.091D 01	5.906D 01
24	5.479457D-11	4.649718D-05	2.672489D-04	1.044243D-01	5.547760D-01	3.408859D-01	1.569D-02	3.818D 01	6.180D 01
25	1.468142D-11	2.707742D-05	1.837246D-04	8.539914D-02	5.421340D-01	3.822877D-01	1.054D-02	3.514D 01	6.485D 01

Table I-5. Study of the Effect of Theoretical Stages

CRYOGENIC DISTILLATION OF HYDROGEN ISOTOPES FOR ANL/TFPR, .. B.MISRA.. ..NOVEMBER, 1975

ISOTOPIC SEPARATION AT PT= 1.000D 03 TORR, AFTER NUMBER OF ITERATIONS= 15
NUMBER OF THEORETICAL STAGES= 30 REFLUX RATIO L/D1= 1.500D 01
SIDE STREAM LOCATION= 6 1ST FEED PLATE LOCATION= 10 2ND FP LOCATION= 12 3RD FP LOCATION= 15
FEED RATES: 0.0 0.0 1.00D 02 PRODUCTS: 3.00D 01 0.0 BOTTOMS: 7.00D 01

FEED COMP.	N-H2	HD	HT	N-D2	DT	N-T2	APH	APD	APT
	2.000000D-03	2.700000D-02	1.100000D-02	2.620000D-01	4.280000D-01	2.700000D-01	2.100D 00	4.895D 01	4.895D 01

EQUILIBRIUM STAGE TEMPERATURES, DEG.K..(FROM L TO R IN ASCENDING ORDER OF PLATE NUMBER)

2.463442D 01	2.471111D 01	2.476739D 01	2.481355D 01	2.485418D 01	2.489165D 01	
2.492732D 01	2.496200D 01	2.499618D 01	2.503015D 01	2.506409D 01	2.509813D 01	
2.513235D 01	2.516681D 01	2.520154D 01	2.522205D 01	2.524050D 01	2.525808D 01	
2.527543D 01	2.529298D 01	2.531109D 01	2.533001D 01	2.535009D 01	2.537162D 01	
2.539495D 01	2.542050D 01	2.544869D 01	2.548002D 01	2.551496D 01	2.555392D 01	

SUMMATION OF LIQUID MOLE FRACTIONS.....(FROM L TO R IN ASCENDING ORDER OF PLATE NUMBER)

1.000010D 00	1.000010D 00	1.000010D 00	1.000010D 00	1.000010D 00	1.000010D 00	
1.000011D 00	1.000010D 00	1.000010D 00	1.000010D 00	1.000009D 00	1.000009D 00	
1.000008D 00	1.000007D 00	1.000006D 00	1.000006D 00	1.000007D 00	1.000007D 00	
1.000007D 00	1.000007D 00	1.000007D 00	1.000007D 00	1.000007D 00	1.000007D 00	
1.000007D 00	1.000006D 00	1.000006D 00	1.000006D 00	1.000005D 00	1.000005D 00	

PLATE NO.	N-H2	HD	HT	N-D2	DT	N-T2	APH	APD	APT
1	6.666129D-03	8.996687D-02	3.642225D-02	7.103798D-01	1.528073D-01	3.767222D-03	6.986D 00	8.318D 01	9.838D 00
1	1.918818D-03	6.109948D-02	2.997418D-02	7.146544D-01	1.867606D-01	5.592578D-03	4.746D 00	8.386D 01	1.140D 01
2	6.291332D-04	4.193648D-02	2.451480D-02	7.041378D-01	2.208321D-01	7.949712D-03	3.385D 00	8.355D 01	1.306D 01
3	2.829710D-04	2.955678D-02	2.009492D-02	6.841218D-01	2.549715D-01	1.097207D-02	2.511D 00	8.264D 01	1.485D 01
4	1.901754D-04	2.168218D-02	1.660324D-02	6.578189D-01	2.888927D-01	1.481276D-02	1.933D 00	8.131D 01	1.676D 01
5	1.647339D-04	1.671702D-02	1.388618D-02	6.274088D-01	3.221773D-01	1.964592D-02	1.547D 00	7.968D 01	1.877D 01
6	1.570939D-04	1.359647D-02	1.179198D-02	5.944686D-01	3.543199D-01	2.566594D-02	1.285D 00	7.784D 01	2.087D 01
7	1.541577D-04	1.162961D-02	1.018669D-02	5.601855D-01	3.847592D-01	3.308480D-02	1.106D 00	7.584D 01	2.306D 01
8	1.524779D-04	1.037659D-02	8.968611D-03	5.254766D-01	4.129082D-01	4.212761D-02	9.820D-01	7.371D 01	2.531D 01
9	1.511456D-04	9.561383D-03	8.017754D-03	4.910594D-01	4.381843D-01	5.302599D-02	8.941D-01	7.149D 01	2.761D 01
10	1.499178D-04	9.012837D-03	7.793296D-03	4.574948D-01	4.600398D-01	6.600936D-02	8.303D-01	6.920D 01	2.997D 01
11	1.487275D-04	8.625875D-03	6.730473D-03	4.252130D-01	4.779881D-01	8.129382D-02	7.827D-01	6.685D 01	3.237D 01
12	1.475539D-04	8.336577D-03	6.287542D-03	3.945320D-01	4.916275D-01	9.906880D-02	7.460D-01	6.445D 01	3.480D 01
13	1.463898D-04	8.106368D-03	5.933021D-03	3.656722D-01	5.006604D-01	1.194817D-01	7.166D-01	6.201D 01	3.728D 01
14	1.452318D-04	7.912149D-03	5.643507D-03	3.387697D-01	5.049082D-01	1.426212D-01	6.923D-01	5.952D 01	3.979D 01
15	1.440782D-04	7.740201D-03	5.401718D-03	3.138905D-01	5.043224D-01	1.685010D-01	6.715D-01	5.699D 01	4.234D 01
16	4.287398D-05	5.237941D-03	4.385234D-03	3.014505D-01	5.174682D-01	1.714152D-01	4.854D-01	5.628D 01	4.323D 01
17	1.271759D-05	3.529122D-03	3.541942D-03	2.877925D-01	5.304539D-01	1.746698D-01	3.548D-01	5.548D 01	4.417D 01
18	3.760457D-06	2.367785D-03	2.846480D-03	2.731270D-01	5.432409D-01	1.784141D-01	2.611D-01	5.459D 01	4.515D 01
19	1.108900D-06	1.581917D-03	2.275804D-03	2.576213D-01	5.556992D-01	1.828207D-01	1.930D-01	5.363D 01	4.618D 01
20	3.259660D-07	1.052274D-03	1.809637D-03	2.414206D-01	5.676171D-01	1.881000D-01	1.431D-01	5.258D 01	4.728D 01
21	9.552096D-08	6.967210D-04	1.430467D-03	2.246583D-01	5.787012D-01	1.945132D-01	1.064D-01	5.144D 01	4.846D 01
22	2.790033D-08	4.589748D-04	1.123348D-03	2.074617D-01	5.885707D-01	2.023852D-01	7.912D-02	5.020D 01	4.972D 01
23	8.121187D-09	3.006409D-04	8.756354D-04	1.899563D-01	5.967502D-01	2.121172D-01	5.881D-02	4.885D 01	5.109D 01
24	2.355146D-09	1.956340D-04	6.767047D-04	1.722674D-01	6.026620D-01	2.241982D-01	4.362D-02	4.737D 01	5.259D 01
25	6.802321D-10	1.263006D-04	5.176793D-04	1.545225D-01	6.056212D-01	2.392123D-01	3.220D-02	4.574D 01	5.423D 01
26	1.955802D-10	8.073829D-05	3.911809D-04	1.368530D-01	6.048366D-01	2.578384D-01	2.360D-02	4.393D 01	5.604D 01
27	5.593099D-11	5.095230D-05	2.911054D-04	1.193966D-01	5.994231D-01	2.808382D-01	1.710D-02	4.191D 01	5.807D 01
28	1.587816D-11	3.159296D-05	2.124246D-04	1.022991D-01	5.884317D-01	3.090251D-01	1.220D-02	3.965D 01	6.033D 01
29	4.449672D-12	1.909415D-05	1.510130D-04	8.571655D-02	5.709038D-01	3.432095D-01	8.505D-03	3.712D 01	6.287D 01
30	1.207618D-12	1.108794D-05	1.034962D-04	6.981538D-02	5.459556D-01	3.841145D-01	5.729D-03	3.428D 01	6.571D 01

Table I-6. Study of the Effect of Reflux Ratio

CRYOGENIC DISTILLATION OF HYDROGEN ISOTOPES FOR ANL/TEPR, .. B.MISRA.. ..NOVEMBER, 1975

ISOTOPIC SEPARATION AT PT= 1.000D 03 TORR, AFTER NUMBER OF ITERATIONS= 15
NUMBER OF THEORETICAL STAGES= 30 REFLUX RATIO L/D1= 5.000D 00
SIDE STREAM LOCATION= 6 1ST FEED PLATE LOCATION= 10 2ND FP LOCATION= 12 3RD FP LOCATION= 15
FEED RATES: 0.0 0.0 1.00D 02 PRODUCTS: 3.00D 01 0.0 BOTTOMS: 7.00D 01

FEED COMP. N-H2	HD	HT	N-D2	DT	N-T2	APH	APD	APT
2.000000D-03	2.700000D-02	1.100000D-02	2.620000D-01	4.280000D-01	2.700000D-01	2.100D 00	4.895D 01	4.895D 01

EQUILIBRIUM STAGE TEMPERATURES, DEG.K..(FROM L TO R IN ASCENDING ORDER OF PLATE NUMBER)

2.481375D 01	2.490605D 01	2.496860D 01	2.501519D 01	2.505209D 01	2.508263D 01
2.510877D 01	2.513173D 01	2.515230D 01	2.517102D 01	2.518825D 01	2.520426D 01
2.521924D 01	2.523332D 01	2.524658D 01	2.525934D 01	2.526930D 01	2.527781D 01
2.528554D 01	2.529294D 01	2.530039D 01	2.530829D 01	2.531708D 01	2.532731D 01
2.533969D 01	2.535515D 01	2.537496D 01	2.540082D 01	2.543495D 01	2.548018D 01

SUMMATION OF LIQUID MOLE FRACTIONS.....(FROM L TO R IN ASCENDING ORDER OF PLATE NUMBER)

1.000000D 00	1.000000D 00	1.000000D 00	1.000000D 00	1.000000D 00	1.000000D 00
1.000000D 00	1.000000D 00	1.000000D 00	1.000000D 00	1.000000D 00	1.000000D 00
1.000000D 00	1.000000D 00	1.000000D 00	1.000000D 00	1.000000D 00	1.000000D 00
1.000000D 00	1.000000D 00	1.000000D 00	1.000000D 00	1.000000D 00	1.000000D 00
1.000000D 00	1.000000D 00	1.000000D 00	1.000000D 00	1.000000D 00	1.000000D 00

PLATE NO.	N-H2	HD	HT	N-D2	DT	N-T2	APH	APD	APT
1	6.666667D-03	8.930623D-02	3.351641D-02	5.194911D-01	3.205416D-01	3.047799D-02	6.808D 00	7.244D 01	2.075D 01
1	1.859134D-03	5.808942D-02	2.635299D-02	4.982974D-01	3.724958D-01	4.290524D-02	4.408D 00	7.136D 01	2.423D 01
2	7.299733D-04	4.027225D-02	2.116153D-02	4.698073D-01	4.120799D-01	5.594904D-02	3.145D 00	6.960D 01	2.726D 01
3	4.666479D-04	3.037075D-02	1.756077D-02	4.403154D-01	4.417241D-01	6.956234D-02	2.443D 00	6.764D 01	2.992D 01
4	4.037947D-04	2.492190D-02	1.511477D-02	4.126404D-01	4.632337D-01	8.368551D-02	2.042D 00	6.567D 01	3.229D 01
5	3.871967D-04	2.191498D-02	1.346688D-02	3.879201D-01	4.780585D-01	9.825239D-02	1.808D 00	6.379D 01	3.440D 01
6	3.814642D-04	2.022889D-02	1.235573D-02	3.664435D-01	4.873991D-01	1.131914D-01	1.667D 00	6.203D 01	3.631D 01
7	3.784698D-04	1.925289D-02	1.159971D-02	3.480606D-01	4.922627D-01	1.284257D-01	1.580D 00	6.038D 01	3.804D 01
8	3.763059D-04	1.865888D-02	1.107652D-02	3.325145D-01	4.934996D-01	1.438742D-01	1.524D 00	5.886D 01	3.962D 01
9	3.744918D-04	1.827207D-02	1.070539D-02	3.193651D-01	4.918305D-01	1.594525D-01	1.486D 00	5.744D 01	4.107D 01
10	3.728830D-04	1.799963D-02	1.043368D-02	3.082540D-01	4.878657D-01	1.750741D-01	1.459D 00	5.612D 01	4.242D 01
11	3.714218D-04	1.779218D-02	1.022734D-02	2.988355D-01	4.821219D-01	1.906518D-01	1.438D 00	5.488D 01	4.368D 01
12	3.700769D-04	1.762332D-02	1.006448D-02	2.908085D-01	4.750346D-01	2.060990D-01	1.421D 00	5.371D 01	4.486D 01
13	3.688285D-04	1.747876D-02	9.931052D-03	2.839198D-01	4.669698D-01	2.213318D-01	1.407D 00	5.261D 01	4.598D 01
14	3.676627D-04	1.735061D-02	9.818052D-03	2.779605D-01	4.582333D-01	2.362699D-01	1.395D 00	5.158D 01	4.703D 01
15	3.665700D-04	1.723444D-02	9.719683D-03	2.727616D-01	4.490793D-01	2.508385D-01	1.384D 00	5.059D 01	4.802D 01
16	1.313720D-04	1.394966D-02	9.131074D-03	2.732796D-01	4.517292D-01	2.517791D-01	1.167D 00	5.061D 01	4.822D 01
17	4.700050D-05	1.125199D-02	8.534901D-03	2.731983D-01	4.542890D-01	2.526789D-01	9.940D-01	5.060D 01	4.841D 01
18	1.679056D-05	9.045077D-03	7.937059D-03	2.725098D-01	4.568840D-01	2.536072D-01	8.508D-01	5.055D 01	4.860D 01
19	5.990308D-06	7.244900D-03	7.341444D-03	2.711615D-01	4.596116D-01	2.546347D-01	7.299D-01	5.046D 01	4.881D 01
20	2.134413D-06	5.779520D-03	6.750753D-03	2.690639D-01	4.625545D-01	2.558491D-01	6.267D-01	5.032D 01	4.905D 01
21	7.595351D-07	4.589074D-03	6.166861D-03	2.660900D-01	4.657818D-01	2.573715D-01	5.379D-01	5.013D 01	4.933D 01
22	2.699112D-07	3.623383D-03	5.591041D-03	2.620700D-01	4.693395D-01	2.593756D-01	4.607D-01	4.986D 01	4.968D 01
23	9.576815D-08	2.841022D-03	5.024112D-03	2.567838D-01	4.732318D-01	2.621192D-01	3.933D-01	4.948D 01	5.012D 01
24	3.391661D-08	2.207949D-03	4.466574D-03	2.499514D-01	4.773881D-01	2.659859D-01	3.337D-01	4.897D 01	5.069D 01
25	1.198267D-08	1.696227D-03	3.918745D-03	2.412232D-01	4.816102D-01	2.715517D-01	2.807D-01	4.829D 01	5.143D 01
26	4.218752D-09	1.283110D-03	3.380920D-03	2.301703D-01	4.854892D-01	2.796765D-01	2.332D-01	4.736D 01	5.241D 01
27	1.476796D-09	9.501260D-04	2.859591D-03	2.162812D-01	4.882850D-01	2.916301D-01	1.902D-01	4.609D 01	5.372D 01
28	5.112169D-10	6.823718D-04	2.337765D-03	1.989710D-01	4.887587D-01	3.092502D-01	1.510D-01	4.437D 01	5.548D 01
29	1.724794D-10	4.679200D-04	1.835418D-03	1.776177D-01	4.849665D-01	3.351125D-01	1.152D-01	4.203D 01	5.785D 01
30	5.427012D-11	2.973313D-04	1.350111D-03	1.516467D-01	4.740536D-01	3.726523D-01	8.237D-02	3.888D 01	6.104D 01

Table I-7. Study of the Effect of Reflux Ratio

CRYOGENIC DISTILLATION OF HYDROGEN ISOTOPES FOR ANL/TEPR, .. B.MISRA.. ..NOVEMBER, 1975

ISOTOPIC SEPARATION AT PT= 1.000D 03 TORR, AFTER NUMBER OF ITERATIONS= 15
NUMBER OF THEORETICAL STAGES= 30 REFLUX RATIO L/D1= 1.000D 01
SIDE STREAM LOCATION= 6 1ST FEED PLATE LOCATION= 10 2ND FP LOCATION= 12 3RD FP LOCATION= 15
FEED RATES: 0.0 0.0 1.00D 02 PRODUCTS: 3.00D 01 0.0 BOTTOMS: 7.00D 01

FEED COMP. N-H2	HD	HT	N-D2	DT	N-T2	APH	APD	APT
2.000000D-03	2.700000D-02	1.100000D-02	2.620000D-01	4.290000D-01	2.700000D-01	2.100D 00	4.895D 01	4.895D 01

EQUILIBRIUM STAGE TEMPERATURES, DEG.K..(FROM L TO R IN ASCENDING ORDER OF PLATE NUMBER)

2.468617D 01	2.476909D 01	2.482925D 01	2.487761D 01	2.491906D 01	2.495613D 01
2.499030D 01	2.502249D 01	2.505329D 01	2.508311D 01	2.511223D 01	2.514089D 01
2.516924D 01	2.519741D 01	2.522547D 01	2.524235D 01	2.525666D 01	2.526979D 01
2.528252D 01	2.529538D 01	2.530881D 01	2.532319D 01	2.533893D 01	2.535645D 01
2.537625D 01	2.539889D 01	2.542505D 01	2.545550D 01	2.549109D 01	2.553270D 01

SUMMATION OF LIQUID MOLE FRACTIONS.....(FROM L TO R IN ASCENDING ORDER OF PLATE NUMBER)

1.000000D 00	1.000000D 00	1.000000D 00	1.000000D 00	1.000000D 00	1.000000D 00
1.000000D 00	1.000000D 00	1.000000D 00	1.000000D 00	1.000000D 00	1.000000D 00
1.000000D 00	1.000000D 00	1.000000D 00	1.000000D 00	1.000000D 00	1.000000D 00
1.000000D 00	1.000000D 00	1.000000D 00	1.000000D 00	1.000000D 00	1.000000D 00
1.000000D 00	1.000000D 00	1.000000D 00	1.000000D 00	1.000000D 00	1.000000D 00

PLATE NO.	N-H2	HD	HT	N-D2	DT	N-T2	APH	APD	APT
1	6.666661D-03	8.992426D-02	3.606983D-02	6.511136D-01	2.084272D-01	7.795561D-03	6.966D 00	8.003D 01	1.300D 01
1	1.901469D-03	6.031202D-02	2.929446D-02	6.460488D-01	2.510429D-01	1.140041D-02	4.670D 00	8.017D 01	1.516D 01
2	6.562108D-04	4.142787D-02	2.378505D-02	6.274998D-01	2.908427D-01	1.579442D-02	3.326D 00	7.936D 01	1.731D 01
3	3.344600D-04	2.970668D-02	1.950307D-02	6.014932D-01	3.278539D-01	2.111474D-02	2.494D 00	7.803D 01	1.948D 01
4	2.509710D-04	2.253393D-02	1.625497D-02	5.715843D-01	3.618763D-01	2.749961D-02	1.965D 00	7.638D 01	2.166D 01
5	2.283758D-04	1.817994D-02	1.382565D-02	5.400346D-01	3.926402D-01	3.509123D-02	1.623D 00	7.454D 01	2.383D 01
6	2.213118D-04	1.553202D-02	1.202246D-02	5.083207D-01	4.198704D-01	4.403306D-02	1.400D 00	7.260D 01	2.600D 01
7	2.182578D-04	1.390551D-02	1.068724D-02	4.774050D-01	4.433183D-01	5.446565D-02	1.251D 00	7.060D 01	2.815D 01
8	2.162889D-04	1.288494D-02	9.696102D-03	4.478978D-01	4.627834D-01	6.652152D-02	1.151D 00	6.857D 01	3.028D 01
9	2.146525D-04	1.222162D-02	8.954929D-03	4.201626D-01	4.781270D-01	8.031920D-02	1.080D 00	6.653D 01	3.239D 01
10	2.131460D-04	1.176826D-02	8.393670D-03	3.943884D-01	4.892802D-01	9.595634D-02	1.029D 00	6.449D 01	3.448D 01
11	2.117074D-04	1.143829D-02	7.961014D-03	3.706397D-01	4.962472D-01	1.135021D-01	9.911D-01	6.245D 01	3.656D 01
12	2.103126D-04	1.118118D-02	7.619839D-03	3.488944D-01	4.991052D-01	1.329891D-01	9.611D-01	6.040D 01	3.864D 01
13	2.089492D-04	1.096750D-02	7.343567D-03	3.290723D-01	4.980023D-01	1.544053D-01	9.364D-01	5.836D 01	4.071D 01
14	2.076093D-04	1.078022D-02	7.113353D-03	3.110569D-01	4.931549D-01	1.776871D-01	9.154D-01	5.630D 01	4.278D 01
15	2.062882D-04	1.060949D-02	6.915963D-03	2.947122D-01	4.848424D-01	2.027137D-01	8.969D-01	5.424D 01	4.486D 01
16	6.471023D-05	7.556579D-03	5.885969D-03	2.891975D-01	4.926177D-01	2.046775D-01	6.786D-01	5.393D 01	4.539D 01
17	2.024677D-05	5.363126D-03	4.986148D-03	2.824263D-01	5.004112D-01	2.067930D-01	5.195D-01	5.353D 01	4.595D 01
18	6.321796D-06	3.793613D-03	4.204509D-03	2.744867D-01	5.083234D-01	2.091855D-01	4.005D-01	5.305D 01	4.654D 01
19	1.969377D-06	2.674330D-03	3.528426D-03	2.655225D-01	5.163778D-01	2.119949D-01	3.103D-01	5.249D 01	4.719D 01
20	6.121453D-07	1.878493D-03	2.945679D-03	2.552523D-01	5.245297D-01	2.153931D-01	2.413D-01	5.185D 01	4.791D 01
21	1.898347D-07	1.314203D-03	2.444900D-03	2.439806D-01	5.326597D-01	2.196004D-01	1.880D-01	5.110D 01	4.872D 01
22	5.872463D-08	9.151763D-04	2.015759D-03	2.316046D-01	5.405600D-01	2.249044D-01	1.466D-01	5.023D 01	4.962D 01
23	1.811698D-08	6.337898D-04	1.649010D-03	2.181205D-01	5.479138D-01	2.316828D-01	1.141D-01	4.924D 01	5.065D 01
24	5.572268D-09	4.359373D-04	1.336463D-03	2.035292D-01	5.542692D-01	2.404292D-01	8.862D-02	4.809D 01	5.182D 01
25	1.707905D-09	2.972596D-04	1.070923D-03	1.878423D-01	5.590087D-01	2.517808D-01	6.841D-02	4.675D 01	5.318D 01
26	5.212963D-10	2.004023D-04	8.461074D-04	1.710893D-01	5.613181D-01	2.665461D-01	5.233D-02	4.518D 01	5.476D 01
27	1.582532D-10	1.330311D-04	6.565645D-04	1.533274D-01	5.601587D-01	2.857243D-01	3.948D-02	4.335D 01	5.661D 01
28	4.764464D-11	8.639958D-05	4.975900D-04	1.346533D-01	5.542556D-01	3.105071D-01	2.920D-02	4.118D 01	5.879D 01
29	1.411005D-11	5.431995D-05	3.651450D-04	1.152167D-01	5.421168D-01	3.422470D-01	2.097D-02	3.863D 01	6.135D 01
30	4.002035D-12	3.242396D-05	2.557731D-04	9.523681D-02	5.221028D-01	3.823722D-01	1.441D-02	3.563D 01	6.436D 01

Table I-8. Study of the Effect of Reflux Ratio

CRYOGENIC DISTILLATION OF HYDROGEN ISOTOPES FOR ANL/TEPR, .. B.MISRA.. ..NOVEMBER, 1975

ISOTOPIC SEPARATION AT PT= 1.000D 03 TORR, AFTER NUMBER OF ITERATIONS= 15
NUMBER OF THEORETICAL STAGES= 30 REFLUX RATIO L/D1= 1.500D 01
SIDE STREAM LOCATION= 6 1ST FEED PLATE LOCATION= 10 2ND FP LOCATION= 12 3RD FP LOCATION= 15
FEED RATES: 0.0 0.0 1.00D 02 PRODUCTS: 3.00D 01 0.0 BOTTOMS: 7.00D 01

FEED COMP. N-H2	HD	HT	N-D2	DT	N-T2	APH	APD	APT
2.000000D-03	2.700000D-02	1.100000D-02	2.620000D-01	4.280000D-01	2.700000D-01	2.100D 00	4.895D 01	4.895D 01

EQUILIBRIUM STAGE TEMPERATURES, DEG.K..(FROM L TO R IN ASCENDING ORDER OF PLATE NUMBER)

2.463442D 01	2.471111D 01	2.476739D 01	2.481355D 01	2.485418D 01	2.489165D 01
2.492732D 01	2.496200D 01	2.499618D 01	2.503015D 01	2.506409D 01	2.509813D 01
2.513235D 01	2.516681D 01	2.520154D 01	2.523705D 01	2.524050D 01	2.525809D 01
2.527543D 01	2.529298D 01	2.531108D 01	2.533001D 01	2.535009D 01	2.537162D 01
2.539495D 01	2.542050D 01	2.544869D 01	2.548002D 01	2.551496D 01	2.555392D 01

SUMMATION OF LIQUID MOLE FRACTIONS.....(FROM L TO R IN ASCENDING ORDER OF PLATE NUMBER)

1.000010D 00	1.000010D 00	1.000010D 00	1.000010D 00	1.000010D 00	1.000010D 00
1.000011D 00	1.000010D 00	1.000010D 00	1.000010D 00	1.000009D 00	1.000009D 00
1.000008D 00	1.000007D 00	1.000006D 00	1.000006D 00	1.000007D 00	1.000007D 00
1.000007D 00	1.000007D 00	1.000007D 00	1.000007D 00	1.000007D 00	1.000007D 00
1.000007D 00	1.000006D 00	1.000006D 00	1.000006D 00	1.000005D 00	1.000005D 00

PLATE NO.	N-H2	HD	HT	N-D2	DT	N-T2	APH	APD	APT
1	6.666129D-03	8.996687D-02	3.642225D-02	7.103798D-01	1.528073D-01	3.767222D-03	6.986D 00	8.318D 01	9.838D 00
1	1.918818D-03	6.109948D-02	2.997418D-02	7.146544D-01	1.867606D-01	5.592578D-03	4.746D 00	8.386D 01	1.140D 01
2	6.291332D-04	4.193648D-02	2.451480D-02	7.047378D-01	2.208321D-01	7.949712D-03	3.385D 00	8.355D 01	1.306D 01
3	2.829710D-04	2.955678D-02	2.009492D-02	6.841218D-01	2.549715D-01	1.097207D-02	2.511D 00	8.264D 01	1.485D 01
4	1.901754D-04	2.168218D-02	1.660324D-02	6.578189D-01	2.888927D-01	1.481276D-02	1.933D 00	8.131D 01	1.676D 01
5	1.647339D-04	1.671702D-02	1.388618D-02	6.274088D-01	3.221773D-01	1.964592D-02	1.547D 00	7.968D 01	1.877D 01
6	1.570939D-04	1.359147D-02	1.179198D-02	5.944686D-01	3.543199D-01	2.566594D-02	1.285D 00	7.784D 01	2.087D 01
7	1.541577D-04	1.162961D-02	1.018669D-02	5.601855D-01	3.847592D-01	3.308480D-02	1.106D 00	7.584D 01	2.306D 01
8	1.524779D-04	1.037159D-02	8.958611D-03	5.254766D-01	4.129082D-01	4.212761D-02	9.820D-01	7.371D 01	2.531D 01
9	1.511456D-04	9.561383D-03	8.017754D-03	4.910594D-01	4.381843D-01	5.302599D-02	8.941D-01	7.149D 01	2.761D 01
10	1.499178D-04	9.012837D-03	7.293296D-03	4.574948D-01	4.600398D-01	6.600936D-02	8.303D-01	6.920D 01	2.997D 01
11	1.487275D-04	8.625875D-03	6.730473D-03	4.252130D-01	4.779881D-01	8.129382D-02	7.827D-01	6.685D 01	3.237D 01
12	1.475539D-04	8.336577D-03	6.287532D-03	3.945320D-01	4.916275D-01	9.906880D-02	7.460D-01	6.445D 01	3.480D 01
13	1.463898D-04	8.106368D-03	5.933021D-03	3.656722D-01	5.006604D-01	1.194817D-01	7.166D-01	6.201D 01	3.728D 01
14	1.452318D-04	7.912149D-03	5.643507D-03	3.387697D-01	5.049082D-01	1.426212D-01	6.923D-01	5.952D 01	3.979D 01
15	1.440782D-04	7.740201D-03	5.401718D-03	3.138905D-01	5.043224D-01	1.685010D-01	6.715D-01	5.699D 01	4.234D 01
16	4.287398D-05	5.237941D-03	4.385234D-03	3.014505D-01	5.174682D-01	1.714152D-01	4.854D-01	5.628D 01	4.323D 01
17	4.271759D-05	3.529122D-03	3.541942D-03	2.877925D-01	5.304539D-01	1.746698D-01	3.548D-01	5.548D 01	4.417D 01
18	3.760957D-06	2.367785D-03	2.846480D-03	2.731270D-01	5.432409D-01	1.784141D-01	2.611D-01	5.459D 01	4.515D 01
19	1.108900D-06	1.581917D-03	2.275804D-03	2.576213D-01	5.556992D-01	1.828207D-01	1.930D-01	5.363D 01	4.618D 01
20	3.259660D-07	1.052274D-03	1.809637D-03	2.414206D-01	5.676171D-01	1.881000B-01	1.431D-01	5.258D 01	4.728D 01
21	9.552096D-08	6.967210D-04	1.430467D-03	2.246583D-01	5.787012D-01	1.945132D-01	1.064D-01	5.144D 01	4.846D 01
22	2.790033D-08	4.589748D-04	1.123348D-03	2.074617D-01	5.885707D-01	2.023852D-01	7.912D-02	5.020D 01	4.972D 01
23	8.121187D-09	3.006409D-04	8.756354D-04	1.899563D-01	5.967502D-01	2.121172D-01	5.881D-02	4.885D 01	5.109D 01
24	2.355146D-09	1.956340D-04	6.767047D-04	1.722674D-01	6.026620D-01	2.241982D-01	4.362D-02	4.737D 01	5.259D 01
25	6.802321D-10	1.263006D-04	5.176793D-04	1.545225D-01	6.058212D-01	2.392123D-01	3.220D-02	4.574D 01	5.423D 01
26	1.955802D-10	8.073829D-05	3.911809D-04	1.368530D-01	6.048366D-01	2.578384D-01	2.360D-02	4.393D 01	5.604D 01
27	5.593099D-11	5.095230D-05	2.911054D-04	1.193966D-01	5.994231D-01	2.808382D-01	1.710D-02	4.191D 01	5.807D 01
28	1.587816D-11	3.159296D-05	2.124246D-04	1.022991D-01	5.884317D-01	3.090251D-01	1.220D-02	3.965D 01	6.033D 01
29	4.449672D-12	1.909415D-05	1.510130D-04	8.571655D-02	5.709038D-01	3.432095D-01	8.505D-03	3.712D 01	6.287D 01
30	1.207618D-12	1.108794D-05	1.034962D-04	6.981538D-02	5.459556D-01	3.841145D-01	5.729D-03	3.428D 01	6.571D 01

Table I-9. Study of the Effect of Reflux Ratio

CRYOGENIC DISTILLATION OF HYDROGEN ISOTOPES FOR ANL/TEPR, .. B.MISRA.. ..NOVEMBER, 1975

ISOTOPIC SEPARATION AT PT= 1.000D 03 TORR, AFTER NUMBER OF ITERATIONS= 15
NUMBER OF THEORETICAL STAGES= 30 REFLUX RATIO L/D1= 2.000D 01
SIDE STREAM LOCATION= 6 1ST FEED PLATE LOCATION= 10 2ND FP LOCATION= 12 3RD FP LOCATION= 15
FEED RATES: 0.0 0.0 1.00D 02 PRODUCTS: 3.00D 01 0.0 BOTTOMS: 7.00D 01

FEED COMP. N-H2	HD	HT	N-D2	DT	N-T2	APH	APD	APT
2.000000D-01	2.700000D-02	1.100000D-02	2.620000D-01	4.280000D-01	2.700000D-01	2.100D 00	4.895D 01	4.895D 01

EQUILIBRIUM STAGE TEMPERATURES, DEG.K..(FROM L TO R IN ASCENDING ORDER OF PLATE NUMBER)

2.460980D 01	2.468292D 01	2.473657D 01	2.478077D 01	2.482002D 01	2.485668D 01
2.489212D 01	2.492715D 01	2.496226D 01	2.499768D 01	2.503357D 01	2.506997D 01
2.510689D 01	2.514435D 01	2.518236D 01	2.522093D 01	2.526007D 01	2.529981D 01
2.526885D 01	2.528963D 01	2.531079D 01	2.533257D 01	2.535523D 01	2.537904D 01
2.540428D 01	2.543131D 01	2.546047D 01	2.549212D 01	2.552660D 01	2.556415D 01

SUMMATION OF LIQUID MOLE FRACTIONS.....(FROM L TO R IN ASCENDING ORDER OF PLATE NUMBER)

1.000045D 00	1.000045D 00	1.000047D 00	1.000050D 00	1.000052D 00	1.000054D 00
1.000056D 00	1.000056D 00	1.000057D 00	1.000056D 00	1.000054D 00	1.000052D 00
1.000048D 00	1.000044D 00	1.000040D 00	1.000041D 00	1.000042D 00	1.000042D 00
1.000042D 00	1.000042D 00	1.000041D 00	1.000040D 00	1.000038D 00	1.000037D 00
1.000035D 00	1.000032D 00	1.000030D 00	1.000027D 00	1.000025D 00	1.000022D 00

PLATE NO.	N-H2	HD	HT	N-D2	DT	N-T2	APH	APD	APT
1	6.663139D-03	8.993888D-02	3.650870D-02	7.391280D-01	1.254135D-01	2.392318D-03	6.989D 00	8.468D 01	8.335D 00
1	1.926314D-03	6.144412D-02	3.023454D-02	7.484695D-01	1.543480D-01	3.577550D-03	4.776D 00	8.563D 01	9.586D 00
2	6.141204D-04	4.215361D-02	2.481845D-02	7.428467D-01	1.844148D-01	5.152302D-03	3.410D 00	8.551D 01	1.098D 01
3	2.550413D-04	2.943904D-02	2.034587D-02	7.270761D-01	2.156530D-01	7.230870D-03	2.515D 00	8.496D 01	1.252D 01
4	1.571391D-04	2.118948D-02	1.674170D-02	7.040731D-01	2.478876D-01	9.950964D-03	1.912D 00	8.386D 01	1.423D 01
5	1.300870D-04	1.588863D-02	1.388170D-02	6.758292D-01	2.807937D-01	1.347666D-02	1.501D 00	8.241D 01	1.608D 01
6	1.221242D-04	1.249999D-02	1.163537D-02	6.438207D-01	3.139218D-01	1.799995D-02	1.219D 00	8.070D 01	1.808D 01
7	1.192846D-04	1.033469D-02	9.882900D-03	6.092086D-01	3.467140D-01	2.374051D-02	1.023D 00	7.877D 01	2.020D 01
8	1.178187D-04	8.943514D-03	8.521050D-03	5.729433D-01	3.785248D-01	3.094349D-02	8.850D-01	7.666D 01	2.245D 01
9	1.167214D-04	8.037611D-03	7.464119D-03	5.358584D-01	4.086483D-01	3.987487D-02	7.867D-01	7.442D 01	2.479D 01
10	1.157222D-04	7.433450D-03	6.642676D-03	4.986430D-01	4.363512D-01	5.081395D-02	7.153D-01	7.205D 01	2.723D 01
11	1.147478D-04	7.015622D-03	6.001474D-03	4.619158D-01	4.609096D-01	6.404276D-02	6.623D-01	6.958D 01	2.975D 01
12	1.137779D-04	6.712263D-03	5.497375D-03	4.261990D-01	4.816457D-01	7.983206D-02	6.218D-01	6.703D 01	3.234D 01
13	1.128072D-04	6.479049D-03	5.096195D-03	3.919240D-01	4.979638D-01	9.842417D-02	5.900D-01	6.441D 01	3.499D 01
14	1.118348D-04	6.288898D-03	4.772797D-03	3.593311D-01	5.093824D-01	1.200129D-01	5.642D-01	6.172D 01	3.771D 01
15	1.108608D-04	6.125429D-03	4.507470D-03	3.289722D-01	5.155619D-01	1.447221D-01	5.427D-01	5.898D 01	4.047D 01
16	3.207999D-05	4.035225D-03	3.566610D-03	3.110862D-01	5.329380D-01	1.483418D-01	3.833D-01	5.795D 01	4.166D 01
17	9.248401D-06	2.644781D-03	2.806206D-03	2.922473D-01	5.498421D-01	1.524503D-01	2.735D-01	5.685D 01	4.288D 01
18	2.656641D-06	1.724923D-03	2.195651D-03	2.727551D-01	5.661099D-01	1.572117D-01	1.963D-01	5.566D 01	4.413D 01
19	7.604168D-07	1.119479D-03	1.708261D-03	2.528606D-01	5.814925D-01	1.628184D-01	1.415D-01	5.441D 01	4.544D 01
20	2.168780D-07	7.229217D-04	1.321305D-03	2.327838D-01	5.956696D-01	1.695021D-01	1.022D-01	5.310D 01	4.680D 01
21	6.163071D-08	4.644250D-04	1.015699D-03	2.127225D-01	6.082541D-01	1.775432D-01	7.401D-02	5.171D 01	4.822D 01
22	1.744822D-08	2.967280D-04	7.755862D-04	1.928554D-01	6.187934D-01	1.872789D-01	5.362D-02	5.024D 01	4.970D 01
23	4.920541D-09	1.884618D-04	5.879073D-04	1.733444D-01	6.267705D-01	1.991087D-01	3.882D-02	4.868D 01	5.128D 01
24	1.381963D-09	1.189097D-04	4.419819D-04	1.543356D-01	6.316060D-01	2.134975D-01	2.804D-02	4.702D 01	5.295D 01
25	3.864438D-10	7.445680D-05	3.291352D-04	1.359606D-01	6.326639D-01	2.309719D-01	2.018D-02	4.523D 01	5.474D 01
26	1.075519D-10	4.619815D-05	2.423643D-04	1.183379D-01	6.292656D-01	2.521080D-01	1.443D-02	4.330D 01	5.668D 01
27	2.977221D-11	2.833702D-05	1.760493D-04	1.015742D-01	6.207130D-01	2.775084D-01	1.022D-02	4.119D 01	5.879D 01
28	8.185258D-12	1.711788D-05	1.257052D-04	8.576655D-02	6.063277D-01	3.077630D-01	7.141D-03	3.889D 01	6.110D 01
29	2.225464D-12	1.011929D-05	8.777087D-05	7.100301D-02	5.855056D-01	3.433935D-01	4.894D-03	3.638D 01	6.362D 01
30	5.895360D-13	5.787536D-06	5.943169D-05	5.736297D-02	5.577887D-01	3.847831D-01	3.261D-03	3.363D 01	6.637D 01

Table I-10. Study of the Effect of Reflux Ratio

CRYOGENIC DISTILLATION OF HYDROGEN ISOTOPES FOR ANL/TEPR, .. B.MISRA.. ..NOVEMBER, 1975

ISOTOPIC SEPARATION AT PT= 1.000D 03 TORR, AFTER NUMBER OF ITERATIONS= 15
NUMBER OF THEORETICAL STAGES= 30 REFLUX RATIO L/D1= 2.500D 01
SIDE STREAM LOCATION= 6 1ST FEED PLATE LOCATION= 10 2ND FP LOCATION= 12 3RD FP LOCATION= 15
FEED RATES: 0.0 0.0 1.00D 02 PRODUCTS: 3.00D 01 0.0 BOTTOMS: 7.00D 01

FEED COMP.	N-H2	HD	HT	N-D2	DT	N-T2	APH	APD	APT
	2.000000D-03	2.700000D-02	1.100000D-02	2.620000D-01	4.280000D-01	2.700000D-01	2.100D 00	4.895D 01	4.895D 01

EQUILIBRIUM STAGE TEMPERATURES, DEG.K.. (FROM L TO R IN ASCENDING ORDER OF PLATE NUMBER)

2.459636D 01	2.466735D 01	2.471931D 01	2.476214D 01	2.480027D 01	2.483609D 01
2.487099D 01	2.490581D 01	2.494103D 01	2.497691D 01	2.501356D 01	2.505100D 01
2.508919D 01	2.512810D 01	2.516764D 01	2.519315D 01	2.521716D 01	2.524045D 01
2.526347D 01	2.528650D 01	2.530975D 01	2.533343D 01	2.535778D 01	2.538304D 01
2.540949D 01	2.543744D 01	2.546720D 01	2.549906D 01	2.553328D 01	2.557001D 01

SUMMATION OF LIQUID MOLE FRACTIONS..... (FROM L TO R IN ASCENDING ORDER OF PLATE NUMBER)

1.000095D 00	1.000098D 00	1.000104D 00	1.000110D 00	1.000117D 00	1.000123D 00
1.000129D 00	1.000133D 00	1.000135D 00	1.000135D 00	1.000133D 00	1.000129D 00
1.000123D 00	1.000114D 00	1.000104D 00	1.000106D 00	1.000107D 00	1.000107D 00
1.000105D 00	1.000103D 00	1.000099D 00	1.000095D 00	1.000090D 00	1.000085D 00
1.000079D 00	1.000073D 00	1.000067D 00	1.000061D 00	1.000054D 00	1.000048D 00

PLATE NO.	N-H2	HD	HT	N-D2	DT	N-T2	APH	APD	APT
1	6.657375D-03	8.986595D-02	3.652088D-02	7.550891D-01	1.102155D-01	1.746614D-03	6.985D 00	8.551D 01	7.511D 00
1	1.929183D-03	6.159199D-02	3.034763D-02	7.673541D-01	1.361548D-01	2.622311D-03	4.789D 00	8.661D 01	8.587D 00
2	6.041384D-04	4.223065D-02	2.495958D-02	7.647428D-01	1.636574D-01	3.805391D-03	3.420D 00	8.676D 01	9.810D 00
3	2.373349D-04	2.931795D-02	2.045883D-02	7.517601D-01	1.928320D-01	5.393788D-03	2.512D 00	8.627D 01	1.120D 01
4	1.362964D-04	2.084127D-02	1.679004D-02	7.311247D-01	2.235989D-01	7.508837D-03	1.895D 00	8.533D 01	1.277D 01
5	1.082325D-04	1.533305D-02	1.384552D-02	7.046837D-01	2.557305D-01	1.029907D-02	1.470D 00	8.401D 01	1.451D 01
6	1.000637D-04	1.177578D-02	1.150724D-02	6.738104D-01	2.888634D-01	1.394311D-02	1.174D 00	8.240D 01	1.641D 01
7	9.729073D-05	9.483714D-03	9.664108D-03	6.396009D-01	3.225028D-01	1.865124D-02	9.670D-01	8.055D 01	1.847D 01
8	9.597389D-05	8.003249D-03	8.218468D-03	6.029846D-01	3.560326D-01	2.466508D-02	8.206D-01	7.849D 01	2.068D 01
9	9.504546D-05	7.038523D-03	7.087803D-03	5.647890D-01	3.887347D-01	3.225494D-02	7.157D-01	7.626D 01	2.301D 01
10	9.421594D-05	6.398757D-03	6.204104D-03	5.257705D-01	4.198181D-01	4.171425D-02	6.395D-01	7.388D 01	2.547D 01
11	9.340682D-05	5.962199D-03	5.512311D-03	4.866258D-01	4.484558D-01	5.335054D-02	5.830D-01	7.137D 01	2.803D 01
12	9.259725D-05	5.651907D-03	4.968473D-03	4.479880D-01	4.738254D-01	6.747267D-02	5.402D-01	6.876D 01	3.068D 01
13	9.178244D-05	5.419735D-03	4.537920D-03	4.104181D-01	4.951583D-01	8.437416D-02	5.070D-01	6.606D 01	3.342D 01
14	9.096217D-05	5.235854D-03	4.193600D-03	3.743941D-01	5.117726D-01	1.043129D-01	4.805D-01	6.328D 01	3.623D 01
15	9.013761D-05	5.081978D-03	3.914622D-03	3.403029D-01	5.231226D-01	1.274878D-01	4.588D-01	6.043D 01	3.910D 01
16	2.563678D-05	3.293067D-03	3.048620D-03	3.183179D-01	5.436920D-01	1.316228D-01	3.196D-01	5.917D 01	4.049D 01
17	7.261390D-06	2.121908D-03	2.359668D-03	2.956750D-01	5.634711D-01	1.363651D-01	2.248D-01	5.784D 01	4.192D 01
18	2.048470D-06	1.359868D-03	1.815424D-03	2.727346D-01	5.821984D-01	1.418898D-01	1.589D-01	5.645D 01	4.339D 01
19	5.755926D-07	8.667072D-04	1.388266D-03	2.498000D-01	5.995422D-01	1.484023D-01	1.128D-01	5.499D 01	4.488D 01
20	1.610936D-07	5.494068D-04	1.055059D-03	2.271326D-01	6.151159D-01	1.561469D-01	8.023D-02	5.349D 01	4.642D 01
21	4.490593D-08	3.463303D-04	7.966830D-04	2.049578D-01	6.284856D-01	1.654135D-01	5.715D-02	5.193D 01	4.800D 01
22	1.246695D-08	2.170543D-04	5.975028D-04	1.834685D-01	6.391753D-01	1.765416D-01	4.073D-02	5.031D 01	4.964D 01
23	3.446670D-09	1.352006D-04	4.448476D-04	1.628266D-01	6.466718D-01	1.899215D-01	2.900D-02	4.862D 01	5.134D 01
24	9.487546D-10	8.365506D-05	3.285326D-04	1.431652D-01	6.504305D-01	2.059921D-01	2.061D-02	4.684D 01	5.313D 01
25	2.599735D-10	5.137585D-05	2.404328D-04	1.245906D-01	6.498868D-01	2.252307D-01	1.459D-02	4.495D 01	5.503D 01
26	7.089081D-11	3.127817D-05	1.741128D-04	1.071859D-01	6.444729D-01	2.481358D-01	1.027D-02	4.294D 01	5.704D 01
27	1.922686D-11	1.884063D-05	1.245102D-04	9.101325D-02	6.336450D-01	2.751984D-01	7.167D-03	4.078D 01	5.920D 01
28	5.180534D-12	1.119330D-05	8.766766D-05	7.611707D-02	6.169221D-01	3.068620D-01	4.943D-03	3.846D 01	6.153D 01
29	1.381915D-12	6.524231D-06	6.051006D-05	6.252651D-02	5.939355D-01	3.434710D-01	3.352D-03	3.595D 01	6.404D 01
30	3.605250D-13	3.695658D-06	4.066108D-05	5.025653D-02	5.644882D-01	3.852109D-01	2.218D-03	3.325D 01	6.674D 01

Table I-11. Analysis of the Effect of Number of Feeds

CRYOGENIC DISTILLATION OF HYDROGEN ISOTOPES FOR ANL/TEPR, .. B.MISRA.. ..NOVEMBER, 1975

ISOTOPIC SEPARATION AT PT= 1.000D 03 TORR, AFTER NUMBER OF ITERATIONS= 15
NUMBER OF THEORETICAL STAGES= 30 REFLUX RATIO L/D1= 1.500D 01
SIDE STREAM LOCATION= 6 1ST FEED PLATE LOCATION= 10 2ND FP LOCATION= 12 3RD FP LOCATION= 15
FEED RATES: 1.50D 00 8.85D 01 1.00D 01 PRODUCTS: 1.80D 01 0.0 BOTTOMS: 8.20D 01

FEED COMP. N-H2	HD	HT	N-D2	DT	N-T2	APH	APD	APT
1.000000D-04	5.000000D-03	5.000000D-03	2.500000D-01	4.899000D-01	2.500000D-01	3.755D 00	8.887D 01	7.379D 00
8.000000D-03	3.198990D-02	3.194160D-02	9.207500D-01	7.326180D-03	6.510520D-08	3.755D 00	8.887D 01	7.379D 00
2.000000D-03	2.700000D-02	1.100000D-02	2.620000D-01	4.280000D-01	2.700000D-01	3.755D 00	8.887D 01	7.379D 00

EQUILIBRIUM STAGE TEMPERATURES, DEG.K..(FROM L TO R IN ASCENDING ORDER OF PLATE NUMBER)

2.424160D 01	2.438097D 01	2.445305D 01	2.449680D 01	2.452618D 01	2.454708D 01
2.456256D 01	2.457454D 01	2.458433D 01	2.459292D 01	2.459651D 01	2.459919D 01
2.461615D 01	2.463272D 01	2.465387D 01	2.465880D 01	2.466304D 01	2.466684D 01
2.467032D 01	2.467357D 01	2.467665D 01	2.467966D 01	2.468269D 01	2.468589D 01
2.468949D 01	2.469383D 01	2.469951D 01	2.470750D 01	2.471946D 01	2.473817D 01

SUMMATION OF LIQUID MOLE FRACTIONS.....(FROM L TO R IN ASCENDING ORDER OF PLATE NUMBER)

1.000000D 00	1.000000D 00	1.000000D 00	1.000000D 00	1.000000D 00	1.000000D 00
1.000000D 00	1.000000D 00	1.000000D 00	1.000000D 00	1.000000D 00	1.000000D 00
1.000000D 00	1.000000D 00	1.000000D 00	1.000000D 00	1.000000D 00	1.000000D 00
1.000000D 00	1.000000D 00	1.000000D 00	1.000000D 00	1.000000D 00	1.000000D 00
1.000000D 00	1.000000D 00	1.000000D 00	1.000000D 00	1.000000D 00	1.000000D 00

PLATE NO.	N-H2	HD	HT	N-D2	DT	N-T2	APH	APD	APT
1	4.045249D-02	1.695094D-01	1.165419D-01	6.708856D-01	2.516199D-03	9.443035D-05	1.835D 01	7.569D 01	5.962D 00
1	1.249230D-02	1.267721D-01	1.062158D-01	7.509188D-01	3.443055D-03	1.578962D-04	1.290D 01	8.160D 01	5.499D 00
2	4.288508D-03	9.352417D-02	9.389763D-02	8.035947D-01	4.448369D-03	2.466451D-04	9.800D 00	8.526D 01	4.942D 00
3	1.946941D-03	6.975669D-02	8.219412D-02	8.401605D-01	5.570041D-03	3.717446D-04	7.792D 00	8.778D 01	4.425D 00
4	1.284225D-03	5.336576D-02	7.191250D-02	8.660520D-01	6.837205D-03	5.483105D-04	6.392D 00	8.962D 01	3.992D 00
5	1.095197D-03	4.227012D-02	6.321220D-02	8.843478D-01	8.277352D-03	7.973178D-04	5.384D 00	9.096D 01	3.654D 00
6	1.039319D-03	3.483939D-02	5.600757D-02	8.970459D-01	9.919769D-03	1.148066D-03	4.646D 00	9.194D 01	3.411D 00
7	1.021184D-03	2.989395D-02	5.012250D-02	9.055240D-01	1.179682D-02	1.641510D-03	4.103D 00	9.264D 01	3.260D 00
8	1.014064D-03	2.661216D-02	4.535740D-02	9.107373D-01	1.394429D-02	2.334790D-03	3.700D 00	9.310D 01	3.199D 00
9	1.010361D-03	2.443387D-02	4.151936D-02	9.133277D-01	1.640136D-02	3.307389D-03	3.399D 00	9.337D 01	3.227D 00
10	1.007814D-03	2.298205D-02	3.843503D-02	9.136956D-01	1.921010D-02	4.669425D-03	3.172D 00	9.348D 01	3.349D 00
11	1.007849D-03	2.209331D-02	3.614140D-02	9.166793D-01	1.941499D-02	4.663142D-03	3.013D 00	9.374D 01	3.244D 00
12	1.007379D-03	2.150508D-02	3.432096D-02	9.188774D-01	1.963868D-02	4.650523D-03	2.892D 00	9.394D 01	3.163D 00
13	3.836968D-04	1.884073D-02	3.335758D-02	9.162239D-01	2.445175D-02	6.742354D-03	2.648D 00	9.379D 01	3.565D 00
14	1.580949D-04	1.650245D-02	3.222473D-02	9.088280D-01	3.169392D-02	1.059284D-02	2.452D 00	9.329D 01	4.255D 00
15	7.660879D-05	1.444251D-02	3.089122D-02	8.944510D-01	4.250837D-02	1.763030D-02	2.274D 00	9.229D 01	5.433D 00
16	2.820809D-05	1.239247D-02	3.005390D-02	8.972602D-01	4.261062D-02	1.765462D-02	2.125D 00	9.248D 01	5.399D 00
17	1.037868D-05	1.060344D-02	2.914247D-02	8.998466D-01	4.271877D-02	1.767831D-02	1.988D 00	9.265D 01	5.361D 00
18	3.816084D-06	9.044957D-03	2.815851D-02	9.022484D-01	4.284120D-02	1.770308D-02	1.861D 00	9.282D 01	5.320D 00
19	1.402251D-06	7.689330D-03	2.710267D-02	9.044857D-01	4.298942D-02	1.773151D-02	1.740D 00	9.298D 01	5.278D 00
20	5.149718D-07	6.511659D-03	2.597501D-02	9.065646D-01	4.318021D-02	1.776800D-02	1.624D 00	9.314D 01	5.235D 00
21	1.890173D-07	5.489725D-03	2.477512D-02	9.084759D-01	4.343865D-02	1.782043D-02	1.513D 00	9.329D 01	5.193D 00
22	6.933973D-08	4.603798D-03	2.350206D-02	9.101884D-01	4.380245D-02	1.790318D-02	1.405D 00	9.344D 01	5.156D 00
23	2.542216D-08	3.836421D-03	2.215440D-02	9.116380D-01	4.432848D-02	1.804263D-02	1.300D 00	9.357D 01	5.128D 00
24	9.314288D-09	3.172194D-03	2.073006D-02	9.127079D-01	4.510248D-02	1.828738D-02	1.195D 00	9.368D 01	5.120D 00
25	3.409434D-09	2.597563D-03	1.922615D-02	9.131959D-01	4.625331D-02	1.872706D-02	1.091D 00	9.376D 01	5.147D 00
26	1.246036D-09	2.100620D-03	1.763874D-02	9.127602D-01	4.797361D-02	1.952679D-02	9.870D-01	9.378D 01	5.233D 00
27	4.539225D-10	1.670925D-03	1.596256D-02	9.108277D-01	5.054889D-02	2.098992D-02	8.817D-01	9.369D 01	5.425D 00
28	1.641214D-10	1.299360D-03	1.419066D-02	9.064429D-01	5.439631D-02	2.367076D-02	7.745D-01	9.343D 01	5.796D 00
29	5.820672D-11	9.780184D-04	1.231433D-02	8.980240D-01	6.011137D-02	2.857231D-02	6.646D-01	9.286D 01	6.479D 00
30	1.955957D-11	7.001848D-04	1.032386D-02	8.829861D-01	6.851082D-02	3.747909D-02	5.512D-01	9.176D 01	7.690D 00

Table I-12. Analysis of the Effect of Number of Feeds

CRYOGENIC DISTILLATION OF HYDROGEN ISOTOPES FOR ANL/TEPR, .. B.MISRA.. ..NOVEMBER, 1975

ISOTOPIC SEPARATION AT PT= 1.000D 03 TORR, AFTER NUMBER OF ITERATIONS= 15
NUMBER OF THEORETICAL STAGES= 50 REFLUX RATIO L/D1= 1.500D 01
SIDE STREAM LOCATION= 6 1ST FEED PLATE LOCATION= 20 2ND FP LOCATION= 25 3RD FP LOCATION= 30
FEED RATES: 1.50D 00 8.85D 01 1.00D 01 PRODUCTS: 1.80D 01 0.0 BOTTOMS: 8.20D 01

FEED COMP.N-H2	HD	HT	N-D2	DT	N-T2	APH	APD	APT
1.000000D-04	5.000000D-03	5.000000D-03	2.500000D-01	4.899000D-01	2.500000D-01	3.755D 00	8.887D 01	7.379D 00
8.000000D-03	3.198990D-02	3.194160D-02	9.207500D-01	7.326180D-03	6.510520D-08	3.755D 00	8.887D 01	7.379D 00
2.000000D-03	2.700000D-02	1.100000D-02	2.620000D-01	4.280000D-01	2.700000D-01	3.755D 00	8.887D 01	7.379D 00

EQUILIBRIUM STAGE TEMPERATURES, DEG.K..(FROM L TO R IN ASCENDING ORDER OF PLATE NUMBER)

2.422811D 01	2.436773D 01	2.444021D 01	2.448417D 01	2.451345D 01	2.453387D 01
2.454842D 01	2.455896D 01	2.456670D 01	2.457249D 01	2.457691D 01	2.458040D 01
2.458326D 01	2.458574D 01	2.458801D 01	2.459022D 01	2.459252D 01	2.459504D 01
2.459795D 01	2.460143D 01	2.460116D 01	2.460078D 01	2.460025D 01	2.459952D 01
2.459854D 01	2.461114D 01	2.462091D 01	2.463116D 01	2.464432D 01	2.466329D 01
2.466681D 01	2.466986D 01	2.467258D 01	2.467502D 01	2.467726D 01	2.467932D 01
2.468124D 01	2.468304D 01	2.468477D 01	2.468646D 01	2.468815D 01	2.468991D 01
2.469180D 01	2.469397D 01	2.469661D 01	2.470008D 01	2.470494D 01	2.471216D 01
2.472339D 01	2.474139D 01				

SUMMATION OF LIQUID MOLE FRACTIONS.....(FROM L TO R IN ASCENDING ORDER OF PLATE NUMBER)

1.000000D 00	1.000000D 00	1.000000D 00	1.000000D 00	1.000000D 00	1.000000D 00
1.000000D 00	1.000000D 00	1.000000D 00	1.000000D 00	1.000000D 00	1.000000D 00
1.000000D 00	1.000000D 00	1.000000D 00	1.000000D 00	1.000000D 00	1.000000D 00
1.000000D 00	1.000000D 00	1.000000D 00	1.000000D 00	1.000000D 00	1.000000D 00
1.000000D 00	1.000000D 00	1.000000D 00	1.000000D 00	1.000000D 00	1.000000D 00
1.000000D 00	1.000000D 00	1.000000D 00	1.000000D 00	1.000000D 00	1.000000D 00
1.000000D 00	1.000000D 00	1.000000D 00	1.000000D 00	1.000000D 00	1.000000D 00
1.000000D 00	1.000000D 00	1.000000D 00	1.000000D 00	1.000000D 00	1.000000D 00
1.000000D 00	1.000000D 00				

PLATE NO.	N-H2	HD	HT	N-D2	DT	N-T2	APH	APD	APT
1	4.045249D-02	1.715724D-01	1.276217D-01	6.598875D-01	4.631483D-04	2.722777D-06	1.900D 01	7.459D 01	6.405D 00
1	1.252276D-02	1.287464D-01	1.167284D-01	7.413616D-01	6.362529D-04	4.571661D-06	1.353D 01	8.061D 01	5.869D 00
2	4.307334D-03	9.526505D-02	1.035231D-01	7.960723D-01	8.250275D-04	7.168951D-06	1.037D 01	8.441D 01	5.218D 00
3	1.956679D-03	7.123074D-02	9.087568D-02	8.348895D-01	1.036596D-03	1.084500D-05	8.301D 00	8.710D 01	4.597D 00
4	1.289824D-03	5.459516D-02	7.970266D-02	8.631197D-01	1.276620D-03	1.605394D-05	6.844D 00	8.911D 01	4.051D 00
5	1.099230D-03	4.329795D-02	7.020859D-02	8.838202D-01	1.550624D-03	2.343016D-05	5.785D 00	9.062D 01	3.590D 00
6	1.042876D-03	3.571207D-02	6.232278D-02	8.990237D-01	1.864675D-03	3.386652D-05	5.006D 00	9.178D 01	3.213D 00
7	1.024733D-03	3.065380D-02	5.586922D-02	9.101779D-01	2.225695D-03	4.862239D-05	4.429D 00	9.266D 01	2.910D 00
8	1.017850D-03	2.729513D-02	5.064120D-02	9.183347D-01	2.641649D-03	6.947447D-05	3.999D 00	9.333D 01	2.671D 00
9	1.014569D-03	2.506991D-02	4.643608D-02	9.242588D-01	3.121695D-03	9.892841D-05	3.677D 00	9.384D 01	2.488D 00
10	1.012630D-03	2.359642D-02	4.307064D-02	9.285034D-01	3.676366D-03	1.405163D-04	3.435D 00	9.421D 01	2.351D 00
11	1.011305D-03	2.261971D-02	4.038650D-02	9.314655D-01	4.317755D-03	1.992146D-04	3.251D 00	9.449D 01	2.255D 00
12	1.010316D-03	2.197047D-02	3.825047D-02	9.334270D-01	5.059745D-03	2.820308D-04	3.112D 00	9.469D 01	2.194D 00
13	1.009532D-03	2.153665D-02	3.655251D-02	9.345842D-01	5.918244D-03	3.988257D-04	3.005D 00	9.483D 01	2.163D 00
14	1.008875D-03	2.124421D-02	3.520278D-02	9.350692D-01	6.911453D-03	5.634640D-04	2.923D 00	9.491D 01	2.162D 00
15	1.008290D-03	2.104422D-02	3.412844D-02	9.349635D-01	8.060131D-03	7.954206D-04	2.859D 00	9.495D 01	2.189D 00
	****	****	**** ****	****	****	****	****	****	
40	1.636670D-09	2.332534D-03	2.008607D-02	9.160584D-01	4.368330D-02	1.783973D-02	1.121D 00	9.391D 01	4.972D 00
41	5.995076D-10	1.961684D-03	1.912322D-02	9.171078D-01	4.392145D-02	1.788588D-02	1.054D 00	9.400D 01	4.941D 00
42	2.195268D-10	1.641596D-03	1.811101D-02	9.180164D-01	4.426789D-02	1.796316D-02	9.876D-01	9.410D 01	4.915D 00
43	8.035592D-11	1.365414D-03	1.704763D-02	9.187095D-01	4.477946D-02	1.809795D-02	9.207D-01	9.418D 01	4.901D 00
44	2.939916D-11	1.127172D-03	1.593089D-02	9.190611D-01	4.554198D-02	1.833887D-02	8.529D-01	9.424D 01	4.908D 00
45	1.074784D-11	9.216865D-04	1.475804D-02	9.188603D-01	4.668447D-02	1.877552D-02	7.840D-01	9.427D 01	4.950D 00
46	3.923664D-12	7.444504D-04	1.352558D-02	9.177572D-01	4.839982D-02	1.957290D-02	7.135D-01	9.423D 01	5.054D 00
47	1.428007D-12	5.915514D-04	1.222904D-02	9.151716D-01	5.097391D-02	2.103392D-02	6.410D-01	9.410D 01	5.264D 00
48	5.158987D-13	4.595991D-04	1.086269D-02	9.101415D-01	5.482443D-02	2.371175D-02	5.661D-01	9.378D 01	5.656D 00
49	1.828458D-13	3.456758D-04	9.419510D-03	9.010802D-01	6.054763D-02	2.860694D-02	4.883D-01	9.315D 01	6.359D 00

Table I-13. Analysis of the Effect of Operating Pressure

CRYOGENIC DISTILLATION OF HYDROGEN ISOTOPES FOR ANL/TEPR, .. B.MISRA.. ..NOVEMBER, 1975

ISOTOPIC SEPARATION AT PT= 1.000D 03 TORR, AFTER NUMBER OF ITERATIONS= 15
NUMBER OF THEORETICAL STAGES= 30 REFLUX RATIO L/D1= 1.500D 01
SIDE STREAM LOCATION= 6 1ST FEED PLATE LOCATION= 10 2ND FP LOCATION= 12 3RD FP LOCATION= 15
FEED RATES: 0.0 0.0 1.00D 02 PRODUCTS: 3.00D 01 0.0 BOTTOMS: 7.00D 01

FEED COMP. N-H2	HD	HT	N-D2	DT	N-T2	APH	APD	APT
2.000000D-03	2.700000D-02	1.100000D-02	2.620000D-01	4.280000D-01	2.700000D-01	2.100D 00	4.895D 01	4.895D 01

EQUILIBRIUM STAGE TEMPERATURES, DEG.K..(FROM L TO R IN ASCENDING ORDER OF PLATE NUMBER)

2.463442D 01	2.471111D 01	2.476739D 01	2.481355D 01	2.485418D 01	2.489165D 01
2.492732D 01	2.496200D 01	2.499618D 01	2.503015D 01	2.506409D 01	2.509813D 01
2.513235D 01	2.516681D 01	2.520154D 01	2.523205D 01	2.524050D 01	2.525808D 01
2.527543D 01	2.529298D 01	2.531106D 01	2.533001D 01	2.535009D 01	2.537162D 01
2.539495D 01	2.542050D 01	2.544869D 01	2.548002D 01	2.551496D 01	2.555392D 01

SUMMATION OF LIQUID MOLE FRACTIONS.....(FROM L TO R IN ASCENDING ORDER OF PLATE NUMBER)

1.000010D 00	1.000010D 00	1.000010D 00	1.000010D 00	1.000010D 00	1.000010D 00
1.000011D 00	1.000010D 00	1.000010D 00	1.000010D 00	1.000009D 00	1.000009D 00
1.000008D 00	1.000007D 00	1.000006D 00	1.000006D 00	1.000007D 00	1.000007D 00
1.000007D 00	1.000007D 00	1.000007D 00	1.000007D 00	1.000007D 00	1.000007D 00
1.000007D 00	1.000006D 00	1.000006D 00	1.000006D 00	1.000005D 00	1.000005D 00

PLATE NO.	N-H2	HD	HT	N-D2	DT	N-T2	APH	APD	APT
1	6.666129D-03	8.996687D-02	3.642225D-02	7.103798D-01	1.528073D-01	3.767222D-03	6.986D 00	8.318D 01	9.838D 00
1	1.918818D-03	6.109 [illegible]D-02	2.997419D-02	7.146544D-01	1.867606D-01	5.592578D-03	4.746D 00	8.186D 01	1.140D 01
2	6.291332D-04	4.193648D-02	2.451480D-02	7.041378D-01	2.208321D-01	7.949712D-03	3.385D 00	8.355D 01	1.306D 01
3	2.829710D-04	2.955678D-02	2.009492D-02	6.841218D-01	2.549715D-01	1.097207D-02	2.511D 00	8.264D 01	1.485D 01
4	1.901754D-04	2.168218D-02	1.660324D-02	6.578189D-01	2.888927D-01	1.481276D-02	1.933D 00	8.131D 01	1.676D 01
5	1.647339D-04	1.671702D-02	1.388618D-02	6.274088D-01	3.221773D-01	1.984592D-02	1.547D 00	7.968D 01	1.877D 01
6	1.570939D-04	1.359647D-02	1.179198D-02	5.944686D-01	3.543199D-01	2.566594D-02	1.285D 00	7.784D 01	2.087D 01
7	1.541577D-04	1.162961D-02	1.018669D-02	5.601855D-01	3.847592D-01	3.308480D-02	1.106D 00	7.584D 01	2.306D 01
8	1.524779D-04	1.037659D-02	8.958611D-03	5.254766D-01	4.129082D-01	4.212761D-02	9.820D-01	7.371D 01	2.531D 01
9	1.511456D-04	9.561383D-03	8.017754D-03	4.910594D-01	4.381843D-01	5.302599D-02	8.941D-01	7.149D 01	2.761D 01
10	1.499178D-04	9.012837D-03	7.293296D-03	4.574948D-01	4.600398D-01	6.600936D-02	8.303D-01	6.920D 01	2.997D 01
11	1.487275D-04	8.625875D-03	6.730473D-03	4.252130D-01	4.779881D-01	8.129382D-02	7.827D-01	6.685D 01	3.237D 01
12	1.475539D-04	8.336577D-03	6.287532D-03	3.945320D-01	4.916275D-01	9.906880D-02	7.460D-01	6.445D 01	3.480D 01
13	1.463898D-04	8.106368D-03	5.933021D-03	3.656722D-01	5.006604D-01	1.194817D-01	7.166D-01	6.201D 01	3.728D 01
14	1.452318D-04	7.912149D-03	5.643507D-03	3.387697D-01	5.049082D-01	1.426212D-01	6.923D-01	5.952D 01	3.979D 01
15	1.440782D-04	7.740201D-03	5.401718D-03	3.138905D-01	5.043224D-01	1.685010D-01	6.715D-01	5.699D 01	4.234D 01
16	4.287398D-05	5.237941D-03	4.385234D-03	3.014505D-01	5.174682D-01	1.714152D-01	4.854D-01	5.628D 01	4.323D 01
17	1.271759D-05	3.529122D-03	3.541942D-03	2.877925D-01	5.304539D-01	1.746698D-01	3.548D-01	5.548D 01	4.417D 01
18	3.760957D-06	2.367785D-03	2.846480D-03	2.731270D-01	5.432409D-01	1.784141D-01	2.611D-01	5.459D 01	4.515D 01
19	1.108900D-06	1.581917D-03	2.275804D-03	2.576213D-01	5.556992D-01	1.828207D-01	1.930D-01	5.363D 01	4.618D 01
20	3.259660D-07	1.052274D-03	1.809637D-03	2.414206D-01	5.676171D-01	1.881000D-01	1.431D-01	5.258D 01	4.728D 01
21	9.552096D-08	6.967210D-04	1.430467D-03	2.246583D-01	5.787012D-01	1.945132D-01	1.064D-01	5.144D 01	4.846D 01
22	2.790033D-08	4.589748D-04	1.123348D-03	2.074617D-01	5.885707D-01	2.023852D-01	7.912D-02	5.020D 01	4.972D 01
23	8.121187D-09	3.006409D-04	8.756354D-04	1.899563D-01	5.967502D-01	2.121172D-01	5.881D-02	4.885D 01	5.109D 01
24	2.355146D-09	1.956340D-04	6.767047D-04	1.722674D-01	6.026620D-01	2.241982D-01	4.362D-02	4.737D 01	5.259D 01
25	6.802321D-10	1.263006D-04	5.176793D-04	1.545225D-01	6.056212D-01	2.392123D-01	3.220D-02	4.574D 01	5.423D 01
26	1.955802D-10	8.073829D-05	3.911909D-04	1.368530D-01	6.048366D-01	2.578384D-01	2.360D-02	4.393D 01	5.604D 01
27	5.593099D-11	5.095230D-05	2.911054D-04	1.193966D-01	5.994231D-01	2.808382D-01	1.710D-02	4.191D 01	5.807D 01
28	1.587816D-11	3.159296D-05	2.124246D-04	1.022991D-01	5.884317D-01	3.090251D-01	1.220D-02	3.965D 01	6.033D 01
29	4.449672D-12	1.909415D-05	1.510130D-04	8.571655D-02	5.709038D-01	3.432095D-01	8.505D-03	3.712D 01	6.287D 01
30	1.207618D-12	1.108794D-05	1.034962D-04	6.981538D-02	5.459556D-01	3.841145D-01	5.729D-03	3.428D 01	6.571D 01

Table I-14. Analysis of the Effect of Operating Pressure

CRYOGENIC DISTILLATION OF HYDROGEN ISOTOPES FOR ANL/TEPR, .. B.MISRA.. ..NOVEMBER, 1975

ISOTOPIC SEPARATION AT PT= 5.000D 02 TORR, AFTER NUMBER OF ITERATIONS= 15
NUMBER OF THEORETICAL STAGES= 30 REFLUX RATIO L/D1= 1.500D 01
SIDE STREAM LOCATION= 6 1ST FEED PLATE LOCATION= 10 2ND FP LOCATION= 12 3RD FP LOCATION= 15
FEED RATES: 0.0 0.0 1.00D 02 PRODUCTS: 3.00D 01 0.0 BOTTOMS: 7.00D 01

FEED COMP. N-H2	HD	HT	N-D2	DT	N-T2	APH	APD	APT
2.000000D-03	2.700000D-02	1.100000D-02	2.620000D-01	4.280000D-01	2.700000D-01	2.100D 00	4.895D 01	4.895D 01

EQUILIBRIUM STAGE TEMPERATURES, DEG.K..(FROM L TO R IN ASCENDING ORDER OF PLATE NUMBER)

2.224057D 01	2.231051D 01	2.236306D 01	2.240634D 01	2.244502D 01	2.248173D 01
2.251793D 01	2.255436D 01	2.259138D 01	2.262911D 01	2.266758D 01	2.270682D 01
2.274683D 01	2.278767D 01	2.282938D 01	2.285392D 01	2.287620D 01	2.289730D 01
2.291786D 01	2.293830D 01	2.295889D 01	2.297991D 01	2.300162D 01	2.302437D 01
2.304858D 01	2.307478D 01	2.310360D 01	2.313572D 01	2.317187D 01	2.321268D 01

SUMMATION OF LIQUID MOLE FRACTIONS.....(FROM L TO R IN ASCENDING ORDER OF PLATE NUMBER)

1.000308D 00	1.000330D 00	1.000358D 00	1.000389D 00	1.000418D 00	1.000444D 00
1.000464D 00	1.000475D 00	1.000477D 00	1.000469D 00	1.000451D 00	1.000423D 00
1.000388D 00	1.000346D 00	1.000300D 00	1.000312D 00	1.000319D 00	1.000322D 00
1.000322D 00	1.000317D 00	1.000310D 00	1.000299D 00	1.000285D 00	1.000269D 00
1.000251D 00	1.000232D 00	1.000211D 00	1.000190D 00	1.000168D 00	1.000146D 00

PLATE NO.	N-H2	HD	HT	N-D2	DT	N-T2	APH	APD	APT
1	6.642038D-03	8.966293D-02	3.645329D-02	7.666511D-01	9.975628D-02	1.142308D-03	6.970D 00	8.614D 01	6.925D 00
1	2.637047D-03	5.728725D-02	2.938929D-02	7.802217D-01	1.286015D-01	1.863214D-03	4.596D 00	8.729D 01	8.083D 00
2	1.126617D-03	3.714960D-02	2.354428D-02	7.756524D-01	1.596350D-01	2.892042D-03	3.146D 00	8.738D 01	9.445D 00
3	5.666082D-04	2.494666D-02	1.891252D-02	7.584564D-01	1.927748D-01	4.343013D-03	2.249D 00	8.670D 01	1.101D 01
4	3.605629D-04	1.766930D-02	1.533645D-02	7.324516D-01	2.278160D-01	6.366108D-03	1.686D 00	8.549D 01	1.279D 01
5	2.842736D-04	1.336466D-02	1.261793D-02	7.002230D-01	2.643575D-01	9.152668D-03	1.327D 00	8.387D 01	1.476D 01
6	2.550006D-04	1.082000D-02	1.056952D-02	6.636246D-01	3.017902D-01	1.294066D-02	1.094D 00	8.196D 01	1.690D 01
7	2.426013D-04	9.302298D-03	9.032074D-03	6.240930D-01	3.393117D-01	1.801832D-02	9.405D-01	7.980D 01	1.921D 01
8	2.362025D-04	8.376713D-03	7.877618D-03	5.828246D-01	3.759598D-01	2.472508D-02	8.359D-01	7.746D 01	2.165D 01
9	2.319164D-04	7.789072D-03	7.006564D-03	5.408592D-01	4.106648D-01	3.344852D-02	7.626D-01	7.497D 01	2.422D 01
10	2.283652D-04	7.392712D-03	6.343081D-03	4.991093D-01	4.423105D-01	4.461609D-02	7.093D-01	7.236D 01	2.688D 01
11	2.250662D-04	7.104021D-03	5.830377D-03	4.583593D-01	4.698014D-01	5.867948D-02	6.689D-01	6.965D 01	2.964D 01
12	2.218522D-04	6.875857D-03	5.426477D-03	4.192548D-01	4.921276D-01	7.609332D-02	6.370D-01	6.685D 01	3.247D 01
13	2.186653D-04	6.681893D-03	5.100713D-03	3.822951D-01	5.084253D-01	9.727833D-02	6.108D-01	6.396D 01	3.539D 01
14	2.154845D-04	6.507544D-03	4.830916D-03	3.478328D-01	5.180300D-01	1.225833D-01	5.883D-01	6.099D 01	3.839D 01
15	2.123018D-04	6.344793D-03	4.601239D-03	3.160844D-01	5.205239D-01	1.522334D-01	5.684D-01	5.793D 01	4.147D 01
16	8.298456D-05	3.907344D-03	3.530427D-03	2.981948D-01	5.390520D-01	1.552324D-01	3.801D-01	5.695D 01	4.264D 01
17	3.226313D-05	2.391545D-03	2.690436D-03	2.790917D-01	5.572737D-01	1.585203D-01	2.572D-01	5.587D 01	4.384D 01
18	1.247983D-05	1.455281D-03	2.036922D-03	2.591829D-01	5.750683D-01	1.622441D-01	1.758D-01	5.473D 01	4.507D 01
19	4.803566D-06	8.805276D-04	1.532141D-03	2.388027D-01	5.922005D-01	1.665793D-01	1.211D-01	5.352D 01	4.633D 01
20	1.839874D-06	5.297455D-04	1.144821D-03	2.182383D-01	6.083371D-01	1.717482D-01	8.389D-02	5.225D 01	4.763D 01
21	7.012414D-07	3.168631D-04	8.495036D-04	1.977416D-01	6.230523D-01	1.780391D-01	5.837D-02	5.093D 01	4.898D 01
22	2.659250D-07	1.883884D-04	6.257181D-04	1.775350D-01	6.358252D-01	1.858254D-01	4.072D-02	4.954D 01	5.039D 01
23	1.003198D-07	1.112859D-04	4.571670D-04	1.578128D-01	6.460319D-01	1.955867D-01	2.842D-02	4.807D 01	5.187D 01
24	3.763814D-08	6.527454D-05	3.309876D-04	1.387421D-01	6.529338D-01	2.079278D-01	1.981D-02	4.651D 01	5.344D 01
25	1.403740D-08	3.797578D-05	2.371092D-04	1.204643D-01	6.566674D-01	2.235931D-01	1.375D-02	4.482D 01	5.514D 01
26	5.200307D-09	2.187687D-05	1.677072D-04	1.030982D-01	6.532420D-01	2.434702D-01	9.478D-03	4.296D 01	5.700D 01
27	1.910469D-09	1.244378D-05	1.167469D-04	8.674381D-02	6.445543D-01	2.685747D-01	6.458D-03	4.089D 01	5.908D 01
28	6.943305D-10	6.955334D-06	7.960692D-05	7.148785D-02	6.284350D-01	2.999906D-01	4.327D-03	3.856D 01	6.141D 01
29	2.476489D-10	3.787392D-06	5.277089D-05	5.740863D-02	6.037399D-01	3.387949D-01	2.827D-03	3.592D 01	6.406D 01
30	8.498651D-11	1.975912D-06	3.357868D-05	4.457942D-02	5.694978D-01	3.858872D-01	1.777D-03	3.293D 01	6.706D 01

Table I-15. Analysis of the Effect of Operating Pressure

CRYOGENIC DISTILLATION OF HYDROGEN ISOTOPES FOR ANL/TEPR, .. B.MISRA.. ..NOVEMBER, 1975

ISOTOPIC SEPARATION AT PT= 1.500D 03 TORR, AFTER NUMBER OF ITERATIONS= 15
NUMBER OF THEORETICAL STAGES= 30 REFLUX RATIO L/D1= 1.500D 01
SIDE STREAM LOCATION= 6 1ST FEED PLATE LOCATION= 10 2ND FP LOCATION= 12 3RD FP LOCATION= 15
FEED RATES: 0.0 0.0 1.00D 02 PRODUCTS: 3.00D 01 0.0 BOTTOMS: 7.00D 01

FEED COMP. N-H2	HD	HT	N-D2	DT	N-T2	APH	APD	APT
2.000000D-03	2.700000D-02	1.100000D-02	2.620000D-01	4.280000D-01	2.700000D-01	2.100D 00	4.895D 01	4.895D 01

EQUILIBRIUM STAGE TEMPERATURES, DEG.K..(FROM L TO R IN ASCENDING ORDER OF PLATE NUMBER)

2.627257D 01	2.634425D 01	2.640111D 01	2.644841D 01	2.648960D 01	2.652685D 01
2.656159D 01	2.659472D 01	2.662681D 01	2.665823D 01	2.668922D 01	2.671995D 01
2.675052D 01	2.678099D 01	2.681141D 01	2.682943D 01	2.684599D 01	2.686183D 01
2.687749D 01	2.689339D 01	2.690989D 01	2.692730D 01	2.694592D 01	2.696607D 01
2.698808D 01	2.701232D 01	2.703917D 01	2.706903D 01	2.710230D 01	2.713933D 01

SUMMATION OF LIQUID MOLE FRACTIONS.....(FROM L TO R IN ASCENDING ORDER OF PLATE NUMBER)

9.999959D-01	9.999960D-01	9.999960D-01	9.999960D-01	9.999960D-01	9.999960D-01
9.999961D-01	9.999962D-01	9.999963D-01	9.999965D-01	9.999967D-01	9.999970D-01
9.999972D-01	9.999976D-01	9.999979D-01	9.999978D-01	9.999977D-01	9.999976D-01
9.999975D-01	9.999974D-01	9.999974D-01	9.999974D-01	9.999974D-01	9.999974D-01
9.999978D-01	9.999975D-01	9.999976D-01	9.999977D-01	9.999979D-01	9.999980D-01

PLATE NO.	N-H2	HD	HT	N-D2	DT	N-T2	APH	APD	APT
1	6.666847D-03	8.993839D-02	3.622720D-02	6.705535D-01	1.893902D-01	7.219742D-03	6.975D 00	8.102D 01	1.200D 01
1	3.258143D-03	6.290812D-02	3.009365D-02	6.693171D-01	2.242731D-01	1.014989D-02	4.976D 00	8.129D 01	1.373D 01
2	1.673004D-03	4.448503D-02	2.490649D-02	6.568752D-01	2.583108D-01	1.374942D-02	3.637D 00	8.083D 01	1.554D 01
3	9.463258D-04	3.219247D-02	2.066388D-02	6.368059D-01	2.912593D-01	1.813210D-02	2.737D 00	7.985D 01	1.741D 01
4	6.159298D-04	2.410610D-02	1.726923D-02	6.117287D-01	3.228553D-01	2.342472D-02	2.130D 00	7.852D 01	1.935D 01
5	4.659111D-04	1.883408D-02	1.459290D-02	5.835429D-01	3.528001D-01	2.976415D-02	1.718D 00	7.694D 01	2.135D 01
6	3.971519D-04	1.541179D-02	1.250353D-02	5.536295D-01	3.807639D-01	3.729408D-02	1.435D 00	7.517D 01	2.339D 01
7	3.647253D-04	1.318912D-02	1.088229D-02	5.230017D-01	4.064010D-01	4.616113D-02	1.240D 00	7.328D 01	2.548D 01
8	3.554636D-04	1.173639D-02	9.627957D-03	4.924084D-01	4.293685D-01	5.651024D-02	1.103D 00	7.130D 01	2.760D 01
9	3.393807D-04	1.077370D-02	8.657426D-03	4.624045D-01	4.493456D-01	6.847937D-02	1.005D 00	6.925D 01	2.975D 01
10	3.334956D-04	1.012089D-02	7.904129D-03	4.333978D-01	4.660503D-01	8.219340D-02	9.346D-01	6.715D 01	3.192D 01
11	3.290510D-04	9.663074D-03	7.315723D-03	4.056807D-01	4.792541D-01	9.775738D-02	8.818D-01	6.501D 01	3.410D 01
12	3.252727D-04	9.327616D-03	6.851628D-03	3.794539D-01	4.887924D-01	1.152492D-01	8.415D-01	6.285D 01	3.631D 01
13	3.218186D-04	9.068939D-03	6.480764D-03	3.548431D-01	4.945732D-01	1.347122D-01	8.097D-01	6.067D 01	3.852D 01
14	3.185371D-04	8.858639D-03	6.179568D-03	3.319141D-01	4.965813D-01	1.561479D-01	7.838D-01	5.846D 01	4.075D 01
15	3.153607D-04	8.679141D-03	5.930355D-03	3.106976D-01	4.948809D-01	1.795096D-01	7.620D-01	5.625D 01	4.299D 01
16	1.587734D-04	6.172007D-03	4.961278D-03	3.008481D-01	5.054603D-01	1.823995D-01	5.725D-01	5.567D 01	4.376D 01
17	7.968836D-05	4.373131D-03	4.132155D-03	2.898679D-01	5.159006D-01	1.856465D-01	4.332D-01	5.500D 01	4.457D 01
18	3.987660D-05	3.087536D-03	3.426267D-03	2.778741D-01	5.261799D-01	1.893923D-01	3.297D-01	5.425D 01	4.542D 01
19	1.989576D-05	2.171995D-03	2.827785D-03	2.649684D-01	5.362102D-01	1.938018D-01	2.520D-01	5.342D 01	4.633D 01
20	9.896890D-06	1.522121D-03	2.322227D-03	2.512361D-01	5.458372D-01	1.990724D-01	1.932D-01	5.249D 01	4.732D 01
21	4.907681D-06	1.062279D-03	1.896615D-03	2.367541D-01	5.548378D-01	2.054443D-01	1.484D-01	5.147D 01	4.838D 01
22	2.425502D-06	7.379248D-04	1.539488D-03	2.215959D-01	5.629140D-01	2.132102D-01	1.141D-01	5.034D 01	4.954D 01
23	1.194370D-06	5.098736D-04	1.240817D-03	2.058372D-01	5.696862D-01	2.227247D-01	8.765D-02	4.909D 01	5.082D 01
24	5.857146D-07	3.500723D-04	9.918929D-04	1.895582D-01	5.746864D-01	2.344128D-01	6.716D-02	4.771D 01	5.223D 01
25	2.858456D-07	2.384983D-04	7.851923D-04	1.728478D-01	5.773531D-01	2.487751D-01	5.121D-02	4.616D 01	5.378D 01
26	1.386626D-07	1.609020D-04	6.142483D-04	1.558064D-01	5.770308D-01	2.663876D-01	3.877D-02	4.444D 01	5.552D 01
27	6.671962D-08	1.071714D-04	4.735226D-04	1.385490D-01	5.729777D-01	2.878926D-01	2.904D-02	4.251D 01	5.746D 01
28	3.171516D-08	7.015022D-05	3.582878D-04	1.212085D-01	5.643853D-01	3.139777D-01	2.143D-02	4.034D 01	5.964D 01
29	1.477161D-08	4.478868D-05	2.645192D-04	1.039381D-01	5.504153D-01	3.453373D-01	1.547D-02	3.792D 01	6.207D 01
30	6.619140D-09	2.753310D-05	1.887950D-04	8.691281D-02	5.302561D-01	3.826147D-01	1.082D-02	3.521D 01	6.478D 01

Table I-16. Analysis of Multiple Feeds

CRYOGENIC DISTILLATION OF HYDROGEN ISOTOPES FOR ANL/TEPR, .. B.MISRA.. ..NOVEMBER, 1975

ISOTOPIC SEPARATION AT PT= 2.000D 03 TORR, AFTER NUMBER OF ITERATIONS= 15
NUMBER OF THEORETICAL STAGES= 30 REFLUX RATIO L/D1= 1.500D 01
SIDE STREAM LOCATION= 6 1ST FEED PLATE LOCATION= 10 2ND FP LOCATION= 12 3RD FP LOCATION= 15
FEED RATES: 0.0 0.0 1.00D 02 PRODUCTS: 3.00D 01 0.0 BOTTOMS: 7.00D 01

FEED COMP. N-H2	HD	HT	N-D2	DT	N-T2	APH	APD	APT
2.000000D-03	2.700000D-02	1.100000D-02	2.620000D-01	4.280000D-01	2.700000D-01	2.100D 00	4.895D 01	4.895D 01

EQUILIBRIUM STAGE TEMPERATURES, DEG.K..(FROM L TO R IN ASCENDING ORDER OF PLATE NUMBER)

2.754899D 01	2.761994D 01	2.767668D 01	2.772391D 01	2.776480D 01	2.780145D 01
2.783524D 01	2.786708D 01	2.789759D 01	2.792717D 01	2.795608D 01	2.798451D 01
2.801257D 01	2.804034D 01	2.806786D 01	2.808448D 01	2.809981D 01	2.811451D 01
2.812906D 01	2.814387D 01	2.815928D 01	2.817559D 01	2.819312D 01	2.821217D 01
2.823307D 01	2.825616D 01	2.828179D 01	2.831035D 01	2.834220D 01	2.837767D 01

SUMMATION OF LIQUID MOLE FRACTIONS.....(FROM L TO R IN ASCENDING ORDER OF PLATE NUMBER)

9.999987D-01	9.999987D-01	9.999988D-01	9.999988D-01	9.999988D-01	9.999988D-01
9.999989D-01	9.999989D-01	9.999989D-01	9.999990D-01	9.999991D-01	9.999991D-01
9.999992D-01	9.999993D-01	9.9999940-01	9.999994D-01	9.999993D-01	9.999993D-01
9.999993D-01	9.999993D-01	9.999992D-01	9.999992D-01	9.999992D-01	9.999992D-01
9.999992D-01	9.999992D-01	9.999993D-01	9.999993D-01	9.999993D-01	9.999994D-01

PLATE NO.	N-H2	HD	HT	N-D2	DT	N-T2	APH	APD	APT
1	6.666680D-03	8.988335D-02	3.601037D-02	6.410251D-01	2.154580D-01	1.095526D-02	6.961D 00	7.937D 01	1.367D 01
1	3.420388D-03	6.415974D-02	3.014099D-02	6.372923D-01	2.501161D-01	1.487051D-02	5.057D 00	7.944D 01	1.550D 01
2	1.835295D-03	4.628014D-02	2.515703D-02	6.240449D-01	2.831668D-01	1.951581D-02	3.755D 00	7.888D 01	1.737D 01
3	1.071589D-03	3.409478D-02	2.105232D-02	6.043652D-01	3.144322D-01	2.498390D-02	2.865D 00	7.786D 01	1.927D 01
4	7.065976D-04	2.590120D-02	1.774068D-02	5.805369D-01	3.437399D-01	3.137470D-02	2.253D 00	7.654D 01	2.121D 01
5	5.325693D-04	2.043983D-02	1.510642D-02	5.542252D-01	3.709043D-01	3.879176D-02	1.831D 00	7.499D 01	2.318D 01
6	4.490998D-04	1.681673D-02	1.303103D-02	5.266380D-01	3.957264D-01	4.733872D-02	1.537D 00	7.329D 01	2.517D 01
7	4.082649D-04	1.441462D-02	1.140606D-02	4.986515D-01	4.180038D-01	5.711579D-02	1.332D 00	7.149D 01	2.718D 01
8	3.874051D-04	1.281544D-02	1.013794D-02	4.709002D-01	4.375430D-01	6.821605D-02	1.186D 00	6.961D 01	2.921D 01
9	3.758847D-04	1.174010D-02	9.148937D-03	4.438413D-01	4.541723D-01	8.072153D-02	1.082D 00	6.768D 01	3.124D 01
10	3.687390D-04	1.100441D-02	8.376051D-03	4.177991D-01	4.677524D-01	9.469926D-02	1.006D 00	6.572D 01	3.328D 01
11	3.636597D-04	1.048791D-02	7.769153D-03	3.929966D-01	4.781856D-01	1.101971D-01	9.492D-01	6.373D 01	3.532D 01
12	3.595758D-04	1.011248D-02	7.288919D-03	3.695780D-01	4.854212D-01	1.272398D-01	9.060D-01	6.173D 01	3.736D 01
13	3.559900D-04	9.827778D-03	6.904857D-03	3.476263D-01	4.894599D-01	1.458251D-01	8.722D-01	5.973D 01	3.940D 01
14	3.526710D-04	9.601604D-03	6.593561D-03	3.271766D-01	4.903549D-01	1.659206D-01	8.450D-01	5.772D 01	4.144D 01
15	3.495107D-04	9.413464D-03	6.337222D-03	3.082269D-01	4.882117D-01	1.874611D-01	8.225D-01	5.570D 01	4.347D 01
16	1.867579D-04	6.918158D-03	5.408146D-03	2.999357D-01	4.972322D-01	1.903190D-01	6.358D-01	5.520D 01	4.416D 01
17	9.952323D-05	5.067847D-03	4.596368D-03	2.905742D-01	5.061225D-01	1.935395D-01	4.932D-01	5.462D 01	4.489D 01
18	5.289861D-05	3.700526D-03	3.890168D-03	2.802300D-01	5.148689D-01	1.972575D-01	3.848D-01	5.385D 01	4.566D 01
19	2.804437D-05	2.693192D-03	3.278045D-03	2.689684D-01	5.234028D-01	2.016295D-01	3.014D-01	5.320D 01	4.650D 01
20	1.482867D-05	1.953151D-03	2.749148D-03	2.568408D-01	5.316006D-01	2.068415D-01	2.366D-01	5.236D 01	4.740D 01
21	7.819050D-06	1.410940D-03	2.293491D-03	2.438912D-01	5.392793D-01	2.131172D-01	1.860D-01	5.142D 01	4.839D 01
22	4.110583D-06	1.014737D-03	1.902025D-03	2.301614D-01	5.461918D-01	2.207259D-01	1.462D-01	5.038D 01	4.948D 01
23	2.153790D-06	7.260131D-04	1.566642D-03	2.156948D-01	5.520194D-01	2.299910D-01	1.148D-01	4.921D 01	5.068D 01
24	1.124169D-06	5.162149D-04	1.280143D-03	2.005401D-01	5.563660D-01	2.412964D-01	8.993D-02	4.790D 01	5.201D 01
25	5.840375D-07	3.642358D-04	1.036167D-03	1.847558D-01	5.587523D-01	2.550909D-01	7.008D-02	4.643D 01	5.350D 01
26	3.016195D-07	2.545131D-04	8.291248D-04	1.684131D-01	5.586142D-01	2.718887D-01	5.421D-02	4.478D 01	5.516D 01
27	1.544874D-07	1.755981D-04	6.541266D-04	1.516004D-01	5.553072D-01	2.922625D-01	4.150D-02	4.293D 01	5.702D 01
28	7.814643D-08	1.190875D-04	5.069039D-04	1.344271D-01	5.481191D-01	3.168277D-01	3.131D-02	4.085D 01	5.911D 01
29	3.871864D-08	7.882683D-05	3.837403D-04	1.170273D-01	5.362968D-01	3.462133D-01	2.313D-02	3.852D 01	6.146D 01
30	1.846409D-08	5.031806D-05	2.814015D-04	9.956260D-02	5.190880D-01	3.810176D-01	1.659D-02	3.591D 01	6.407D 01

Table I-17. Analysis of Multiple Feeds

CRYOGENIC DISTILLATION OF HYDROGEN ISOTOPES FOR ANL/TEPR, .. B.MISRA.. ..NOVEMBER, 1975

ISOTOPIC SEPARATION AT PT= 2.500D 03 TORR, AFTER NUMBER OF ITERATIONS= 15
NUMBER OF THEORETICAL STAGES= 30 REFLUX RATIO L/D1= 1.500D 01
SIDE STREAM LOCATION= 6 1ST FEED PLATE LOCATION= 10 2ND FP LOCATION= 12 3RD FP LOCATION= 15
FEED RATES: 0.0 0.0 1.000 02 PRODUCTS: 3.000 01 0.0 BOTTOMS: 7.000 01

FEED COMP. N-H2	HD	HT	N-D2	DT	N-T2	APH	APD	APT
2.000000D-03	2.700000D-02	1.100000D-02	2.620000D-01	4.280000D-01	2.700000D-01	2.100D 00	4.895D 01	4.895D 01

EQUILIBRIUM STAGE TEMPERATURES, DEG.K..(FROM L TO R IN ASCENDING ORDER OF PLATE NUMBER)

2.861130D 01	2.868126D 01	2.873753D 01	2.878443D 01	2.882489D 01	2.886094D 01
2.889393D 01	2.892477D 01	2.895409D 01	2.898230D 01	2.900969D 01	2.903645D 01
2.906272D 01	2.908856D 01	2.911405D 01	2.913968D 01	2.916417D 01	2.918808D 01
2.917187D 01	2.918593D 01	2.920056D 01	2.921609D 01	2.923281D 01	2.925103D 01
2.927105D 01	2.929323D 01	2.931790D 01	2.934542D 01	2.937615D 01	2.941042D 01

SUMMATION OF LIQUID MOLE FRACTIONS.....(FROM L TO R IN ASCENDING ORDER OF PLATE NUMBER)

9.999996D-01	9.999996D-01	9.999996D-01	9.999996D-01	9.999996D-01	9.999996D-01
9.999997D-01	9.999997D-01	9.999997D-01	9.999997D-01	9.999997D-01	9.999997D-01
9.999998D-01	9.999998D-01	9.999998D-01	9.999998D-01	9.999998D-01	9.999998D-01
9.999998D-01	9.999998D-01	9.999998D-01	9.999998D-01	9.999998D-01	9.999998D-01
9.999998D-01	9.999998D-01	9.999998D-01	9.999998D-01	9.999998D-01	9.999998D-01

PLATE NO.	N-H2	HD	HT	N-D2	DT	N-T2	APH	APD	APT
1	6.666591D-03	8.981702D-02	3.578689D-02	6.182815D-01	2.348239D-01	1.462364D-02	6.947D 00	7.806D 01	1.499D 01
1	3.546679D-03	6.510465D-02	3.013903D-02	6.130815D-01	2.687669D-01	1.936124D-02	5.117D 00	7.800D 01	1.688D 01
2	1.966944D-03	4.767519D-02	2.532726D-02	5.995646D-01	3.006185D-01	2.484751D-02	3.847D 00	7.737D 01	1.878D 01
3	1.177065D-03	3.560658D-02	2.134255D-02	5.804510D-01	3.302672D-01	3.115557D-02	2.965D 00	7.634D 01	2.070D 01
4	7.852209D-04	2.735624D-02	1.810638D-02	5.577710D-01	3.576185D-01	3.836264D-02	2.352D 00	7.503D 01	2.262D 01
5	5.913971D-04	2.176405D-02	1.551354D-02	5.330110D-01	3.825736D-01	4.654633D-02	1.923D 00	7.352D 01	2.456D 01
6	4.951491D-04	1.799200D-02	1.345553D-02	5.072487D-01	4.050273D-01	5.578128D-02	1.622D 00	7.188D 01	2.650D 01
7	4.466447D-04	1.545090D-02	1.183210D-02	4.812607D-01	4.248735D-01	6.613616D-02	1.409D 00	7.014D 01	2.845D 01
8	4.213897D-04	1.373426D-02	1.055598D-02	4.556033D-01	4.420143D-01	7.767072D-02	1.257D 00	6.835D 01	3.040D 01
9	4.074299D-04	1.256568D-02	9.553937D-03	4.306704D-01	4.563695D-01	9.043303D-02	1.147D 00	6.651D 01	3.234D 01
10	3.989634D-04	1.175922D-02	8.766094D-03	4.067352D-01	4.678838D-01	1.044568D-01	1.066D 00	6.466D 01	3.428D 01
11	3.931852D-04	1.119097D-02	8.144335D-03	3.839798D-01	4.765329D-01	1.197588D-01	1.006D 00	6.278D 01	3.621D 01
12	3.887425D-04	1.077898D-02	7.650553D-03	3.625172D-01	4.823278D-01	1.363367D-01	9.604D-01	6.091D 01	3.813D 01
13	3.849831D-04	1.046940D-02	7.254908D-03	3.424073D-01	4.853164D-01	1.541669D-01	9.247D-01	5.903D 01	4.005D 01
14	3.815923D-04	1.022707D-02	6.934257D-03	3.236697D-01	4.855840D-01	1.732033D-01	8.962D-01	5.716D 01	4.195D 01
15	3.784174D-04	1.002913D-02	6.670805D-03	3.062932D-01	4.832523D-01	1.933762D-01	8.728D-01	5.529D 01	4.383D 01
16	2.113280D-04	7.552273D-03	5.776262D-03	2.990326D-01	4.912297D-01	1.961978D-01	6.876D-01	5.484D 01	4.447D 01
17	1.177306D-04	5.670089D-03	4.982173D-03	2.907637D-01	4.990833D-01	1.993830D-01	5.444D-01	5.431D 01	4.514D 01
18	6.543439D-05	4.244216D-03	4.280062D-03	2.815477D-01	5.068021D-01	2.030605D-01	4.328D-01	5.371D 01	4.586D 01
19	3.628357D-05	3.166972D-03	3.661324D-03	2.714271D-01	5.143288D-01	2.073796D-01	3.450D-01	5.302D 01	4.664D 01
20	2.007111D-05	2.355154D-03	3.117620D-03	2.604322D-01	5.215583D-01	2.125167D-01	2.756D-01	5.224D 01	4.749D 01
21	1.107457D-05	1.744824D-03	2.641088D-03	2.485867D-01	5.283336D-01	2.186827D-01	2.204D-01	5.136D 01	4.842D 01
22	6.093582D-06	1.287055D-03	2.224461D-03	2.359113D-01	5.344409D-01	2.261302D-01	1.762D-01	5.038D 01	4.945D 01
23	3.342345D-06	9.445366D-04	1.861100D-03	2.224281D-01	5.396029D-01	2.351600D-01	1.406D-01	4.927D 01	5.059D 01
24	1.826510D-06	6.888995D-04	1.545003D-03	2.081639D-01	5.434726D-01	2.461278D-01	1.119D-01	4.802D 01	5.186D 01
25	9.935912D-07	4.986237D-04	1.270780D-03	1.931544D-01	5.456277D-01	2.594475D-01	8.857D-02	4.662D 01	5.329D 01
26	5.372708D-07	3.574223D-04	1.033620D-03	1.774478D-01	5.455682D-01	2.755925D-01	6.961D-02	4.504D 01	5.489D 01
27	2.880896D-07	2.529935D-04	8.292441D-04	1.611094D-01	5.427179D-01	2.950902D-01	5.414D-02	4.326D 01	5.669D 01
28	1.525200D-07	1.760632D-04	6.538648D-04	1.442263D-01	5.364338D-01	3.185098D-01	4.151D-02	4.125D 01	5.871D 01
29	7.907110D-08	1.196523D-04	5.041322D-04	1.269117D-01	5.260258D-01	3.464387D-01	3.120D-02	3.900D 01	6.097D 01
30	3.947249D-08	7.851774D-05	3.770867D-04	1.093084D-01	5.107894D-01	3.794466D-01	2.278D-02	3.647D 01	6.350D 01

I-2 to I-5). For example, if the number of theoretical stages is increased from 15 to 30, the deuterium atom percentage in the distillate is increased from 75 to 83. However, the atom percentage of protium remains unchanged. This is due to the fact that essentially all of the protium appears in the distillate even when the column has only 15 theoretical stages.

(2) Effect of Reflux Ratio

The degree of separation of the lighter constituents from the heavier constituents increases as the reflux ratio is increased (see Tables I-6 to I-10). However, the increase in the degree of separation becomes asymptotic, as higher and higher reflux ratios are employed.

(3) Feed Plate Location

The effect of the feed plate on degree of separation depends on the feed composition. For the few cases analyzed by varying the feed plate location for a feed of fixed composition, the effect of the feed plate location was found to be minor.

(4) Operating Pressure

As discussed in the previous sections, for a fixed feed composition, the separation of the more volatile fractions depends on the number of theoretical stages, reflux ratio, and the design characteristics of the distillation column. As the number of theoretical stages and reflux ratio are increased, the degree of separation of the more volatile fraction from the less volatile fraction increases. In many situations, the effects of these two variables do not significantly change the degree of separation. Also, increase in the number of equilibrium stages as well as increase in the reflux ratio results in increased liquid holdup and operating cost. However, similar results can be achieved by varying the operating pressure, which is conceptually much simpler.

For ideal solutions, the distribution constant, k_i, can be expressed as

$$k_i = \frac{y_i}{x_i} \qquad (I\text{-}8)$$

$$= \frac{p_i}{P} \qquad (I\text{-}9)$$

where

k_i = distribution constant for component i

y_i = mole fraction of component i in vapor phase

x_i = mole fraction of component i in liquid phase

p_i = vapor pressure of component i

P = total operating pressure of the system

The relative volatility of component 1 with response to component 2 can be expressed by

$$\alpha_{1,2} = \frac{k_1}{k_2} = \frac{p_1}{p_2} \qquad \text{(I-10)}$$

Hence, for ideal mixtures, the relative volatility is independent of pressure, provided, of course, that the column is operated at the same temperature. As the column will be operated at the saturation temperature corresponding to the composition of the liquid mixture at each equilibrium stage, the degree of separation can be controlled to some extent by the operating pressure.

In order to study the effect of pressure, a single distillation column was used for simplicity. The results for a typical feed mixture at pressures of 500, 1000, 1500, 2000, and 2500 Torr, respectively, are summarized in Table I-13 to I-17. The most significant effect of pressure seems to be on the atom fraction of tritium in the distillate. The tritium fraction increases from 7% to 15% when the pressure is increased from 500 Torr to 2500 Torr. The pressure has lesser effect on the other two hydrogen isotopes. As the atom percent of hydrogen in the bottom fraction is essentially zero, for all cases, the operating pressure should have no effect on protium fraction. The atom fraction of deuterium in the distillate decreases from 86% to 78% as the pressure is increased from 500 Torr to 2500 Torr. The other significant observation that can be made is that the composition of the liquid in the bottom product is not very sensitive to operating pressure.

To further demonstrate the general utility of the computer code, two other cases consisting of 30 and 50 theoretical stages respectively and each with three feeds were analyzed. The analytical results are shown in Tables I-11 and I-12.

2. Cryogenic Enrichment Scenario for the EPR

Before an enrichment scheme for the EPR can be developed, the composition of the spent fuels and the purity requirements on the reinjectable fuels must be established. The composition of the spent gases as given below may be considered as representative of a typical experimental power reactor such as the ANL/EPR.

Protium (atom %)	2.1
Deuterium (Atom %)	48.95
Tritium (atom %)	48.95

For the presently conceived fuel injection scheme, the following are some of the requirements for the light and the heavy fractions:

(1) The lightest fraction should contain all of the protium atoms with as little tritium as possible so that it can (if necessary) be sent to waste consolidation and burial without further reprocessing.

(2) One of the heavy fractions must contain > 98 atomic % deuterium so that it may serve as the fuel for the neutral beam injector.

(3) The composition of the other heavy fraction should be such that the ratio of tritium to deuterium atoms is approximately 1.1 so that the fuel composition resulting from cold fuel and neutral injection has $T/D \lesssim 1.0$.

An examination of the feed composition and reinjection requirements as listed above, indicated that several distillation columns operating in cascade would be required. Figure I-2 shows the 6-column cascade developed for the ANL/EPR. It should be noted that a large number of cascade arrangements are possible to meet the above requirements and that Figure I-2 represents an adequate but not necessarily an optimum separation scheme.

a. Analysis of the EPR Cascade

A second computer program was developed based on the computer code described in Section 2 as a subroutine to analyze the 6-column cascade. With flow schematics as shown in Figure I-2, convergence was observed to be very slow and tedious. To avoid this difficulty, feed No. 3 (bottom product from column No. 5) to column No. 1 was fixed after establishing its

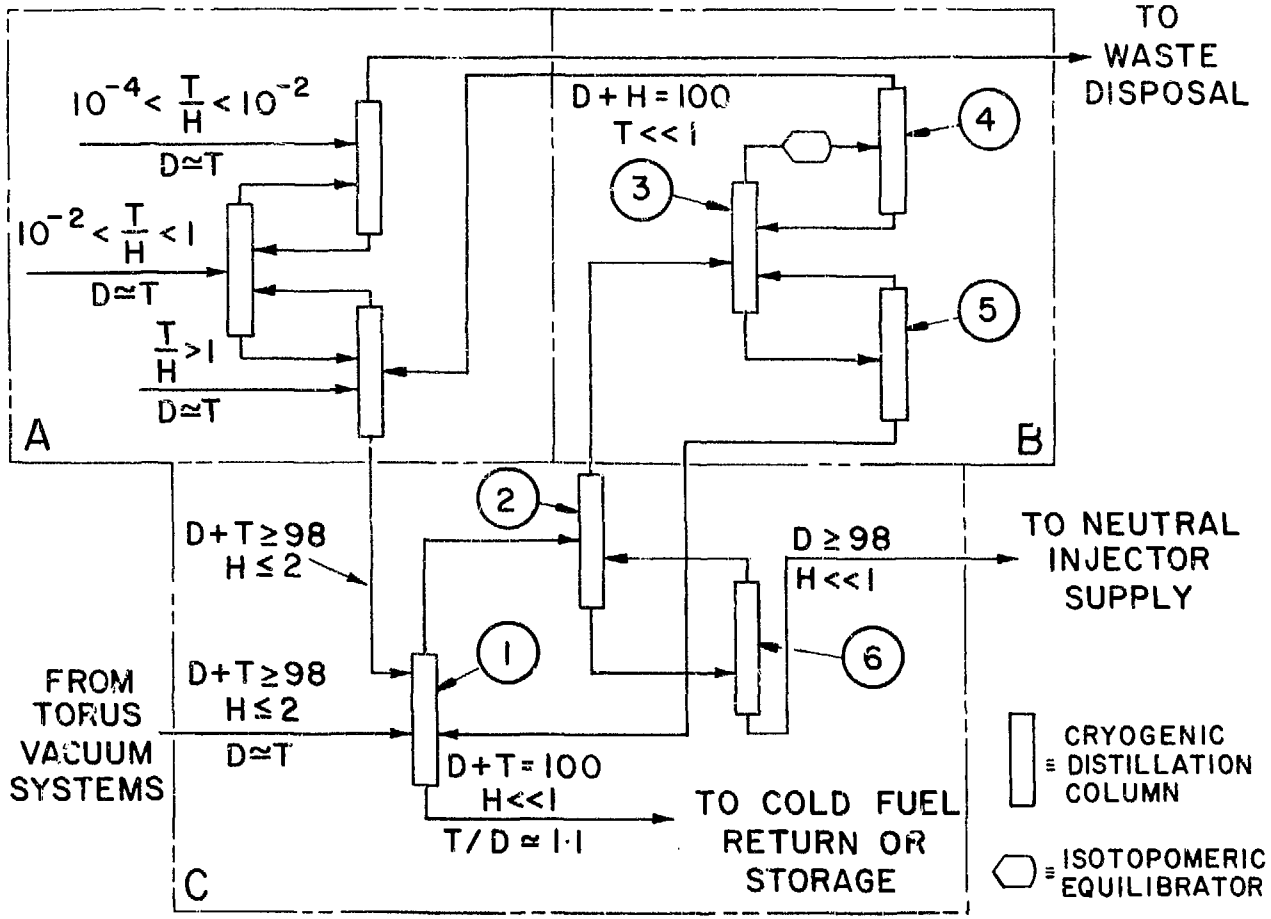

Figure I-2. Cryogenic Enrichment Scenario for EPR-1

approximate composition during initial iterative calculations. This speeded up the convergence, although it was not possible to exactly match the composition of these two liquid mixtures. The analytical results are summarized in Table I-18 and detailed operating characteristics (in the form of computer printouts) are given in Tables I-19 through I-24.

An examination of the bottom products from columns No. 1 and No. 6 shows that the composition of these two feed mixtures essentially meets requirements (2) and (3) above. However, the distillate from column No. 4 cannot be directly discharged into waste consolidation and burial without further reprocessing because of its high tritium content.

Figure I-2 shows that columns No. 1, 4 and 6 are the main columns with columns No. 2, 3 and 5 serving as intermediaries. Since the deuterium content in the feed to column No. 6 is 97%, the effect of the operating parameters on column No. 6 was minimal. The parametric investigations to study the effects of the operating parameters were carried out for column No. 1, and the results were found to be not very significant for the overall cascade performance.

An attempt was made to reduce the tritium content in the distillate from column No. 4 by varying the number of theoretical stages, reflux ratio and operating pressure. The tritium content could not be reduced to acceptable levels due to the presence of tritium as HT which is relatively volatile. Hence, all of the protium atoms cannot be removed easily by distillation alone without carryover of some tritium atoms. An examination of the equilibrium relationship among the six species of hydrogen isotopes shows that it is feasible to separate the protium atoms without carryover of tritium atoms by means of a chemical equilibration followed by cryogenic distillation as described below.

b. Equilibration

The isotopomeric composition of the equilibrium feed mixture that distills from the top of column No. 3 can be altered by shifting the equilibrium among the various molecular hydrogen species. In the liquid state, the chemical equilibrium among the six species is essentially frozen. By warming up the mixture to room temperature in a chemical equilibrator, especially in the presence of a catalyst (e.g., palladium on asbestos), a new equilibrium among the six species can be established, as described by the following equations,

Table I-18. Summary of Operating Parameters for the ETR Cryogenic Distillation Cascade

Column Number+	Feed Plate	Total Feed (moles)	Feed Composition (at %) H	D	T	Top Product Total Moles	Top Product Atomic Percentates H	D	T	Bottom Product Total Moles	Bottom Product Atomic Percentates H	D	T
1	10 15 20	100	4.12	49.57	46.31	18	21.9	63.0	15.1	82	0.2	46.6	53.2
2	15 20	23	17.35	70.57	12.08	13	30.3	50.0	19.7	10	0.5	97.3	2.2
3	10 15 20	23	38.51	34.86	26.63	8	50.9	31.1	18.0	15	31.9	36.9	31.2
4	15	8	50.9	31.1	18.0	3	53.0	45.9	1.1	5	49.7	22.3	28.0
5	15	15	31.9	36.9	31.2	5	48.7	4.6	46.7	10	23.5	53.0	23.5
6	15	15	0.5	97.3	21.7	5	1.0	97.9	1.1	5	0	96.7	3.3
4**	15	8	50.8	29.2	20.0	3	96.1	4.5	0	5	22.2	44.8	32.7

* 30 Theoretical Stages per Column; Column Pressure 1000 Torr, except for Column No. 1 operating at 500 Torr.

+ See Fig. I-2 for location in Cascade.

** After Chemical equilibration at 300°K.

Table I-19. Analysis of ANL/EPR

CRYOGENIC DISTILLATION OF HYDROGEN ISOTOPES FOR ANL/TEPR, .. B.MISRA.. ..DECEMBER, 1975

ANALYTICAL RESULTS AT PT= 5.000D 02 TORR AFTER 6 ITERATIONS FOR COLUMN NO: 1
NUMBER OF THEORETICAL STAGES: 30 REFLUX RATIO L/D1= 2.000D 01
FIRST FEED PLATE LOCATION: 10 2ND FP LOCATION: 15 3RD FP LOCATION= 20
FEED RATES: 1.50D 00 8.85D 01 1.00D 01 DISTILLATE: 1.80D 01 BOTTOMS: 8.20D 01

FEED COMP. N-H2	HD	HT	N-D2	DT	N-T2	APH	APD	APT
1.000000D-04	5.000000D-03	5.000000D-03	2.500000D-01	4.899000D-01	2.500000D-01	5.100D-01	4.975D 01	4.975D 01
2.000000D-03	2.700000D-02	1.100000D-02	2.620000D-01	4.280000D-01	2.700000D-01	2.100D 00	4.895D 01	4.895D 01
4.009430D-11	4.487540D-04	4.493900D-01	5.501030D-01	5.826820D-05	4.076860D-09	2.249D 01	5.504D 01	2.247D 01

SUMMATION OF LIQUID MOLE FRACTIONS

1.000000D 00	1.000000D 00	1.000000D 00	1.000000D 00	1.000000D 00	1.000000D 00
1.000000D 00	1.000000D 00	1.000000D 00	1.000000D 00	1.000000D 00	1.000000D 00
1.000000D 00	1.000000D 00	1.000000D 00	1.000000D 00	1.000000D 00	1.000000D 00
1.000000D 00	1.000000D 00	1.000000D 00	1.000000D 00	1.000000D 00	1.000000D 00
1.000000D 00	1.000000D 00	1.000000D 00	1.000000D 00	1.000000D 00	1.000000D 00

EQUILIBRIUM STAGE TEMPERATURES

2.193390D 01	2.202349D 01	2.209279D 01	2.214807D 01	2.219389D 01	2.223373D 01
2.227033D 01	2.230590D 01	2.234232D 01	2.238119D 01	2.242128D 01	2.246605D 01
2.251644D 01	2.257308D 01	2.263613D 01	2.264107D 01	2.264397D 01	2.264561D 01
2.264642D 01	2.264657D 01	2.266392D 01	2.268249D 01	2.270302D 01	2.272637D 01
2.275361D 01	2.278599D 01	2.282501D 01	2.287237D 01	2.292988D 01	2.299913D 01

PLATE NO.	N-H2	HD	HT	N-D2	DT	N-T2	APH	APD	APT
1	9.841662D-03	1.333446D-01	2.846100D-01	5.543318D-01	1.763039D-02	2.415462D-04	2.188D 01	6.298D 01	1.514D 01
2	1.886715D-03	6.476904D-02	2.193332D-01	6.785727D-01	3.467491D-02	7.634695D-04	1.439D 01	7.283D 01	1.278D 01
3	9.341696D-04	4.538907D-02	1.878237D-01	7.186189D-01	4.596174D-02	1.272359D-03	1.175D 01	7.643D 01	1.182D 01
4	5.522462D-04	3.546430D-02	1.597056D-01	7.457319D-01	5.939914D-02	2.064722D-03	9.668D 00	7.917D 01	1.116D 01
5	3.996775D-04	2.919257D-02	1.355367D-01	7.613527D-01	7.523557D-02	3.282823D-03	8.026D 00	8.119D 01	1.087D 01
6	3.378559D-04	1.882040D-02	1.152723D-01	7.667318D-01	9.370459D-02	5.132999D-03	6.738D 00	8.230D 01	1.096D 01
7	3.115371D-04	1.538076D-02	9.855567D-02	7.628570D-01	1.149858D-01	7.909257D-03	5.728D 00	8.280D 01	1.147D 01
8	2.989631D-04	1.316955D-02	8.489919D-02	7.504609D-01	1.391504D-01	1.202093D-02	4.933D 00	8.266D 01	1.240D 01
9	2.916016D-04	1.172558D-02	7.379017D-02	7.300787D-01	1.660922D-01	1.802173D-02	4.305D 00	8.190D 01	1.380D 01
10	2.860847D-04	1.075180D-02	6.474643D-02	7.021377D-01	1.956445D-01	2.663354D-02	3.804D 00	8.052D 01	1.567D 01
11	2.815172D-04	1.008066D-02	5.756931D-02	6.693525D-01	2.252810D-01	3.743508D-02	3.411D 00	7.870D 01	1.789D 01
12	2.767529D-04	9.568637D-03	5.162537D-02	6.301758D-01	2.559733D-01	5.238013D-02	3.087D 00	7.629D 01	2.062D 01
13	2.716205D-04	9.143821D-03	4.663024D-02	5.852565D-01	2.881307D-01	7.456715D-02	2.816D 00	7.329D 01	2.389D 01
14	2.660660D-04	8.762780D-03	4.236006D-02	5.355490D-01	3.139273D-01	9.908480D-02	2.583D 00	6.969D 01	2.773D 01
15	2.600269D-04	8.400979D-03	3.864668D-02	4.823750D-01	3.374886D-01	1.328287D-01	2.378D 00	6.553D 01	3.209D 01
16	1.112449D-04	5.708606D-03	4.067578D-02	4.822938D-01	3.383922D-01	1.328184D-01	2.330D 00	6.543D 01	3.226D 01
17	4.755891D-05	3.877494D-03	4.236388D-02	4.817687D-01	3.392764D-01	1.326659D-01	2.317D 00	6.533D 01	3.235D 01
18	2.032394D-05	2.634073D-03	4.377610D-02	4.809614D-01	3.402750D-01	1.323331D-01	2.323D 00	6.524D 01	3.244D 01
19	8.683534D-06	1.790531D-03	4.496408D-02	4.799800D-01	3.415202D-01	1.317365D-01	2.339D 00	6.516D 01	3.250D 01
20	3.709928D-06	1.218619D-03	4.597017D-02	4.789115D-01	3.431690D-01	1.307270D-01	2.360D 00	6.511D 01	3.253D 01
21	1.613331D-06	8.384442D-04	3.901336D-02	4.735093D-01	3.535379D-01	1.330994D-01	1.993D 00	6.507D 01	3.294D 01
22	6.983746D-07	5.732929D-04	3.282722D-02	4.649528D-01	3.653857D-01	1.362603D-01	1.670D 00	6.479D 01	3.354D 01
23	3.007698D-07	3.891547D-04	2.735026D-02	4.528318D-01	3.788199D-01	1.406086D-01	1.387D 00	6.424D 01	3.437D 01
24	1.287701D-07	2.618414D-04	2.252138D-02	4.366791D-01	3.938078D-01	1.467299D-01	1.139D 00	6.337D 01	3.549D 01
25	5.474061D-08	1.762377D-04	1.828242D-02	4.159920D-01	4.100792D-01	1.554721D-01	9.226D-01	6.211D 01	3.697D 01
26	2.306248D-08	1.142842D-04	1.458002D-02	3.902750D-01	4.269950D-01	1.680356D-01	7.347D-01	6.038D 01	3.888D 01
27	9.599561D-09	7.352288D-05	1.156689D-02	3.591134D-01	4.433874D-01	1.860588D-01	5.720D-01	5.808D 01	4.134D 01
28	3.925108D-09	4.603847D-05	8.602569D-03	3.222887D-01	4.574002D-01	2.116625D-01	4.324D-01	5.510D 01	4.447D 01
29	1.557772D-09	2.770836D-05	6.253428D-03	2.799386D-01	4.663942D-01	2.473861D-01	3.141D-01	5.131D 01	4.837D 01
30	5.829175D-10	1.566503D-05	4.291686D-03	2.327446D-01	4.670255D-01	2.959226D-01	2.154D-01	4.663D 01	5.316D 01

Table I-20. Analysis of ANL/EPR

CRYOGENIC DISTILLATION OF HYDROGEN ISOTOPES FOR ANL/TEPR, .. B.MISRA.. ..DECEMBER, 1975

ANALYTICAL RESULTS AT PT= 1.000D 03 TORR AFTER 6 ITERATIONS FOR COLUMN NO: 2
NUMBER OF THEORETICAL STAGES: 30 REFLUX RATIO L/D1= 1.500D 01
FIRST FEED PLATE LOCATION: 10 2ND FP LOCATION: 15 3RD FP LOCATION= 20
FEED RATES: 0.0 1.80D 01 5.00D 00 DISTILLATE: 1.30D 01 BOTTOMS: 1.00D 01

FEED COMP. N-H2	HD	HT	N-D2	DT	N-T2	APH	APD	APT
9.841662D-03	1.333446D-01	2.846100D-01	5.543318D-01	1.763039D-02	2.415462D-04	2.188D 01	6.298D 01	1.514D 01
1.885638D-08	2.472001D-04	2.022666D-02	9.778093D-01	1.715906D-03	8.917547D-07	1.024D 00	9.788D 01	1.097D 00

SUMMATION OF LIQUID MOLE FRACTIONS

1.000000D 00	1.000000D 00	1.000000D 00	1.000000D 00	1.000000D 00	1.000000D 00
1.000000D 00	1.000000D 00	1.000000D 00	1.000000D 00	1.000000D 00	1.000000D 00
1.000000D 00	1.000000D 00	1.000000D 00	1.000000D 00	1.000000D 00	1.000000D 00
1.000000D 00	1.000000D 00	1.000000D 00	1.000000D 00	1.000000D 00	1.000000D 00
1.000000D 00	1.000000D 00	1.000000D 00	1.000000D 00	1.000000D 00	1.000000D 00

EQUILIBRIUM STAGE TEMPERATURES

2.409104D 01	2.417640D 01	2.424501D 01	2.430042D 01	2.434522D 01	2.438146D 01
2.441076D 01	2.443446D 01	2.445365D 01	2.446922D 01	2.448190D 01	2.449228D 01
2.450084D 01	2.450797D 01	2.451400D 01	2.451182D 01	2.456403D 01	2.458192D 01
2.459645D 01	2.460833D 01	2.461755D 01	2.462545D 01	2.463233D 01	2.463843D 01
2.464395D 01	2.464911D 01	2.465409D 01	2.465908D 01	2.466429D 01	2.466995D 01

PLATE NO.	N-H2	HD	HT	N-D2	DT	N-T2	APH	APD	APT
1	1.362692D-02	1.846309D-01	3.939115D-01	4.075728D-01	2.578998D-04	1.119353D-07	3.029D 01	5.000D 01	1.971D 01
2	3.717866D-03	1.109476D-01	3.476154D-01	5.372140D-01	5.047691D-04	3.255690D-07	2.330D 01	5.929D 01	1.741D 01
3	2.147492D-03	8.634593D-02	3.191645D-01	5.916726D-01	6.689244D-04	5.215145D-07	2.049D 01	6.352D 01	1.599D 01
4	1.401397D-03	6.816748D-02	2.906116D-01	6.389535D-01	8.652262D-04	8.144000D-07	1.808D 01	6.735D 01	1.457D 01
5	1.048921D-03	5.499377D-02	2.634782D-01	6.793794D-01	1.098403D-03	1.248116D-06	1.603D 01	7.074D 01	1.323D 01
6	8.818601D-04	4.558215D-02	2.386471D-01	7.135128D-01	1.374177D-03	1.885845D-06	1.430D 01	7.370D 01	1.200D 01
7	8.014649D-04	3.892618D-02	2.165350D-01	7.420351D-01	1.699448D-03	2.818497D-06	1.285D 01	7.623D 01	1.091D 01
8	7.615427D-04	3.425066D-02	1.972419D-01	7.656600D-01	2.082485D-03	4.176783D-06	1.165D 01	7.838D 01	9.967D 00
9	7.406711D-04	3.097891D-02	1.806649D-01	7.850763D-01	2.533148D-03	6.148525D-06	1.066D 01	8.018D 01	9.161D 00
10	7.289499D-04	2.869233D-02	1.665917D-01	8.009149D-01	3.063130D-03	9.003423D-06	9.837D 00	8.168D 01	8.484D 00
11	7.217840D-04	2.709251D-02	1.547525D-01	8.137339D-01	3.686251D-03	1.312849D-05	9.164D 00	8.291D 01	7.923D 00
12	7.170727D-04	2.596937D-02	1.448625D-01	8.240133D-01	4.418788D-03	1.907871D-05	8.613D 00	8.392D 01	7.466D 00
13	7.135915D-04	2.517637D-02	1.366448D-01	8.321578D-01	5.279866D-03	2.764938D-05	8.162D 00	8.474D 01	7.099D 00
14	7.109922D-04	2.461186D-02	1.298431D-01	8.385022D-01	6.291898D-03	3.997934D-05	7.794D 00	8.540D 01	6.811D 00
15	7.089286D-04	2.420556D-02	1.242281D-01	8.433186D-01	7.481093D-03	5.769808D-05	7.493D 00	8.592D 01	6.591D 00
16	3.369561D-04	1.721707D-02	1.072058D-01	8.674632D-01	7.718741D-03	5.828788D-05	6.255D 00	8.799D 01	5.752D 00
17	1.593918D-04	1.218023D-02	9.198707D-02	8.876410D-01	7.973493D-03	5.881640D-05	5.224D 00	8.977D 01	5.004D 00
18	7.510796D-05	8.579502D-03	7.856516D-02	9.044643D-01	8.256633D-03	5.931809D-05	4.365D 00	9.129D 01	4.347D 00
19	3.528169D-05	6.021936D-03	6.685041D-02	9.184517D-01	8.580823D-03	5.983207D-05	3.647D 00	9.258D 01	3.778D 00
20	1.653119D-05	4.214611D-03	5.670793D-02	9.300398D-01	8.960685D-03	6.040734D-05	3.048D 00	9.366D 01	3.289D 00
21	7.911615D-06	3.008158D-03	4.871426D-02	9.395775D-01	9.628874D-03	6.325488D-05	2.587D 00	9.449D 01	2.923D 00
22	3.779878D-06	2.141790D-03	4.170498D-02	9.476165D-01	1.046543D-02	6.754827D-05	2.193D 00	9.519D 01	2.615D 00
23	1.803113D-06	1.521239D-03	3.558256D-02	9.543030D-01	1.151729D-02	7.409423D-05	1.855D 00	9.578D 01	2.362D 00
24	8.589076D-07	1.077720D-03	3.025166D-02	9.557423D-01	1.284331D-02	8.413266D-05	1.567D 00	9.627D 01	2.163D 00
25	4.085461D-07	7.613141D-04	2.562201D-02	9.589995D-01	1.451724D-02	9.956909D-05	1.319D 00	9.666D 01	2.017D 00
26	1.940058D-07	5.359490D-04	2.160997D-02	9.610991D-01	1.663144D-02	1.233295D-04	1.107D 00	9.697D 01	1.928D 00
27	9.192124D-08	3.756527D-04	1.813931D-02	9.620238D-01	1.930123D-02	1.599007D-04	9.258D-01	9.719D 01	1.888D 00
28	4.339842D-08	2.617806D-04	1.514143D-02	9.617104D-01	2.267016D-02	2.161494D-04	7.702D-01	9.732D 01	1.912D 00
29	2.035849D-08	1.809815D-04	1.255518D-02	9.600453D-01	2.691599D-02	3.025590D-04	6.368D-01	9.736D 01	2.004D 00
30	9.430068D-09	1.237141D-04	1.032648D-02	9.568573D-01	3.225739D-02	4.338835D-04	5.225D-01	9.730D 01	2.173D 00

Table I-21. Analysis of ANL/EPR

CRYOGENIC DISTILLATION OF HYDROGEN ISOTOPES FOR ANL/TEPR, .. B. MISRA.. ..DECEMBER, 1975

ANALYTICAL RESULTS AT PT= 1.000D 03 TORR AFTER 6 ITERATIONS FOR COLUMN NO: 3
NUMBER OF THEORETICAL STAGES: 30 REFLUX RATIO L/D1= 1.500D 01
FIRST FEED PLATE LOCATION: 10 2ND FP LOCATION: 15 3RD FP LOCATION= 20
FEED RATES: 5.00D 00 1.30D 01 5.00D 00 DISTILLATE: 8.00D 00 BOTTOMS: 1.50D 01

FEED COMP. N-H2	HD	HT	N-D2	DT	N-T2	APH	APD	APT
1.168450D-05	4.985219D-01	4.955165D-01	5.949857D-03	1.075177D-07	5.922251D-12	4.970D 01	2.552D 01	2.478D 01
1.362692D-02	1.846309D-01	3.939115D-01	4.075728D-01	2.578998D-04	1.119351D-07	3.029D 01	5.000D 01	1.971D 01
1.135646D-06	4.349908D-02	9.297776D-01	2.672149D-02	5.646398D-07	9.230713D-12	4.866D 01	4.847D 00	4.649D 01

SUMMATION OF LIQUID HOLE FRACTIONS

9.999034D-01	9.999026D-01	9.999032D-01	9.999054D-01	9.999090D-01	9.999138D-01
9.999194D-01	9.999255D-01	9.999319D-01	9.999382D-01	9.999421D-01	9.999465D-01
9.999511D-01	9.999559D-01	9.999608D-01	9.999625D-01	9.999644D-01	9.999663D-01
9.999683D-01	9.999702D-01	9.999708D-01	9.999712D-01	9.999715D-01	9.999716D-01
9.999715D-01	9.999712D-01	9.999708D-01	9.999702D-01	9.999697D-01	9.999693D-01

EQUILIBRIUM STAGE TEMPERATURES

2.340412D 01	2.345598D 01	2.350139D 01	2.354199D 01	2.357874D 01	2.361224D 01
2.364292D 01	2.367118D 01	2.369742D 01	2.372206D 01	2.375410D 01	2.378572D 01
2.381732D 01	2.384932D 01	2.388215D 01	2.389946D 01	2.391434D 01	2.392717D 01
2.393824D 01	2.394774D 01	2.395954D 01	2.397178D 01	2.398484D 01	2.399914D 01
2.401519D 01	2.403356D 01	2.405491D 01	2.407993D 01	2.410934D 01	2.414376D 01

PLATE NO.	N-H2	HD	HT	N-D2	DT	N-T2	APH	APD	APT
1	2.216169D-02	6.143218D-01	3.591827D-01	4.237212D-03	7.711280D-08	1.150397D-12	5.089D 01	3.114D 01	1.796D 01
2	8.182073D-03	5.232865D-01	4.602604D-01	8.270823D-03	2.291789D-07	5.204202D-12	5.000D 01	2.699D 01	2.302D 01
3	5.302094D-03	4.779390D-01	5.056847D-01	1.107379D-02	3.755040D-07	1.046538D-11	4.972D 01	2.501D 01	2.529D 01
4	3.686492D-03	4.348782D-01	5.469051D-01	1.452964D-02	6.023908D-07	2.061737D-11	4.946D 01	2.320D 01	2.735D 01
5	2.784240D-03	3.949792D-01	5.834859D-01	1.874975D-02	9.506313D-07	3.999202D-11	4.921D 01	2.163D 01	2.918D 01
6	2.280084D-03	3.587148D-01	6.151448D-01	2.385889D-02	1.480234D-06	7.659943D-11	4.893D 01	2.032D 01	3.076D 01
7	1.996195D-03	3.262606D-01	6.417445D-01	2.999638D-02	2.278926D-06	1.451374D-10	4.860D 01	1.931D 01	3.209D 01
8	1.833434D-03	2.975768D-01	6.632694D-01	3.731688D-02	3.474181D-06	2.723802D-10	4.823D 01	1.861D 01	3.317D 01
9	1.737048D-03	2.724742D-01	6.797933D-01	4.599020D-02	5.250044D-06	5.067604D-10	4.779D 01	1.822D 01	3.399D 01
10	1.677005D-03	2.506676D-01	6.914477D-01	5.619983D-02	7.870457D-06	9.352806D-10	4.728D 01	1.815D 01	3.457D 01
11	1.669653D-03	2.231163D-01	7.047098D-01	7.049215D-02	1.216046D-05	1.779494D-09	4.656D 01	1.821D 01	3.524D 01
12	1.653760D-03	1.987278D-01	7.119872D-01	8.761259D-02	1.860918D-05	3.451703D-09	4.570D 01	1.870D 01	3.560D 01
13	1.633503D-03	1.772956D-01	7.131389D-01	1.079038D-01	2.820653D-05	6.249774D-09	4.469D 01	1.966D 01	3.566D 01
14	1.611027D-03	1.585670D-01	7.080954D-01	1.316803D-01	4.234263D-05	1.153583D-08	4.350D 01	2.110D 01	3.541D 01
15	1.587361D-03	1.422673D-01	6.968858D-01	1.591965D-01	6.293855D-05	2.107257D-08	4.212D 01	2.304D 01	3.485D 01
16	9.150736D-04	1.251576D-01	7.134164D-01	1.604478D-01	6.308902D-05	2.111762D-08	4.202D 01	2.231D 01	3.568D 01
17	5.257553D-04	1.097038D-01	7.282786D-01	1.614287D-01	6.305327D-05	2.110879D-08	4.195D 01	2.163D 01	3.642D 01
18	3.012028D-04	9.585977D-02	7.416396D-01	1.621367D-01	6.275385D-05	2.100614D-08	4.191D 01	2.101D 01	3.709I 01
19	1.721297D-04	8.354274D-02	7.536624D-01	1.625607D-01	6.206356D-05	2.072975D-08	4.188D 01	2.044D 01	3.769D 01
20	9.815862D-05	7.264853D-02	7.645114D-01	1.626812D-01	6.077718D-05	2.012201D-08	4.187D 01	1.990D 01	3.823D 01
21	5.782736D-05	6.391587D-02	7.672357D-01	1.687286D-01	6.199870D-05	2.048558D-08	4.156D 01	2.007D 01	3.837D 01
22	3.396469D-05	5.590964D-02	7.676920D-01	1.763005D-01	6.379511D-05	2.054015D-08	4.118D 01	2.043D 01	3.839D 01
23	1.988146D-05	4.859007D-02	7.654989D-01	1.858247D-01	6.650994D-05	2.097136D-08	4.071D 01	2.102D 01	3.828D 01
24	1.159123D-05	4.191512D-02	7.601820D-01	1.978206D-01	7.068544D-05	2.174626D-08	4.011D 01	2.188D 01	3.801D 01
25	6.724327D-06	3.584238D-02	7.511663D-01	2.129074D-01	7.717278D-05	2.319040D-08	3.935D 01	2.309D 01	3.756D 01
26	3.875566D-06	3.033090D-02	7.377754D-01	2.310025D-01	8.729693D-05	2.593526D-08	3.841D 01	2.470D 01	3.689D 01
27	2.213641D-06	2.534258D-02	7.192456D-01	2.553065D-01	1.030971D-04	3.119612D-08	3.723D 01	2.680D 01	3.597D 01
28	1.247964D-06	2.084345D-02	6.947605D-01	2.842671D-01	1.276659D-04	4.128592D-08	3.578D 01	2.948D 01	3.475D 01
29	6.892596D-07	1.680448D-02	6.635167D-01	3.195125D-01	1.656080D-04	6.054543D-08	3.402D 01	3.280D 01	3.319D 01
30	3.680435D-07	1.320192D-02	6.248237D-01	3.617502D-01	2.236273D-04	9.698380D-08	3.190D 01	3.685D 01	3.125D 01

Table I-22. Analysis of ANL/EPR

CRYOGENIC DISTILLATION OF HYDROGEN ISOTOPES FOR ANL/TEPR, .. B.MISRA.. ..DECEMBER, 1975

ANALYTICAL RESULTS AT PT= 1.000D 03 TORR AFTER 6 ITERATIONS FOR COLUMN NO: 4
NUMBER OF THEORETICAL STAGES: 30 REFLUX RATIO L/D1= 1.500D 01
FIRST FEED PLATE LOCATION: 10 2ND FP LOCATION: 12 3RD FP LOCATION= 15
FEED RATES: 0.0 0.0 8.00D 00 DISTILLATE: 3.00D 00 BOTTOMS: 5.00D 00

FEED COMP. N-H2	HD	HT	N-D2	DT	N-T2	APH	APD	APT
2.216169D-02	6.143218D-01	3.591827D-01	4.237212D-03	7.711280D-08	1.150397D-12	5.089D 01	3.114D 01	1.796D 01

SUMMATION OF LIQUID MOLE FRACTIONS

9.999991D-01	9.999994D-01	9.999996D-01	9.999997D-01	9.999998D-01	9.999998D-01
9.999999D-01	9.999999D-01	9.999999D-01	1.000000D 00	1.000000D 00	1.000000D 00
1.000000D 00	1.000000D 00	1.000000D 00	1.000000D 00	1.000000D 00	1.000000D 00
9.999998D-01	9.999996D-01	9.999993D-01	9.999990D-01	9.999986D-01	9.999983D-01
9.999979D-01	9.999976D-01	9.999974D-01	9.999973D-01	9.999972D-01	9.999973D-01

EQUILIBRIUM STAGE TEMPERATURES

2.306094D 01	2.309225D 01	2.311400D 01	2.313015D 01	2.314327D 01	2.315496D 01
2.316628D 01	2.317789D 01	2.319020D 01	2.320351D 01	2.321800D 01	2.323375D 01
2.325082D 01	2.326920D 01	2.328884D 01	2.329621D 01	2.330310D 01	2.331008D 01
2.331764D 01	2.332621D 01	2.333618D 01	2.334797D 01	2.336197D 01	2.337857D 01
2.339816D 01	2.342110D 01	2.344766D 01	2.347804D 01	2.351228D 01	2.355026D 01

PLATE NO.	N-H2	HD	HT	N-D2	DT	N-T2	APH	APD	APT
1	5.908706D-02	9.182028D-01	2.270239D-02	6.922534D-06	3.767023D-12	1.839801D-18	5.295D 01	4.591D 01	1.135D 00
2	2.555890D-02	9.390396D-01	3.531492D-02	1.660835D-05	1.394210D-11	1.049658D-17	5.128D 01	4.695D 01	1.769D 00
3	1.773025D-02	9.392408D-01	4.300113D-02	2.479316D-05	2.569115D-11	2.392750D-17	5.089D 01	4.696D 01	2.150D 00
4	1.297487D-02	9.353449D-01	5.164374D-02	3.650305D-05	4.671648D-11	5.389641D-17	5.065D 01	4.677D 01	2.582D 00
5	1.009606D-02	9.284162D-01	6.143456D-02	5.321801D-05	8.422562D-11	1.205241D-16	5.050D 01	4.643D 01	3.072D 00
6	8.354497D-03	9.190623D-01	7.250623D-02	7.701118D-05	1.509261D-10	2.681241D-16	5.041D 01	4.596D 01	3.625D 00
7	7.298241D-03	9.076081D-01	8.498294D-02	1.107687D-04	2.691219D-10	5.938887D-16	5.036D 01	4.539D 01	4.249D 00
8	6.652899D-03	8.942104D-01	9.897824D-02	1.584814D-04	4.777653D-10	1.310014D-15	5.032D 01	4.473D 01	4.949D 00
9	6.252606D-03	8.789331D-01	1.145887D-01	2.256280D-04	8.445086D-10	2.877441D-15	5.030D 01	4.397D 01	5.729D 00
10	5.997428D-03	8.617965D-01	1.318864D-01	3.196691D-04	1.486141D-09	6.291887D-15	5.028D 01	4.312D 01	6.594D 00
11	5.827325D-03	8.428113D-01	1.509107D-01	4.506772D-04	2.602957D-09	1.369127D-14	5.027D 01	4.219D 01	7.546D 00
12	5.706341D-03	8.220021D-01	1.716594D-01	6.321260D-04	4.536036D-09	2.963592D-14	5.025D 01	4.116D 01	8.583D 00
13	5.613052D-03	7.994242D-01	1.940809D-01	8.818637D-04	7.861839D-09	6.378521D-14	5.024D 01	4.006D 01	9.704D 00
14	5.534796D-03	7.751751D-01	2.180668D-01	1.223294D-03	1.354696D-08	1.364471D-13	5.022D 01	3.888D 01	1.090D 01
15	5.464207D-03	7.494012D-01	2.434478D-01	1.686784D-03	2.319882D-08	2.899846D-13	5.019D 01	3.764D 01	1.217D 01
16	3.704773D-03	7.463486D-01	2.482498D-01	1.696854D-03	2.325746D-08	2.904528D-13	5.010D 01	3.749D 01	1.241D 01
17	2.507604D-03	7.417721D-01	2.540106D-01	1.709663D-03	2.332482D-08	2.909560D-13	5.004D 01	3.726D 01	1.270D 01
18	1.694309D-03	7.355930D-01	2.609859D-01	1.726785D-03	2.340858D-08	2.915334D-13	5.000D 01	3.695D 01	1.305D 01
19	1.142559D-03	7.276448D-01	2.694622D-01	1.750476D-03	2.352042D-08	2.922354D-13	4.997D 01	3.656D 01	1.347D 01
20	7.687343D-04	7.176856D-01	2.797616D-01	1.784070D-03	2.368014D-08	2.931430D-13	4.995D 01	3.606D 01	1.399D 01
21	5.158045D-04	7.054082D-01	2.922434D-01	1.832579D-03	2.392348D-08	2.944134D-13	4.993D 01	3.545D 01	1.461D 01
22	3.449329D-04	6.904512D-01	3.073003D-01	1.903576D-03	2.431696D-08	2.963867D-13	4.992D 01	3.471D 01	1.537D 01
23	2.297040D-04	6.724140D-01	3.253477D-01	2.008501D-03	2.498617D-08	2.998415D-13	4.991D 01	3.382D 01	1.627D 01
24	1.521668D-04	6.508782D-01	3.468050D-01	2.164543D-03	2.616899D-08	3.065993D-13	4.990D 01	3.276D 01	1.734D 01
25	1.001317D-04	6.254377D-01	3.720648D-01	2.397328D-03	2.831454D-08	3.209433D-13	4.989D 01	3.151D 01	1.860D 01
26	6.532646D-05	5.957395D-01	4.014505D-01	2.744604D-03	3.226445D-08	3.529033D-13	4.987D 01	3.006D 01	2.007D 01
27	4.214166D-05	5.615340D-01	4.351627D-01	3.261197D-03	3.957911D-08	4.257583D-13	4.984D 01	2.840D 01	2.176D 01
28	2.677600D-05	5.227309D-01	4.732169D-01	4.025394D-03	5.311331D-08	5.928911D-13	4.980D 01	2.654D 01	2.366D 01
29	1.665602D-05	4.794550D-01	5.153814D-01	5.146859D-03	7.801134D-08	9.750059D-13	4.974D 01	2.449D 01	2.577D 01
30	1.004163D-05	4.320891D-01	5.611247D-01	6.776020D-03	1.233898D-07	1.840806D-12	4.966D 01	2.228D 01	2.806D 01

Table I-23. Analysis of ANL/EPR

CRYOGENIC DISTILLATION OF HYDROGEN ISOTOPES FOR ANL/TEPR, .. B.MISRA.. ..DECEMBER, 1975

ANALYTICAL RESULTS AT PT= 1.000D 03 TORR AFTER 6 ITERATIONS FOR COLUMN NO: 5
NUMBER OF THEORETICAL STAGES: 30 REFLUX RATIO L/D1= 1.500D 01
FIRST FEED PLATE LOCATION: 10 2ND FP LOCATION: 12 3RD FP LOCATION= 15
FEED RATES: 0.0 0.0 1.50D 01 DISTILLATE: 5.00D 00 BOTTOMS: 1.00D 01

FEED COMP. N-H2	HD	HT	N-D2	DT	N-T2	APH	APD	APT
3.680435D-07	1.320192D-02	6.248237D-01	3.617502D-01	2.236273D-04	9.698380D-08	3.190D 01	3.685D 01	3.125D 01

SUMMATION OF LIQUID MOLE FRACTIONS

1.000000D 00	1.000000D 00	1.000000D 00	1.000000D 00	1.000000D 00	1.000000D 00
1.000000D 00	1.000000D 00	1.000000D 00	1.000000D 00	1.000000D 00	1.000000D 00
1.000000D 00	1.000000D 00	1.000000D 00	1.000000D 00	1.000000D 00	1.000000D 00
1.000000D 00	1.000000D 00	1.000000D 00	1.000000D 00	1.000000D 00	1.000000D 00
1.000000D 00	9.999999D-01	9.999999D-01	9.999999D-01	9.999999D-01	9.999999D-01

EQUILIBRIUM STAGE TEMPERATURES

2.389124D 01	2.390082D 01	2.391008D 01	2.391931D 01	2.392877D 01	2.393869D 01
2.394924D 01	2.396057D 01	2.397282D 01	2.398607D 01	2.400037D 01	2.401577D 01
2.403224D 01	2.404974D 01	2.406818D 01	2.407742D 01	2.407514D 01	2.407948D 01
2.408463D 01	2.409085D 01	2.409825D 01	2.410727D 01	2.411821D 01	2.413145D 01
2.414739D 01	2.416648D 01	2.418911D 01	2.421565D 01	2.424635D 01	2.428130D 01

PLATE NO.	N-H2	HD	HT	N-D2	DT	N-T2	APH	APD	APT
1	1.104104D 06	3.853025D-02	9.345853D-01	2.688281D-02	5.687184D-07	9.304515D-12	4.866D 01	4.615D 00	4.673D 01
2	3.332701D-07	2.600698D-02	9.336227D-01	4.036868D-02	1.278632D-06	3.133306D-11	4.798D 01	5.337D 00	4.668D 01
3	2.034694D-07	2.177889D-02	9.296867D-01	4.853238D-02	1.862872D-06	5.553972D-11	4.757D 01	5.942D 00	4.648D 01
4	1.382720D-07	1.851290D-02	9.237055D-01	5.777878D-02	2.682129D-06	9.733064D-11	4.711D 01	6.704D 00	4.619D 01
5	1.055114D-07	1.599103D-02	9.157929D-01	6.821211D-02	3.827298D-06	1.692525D-10	4.659D 01	7.621D 00	4.579D 01
6	8.899961D-08	1.404267D-02	9.060171D-01	7.993476D-02	5.422532D-06	2.926133D-10	4.600D 01	8.696D 00	4.530D 01
7	8.060350D-08	1.253487D-02	8.944144D-01	9.304301D-02	7.636390D-06	5.034334D-10	4.535D 01	9.931D 00	4.472D 01
8	7.624787D-08	1.136434D-02	8.810031D-01	1.076218D-01	1.069620D-05	8.622968D-10	4.462D 01	1.133D 01	4.405D 01
9	7.389133D-08	1.045109D-02	8.657952D-01	1.237387D-01	1.490631D-05	1.470545D-09	4.381D 01	1.290D 01	4.329D 01
10	7.251407D-08	9.733342D-03	8.488083D-01	1.414376D-01	2.067110D-05	2.496690D-09	4.293D 01	1.463D 01	4.244D 01
11	7.160752D-08	9.163510D-03	8.300764D-01	1.607315D-01	2.852331D-05	4.219175D-09	4.196D 01	1.653D 01	4.151D 01
12	7.091896D-08	8.705096D-03	8.096594D-01	1.815963D-01	3.915882D-05	7.094999D-09	4.092D 01	1.860D 01	4.048D 01
13	7.032376D-08	8.330227D-03	7.876507D-01	2.039655D-01	5.347843D-05	1.186899D-08	3.980D 01	2.082D 01	3.939D 01
14	6.976156D-08	8.017761D-03	7.641833D-01	2.277262D-01	7.263768D-05	1.974633D-08	3.861D 01	2.318D 01	3.821D 01
15	6.920451D-08	7.751804D-03	7.394323D-01	2.527177D-01	9.810555D-05	3.266276D-08	3.736D 01	2.566D 01	3.698D 01
16	4.005652D-08	6.753376D-03	7.371559D-01	2.559922D-01	9.850155D-05	3.271599D-08	3.720D 01	2.594D 01	3.686D 01
17	2.316574D-08	5.871290D-03	7.339850D-01	2.600446D-01	9.903343D-05	3.278354D-08	3.699D 01	2.630D 01	3.670D 01
18	1.338408D-08	5.092005D-03	7.297410D-01	2.650672D-01	9.976509D-05	3.287285D-08	3.674D 01	2.677D 01	3.649D 01
19	7.723489D-09	4.403698D-03	7.242033D-01	2.712924D-01	1.007929D-04	3.299656D-08	3.643D 01	2.735D 01	3.622D 01
20	4.450495D-09	3.795124D-03	7.171032D-01	2.789994D-01	1.022637D-04	3.317711D-08	3.604D 01	2.809D 01	3.589D 01
21	2.559905D-09	3.257486D-03	7.081194D-01	2.885187D-01	1.043991D-04	3.345536D-08	3.557D 01	2.902D 01	3.541D 01
22	1.469142D-09	2.782317D-03	6.968746D-01	3.002355D-01	1.075419D-04	3.390727D-08	3.498D 01	3.017D 01	3.485D 01
23	8.407445D-10	2.362381D-03	6.829361D-01	3.145893D-01	1.122118D-04	3.467582D-08	3.426D 01	3.158D 01	3.415D 01
24	4.793631D-10	1.991380D-03	6.658223D-01	3.320671D-01	1.192000D-04	3.602827D-08	3.339D 01	3.331D 01	3.330D 01
25	2.719926D-10	1.663866D-03	6.450181D-01	3.531882D-01	1.297007D-04	3.847062D-08	3.233D 01	3.541D 01	3.226D 01
26	1.533188D-10	1.375169D-03	6.200023D-01	3.784769D-01	1.454997D-04	4.294610D-08	3.107D 01	3.792D 01	3.101D 01
27	8.563061D-11	1.121317D-03	5.902895D-01	4.084199D-01	1.692342D-04	5.120304D-08	2.957D 01	4.091D 01	2.952D 01
28	4.718233D-11	8.989511D-04	5.554876D-01	4.434086D-01	2.047393D-04	6.644253D-08	2.782D 01	4.440D 01	2.778D 01
29	2.545416D-11	7.052373D-04	5.153684D-01	4.836688D-01	2.574920D-04	9.444342D-08	2.580D 01	4.842D 01	2.578D 01
30	1.325243D-11	5.377581D-04	4.699430D-01	5.291840D-01	3.351566D-04	1.454710D-07	2.352D 01	5.296D 01	2.351D 01

Table I-24. Analysis of ANL/EPR

CRYOGENIC DISTILLATION OF HYDROGEN ISOTOPES FOR ANL/TEPR, .. B.MISRA.. ..DECEMBER, 1975

ANALYTICAL RESULTS AT PT= 1.000D 03 TORR AFTER 6 ITERATIONS FOR COLUMN NO: 6
NUMBER OF THEORETICAL STAGES: 30 REFLUX RATIO L/D1= 1.500D 01
FIRST FEED PLATE LOCATION: 10 2ND FP LOCATION: 12 3RD FP LOCATION= 15
FEED RATES: 0.0 0.0 1.00D 01 DISTILLATE: 5.00D 00 BOTTOMS: 5.00D 00

FEED COMP. N-H2	HD	HT	N-D2	DT	N-T2	APH	APD	APT
9.430068D-09	1.237141D-04	1.032648D-02	9.568573D-01	3.225739D-02	4.350835D-04	5.225D-01	9.730D 01	2.173D 00

SUMMATION OF LIQUID MOLE FRACTIONS

1.000000D 00	1.000000D 00	1.000000D 00	1.000000D 00	1.000000D 00	1.000000D 00
1.000000D 00	1.000000D 00	1.000000D 00	1.000000D 00	1.000000D 00	1.000000D 00
1.000000D 00	1.000000D 00	1.000000D 00	1.000000D 00	1.000000D 00	1.000000D 00
1.000000D 00	1.000000D 00	1.000000D 00	1.000000D 00	1.000000D 00	1.000000D 00
1.000000D 00	1.000000D 00	1.000000D 00	1.000000D 00	1.000000D 00	1.000000D 00

EQUILIBRIUM STAGE TEMPERATURES

2.464417D 01	2.464687D 01	2.464904D 01	2.465082D 01	2.465233D 01	2.465364D 01
2.465482D 01	2.465593D 01	2.465701D 01	2.465809D 01	2.465923D 01	2.466043D 01
2.466174D 01	2.466319D 01	2.466480D 01	2.466557D 01	2.466633D 01	2.466710D 01
2.466792D 01	2.466881D 01	2.466983D 01	2.467103D 01	2.467246D 01	2.467422D 01
2.467639D 01	2.467911D 01	2.468254D 01	2.468686D 01	2.469235D 01	2.469930D 01

PLATE NO.	N-H2	HD	HT	N-D2	DT	N-T2	APH	APD	APT
1	1.886012D-08	2.472674D-04	2.024849D-02	9.777889D-01	1.714392D-03	8.915961D-07	1.025D 00	9.788D 01	1.098D 00
2	4.177950D-09	1.168108D-04	1.382216D-02	9.835427D-01	2.516364D-03	1.912497D-06	6.969D-01	9.849D 01	8.171D-01
3	2.311220D-09	8.456869D-05	1.166207D-02	9.852488D-01	3.001823D-03	2.732585D-06	5.873D-01	9.868D 01	7.335D-01
4	1.516860D-09	6.408511D-05	9.997148D-03	9.863809D-01	3.553981D-03	3.866953D-06	5.031D-01	9.882D 01	6.779D-01
5	1.178828D-09	5.107639D-05	8.714625D-03	9.870469D-01	4.181946D-03	5.435614D-06	4.383D-01	9.892D 01	6.454D-01
6	1.034899D-09	4.281607D-05	7.727048D-03	9.873265D-01	4.896032D-03	7.604269D-06	3.885D-01	9.898D 01	6.319D-01
7	9.735113D-10	3.757044D-05	6.966730D-03	9.872772D-01	5.707903D-03	1.060161D-05	3.502D-01	9.901D 01	6.348D-01
8	9.472153D-10	3.423785D-05	6.381365D-03	9.869389D-01	6.630733D-03	1.474312D-05	3.208D-01	9.903D 01	6.521D-01
9	9.358339D-10	3.211864D-05	5.930577D-03	9.863375D-01	7.679375D-03	2.046382D-05	2.981D-01	9.902D 01	6.825D-01
10	9.307857D-10	3.076861D-05	5.583229D-03	9.854871D-01	8.870549D-03	2.836323D-05	2.807D-01	9.899D 01	7.255D-01
11	9.284182D-10	2.990578D-05	5.315318D-03	9.843925D-01	1.022304D-02	3.926701D-05	2.673D-01	9.895D 01	7.808D-01
12	9.271742D-10	2.935114D-05	5.108347D-03	9.830501D-01	1.175791D-02	5.431148D-05	2.569D-01	9.889D 01	8.487D-01
13	9.263866D-10	2.899104D-05	4.948062D-03	9.814492D-01	1.349870D-02	7.505923D-05	2.489D-01	9.882D 01	9.298D-01
14	9.257665D-10	2.875324D-05	4.823478D-03	9.795725D-01	1.547166D-02	1.036570D-04	2.426D-01	9.873D 01	1.025D 00
15	9.251851D-10	2.859176D-05	4.726119D-03	9.773963D-01	1.770595D-02	1.430509D-04	2.377D-01	9.863D 01	1.136D 00
16	4.442910D-10	2.046982D-05	4.079121D-03	9.777206D-01	1.803612D-02	1.436470D-04	2.050D-01	9.867D 01	1.120D 00
17	2.133220D-10	1.465043D-05	3.517188D-03	9.778665D-01	1.845716D-02	1.445461D-04	1.766D-01	9.871D 01	1.113D 00
18	1.024073D-10	1.048156D-05	3.029226D-03	9.778195D-01	1.899486D-02	1.459173D-04	1.520D-01	9.873D 01	1.116D 00
19	4.915285D-11	7.495559D-06	2.605557D-03	9.775568D-01	1.968216D-02	1.480233D-04	1.307D-01	9.874D 01	1.129D 00
20	2.358736D-11	5.357126D-06	2.237744D-03	9.770446D-01	2.056106D-02	1.512718D-04	1.122D-01	9.873D 01	1.155D 00
21	1.131637D-11	3.825899D-06	1.918443D-03	9.762363D-01	2.168510D-02	1.562963D-04	9.611D-02	9.871D 01	1.196D 00
22	5.427594D-12	2.729620D-06	1.641260D-03	9.750695D-01	2.312242D-02	1.640801D-04	8.220D-02	9.866D 01	1.255D 00
23	2.602194D-12	1.944857D-06	1.400634D-03	9.734617D-01	2.495960D-02	1.761498D-04	7.013D-02	9.859D 01	1.336D 00
24	1.246915D-12	1.383182D-06	1.191732D-03	9.713057D-01	2.730629D-02	1.948717D-04	5.966D-02	9.850D 01	1.444D 00
25	5.970091D-13	9.812502D-07	1.010354D-03	9.684638D-01	3.030099D-02	2.239102D-04	5.057D-02	9.836D 01	1.588D 00
26	2.854676D-13	6.936942D-07	8.528568D-04	9.647597D-01	3.411782D-02	2.689280D-04	4.268D-02	9.818D 01	1.775D 00
27	1.361924D-13	4.880239D-07	7.160784D-04	9.599703D-01	3.897444D-02	3.386535D-04	3.583D-02	9.795D 01	2.018D 00
28	6.470730D-14	3.409746D-07	5.972802D-04	9.538150D-01	4.514086D-02	4.464968D-04	2.988D-02	9.764D 01	2.332D 00
29	3.049902D-14	2.358901D-07	4.940938D-04	9.459439D-01	5.294879D-02	6.129703D-04	2.472D-02	9.724D 01	2.733D 00
30	1.414433D-14	1.608468D-07	4.044754D-04	9.359257D-01	6.280039D-02	8.692753D-04	2.023D-02	9.673D 01	3.247D 00

$$H_2 + D_2 \rightleftarrows 2HD \quad \text{(I-11)}$$

$$H_2 + T_2 \rightleftarrows 2HT \quad \text{(I-12)}$$

$$D_2 + T_2 \rightleftarrows 2DT \quad \text{(I-13)}$$

$$H_2 + DT \rightleftarrows HT + HD \quad \text{(I-14)}$$

$$T_2 + HD \rightleftarrows HT + DT \quad \text{(I-15)}$$

$$D_2 + HT \rightleftarrows DT + HD \quad \text{(I-16)}$$

Equation (13) shows that DT can be split into T_2 and D_2, and equation (16) shows that by adding D_2 to HT, a more volatile component HD is produced which can be separated from less volatile DT. Thus, a chemical equilibration followed by cryogenic distillation will lead to removal of essentially all protium atoms without significant loss of tritium atoms.

Although there are six chemical equations as shown above, there are only three independent equations that need to be solved to estimate a new composition of the feed mixture. However, the resultant three equations are non-linear and, hence, cumbersome to solve. A subroutine was written to solve the resultant equations to establish the new composition of the feed mixture. The analytical results after chemical equilibration are shown in Table I-25. By comparing the composition of the distillate as shown in Table I-22 and I-25, the effect of chemical equilibration can be observed.

3. Cryogenic Enrichment Scenario for More Stringent Enrichment Requirements

Based on the studies presented in this Appendix, it is apparent that the enrichment requirements of a fusion device are largely determined by the fuel supply stream(s) composition requirements. It is also a reasonable assumption that most D-T burning experimental reactors (tokamaks or otherwise) will produce an exhaust system composition that is not significantly different from the one used above for the ANL/EPR. In order to extend the cryogenic distillation analyses to a machine with more stringent mainstream enrichment requirements than the EPR, the case of a fully-injected tokamak reactor was considered. The previously described Tokamak Engineering Technology Facility[6] (TETF) was used as a point of departure for this analysis. because the TETF has the requirement that all deuterium and tritium atoms are delivered to the plasma chamber in the form of isotopically separated energetic neutral particle beams. The exhaust stream composition was taken to be 0.2 a% H_2, 0.8 a% HD, 0.8 a% HT, 27.7 a% D_2, 42.8 a% DT, and 27.7 a% T_2.

Table I-25. Analysis of ANL/EPR

CRYOGENIC DISTILLATION OF HYDROGEN ISOTOPES FOR ANL/TEPR, .. B.MISRA.. ..DECEMBER, 1975

ANALYTICAL RESULTS AT PT= 1.000D 03 TORR AFTER 7 ITERATIONS FOR COLUMN NO: 4
NUMBER OF THEORETICAL STAGES: 30 REFLUX RATIO L/D= 1.500D 01
FIRST FEED PLATE LOCATION: 10 2ND FP LOCATION: 12 3RD FP LOCATION= 15
FEED RATES: 0.0 0.0 8.01D 00 DISTILLATE: 3.00D 00 BOTTOMS: 5.01D 00

FEED COMP.N-H2	HD	HT	N-D2	DT	N-T2	APH	APD	APT
3.545824D-01	2.226372D-01	8.432479D-02	1.051058D-01	1.504835D-01	8.286629D-02	5.081D 01	2.917D 01	2.003D 01

SUMMATION OF LIQUID MOLE FRACTIONS

1.006368D 00	1.008674D 00	1.010821D 00	1.012268D 00	1.012597D 00	1.011761D 00
1.010086D 00	1.008059D 00	1.006091D 00	1.004421D 00	1.003126D 00	1.002190D 00
1.001552D 00	1.001142D 00	1.000886D 00	1.000803D 00	1.000734D 00	1.000689D 00
1.000673D 00	1.000690D 00	1.000744D 00	1.000841D 00	1.000990D 00	1.001202D 00
1.001486D 00	1.001841D 00	1.002242D 00	1.002612D 00	1.002820D 00	1.002733D 00

EQUILIBRIUM STAGE TEMPERATURES

2.157285D 01	2.167761D 01	2.181072D 01	2.196710D 01	2.213539D 01	2.230096D 01
2.245083D 01	2.257743D 01	2.267930D 01	2.275969D 01	2.282458D 01	2.288159D 01
2.294004D 01	2.301233D 01	2.311591D 01	2.319312D 01	2.325054D 01	2.329318D 01
2.332568D 01	2.335204D 01	2.337572D 01	2.339999D 01	2.342836D 01	2.346516D 01
2.351627D 01	2.358992D 01	2.369710D 01	2.385045D 01	2.405998D 01	2.432523D 01

PLATE NO.	N-H2	HD	HT	N-D2	DT	N-T2	APH	APD	APT
1	9.157276D-01	9.034647D-02	2.875903D-04	6.372548D-06	2.144628D-07	3.121894D-09	9.610D 01	4.518D 00	1.439D-02
2	7.927880D-01	2.061112D-01	1.060847D-03	3.789234D-05	2.084141D-06	4.963883D-08	8.887D 01	1.022D 01	5.269D-02
3	7.101236D-01	2.879219D-01	1.864438D-03	8.400759D-05	5.873616D-06	1.780234D-07	8.459D 01	1.425D 01	9.253D-02
4	6.160686D-01	3.806479D-01	3.091694D-03	1.755468D-04	1.557716D-05	5.994795D-07	7.981D 01	1.882D 01	1.535D-01
5	5.183917D-01	4.763810D-01	4.840622D-03	3.459259D-04	3.886987D-05	1.893851D-06	7.496D 01	2.356D 01	2.411D-01
6	4.257883D-01	5.662882D-01	7.181422D-03	6.449766D-04	9.153515D-05	5.629856D-06	7.042D 01	2.805D 01	3.600D-01
7	3.450212D-01	6.434510D-01	1.016186D-02	1.145327D-03	2.048138D-04	1.585898D-05	6.651D 01	3.197D 01	5.147D-01
8	2.793676D-01	7.043697D-01	1.382747D-02	1.953305D-03	4.392354D-04	4.272319D-05	6.334D 01	3.515D 01	7.119D-01
9	2.288574D-01	7.486533D-01	1.824116D-02	3.226277D-03	9.107733D-04	1.110896D-04	6.086D 01	3.757D 01	9.628D-01
10	1.914968D-01	7.776955D-01	2.348967D-02	5.197461D-03	1.839565D-03	2.809889D-04	5.895D 01	3.932D 01	1.289D 00
11	1.645974D-01	7.932803D-01	2.967108D-02	8.207679D-03	3.638294D-03	6.952018D-04	5.742D 01	4.054D 01	1.730D 00
12	1.451216D-01	7.965313D-01	3.685663D-02	1.273813D-02	7.065169D-03	1.687164D-03	5.606D 01	4.136D 01	2.360D 00
13	1.309208D-01	7.871676D-01	4.500943D-02	1.942221D-02	1.346538D-02	4.014581D-03	5.462D 01	4.191D 01	3.320D 00
14	1.198744D-01	7.629232D-01	5.382801D-02	2.897420D-02	2.507739D-02	9.322805D-03	5.276D 01	4.225D 01	4.872D 00
15	1.102499D-01	7.192690D-01	6.248569D-02	4.189821D-02	4.518760D-02	2.090960D-02	5.007D 01	4.238D 01	7.468D 00
16	7.654605D-02	7.470017D-01	6.644858D-02	4.299880D-02	4.586808D-02	2.113680D-02	4.829D 01	4.391D 01	7.723D 00
17	5.242810D-02	7.651519D-01	7.059817D-02	4.407493D-02	4.643337D-02	2.131355D-02	4.700D 01	4.495D 01	7.977D 00
18	3.554818D-02	7.756113D-01	7.515784D-02	4.526582D-02	4.695736D-02	2.145954D-02	4.606D 01	4.562D 01	8.246D 00
19	2.391712D-02	7.798484D-01	8.035902D-02	4.674656D-02	4.753247D-02	2.159845D-02	4.537D 01	4.601D 01	8.548D 00
20	1.598993D-02	7.787950D-01	8.643096D-02	4.874551D-02	4.828717D-02	2.175139D-02	4.483D 01	4.620D 01	8.905D 00
21	1.062850D-02	7.728277D-01	9.358755D-02	5.157049D-02	4.942017D-02	2.196554D-02	4.435D 01	4.624D 01	9.340D 00
22	7.022302D-03	7.617644D-01	1.020002D-01	5.564044D-02	5.125985D-02	2.231278D-02	4.385D 01	4.618D 01	9.886D 00
23	4.606613D-03	7.448356D-01	1.117432D-01	6.151449D-02	5.436161D-02	2.293848D-02	4.325D 01	4.607D 01	1.059D 01
24	2.993737D-03	7.206215D-01	1.226920D-01	6.989693D-02	5.965663D-02	2.413921D-02	4.241D 01	4.595D 01	1.152D 01
25	1.920216D-03	6.869914D-01	1.343522D-01	8.156956D-02	6.864766D-02	2.651902D-02	4.120D 01	4.587D 01	1.278D 01
26	1.208435D-03	6.411695D-01	1.456115D-01	9.716038D-02	8.358185D-02	3.126827D-02	3.939D 01	4.587D 01	1.456D 01
27	7.395340D-04	5.802107D-01	1.544784D-01	1.166274D-01	1.073691D-01	4.057493D-02	3.673D 01	4.594D 01	1.711D 01
28	4.345109D-04	5.023046D-01	1.580476D-01	1.384338D-01	1.427793D-01	5.800014D-02	3.297D 01	4.598D 01	2.079D 01
29	2.409153D-04	4.090387D-01	1.531514D-01	1.588152D-01	1.904817D-01	8.827204D-02	2.805D 01	4.573D 01	2.594D 01
30	1.232261D-04	3.074383D-01	1.379637D-01	1.721868D-01	2.465313D-01	1.357567D-01	2.222D 01	4.479D 01	3.271D 01

Since the D_2 and T_2 fractions represent less than 56% of the exhaust stream, complete recycling of the spent fuel cannot be carried by cryogenic distillation alone. The other requirement, as in ANL/EPR, is to remove most of the protium atoms without carryover of significant quantities of tritium atoms. To fulfill the above reinjection requirements (separate streams of > 95% D_2 and > 95% T_2), one can qualitatively visualize the following steps:

(1) Separate the heaviest component (T_2) as the bottom product containing a T_2 fraction ≥ 0.95 with no protium atoms. Based on the multicomponent distillation program, as discussed in Section 1, this can be accomplished with one or more distillation steps.

(2) Remove a lighter product containing most of the D_2 molecules and the protium atoms.

(3) The above product on further distillation will lead to separation of D_2 from protium and tritium bearing compounds.

(4) The protium bearing atoms may be subjected to a chemical equilibration followed by cryogenic distillation to remove most of the protium fraction with very little carryover of tritium atoms.

Carrying out the above steps will automatically lead to liquid fractions that are rich in DT with lesser amounts of T_2 and D_2; hence, a second type of equilibration is now required to breakup the DT fraction as follows:

$$2DT \rightleftarrows D_2 + T_2$$

The data on the equilibrium constants for the above reaction shows that when a mixture containing equal atomic fractions of D and T is heated up (in the presence of an appropriate catalyst to speed up the reaction), the equilibrium mixture has the following approximate composition (above 500°K, the equilibration temperature has only a minor effect on the composition of the equilibrium mixture).

D_2 = 25%
T_2 = 25%
DT = 50%

It may be observed that the composition of the above mixture is very similar to that of the original feed and, hence may be returned to the first distillation column.

Figure I-3 represents a schematic of the separation scheme derived for the TETF type device. A fairly comprehensive parametric investigation to study the effect of the operating variables was carried out for the enrichment scheme represented in Figure I-3. The analytical results for the five column cascade in Figure I-3 are summarized in Table I-26. Tables I-27 through I-31 show the detailed operating characteristics of the individual columns. An examination of the composition of the bottom product from column No. 4 will show that tritium rich and deuterium rich fractions containing little or no protium atoms can be obtained to meet the fuel recycle requirements. Comparison of the top products from column No. 5, with and without a chemical equilibrator as summarized in Tables I-31 and I-32, respectively, show that a chemical equilibrator reduces the tritium fraction in the top product from 8.4% to 0.6%. One drawback to the TETF enrichment design is that the equilibrator feeding back to column No. 1 handles a significant fraction of the total liquid load; hence its associated refrigeration requirements may be quite large. For this reason, the location of equilibrators in the high flow regions of cryogenic distillation cascades should be avoided whereever possible.

4. Conclusions

Mathematical simulation of multicomponent distillation and computer solution of the resultant equations were carried out. Since the computational steps are based on an exact solution method, the accuracy of the analytical results is expected to be limited only by the accuracy of the thermodynamic and phase equilibrium data. Although the computer code was developed specifically for enrichment of the spent fuels from presently conceived tokamak-type fusion reactors, the scope of this program is much broader, in that it can be used in the design and analysis of multicomponent distillation for any liquid mixture, provided of course, the necessary thermodynamic and phase equilibrium data are available. The program is very efficient so that a number of parametric investigations to study the effects of design and operating variables can be carried out even with limited resources. The program does, however, require a fairly large computer storage (approximately 250 K bytes).

Using this general purpose computer code as a basis, a distillation cascade consisting of six cryogenic columns was developed and analyzed for

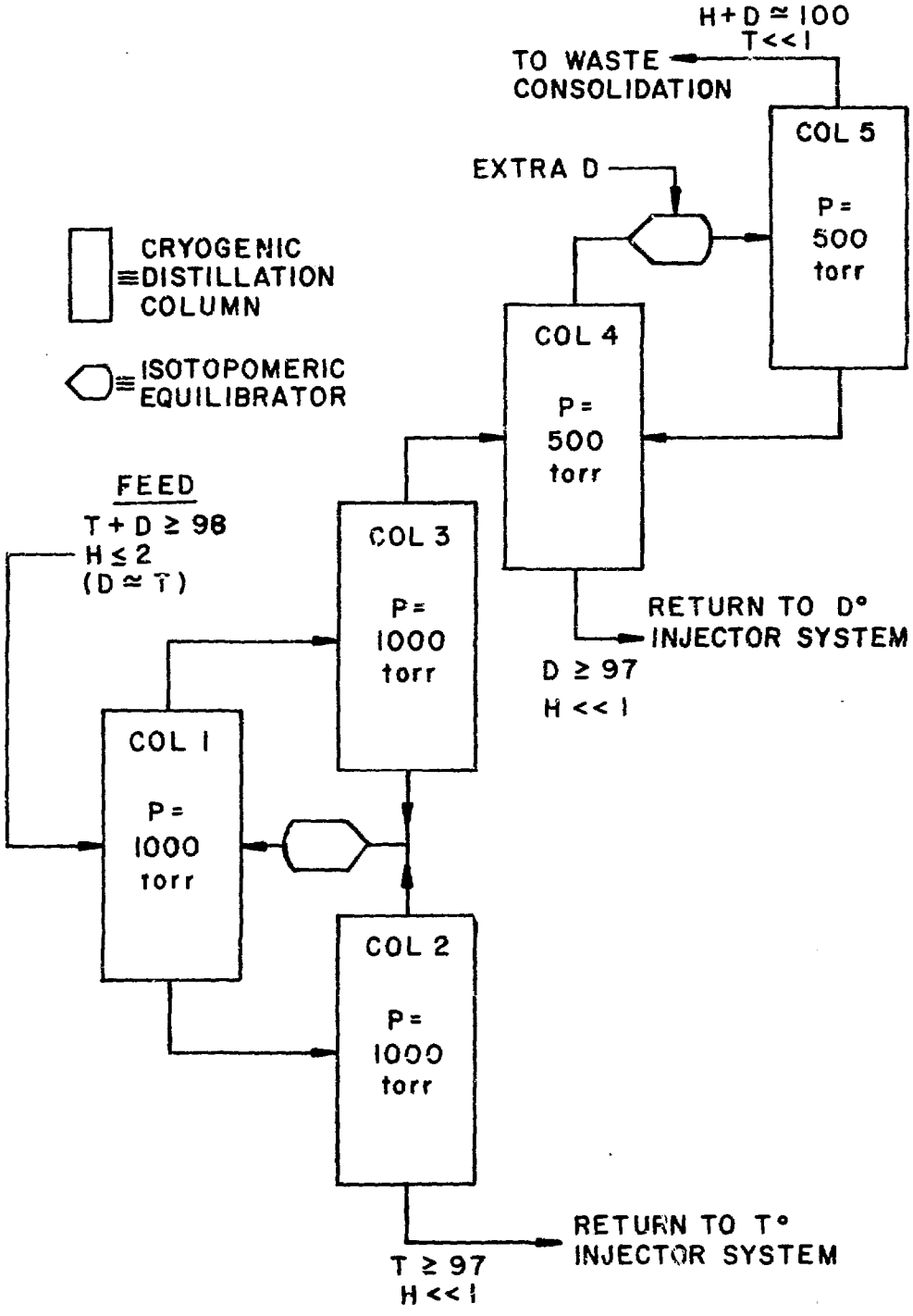

Figure I-3. Cryogenic Enrichment Scenario for TETF

Table I-26. Summary of Operating Parameters for the TETF Cryogenic Distillation Cascade*

Column Number+	Feed Plate	Total Feed (moles)	Feed Composition (at %)			Top Product				Bottom Product			
						Total Moles	Atomic Percentates			Total Moles	Atomic Percentates		
			H	D	T		H	D	T		H	D	T
1	15 20	100	0.49	49.64	49.87	50	1.0	74.9	24.1	50	0	24.4	75.6
2	15	50	0	24.4	75.6	27	0	42.5	57.5	23	0	3.2	96.8
3	15	50	1.0	74.9	24.1	25	2.0	93.9	4.1	25	0	55.9	44.1
4	15 20	28	1.77	94.51	3.72	5	9.4	87.1	3.5	23	0.1	96.1	3.8
5	15	5	9.4	87.0	3.6	2	23.1	68.5	8.4	3	0.2	99.4	0.4
5*	15	5.5	8.6	88.2	3.2	2.5	18.8	80.6	0.6	3	0	94.6	5.4

* 30 Theoretical Stages per Column; Pressure for Columns 1, 2, 3 equal to 1000 torr, pressure for Columns 4 and 5 equal to 500 torr.

+ See Figure I-3 for location in Cascade.

**After chemical equilibration at 300°K.

Table I-27. Analysis of TETF

CRYOGENIC DISTILLATION OF HYDROGEN ISOTOPES FOR ANL/TETF, ...B. MISRA...., APRIL 1976

ANALYTICAL RESULTS AT PT= 1.000D 03 TORR AFTER 2 ITERATIONS FOR COLUMN NO: 1
NUMBER OF THEORETICAL STAGES: 30 REFLUX RATIO L/D1= 2.000D 00
FIRST FEED PLATE LOCATION: 10 2ND FP LOCATION: 15 3RD FP LOCATION= 20
FEED RATES: 0.0 5.20D 01 4.80D 01 DISTILLATE: 5.00D 01 BOTTOMS: 5.00D 01

FEED COMP. N-H2	HD	HT	N-D2	DT	N-T2	APH	APD	APT
1.638650D-07	3.657700D-04	1.000000D-06	2.504460D-01	4.942150D-01	2.553020D-01	1.835D-02	4.977D 01	5.024D 01
2.000000D-03	8.000000D-03	8.000000D-03	2.770000D-01	4.280000D-01	2.770000D-01	1.000D 00	4.950D 01	4.950D 01

COMPOSITION OF LIQUID AFTER EQUILIBRATION

5.194123D-09	2.294879D-06	3.185635D-05	2.499580D-01	4.933705D-01	2.549271D-01

SUMMATION OF LIQUID MOLE FRACTIONS.....(FROM L TO R IN ASCENDING ORDER OF PLATE NUMBER)

9.999495D-01	9.999504D-01	9.999517D-01	9.999534D-01	9.999554D-01	9.999577D-01
9.999600D-01	9.999623D-01	9.999644D-01	9.999664D-01	9.999682D-01	9.999697D-01
9.999710D-01	9.999722D-01	9.999731D-01	9.999725D-01	9.999717D-01	9.999710D-01
9.999702D-01	9.999693D-01	9.999669D-01	9.999645D-01	9.999622D-01	9.999599D-01
9.999579D-01	9.999562D-01	9.999549D-01	9.999541D-01	9.999539D-01	9.999544D-01

EQUILIBRIUM STAGE TEMPERATURES, DEG.K..(FROM L TO R IN ASCENDING ORDER OF PLATE NUMBER)

2.499736D 01	2.503907D 01	2.507567D 01	2.510843D 01	2.513801D 01	2.516486D 01
2.518933D 01	2.521176D 01	2.523248D 01	2.525184D 01	2.527016D 01	2.528774D 01
2.530500D 01	2.532213D 01	2.533940D 01	2.535591D 01	2.537242D 01	2.538921D 01
2.540650D 01	2.542455D 01	2.544761D 01	2.547077D 01	2.549448D 01	2.551906D 01
2.554477D 01	2.557177D 01	2.560014D 01	2.562984D 01	2.566075D 01	2.569262D 01

PLATE NO.	N-H2	HD	HT	N-D2	DT	N-T2	APH	APD	APT
1	1.920447D-03	8.059882D-03	7.665961D-03	5.150364D-01	4.605730D-01	6.693781D-03	9.783D-01	7.494D 01	2.408D 01
2	3.600339D-04	3.183746D-03	4.344913D-03	4.276449D-01	5.528334D-01	1.163304D-02	4.125D-01	7.057D 01	2.902D 01
3	1.800179D-04	2.088086D-03	3.315855D-03	3.867713D-01	5.927781D-01	1.486663D-02	2.882D-01	6.842D 01	3.129D 01
4	1.082177D-04	1.439104D-03	2.573206D-03	3.489345D-01	6.282389D-01	1.870612D-02	2.114D-01	6.638D 01	3.341D 01
5	7.957634D-05	1.056821D-03	2.041607D-03	3.145190D-01	6.590705D-01	2.323245D-02	1.629D-01	6.446D 01	3.538D 01
6	6.803505D-05	8.322480D-04	1.663444D-03	2.836612D-01	6.852405D-01	2.853463D-02	1.316D-01	6.267D 01	3.720D 01
7	6.324051D-05	7.001932D-04	1.395582D-03	2.563189D-01	7.068117D-01	3.471040D-02	1.111D-01	6.101D 01	3.888D 01
8	6.110698D-05	6.220669D-04	1.206256D-03	2.323267D-01	7.239173D-01	4.186654D-02	9.753D-02	5.946D 01	4.044D 01
9	6.002990D-05	5.752227D-04	1.072393D-03	2.114393D-01	7.367347D-01	5.011843D-02	8.839D-02	5.801D 01	4.190D 01
10	5.938003D-05	5.466465D-04	9.774248D-04	1.933660D-01	7.454618D-01	5.958898D-02	8.214D-02	5.664D 01	4.329D 01
11	5.890923D-05	5.281420D-04	9.095605D-04	1.777970D-01	7.502999D-01	7.040648D-02	7.778D-02	5.532D 01	4.460D 01
12	5.851757D-05	5.158334D-04	8.604753D-04	1.644225D-01	7.514413D-01	8.270136D-02	7.467D-02	5.404D 01	4.589D 01
13	5.816275D-05	5.069838D-04	8.243251D-04	1.529452D-01	7.490537D-01	9.660160D-02	7.238D-02	5.277D 01	4.716D 01
14	5.782503D-05	5.001122D-04	7.970253D-04	1.430991D-01	7.433291D-01	1.122268D-01	7.064D-02	5.150D 01	4.843D 01
15	5.749378D-05	4.943547D-04	7.757310D-04	1.346039D-01	7.343876D-01	1.296809D-01	6.926D-02	5.021D 01	4.973D 01
16	5.826680D-05	4.929845D-04	7.850528D-04	1.225245D-01	7.345335D-01	1.496056D-01	6.973D-02	4.901D 01	5.093D 01
17	5.839960D-05	4.903264D-04	7.883095D-04	1.119655D-01	7.314320D-01	1.552655D-01	6.977D-02	4.779D 01	5.214D 01
18	5.824320D-05	4.869199D-04	7.873247D-04	1.027455D-01	7.250650D-01	1.708570D-01	6.954D-02	4.655D 01	5.338D 01
19	5.797685D-05	4.830527D-04	7.833581D-04	9.469406D-02	7.158122D-01	1.885693D-01	6.912D-02	4.527D 01	5.467D 01
20	5.766056D-05	4.788682D-04	7.772545D-04	8.765438D-02	7.024589D-01	2.085730D-01	6.857D-02	4.391D 01	5.602D 01
21	2.318903D-05	2.812441D-04	5.468911D-04	7.435197D-02	6.977234D-01	2.270733D-01	4.373D-02	4.234D 01	5.762D 01
22	9.281852D-06	1.642840D-04	3.825036D-04	6.263451D-02	6.886116D-01	2.481978D-01	2.027D-02	4.070D 01	5.927D 01
23	3.697315D-06	9.542566D-05	2.658498D-04	5.238099D-02	6.750687D-01	2.721853D-01	1.843D-02	3.900D 01	6.099D 01
24	1.465393D-06	5.509942D-05	1.835267D-04	4.346521D-02	6.570695D-01	2.992252D-01	1.208D-02	3.720D 01	6.279D 01
25	5.777194D-07	3.160986D-05	1.257584D-04	3.576169D-02	6.346452D-01	3.294351D-01	7.927D-03	3.531D 01	6.468D 01
26	2.264662D-07	1.800414D-05	8.545695D-05	2.914927D-02	6.079094D-01	3.628377D-01	5.196D-03	3.331D 01	6.669D 01
27	8.821430D-08	1.016985D-05	5.752020D-05	2.351296D-02	5.770808D-01	3.993388D-01	3.393D-03	3.121D 01	6.879D 01
28	3.410354D-08	5.687001D-06	3.827929D-05	1.874480D-02	5.425014D-01	4.387090D-01	2.202D-03	2.900D 01	7.100D 01
29	1.304985D-08	3.138923D-06	2.512278D-05	1.474303D-02	5.046439D-01	4.805838D-01	1.418D-03	2.671D 01	7.330D 01
30	4.901960D-09	1.700836D-06	1.619554D-05	1.141691D-02	4.641074D-01	5.244578D-01	8.954D-04	2.435D 01	7.566D 01

Table I-28. Analysis of TETF

CRYOGENIC DISTILLATION OF HYDROGEN ISOTOPES FOR ANL/TETF, ...B. MISRA...., APRIL 1976

ANALYTICAL RESULTS AT PT= 1.000D 03 TORR AFTER 2 ITERATIONS FOR COLUMN NO: 2
NUMBER OF THEORETICAL STAGES: 30 REFLUX RATIO L/D1= 2.000D 01
FIRST FEED PLATE LOCATION: 10 2ND FP LOCATION: 12 3RD FP LOCATION= 15
FEED RATES: 0.0 0.0 5.00D 01 DISTILLATE: 2.70D 01 BOTTOMS: 2.30D 01

FEED COMP. N-H2	HD	HT	N-D2	DT	N-T2	APH	APD	APT
4.908960D-09	1.700836D-06	1.619554D-05	1.141691D-02	4.641074D-01	5.244578D-01	8.953D-04	2.435D 01	7.565D 01

SUMMATION OF LIQUID MOLE FRACTIONS.....(FROM L TO R IN ASCENDING ORDER OF PLATE NUMBER)

9.995715D-01	9.995282D-01	9.994880D-01	9.995250D-01	9.994231D-01	9.994009D-01
9.992869D-01	9.993815D-01	9.993848D-01	9.993965D-01	9.994157D-01	9.994416D-01
9.994729D-01	9.995082D-01	9.995462D-01	9.995472D-01	9.995541D-01	9.995663D-01
9.995832D-01	9.996041D-01	9.996281D-01	9.996543D-01	9.996818D-01	9.997099D-01
9.997380D-01	9.997654D-01	9.997917D-01	9.998167D-01	9.998400D-01	9.998616D-01

EQUILIBRIUM STAGE TEMPERATURES, DEG.K..(FROM L TO R IN ASCENDING ORDER OF PLATE NUMBER)

2.547534D 01	2.549691D 01	2.551896D 01	2.554142D 01	2.556416D 01	2.558701D 01
2.560977D 01	2.563223D 01	2.565416D 01	2.567538D 01	2.569568D 01	2.571492D 01
2.573299D 01	2.574979D 01	2.576530D 01	2.578550D 01	2.580535D 01	2.582469D 01
2.584336D 01	2.586123D 01	2.587818D 01	2.589414D 01	2.590904D 01	2.592286D 01
2.593559D 01	2.594723D 01	2.595783D 01	2.596742D 01	2.597605D 01	2.598380D 01

PLATE NO.	N-H2	HD	HT	N-D2	DT	N-T2	APH	APD	APT
1	9.127101D-09	3.162112D-06	3.011024D-05	2.119121D-02	8.074608D-01	1.708863D-01	1.665D-03	4.249D 01	5.746D 01
2	1.426508D-09	1.014051D-06	1.367841D-05	1.394870D-02	7.572326D-01	2.288040D-01	7.351D-04	3.928D 01	6.077D 01
3	6.783349D-10	6.157389D-07	9.555241D-06	1.143478D-02	7.285564D-01	2.599986D-01	5.089D-04	3.759D 01	6.246D 01
4	4.068341D-10	4.043829D-07	6.922635D-06	9.465732D-03	6.981909D-01	2.923361D-01	3.666D-04	3.588D 01	6.418D 01
5	3.079579D-10	2.923632D-07	5.245697D-06	7.926384D-03	6.665909D-01	3.254751D-01	2.771D-04	3.414D 01	6.592D 01
6	2.713243D-10	2.328674D-07	4.178398D-06	6.731389D-03	6.342240D-01	3.590402D-01	2.207D-04	3.240D 01	6.766D 01
7	2.570466D-10	2.010137D-07	3.498079D-06	5.801420D-03	6.015573D-01	3.926376D-01	1.851D-04	3.068D 01	6.938D 01
8	2.507852D-10	1.836482D-07	3.062278D-06	5.079945D-03	5.690434D-01	4.258734D-01	1.624D-04	2.898D 01	7.108D 01
9	2.474161D-10	1.738571D-07	2.780386D-06	4.520528D-03	5.371041D-01	4.583724D-01	1.478D-04	2.732D 01	7.274D 01
10	2.451228D-10	1.680291D-07	2.595130D-06	4.086557D-03	5.061172D-01	4.897935D-01	1.383D-04	2.573D 01	7.433D 01
11	2.432694D-10	1.642899D-07	2.470537D-06	3.749354D-03	4.764049D-01	5.198431D-01	1.318D-04	2.421D 01	7.585D 01
12	2.416380D-10	1.616734D-07	2.384157D-06	3.486596D-03	4.482268D-01	5.482841D-01	1.274D-04	2.277D 01	7.728D 01
13	2.401555D-10	1.596846D-07	2.322057D-06	3.281019D-03	4.217767D-01	5.749398D-01	1.242D-04	2.143D 01	7.862D 01
14	2.388020D-10	1.580710D-07	2.275628D-06	3.119345D-03	3.971839D-01	5.996943D-01	1.218D-04	2.018D 01	7.987D 01
15	2.375673D-10	1.567037D-07	2.239567D-06	2.991415D-03	3.745176D-01	6.224886D-01	1.199D-04	1.903D 01	8.101D 01
16	8.864770D-11	8.468552D-08	1.445261D-06	2.329613D-03	3.461837D-01	6.514851D-01	7.654D-05	1.755D 01	8.250D 01
17	3.294754D-11	4.556160D-08	9.282830D-07	1.805081D-03	3.181656D-01	6.800283D-01	4.872D-05	1.610D 01	8.395D 01
18	1.219832D-11	2.440622D-08	5.934956D-07	1.391721D-03	2.907591D-01	7.078485D-01	3.091D-05	1.468D 01	8.536D 01
19	4.499443D-12	1.301906D-08	3.777644D-07	1.067815D-03	2.642281D-01	7.347037D-01	1.955D-05	1.332D 01	8.672D 01
20	1.653753D-12	6.916943D-09	2.394218D-07	8.154144D-04	2.387970D-01	7.603873D-01	1.232D-05	1.203D 01	8.801D 01
21	6.057818D-13	3.660912D-09	1.511201D-07	6.197944D-04	2.146468D-01	7.847333D-01	7.742D-06	1.080D 01	8.924D 01
22	2.211988D-13	1.930604D-09	9.501003D-08	4.689679D-04	1.919130D-01	8.076179D-01	4.849D-06	9.646D 00	9.039D 01
23	8.053057D-14	1.014636D-09	5.950673D-08	3.532522D-04	1.706866D-01	8.289601D-01	3.027D-06	8.572D 00	9.146D 01
24	2.923748D-14	5.315074D-10	3.713168D-08	2.648878D-04	1.510170D-01	8.487181D-01	1.884D-06	7.580D 00	9.245D 01
25	1.058768D-14	2.775392D-10	2.308281D-08	1.977043D-04	1.329166D-01	8.668857D-01	1.168D-06	6.667D 00	9.336D 01
26	3.824690D-15	1.444509D-10	1.429219D-08	1.468319D-04	1.163659D-01	8.834873D-01	7.222D-07	5.834D 00	9.419D 01
27	1.378175D-15	7.490770D-11	8.809215D-09	1.084549D-04	1.013197D-01	8.985718D-01	4.443D-07	5.078D 00	9.494D 01
28	4.951035D-16	3.866423D-11	5.399268D-09	7.960377D-05	8.771300D-02	9.122074D-01	2.719D-07	4.394D 00	9.562D 01
29	1.769985D-16	1.982047D-11	3.284206D-09	5.798230D-05	7.546601D-02	9.244760D-01	1.652D-07	3.780D 00	9.624D 01
30	6.261726D-17	1.004446D-11	1.975489D-09	4.182531D-05	6.448961D-02	9.354686D-01	9.929D-08	3.229D 00	9.678D 01

Table I-29. Analysis of TETF

CRYOGENIC DISTILLATION OF HYDROGEN ISOTOPES FOR ANL/TETF, ...B. MISRA...., APRIL 1976

ANALYTICAL RESULTS AT PT= 1.000D 03 TORR AFTER 2 ITERATIONS FOR COLUMN NO: 3
NUMBER OF THEORETICAL STAGES: 30 REFLUX RATIO L/D1= 2.000D 01
FIRST FEED PLATE LOCATION: 10 2ND FP LOCATION: 12 3RD FP LOCATION= 15
FEED RATES: 0.0 0.0 5.00D 01 DISTILLATE: 2.50D 01 BOTTOMS: 2.50D 01

FEED COMP. N-H2	HD	HT	N-D2	DT	N-T2	APH	APD	APT
1.920447D-03	8.059882D-03	7.665961D-03	5.150364D-01	4.605730D-01	6.693781D-03	9.783D-01	7.494D 01	2.408D 01

SUMMATION OF LIQUID MOLE FRACTIONS.....(FROM L TO R IN ASCENDING ORDER OF PLATE NUMBER)

1.000104D 00	1.000115D 00	1.000128D 00	1.000143D 00	1.000159D 00	1.000175D 00
1.000191D 00	1.000206D 00	1.000220D 00	1.000232D 00	1.000241D 00	1.000247D 00
1.000250D 00	1.000250D 00	1.000246D 00	1.000263D 00	1.000277D 00	1.000288D 00
1.000296D 00	1.000300D 00	1.000299D 00	1.000294D 00	1.000285D 00	1.000273D 00
1.000258D 00	1.000240D 00	1.000220D 00	1.000200D 00	1.000179D 00	1.000158D 00

EQUILIBRIUM STAGE TEMPERATURES, DEG.K..(FROM L TO R IN ASCENDING ORDER OF PLATE NUMBER)

2.467350D 01	2.469611D 01	2.471495D 01	2.473224D 01	2.474918D 01	2.476640D 01
2.478425D 01	2.480290D 01	2.482238D 01	2.484265D 01	2.486359D 01	2.488505D 01
2.490684D 01	2.492873D 01	2.495051D 01	2.497088D 01	2.499190D 01	2.501365D 01
2.503608D 01	2.505905D 01	2.508237D 01	2.510580D 01	2.512911D 01	2.515206D 01
2.517443D 01	2.519605D 01	2.521676D 01	2.523648D 01	2.525516D 01	2.527282D 01

PLATE NO.	N-H2	HD	HT	N-D2	DT	N-T2	APH	APD	APT
1	3.831929D-03	1.608093D-02	1.526214D-02	8.971277D-01	6.777789D-02	2.349186D-05	1.950D 00	9.391D 01	4.154D 00
2	8.212833D-04	7.405627D-03	1.018204D-02	8.839589D-01	9.758267D-02	4.947646D-05	9.614D-01	9.363D 01	5.393D 00
3	4.314329D-04	5.207827D-03	8.404060D-03	8.709987D-01	1.148881D-01	6.991840D-05	7.236D-01	9.309D 01	6.171D 00
4	2.644132D-04	3.797867D-03	7.008014D-03	8.549070D-01	1.339251D-01	9.763426D-05	5.667D-01	9.236D 01	7.055D 00
5	1.928483D-04	2.895423D-03	5.915334D-03	8.361195D-01	1.547419D-01	1.350181D-04	4.597D-01	9.148D 01	8.045D 00
6	1.620038D-04	2.318112D-03	5.061503D-03	8.149325D-01	1.773408D-01	1.851554D-04	3.851D-01	9.046D 01	9.137D 00
7	1.484563D-04	1.948109D-03	4.394562D-03	7.915846D-01	2.016723D-01	2.519844D-04	3.319D-01	8.932D 01	1.033D 01
8	1.422186D-04	1.709694D-03	3.873152D-03	7.663035D-01	2.276310D-01	3.404820D-04	2.933D-01	8.808D 01	1.161D 01
9	1.390481D-04	1.554432D-03	3.464615D-03	7.393322D-01	2.550528D-01	4.568748D-04	2.648D-01	8.674D 01	1.297D 01
10	1.371513D-04	1.451481D-03	3.143321D-03	7.109430D-01	2.837162D-01	6.028769D-04	2.434D-01	8.533D 01	1.440D 01
11	1.357754D-04	1.381302D-03	2.889272D-03	6.814412D-01	3.133465D-01	8.059557D-04	2.271D-01	8.386D 01	1.589D 01
12	1.346090D-04	1.331593D-03	2.686946D-03	6.511623D-01	3.436249D-01	1.059631D-03	2.143D-01	8.234D 01	1.742D 01
13	1.335277D-04	1.294668D-03	2.524370D-03	6.204633D-01	3.742003D-01	1.383810D-03	2.043D-01	8.080D 01	1.897D 01
14	1.324855D-04	1.265769D-03	2.392358D-03	5.897099D-01	4.047043D-01	1.795174D-03	1.961D-01	7.925D 01	2.053D 01
15	1.314691D-04	1.241986D-03	2.283909D-03	5.592620D-01	4.347670D-01	2.313624D-03	1.894D-01	7.771D 01	2.208D 01
16	5.834558D-05	8.151423D-04	1.807902D-03	5.334809D-01	4.614356D-01	2.403038D-03	1.369D-01	7.644D 01	2.340D 01
17	2.577993D-05	5.323339D-04	1.421950D-03	5.058464D-01	4.896601D-01	2.513467D-03	1.003D-01	7.507D 01	2.480D 01
18	1.133917D-05	3.458531D-04	1.112647D-03	4.766439D-01	5.192351D-01	2.651150D-03	7.404D-02	7.362D 01	2.627D 01
19	4.964176D-06	2.235020D-04	8.655202D-04	4.461936D-01	5.498883D-01	2.824137D-03	5.493D-02	7.210D 01	2.781D 01
20	2.162883D-06	1.436442D-04	6.691888D-04	4.148510D-01	5.812912D-01	3.042799D-03	4.085D-02	7.054D 01	2.939D 01
21	9.377977D-07	9.180336D-05	5.141420D-04	3.829984D-01	6.130743D-01	3.320438D-03	3.038D-02	6.894D 01	3.100D 01
22	4.046366D-07	5.833780D-05	3.924608D-04	3.510321D-01	6.448426D-01	3.674021D-03	2.257D-02	6.733D 01	3.262D 01
23	1.737436D-07	3.685727D-05	2.975791D-04	3.193458D-01	6.761945D-01	4.125273D-03	1.673D-02	6.573D 01	3.423D 01
24	7.424377D-08	2.314879D-05	2.240794D-04	2.883135D-01	7.067384D-01	4.700749D-03	1.237D-02	6.415D 01	3.581D 01
25	3.157465D-08	1.445045D-05	1.675184D-04	2.582745D-01	7.361083D-01	5.435144D-03	9.099D-03	6.262D 01	3.735D 01
26	1.336386D-08	8.962394D-06	1.242774D-04	2.295205D-01	7.639753D-01	6.370880D-03	6.662D-03	6.114D 01	3.883D 01
27	5.627641D-09	5.518934D-06	9.143208D-05	2.022874D-01	7.900546D-01	7.561037D-03	4.847D-03	5.972D 01	4.025D 01
28	2.355908D-09	3.369909D-06	6.663896D-05	1.767513D-01	8.141072D-01	9.071489D-03	3.500D-03	5.837D 01	4.161D 01
29	9.779611D-10	2.035626D-06	4.803651D-05	1.530286D-01	8.359376D-01	1.098371D-02	2.503D-03	5.709D 01	4.289D 01
30	4.000723D-10	1.211282D-06	3.415927D-05	1.311800D-01	8.553865D-01	1.339811D-02	1.768D-03	5.588D 01	4.410D 01

Table I-30. Analysis of TETF

CRYOGENIC DISTILLATION OF HYDROGEN ISOTOPES FOR ANL/TETF, ...B. MISRA...., APRIL 1976

ANALYTICAL RESULTS AT PT= 5.000D 02 TORR AFTER 2 ITERATIONS FOR COLUMN NO: 4
NUMBER OF THEORETICAL STAGES: 30 REFLUX RATIO L/D1= 2.000D 01
FIRST FEED PLATE LOCATION: 10 2ND FP LOCATION: 15 3RD FP LOCATION= 20
FEED RATES: 0.0 2.50D 01 3.00D 00 DISTILLATE: 5.00D 00 BOTTOMS: 2.30D 01

FEED COMP.	N-H2	HD	HT	N-D2	DT	N-T2	APH	APD	APT
	3.831929D-03	1.698093D-02	1.526214D-02	8.971277D-01	6.777789D-02	2.349186D-03	1.950D 00	9.391D 01	4.154D 00
	3.738764D-08	1.439434D-04	4.205361D-03	9.924330D-01	3.217657D-03	4.954006D-08	2.175D-01	9.941D 01	3.712D-01

SUMMATION OF LIQUID MOLE FRACTIONS.....(FROM L TO R IN ASCENDING ORDER OF PLATE NUMBER)

1.000001D 00	1.000001D 00	1.000000D 00	1.000000D 00	1.000000D 00	1.000000D 00	1.000000D 00
1.000000D 00	1.000000D 00	1.000000D 00	1.000000D 00	1.000000D 00	1.000000D 00	1.000000D 00
1.000000D 00	1.000000D 00	1.000000D 00	1.000000D 00	1.000000D 00	1.000000D 00	1.000000D 00
1.000000D 00	1.000000D 00	1.000000D 00	1.000000D 00	1.000000D 00	1.000000D 00	1.000000D 00
1.000000D 00	1.000000D 00	1.000000D 00	1.000000D 00	1.000000D 00	1.000000D 00	1.000000D 00

EQUILIBRIUM STAGE TEMPERATURES, DEG.K..(FROM L TO R IN ASCENDING ORDER OF PLATE NUMBER)

2.211884D 01	2.217916D 01	2.221432D 01	2.223584D 01	2.224966D 01	2.225899D 01
2.226562D 01	2.227066D 01	2.227476D 01	2.227839D 01	2.228187D 01	2.228542D 01
2.228925D 01	2.229353D 01	2.229844D 01	2.230344D 01	2.230687D 01	2.230930D 01
2.231102D 01	2.231218D 01	2.231356D 01	2.231485D 01	2.231615D 01	2.231757D 01
2.231925D 01	2.232138D 01	2.232423D 01	2.232820D 01	2.233390D 01	2.234218D 01

PLATE NO.	N-H2	HD	HT	N-D2	DT	N-T2	APH	APD	APT
1	1.915772D-02	8.021310D-02	6.939191D-02	8.296628D-01	1.575413D-03	1.255968D-08	9.396D 00	8.706D 01	3.548D 00
2	3.382411D-03	3.539018D-02	4.821069D-02	9.102597D-01	2.756972D-03	3.505349D-08	4.538D 00	9.293D 01	2.548D 00
3	1.652494D-03	2.416466D-02	4.001680D-02	9.306516D-01	3.514393D-03	5.598208D-08	3.374D 00	9.445D 01	2.177D 00
4	9.884520D-04	1.717277D-02	3.344870D-02	9.439698D-01	4.420191D-03	8.812299D-08	2.630D 00	9.548D 01	1.893D 00
5	7.344309D-04	285979D-02	2.827567D-02	9.526217D-01	5.508225D-03	1.374617D-07	2.130D 00	9.618D 01	1.689D 00
6	6.370749D-04	1.622399D-02	2.424380D-02	9.580865D-01	6.818460D-03	2.131554D-07	1.787D 00	9.666D 01	1.553D 00
7	5.994188D-04	8.595660D-03	2.112138D-02	9.612849D-01	8.398331D-03	3.292007D-07	1.546D 00	9.698D 01	1.476D 00
8	5.845233D-04	7.606693D-03	1.871262D-02	9.627914D-01	1.030423D-02	5.069688D-07	1.374D 00	9.717D 01	1.451D 00
9	5.783324D-04	7.001656D-03	1.685831D-02	9.629578D-01	1.260315D-02	7.790462D-07	1.251D 00	9.728D 01	1.473D 00
10	5.754834D-04	6.630069D-03	1.543179D-02	9.619870D-01	1.537449D-02	1.195048D-06	1.161D 00	9.730D 01	1.540D 00
11	5.739129D-04	6.399948D-03	1.433352D-02	9.599789D-01	1.871194D-02	1.830366D-06	1.094D 00	9.725D 01	1.652D 00
12	5.728112D-04	6.255136D-03	1.348590D-02	9.569579D-01	2.272547D-02	2.799314D-06	1.044D 00	9.714D 01	1.811D 00
13	5.718462D-04	6.161328D-03	1.282869D-02	9.528906D-01	2.754325D-02	4.274741D-06	1.007D 00	9.697D 01	2.019D 00
14	5.708686D-04	6.097506D-03	1.231519D-02	9.476966D-01	3.331330D-02	6.517182D-06	9.777D-01	9.674D 01	2.282D 00
15	5.697993D-04	6.050712D-03	1.190922D-02	9.412556D-01	4.020471D-02	9.917824D-06	9.550D-01	9.644D 01	2.607D 00
16	2.651358D-04	4.515428D-03	1.095393D-02	9.441199D-01	4.013569D-02	9.911585D-06	8.000D-01	9.664D 01	2.555D 00
17	1.232648D-04	3.364990D-03	1.004380D-02	9.464730D-01	3.998502D-02	9.867440D-06	6.828D-01	9.681D 01	2.502D 00
18	5.727227D-05	2.504517D-03	9.180830D-03	9.485216D-01	3.972591D-02	9.833002D-06	5.900D-01	9.696D 01	2.446D 00
19	2.659871D-05	1.861759D-03	8.365265D-03	9.504224D-01	3.931424D-02	9.723796D-06	5.140D-01	9.710D 01	2.385D 00
20	1.234947D-05	1.382093D-03	7.596372D-03	9.523177D-01	3.868196D-02	9.513020D-06	4.502D-01	9.723D 01	2.315D 00
21	5.868801D-06	1.046331D-03	6.947774D-03	9.529991D- 1	3.899134D-02	9.539364D-06	4.003D-01	9.730D 01	2.298D 00
22	2.787832D-06	7.898902D-04	6.321799D-03	9.534277D-01	3.944824D-02	9.585322D-06	3.559D-01	9.735D 01	2.289D 00
23	1.323584D-06	5.941070D-04	5.718031D-03	9.535463D-01	4.013058D-02	9.670132D-06	3.157D-01	9.739D 01	2.293D 00
24	6.279023D-07	4.446773D-04	5.135879D-03	9.532532D-01	4.115581D-02	9.849297D-06	2.791D-01	9.741D 01	2.316D 00
25	2.974745D-07	3.306524D-04	4.574618D-03	9.523832D-01	4.270106D-02	1.020075D-05	2.453D-01	9.739D 01	2.365D 00
26	1.405820D-07	2.436582D-04	4.033415D-03	9.506792D-01	4.503288D-02	1.070534D-05	2.139D-01	9.733D 01	2.454D 00
27	6.611503D-08	1.772957D-04	3.511358D-03	9.477483D-01	4.855119D-02	1.180330D-05	1.844D-01	9.721D 01	2.604D 00
28	3.078726D-08	1.266792D-04	3.007499D-03	9.429993D-01	5.385261D-02	1.390178D-05	1.567D-01	9.700D 01	2.844D 00
29	1.403870D-08	8.808289D-05	2.520931D-03	9.355532D-01	6.181984D-02	1.790853D-05	1.305D-01	9.665D 01	3.219D 00
30	6.106553D-09	5.867049D-05	2.050917D-03	9.241228D-01	7.374208D-02	2.553603D-05	1.055D-01	9.610D 01	3.792D 00

Table I-31. Analysis of TETF

CRYOGENIC DISTILLATION OF HYDROGEN ISOTOPES FOR ANL/TETF, ...B. MISRA...., APRIL 1976

ANALYTICAL RESULTS AT PT= 5.0000 02 TORR AFTER 2 ITERATIONS FOR COLUMN NO: 5
NUMBER OF THEORETICAL STAGES: 30 REFLUX RATIO L/D1= 2.0000 01
FIRST FEED PLATE LOCATION: 10 2ND FP LOCATION: 12 3RD FP LOCATION= 15
FEED RATES: 0.0 0.0 5.000 00 DISTILLATE: 2.000 00 BOTTOMS: 1.000 00

FEED COMP.H-H2	HD	HT	H-D2	DT	H-T2	APH	APD	APT
1.9157720-02	8.9221310D-02	6.7391910-02	4.2966280-01	1.5750330-03	1.2559680-03	2.3960 00	8.7060 01	3.5480 00

SUMMATION OF LIQUID MOLE FRACTIONS.....(FROM L TO R IN ASCENDING ORDER OF PLATE NUMBER)

9.9999830-01	9.9999470-01	9.9999900-01	9.9999920-01	9.9999950-01	9.9999960-01
9.9999940-01	9.9999990-01	1.0000000D 00	1.0000000D 00	1.0000000D 00	1.0000000D 00
1.0000000D 00	1.0000000D 00	1.0000000D 00	1.0000000D 00	1.0000000D 00	1.0000000D 00
1.0000000D 00	1.0000000D 00	1.0000000D 00	1.0000000D 00	1.0000000D 00	1.0000000D 00
1.0000000D 00	1.0000000D 00	1.0000000D 00	1.0000000D 00	1.0000000D 00	1.0000000D 00

EQUILIBRIUM STAGE TEMPERATURES, DEG.K..(FROM L TO R IN ASCENDING ORDER OF PLATE NUMBER)

2.4116752D 01	2.4291690 01	2.4376430 01	2.4435030 01	2.4476170 01	2.4505950 01
2.4526560 01	2.4541940 01	2.4553260 01	2.4561660 01	2.4567950 01	2.4572700 01
2.4576320 01	2.4579110 01	2.4581280 01	2.4582860D 01	2.4611050 01	2.4620300 01
2.4627360 01	2.4632870 01	2.4637240 01	2.4640770 01	2.4643660 01	2.4646050 01
2.4648060 01	2.4649770 01	2.4651250 01	2.4652570 01	2.4653760 01	2.4654980 01

PLATE NO.	H-H2	HD	HT	H-D2	DT	H-T2	APH	APD	APT
1	4.7859421D-02	2.0032260-01	1.6719430-01	5.8455370-01	3.3456050-05	9.3542000-12	2.3170 01	6.4470 01	8.3610 00
2	1.2177030-02	1.3440180-01	1.4027620-01	7.3288110-01	6.2233410-05	2.5643020-11	1.3930 01	7.9010 01	7.0170 00
3	6.7681750-03	8.5708420-02	1.2453250-01	7.8291080-01	8.0084710-05	4.0207220-11	1.1190 01	8.2580 01	6.2310 00
4	4.1450980-03	6.4998820-02	1.1965580-01	8.2109950-01	1.0073930-04	6.1663960-11	9.3470 00	8.5160 01	5.4880 00
5	2.9121940-03	5.0425550-02	9.6346480-02	8.5017110-01	1.2470760-04	9.1227230-11	7.6120 00	8.7540 01	4.8245 00
6	2.1732870-03	4.0339350-02	8.4835490-02	8.7229950-01	1.5260870-04	1.3479630-10	6.4960 00	8.9250 01	4.2490 00
7	2.1146120-03	3.3434980-02	7.5099800-02	8.8916680-01	1.8517950-04	1.9746420-10	5.6380 00	9.0690 01	3.7680 00
8	1.9912630-03	2.8742640-02	6.6985790-02	9.0205500-01	2.2329090-04	2.8773140-10	4.9860 00	9.1950 01	3.3600 00
9	1.9348980-03	2.5569130-02	6.0299320-02	9.1193070-01	2.6796880-04	4.1746490-10	4.4870 00	9.2480 01	3.0280 00
10	1.9057100-03	2.3426040-02	5.4827690-02	9.1952020-01	3.2041980-04	6.0391600-10	4.1030 00	9.3140 01	2.7570 00
11	1.8903000-03	2.1982180-02	5.0377410-02	9.2536800-01	3.8206340-04	8.7166280-10	3.8070 00	9.3660 01	2.5380 00
12	1.8816010-03	2.1009800-02	4.6772120-02	9.2944290-01	4.5456910-04	1.2560830-09	3.5770 00	9.4060 01	2.3610 00
13	1.8761180-03	2.0351790-02	4.3463370-02	9.3237160-01	5.3990160-04	1.8077390-09	3.3980 00	9.4380 01	2.2200 00
14	1.8728760-03	1.9907320-02	4.1514140-02	9.3606530-01	6.4037140-04	2.5992070-09	3.2580 00	9.4630 01	2.1080 00
15	1.8704950-03	1.9605620-02	3.9626850-02	9.3813830-01	7.5870640-04	3.7344770-09	3.1490 00	9.4830 01	2.0190 00
16	1.8889490-04	1.4383620-02	3.5014980-02	9.4890440-01	7.7408340-04	3.7610750-09	2.5620 00	9.5650 01	1.6789 00
17	4.5020780-04	1.0513880-02	3.0812310-02	9.5742700-01	7.9162280-04	3.7897320-09	2.1120 00	9.6310 01	1.5800 00
18	2.2013880-04	7.6734760-03	2.7020160-02	9.6427360-01	8.1260770-04	3.8249730-09	1.7570 00	9.6850 01	1.3920 00
19	1.0747810-04	5.5863630-03	2.3621520-02	9.6984610-01	8.3851860-04	3.8733400-09	1.4710 00	9.7310 01	1.2230 00
20	5.2411170-05	4.0596570-03	2.0599260-02	9.7442650-01	8.7115680-04	3.9434310-09	1.2380 00	9.7690 01	1.0730 00
21	2.5531640-05	2.9452040-03	1.7896310-02	9.7822020-01	9.1278420-04	4.0500030-09	1.0450 00	9.8010 01	9.4050-01
22	1.2429450-05	2.1330110-03	1.5508620-02	9.8117970-01	9.6628670-04	4.2149350-09	8.8330-01	9.8290 01	8.2370-01
23	6.0461420-06	1.5413460-03	1.3396780-02	9.8401990-01	1.0353770-03	4.4729350-09	7.4750-01	9.8530 01	7.2160-01
24	2.9389560-06	1.1120010-03	1.1531990-02	9.8622820-01	1.1244540-03	4.8787080-09	6.3250-01	9.8710 01	6.3280-01
25	1.4273730-06	7.9971400-04	9.8875150-03	9.8807040-01	1.2409350-03	5.5386000-09	5.3450-01	9.8910 01	5.5640-01
26	6.9237540-07	5.7294950-04	8.4384810-03	9.8959580-01	1.3916850-03	6.5289540-09	4.5070-01	9.9060 01	4.9150-01
27	3.3511370-07	4.0847820-04	7.1637520-03	9.9084990-01	1.5875700-03	8.1253210-09	3.7860-01	9.9180 01	4.3760 01
28	1.6156870-07	2.8916600-04	6.0422360-03	9.9184620-01	1.8421800-03	1.0647120-08	3.1660-01	9.9290 01	3.9120-01
29	7.7262630-08	2.0267030-04	5.0563720-03	9.9256770-01	2.1711540-03	1.4633410-08	2.6300-01	9.9380 01	3.615 -01
30	1.6125090-08	1.3994770-04	4.1931750-03	9.9316640-01	2.6031800-03	2.0926520-08	2.1650-01	9.9440 01	3.4970-01

Table I-32. Analysis of TEFF

CRYOGENIC DISTILLATION OF HYDROGEN ISOTOPES FOR AEL/TEFF, ...R. MICHA...., APRIL 1976

ANALYTICAL RESULTS AT PT= 5.0000 02 TORR AFTER 4 ITERATIONS FOR COLUMN NO: 5
NUMBER OF THEORETICAL STAGES: 10 REFLUX RATIO L/D1= 2.0000 01
FIRST FEED PLATE LOCATION: 10 2ND FP LOCATION: 12 3RD FP LOCATION: 14
FEED RATES: 0.0 0.0 5.500 00 DISTILLATE: 2.500 00 BOTTOMS: 3.000 00

FEED COMP. N-H2	HD	HT	N-D2	DT	N-T2	APH	APD	APT
8.7104990-01	1.4877470-01	4.1682660-01	7.7905610-01	5.7401290-02	1.1072390-01	8.5570 00	4.8210 01	3.2300 00

SUMMATION OF LIQUID MOLE FRACTIONS.....(FROM L TO R IN ASCENDING ORDER OF PLATE NUMBER)

9.9995150-01	9.9996440-01	9.9997400-01	9.9998210-01	9.9998860-01	9.9999360-01
9.9999720-01	9.9999970-01	1.0000010 00	1.0000020 00	1.0000010 00	1.0000030 00
1.0000030 00	1.0000020 00	1.0000020 00	1.0000010 00	1.0000000 00	9.9999960-01
9.9999920-01	9.9999810-01	9.9999660-01	9.9999480-01	9.9999480-01	9.9999270-01
9.9999730-01	9.9999660-01	9.9999640-01	9.9999590-01	9.9999520-01	9.9999440-01

EQUILIBRIUM STAGE TEMPERATURES, DEG.K..(FROM L TO R IN ASCENDING ORDER OF PLATE NUMBER)

2.4141560 01	2.4307000 01	2.4397970 01	2.4462190 01	2.4507250 01	2.4534240 01
2.4559590 01	2.4574190 01	2.4584800 01	2.4594230 01	2.4598050 01	2.4602640 01
2.4606620 01	2.4610340 01	2.4614070 01	2.4632330 01	2.4645460 01	2.4655030 01
2.4662220 01	2.4667830 01	2.4672450 01	2.4676510 01	2.4680390 01	2.4684190 01
2.4688810 01	2.4693920 01	2.4700350 01	2.4707530 01	2.4716760 01	2.4728200 01

PLATE NO.	N-H2	HD	HT	N-D2	DT	N-T2	APH	APD	APT
1	1.9162860-02	3.2702120-01	1.0740370-02	6.4166460-01	1.3636030-03	6.7422510-07	1.8800 01	4.0590 01	6.0530-01
2	4.9218130-03	1.9544590-01	9.9438230-03	7.0817070-01	2.5159360-03	2.3041070-06	1.0210 01	9.4220 01	5.7320-01
3	2.6814790-03	1.3827750-01	7.4989970-03	8.6792090-01	3.2175360-03	3.6933730-06	7.5770 00	9.1670 01	5.5620-01
4	1.6367190-03	1.0424340-01	6.0116240-03	8.8313540-01	4.0166920-03	5.5635430-06	5.7240 00	9.1730 01	5.4700-01
5	1.1556090-03	8.0481410-02	4.8322570-03	9.0736010-01	4.9303190-03	8.2363720-06	4.4410 00	9.5010 01	5.4490-01
6	9.3506560-04	6.4112790-02	3.8777160-03	9.2164270-01	5.9796180-03	1.2044930-05	3.5630 00	9.5870 01	5.6410-01
7	8.1165940-04	5.2997600-02	3.0458910-03	9.3411440-01	7.1939960-03	1.7464730-05	2.9660 00	9.6440 01	5.9360-01
8	7.4644940-04	4.5512390-02	2.4253220-03	9.4095550-01	8.5953490-03	2.5231960-05	2.5630 00	9.6900 01	6.3850-01
9	7.6407470-04	4.0497290-02	1.9013680-03	9.4477420-01	1.0227130-02	3.6273750-05	2.2860 00	9.7010 01	7.0000-01
10	7.5303810-04	3.7146180-02	1.3577660-03	9.4656420-01	1.2127840-02	5.1933960-05	2.1000 00	9.7120 01	7.7950-01
11	7.4729760-04	3.4904110-02	3.0812550-03	9.4684540-01	1.4343580-02	7.4437680-05	1.9740 00	9.7150 01	8.7870-01
12	7.4405990-04	3.3410520-02	2.0591300-01	9.4595270-01	1.6727310-02	1.0624630-04	1.8880 00	9.7110 01	9.9990-01
13	7.4291510-04	3.2403170-02	2.6404720-01	9.4438240-01	1.9939610-02	1.5150400-04	1.8280 00	9.7030 01	1.1860 00
14	7.4053480-04	3.1714630-02	2.5377160-01	9.4111810-01	2.3848930-02	2.1582420-04	1.7870 00	9.6890 01	1.3210 00
15	7.3929960-04	3.1285040-02	2.4225360-01	9.3775360-01	2.7512640-02	3.0720200-04	1.7570 00	9.6710 01	1.5280 00
16	3.5575960-04	2.2437820-02	2.0995660-01	9.4647710-01	2.8319460-02	3.0997450-04	1.2620 00	9.7190 01	1.5520 00
17	1.7071520-04	1.6059750-02	1.8124300-01	9.5241480-01	2.9229120-02	3.1330520-04	9.1075-01	9.7510 01	1.5830 00
18	8.1751360-05	1.1466420-02	1.5593240-01	9.5625710-01	3.0317730-02	3.1766650-04	6.5950-01	9.7710 01	1.6260 00
19	3.9048140-05	8.1704940-01	1.3373020-01	9.5847670-01	3.1651750-02	3.2362150-04	4.7910-01	9.7840 01	1.6820 00
20	1.8667020-05	5.8129210-03	1.1447850-01	9.5938210-01	3.3104950-02	3.3122770-04	3.4780-01	9.7890 01	1.7560 00
21	8.9656960-06	4.1288660-03	9.7742140-04	9.5915530-01	3.4593890-02	3.4063710-04	2.5620-01	9.7840 01	1.8530 00
22	4.2449060-06	2.9240620-03	8.3213140-04	9.5787710-01	3.7992510-02	3.6506420-04	1.8860-01	9.7810 01	1.9750 00
23	2.0215210-06	2.0727330-03	7.0643240-04	9.5556460-01	4.1277900-02	3.9031810-04	1.3920-01	9.7720 01	2.1190 00
24	9.6171290-07	1.4640220-03	5.9783100-04	9.5207710-01	4.5416670-02	4.2420160-04	1.0220-01	9.7550 01	2.3450 00
25	4.5697020-07	1.0311460-03	5.0387140-04	9.4732380-01	5.0626040-02	5.1501870-04	7.6800-02	9.7320 01	2.6090 00
26	2.1675140-07	7.2352800-04	4.2272960-04	9.4105680-01	5.7121710-02	6.2496910-04	5.7330-02	9.7030 01	2.9420 00
27	1.0251820-07	5.0939010-04	3.5265060-04	9.3297610-01	6.5375040-02	7.9505450-04	4.2900-02	9.6590 01	3.3660 00
28	4.8243410-08	3.5308110-04	2.9213720-04	9.2268440-01	7.5617960-02	1.0494170-03	3.2120-02	9.6070 01	3.9010 00
29	2.2556910-08	2.4021280-04	2.3993040-04	9.0972420-01	8.7156510-02	1.4331560-03	2.4010-02	9.5430 01	4.5740 00
30	1.0370140-08	1.6243780-04	1.9483170-04	8.9351460-01	1.0002900-01	2.0249130-03	1.7860-02	9.4570 01	5.4186 00

the ANL/EPR. The analytical results show that enrichment of the spent fuel sufficient to meet the fuel injection requirements of ANL/EPR can be carried out in a straightforward manner.

Similar analytical studies of spent fuel enrichment for the ANL/TETF show that complete recycling of the fuel for a totally beam driven device is possible with an enrichment system consisting of only five distillation columns and two chemical equilibrators.

The most important conclusion that may be drawn from the study of the two systems is that, aside from meeting fuel injection requirements, separation of the isotopomeric species of hydrogen can be carried out to any degree of purity by judicious selection of (1) the design and operating parameters (e.g. number of theoretical stages, reflux ratio, operating pressure, etc.) and (2) the number of distillation columns, appropriately interspersed with chemical equilibrators.

---

1. R. H. Perry and C. H. Chilton, Chemical Engineers Handbook, McGraw-Hill Publishing Co., (1973).

2. N. R. Amundson, Mathematical Methods in Chemical Engineering, Matrices and Their Applications, Prentice Hall, (1966).

3. B. D. Smith, Design of Equilibrium Stage Processes, McGraw-Hill Publishing Co., (1963).

4. H. M. Mittelhauser, and G. Thodos, "Vapor Pressure Relationship up to Critical Point of Hydrogen, Deuterium and Tritium, and Their Atomic Combinations," [illegible], 8, 368 (1964).

5. B. Misra, "A Computer Program for Design of Multicomponent Distillation Columns," Argonne National Laboratory, June, 1976.

6. W. M. Stacey, Jr., et al., "Tokamak Engineering Technology Facility Scoping Study," ANL/CTR-76-1, Argonne National Laboratory (March 1976).

APPENDIX J

NONCIRCULAR PLASMA CONSIDERATIONS*

In comparison with circular cross-section tokamaks with similar values of β_p and q, noncircular cross-section tokamaks have the following advantages: (1) noncircular tokamaks offer the potential for achieving larger values of β_t and, hence, total power;[1] (2) certain noncircular shapes, in particular the "D", are predicted to be more stable;[2-4] and (3) noncircular plasmas fill the available volume inside a "pure-tension" toroidal-field coil more efficiently. For these reasons, a noncircular design, which would fit inside the same TF coils as the circular design, was considered.

The MHD calculations use the free boundary method described in Appendix C, except that the original Princeton code has been modified to calculate stability criteria associated with quasi-rigid motions.[5] The pressure and $F = RB_t$ are taken to be essentially the same as given in Eqs. C-30 and C-31 with $\alpha = \beta = 1.4$. The flux function, ψ; the flux surfaces (ψ = constant); the pressure, p; and the current density, J_t, are shown in Figure J-1. The shape factor, ℓ, the ratio of the circumference of the boundary to that of a circle with the same width, is 1.2. The height to width ratio, κ, is 1.3 and is the largest elongation that can be obtained without violating stability criteria for localized interchange modes[6,7] and for quasi-rigid motions (horizontal and vertical displacements and flipping).[2,5] The usual criteria that the decay index of the field should be greater than zero[8] applies to a circular plasma with uniform current density and large aspect ratio and is not used. Stability with respect to general kink modes is assured by requiring $q(\psi) > 1$ over the plasma cross-section.

---

* The MHD equilibrium and stability calculations in this appendix were performed by T. Yang and R. Conn, Nuclear Engineering Department, University of Wisconsin, Madison, Wisconsin. A more detailed presentation of these results will be published in the UW-FDM series of reports.

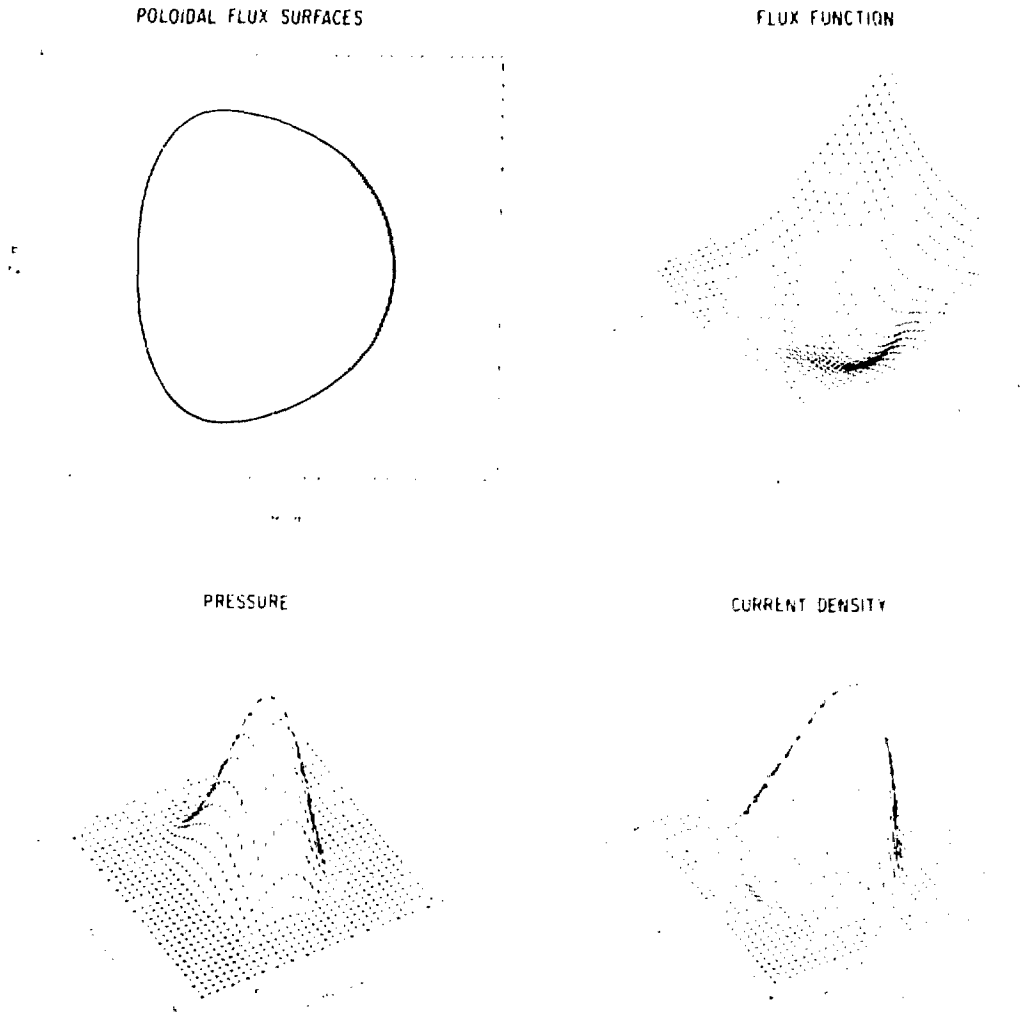

Figure J-.. Noncircular Plasma Distribitions

The pressure and current density on the midplane are shown in Figure J-2. The pressure is shifted substantially (0.7 m) from the center of the chamber. The current is shifted even more (1.2 m) toward the outside and has a small region of current reversal near the inside edge.

The plasma parameters are shown in Table J-1. The performance parameters are obtained using the global model described in Appendix C and the calculational procedure described in Chapter III. It should be noted that the plasma center, the minor radius, the toroidal field, and the pressure profile exponent were chosen slightly different from the corresponding values for the circular reference design in Table III-1. The noncircular plasma clearly has superior performance parameters. In spite of the slightly sharper profile, it can be seen that β_t is 25% higher and I_p is 11% higher than for the circular reference design of Chapter III. This results in 20% higher densities and a 15% lower τ_{TIM}. These improvements, coupled with the 37% greater volume of the noncircular plasma, lead to better than a factor of two increase in power with only a 70% increase in wall loading. The noncircular plasma design is definitely attractive from the standpoint of power performance.

The reference plasma cross-section can be maintained with equilibrium field coils located outside the toroidal field coils. This would not be possible for more elongated or more complicated plasma cross-sections. The equilibrium coil locations and the currents in the coils are shown in Table J-2. No attempt was made to decouple the equilibrium coils from the ohmic heating coils, as was done for the reference design in Chapter IV.

---

1. T. Ohkawa and T. H. Jensen, "Parameter Studies for Tokamaks and Doublets," *Plasma Physics*, 13, 789 (1971).

2. E. Rebhan, "Stability Boundaries of Tokamaks with Respect to Rigid Displacements," *Nuclear Fusion*, 15, 277 (1975).

3. J. P. Freidberg and W. Grossman, "Magnetohydrodynamic Stability of a Sharp Boundary Model of Tokamak," *Phys. Fluids*, 18, 1494 (1975).

Table J-1. Noncircular Plasma Performance Reference Design Summary -- Steady-State Conditions

Beta poloidal, β_p	1.9	
Beta toroidal, β_t	0.060	
Safety factor, q(0)	1.00	
Safety factor, $q(\psi_\ell)$	3.10	
Plasma center, R_0 (m)	6.30	
Magnetic axis, R_m (m)	7.00	
Minor radius, a (m)	2.15	
Aspect ratio, A	2.94	
Height-to-width ratio, κ	1.0	
Shape factor, ϵ	1.2	
Volume, V_p (m^3)	747	
Profile exponents		
Pressure, $\alpha = \beta$	1.4	
Density, α_n	0.3	
Temperature, α_T	1.1	
Diamagnetic/paramagnetic parameter, δ	0.098	
Plasma temperature, $\bar{T}_e$ (keV)	10.0	
Plasma temperature, $\bar{T}_{DT}$ (keV)	9.6	
Confinement required for ignition, $n\tau_E$ (s/m^3)	2.4×10^{20}	
Impurity (%)		
^{16}O	0.5	
^{9}Be	5.0	
Effective charge, $\bar{Z}_{eff}$	1.3	
Peak field at TF coils, B_{max}^{TFC} (T)	10.0	8.0
Vacuum field at centerline, B_{t0} (T)	4.32	3.46
Vacuum F, F_0 (T)	27.2	21.8
Plasma current, I_p (MA)	8.40	6.72
Plasma pressure (Nt/m^2)		
Peak, p_0	13.0×10^5	8.3×10^5
Average, $\bar{p}$	4.4×10^5	2.8×10^5
Flux function (Wb)		
Magnetic axis, ψ_m	0.0	0.0
Limiter, ψ_ℓ	47.9	38.3
Density (m^{-3})		
D-T, $\bar{n}_{DT}$	1.1×10^{20}	7.2×10^{19}
Electron, $\bar{n}_e$	1.2×10^{20}	7.8×10^{19}
Alpha, $\bar{n}_\alpha$	1.3×10^{18}	8.3×10^{17}
Thermonuclear power, P_T (MWt)	1310	539
Neutron wall load, P_w (MW/m^2)	1.44	0.59
Ratio of $n\tau$ required for ignition to $n\tau$ predicted by TIM, α_{TIM}	0.9	3.4

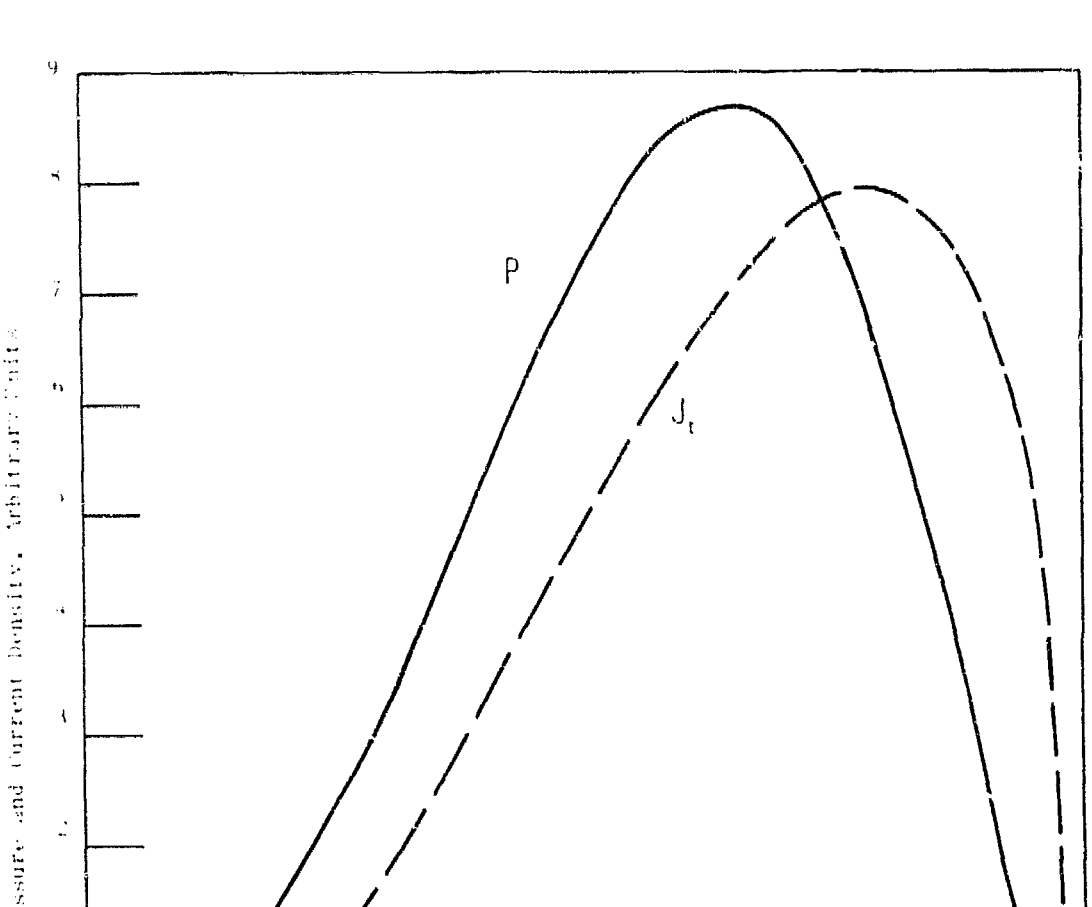

Figure J-[illegible]. The Pressure and Current Density Profiles on the Midplane for the Noncircular Reference Design

Table J-2. Equilibrium Field Coils for the Noncircular Design

Number	Z[a] (m)	R[a] (m)	I (MA)
1	0.0	2.0	- 0.230
2	1.0	2.0	- 0.230
3	4.0	2.0	+ 1.110
4	5.0	2.2	- 0.294
5	7.5	5.0	- 10.012
6	7.8	6.5	- 1.200
7	7.5	6.5	- 0.920
8	7.0	6.5	- 1.473
9	6.9	7.4	- 1.473
10	6.3	8.5	- 1.473
11	5.3	9.7	- 1.473
12	3.8	11.0	- 1.110
13	1.8	11.8	- 1.110
14	0.0	11.8	- 1.110

[a] Z is the vertical displacement from the horizontal mid-plane and R is the radial displacement from the major toroidal axis. Coils are located symmetrically above and below the horizontal midplane.

4. K. E. Weimer, E. A. Frieman, and J. L. Johnson, "Localized Magneto-hydrodynamic Instabilities in Tokamaks with Noncircular Cross Sections," *Plasma Physics*, 17, 645 (1975).

5. T. Yang and R. Conn, "Computational Study of MHD Equilibrium of Noncircular Tokamak Reacto lasmas," to be published in IEEE Transactions of Plasma Science.

6. A. H. Glasser, J. M. Greene, and J. L. Johnson, "Resistive Instabilities in General Toroidal Plasma Configuration," *Phys. Fluids*, 19. 567 (1976).

7. U. Ascoli-Bortoli, et al., "High and Low Current Density Plasma Experiments within the MIT Alcator Programme," Fifth IAEA Conference on Plasma Physics and Controlled Nuclear Fusion Research, 1974, (IAEA, Vienna, 1975), Vol. 1, p. 191.

8. S. Yoshikawa, "Application of the Virial Theorem to Equilibria of Toroidal Plasmas," *Phys. Fluids*, 7, 278 (1964).